

Università degli Studi di Ferrara  
Dipartimento di Fisica e Scienze della Terra



# Innovative applications of strong crystalline field effects to particle accelerators and detectors

---

PHD IN PHYSICS

TUTOR

Prof. Vincenzo Guidi

*Università degli Studi di Ferrara*

*INFN Sezione di Ferrara*

AUTHOR

Mattia Soldani

*Università degli Studi di Ferrara*

*INFN Sezione di Ferrara*

COTUTOR

Dr. Laura Bandiera

*INFN Sezione di Ferrara*

Ferrara, June 2023





*Di Inferno della Valtellina e polenta uncia,  
di lambrusco e cappellacci di zucca al ragù*

*To both our best and worst selves*



# Contents

<b>Introduction</b>	<b>1</b>
<b>1 Electromagnetic interactions in oriented crystals</b>	<b>5</b>
1.1 Crystalline matter . . . . .	6
1.1.1 Crystalline lattices . . . . .	6
1.1.2 Single-atom potential . . . . .	10
1.2 Particle motion in an oriented crystal . . . . .	13
1.2.1 Axial (and planar) continuous potential . . . . .	13
1.2.2 Particle dynamics in the lattice . . . . .	16
1.2.3 Bound versus unbound motion . . . . .	17
1.2.4 Axial channelling . . . . .	18
1.3 Electromagnetic radiation by a moving charged particle . . . . .	22
1.3.1 Bethe-Heitler bremsstrahlung . . . . .	23
1.3.2 Radiation formation length . . . . .	27
1.3.3 Channelling radiation . . . . .	28
1.3.4 Coherent bremsstrahlung . . . . .	32
1.4 Crystalline strong field and shower enhancement . . . . .	33
1.4.1 The strong field regime in crystals . . . . .	35
1.4.2 Strong field radiation . . . . .	36
1.4.3 Strong field and photons . . . . .	38
1.4.4 Compact electromagnetic showers . . . . .	42
1.4.5 Behaviour at extremely high energies . . . . .	45
<b>2 Experimental techniques</b>	<b>47</b>
2.1 The AXIAL/ELIOT/STORM project . . . . .	48
2.1.1 Heavy metals . . . . .	49
2.1.2 Inorganic scintillating crystals . . . . .	51
2.2 The experimental facilities . . . . .	53
2.2.1 DESY T21 . . . . .	54
2.2.2 The CERN NA beamlines . . . . .	55
2.3 SF (and sub-SF) measurements . . . . .	58

2.3.1	The detectors . . . . .	60
2.3.2	Sample (pre-)alignment . . . . .	70
2.3.3	Measurement of the electromagnetic radiation . . . . .	71
2.3.4	Measurement of the pair production . . . . .	74
2.3.5	Measurement of the total output energy . . . . .	77
2.4	Monte Carlo simulation tools . . . . .	78
2.4.1	Sub- $X_0$ crystals . . . . .	79
2.4.2	Multi- $X_0$ crystals . . . . .	80
<b>3</b>	<b>An optimised positron source for next-generation lepton col- liders</b>	<b>83</b>
3.1	Positron source schemes and features . . . . .	84
3.1.1	Novel concepts . . . . .	87
3.1.2	The FCC- $ee$ requirements . . . . .	89
3.2	The FCC- $ee$ hybrid source radiator: an experimental study . . . . .	92
3.2.1	The sample(s) . . . . .	92
3.2.2	Photon energy and multiplicity at 5.6 GeV . . . . .	93
3.3	Towards the FCC- $ee$ PS full simulation . . . . .	99
3.3.1	The two-stage setup . . . . .	99
3.3.2	Crystalline radiator . . . . .	100
3.3.3	Amorphous target optimisation . . . . .	103
3.3.4	Collimator or/and magnet? . . . . .	111
3.3.5	Result summary . . . . .	112
<b>4</b>	<b>A highly efficient photon converter for the HIKE beamline</b>	<b>117</b>
4.1	The HIKE experiment and beamline . . . . .	118
4.1.1	Physics motivation . . . . .	119
4.1.2	The HIKE experimental setup . . . . .	122
4.2	Pair production measurements in oriented tungsten . . . . .	130
4.2.1	The sample . . . . .	130
4.2.2	Analysis and simulation strategy and results . . . . .	131
4.2.3	Final comments . . . . .	137
<b>5</b>	<b>Towards ultra-compact homogeneous calorimeters</b>	<b>143</b>
5.1	Homogeneous calorimetry . . . . .	144
5.1.1	Energy resolution . . . . .	145
5.1.2	Segmentation, spatial and angular resolution . . . . .	147
5.1.3	Particle identification . . . . .	148
5.2	Scintillation in PWO . . . . .	149
5.2.1	PWO-II . . . . .	151
5.2.2	PWO-UF . . . . .	152

5.3	Oriented detectors: preliminary studies with electrons . . . . .	153
5.3.1	The samples under test . . . . .	154
5.3.2	Simulations . . . . .	161
5.3.3	Sample alignment . . . . .	166
5.3.4	Output radiative energy loss . . . . .	169
5.3.5	Scintillation light and energy deposit . . . . .	174
5.3.6	Total output energy and setup hermeticity . . . . .	180
5.3.7	Angular range . . . . .	182
5.4	Future applications . . . . .	186
5.4.1	OREO . . . . .	186
5.4.2	The HIKE SAC . . . . .	187
5.4.3	Satellite-borne calorimeter . . . . .	188
<b>Conclusions</b>		<b>191</b>
<b>A Calorimeter calibrations</b>		<b>195</b>
A.1	General information . . . . .	195
A.2	Genni at the 2019 beamtest on DESY T21 . . . . .	198
A.3	Lead glass blocks on CERN H2 . . . . .	200
A.3.1	Single-block performance . . . . .	200
A.3.2	The 2022 hibiscus-like configuration . . . . .	203
<b>B Radiation and heating in tungsten towards the FCC-<i>ee</i> in-</b>		<b>207</b>
<b>tensity</b>		
B.1	The MAMI B beamtest facility . . . . .	207
B.2	Crystalline tungsten irradiation at the MAMI B hall . . . . .	209
B.3	Amorphous tungsten irradiation at the MAMI B dump . . . . .	211
B.3.1	The simulation software . . . . .	212
B.3.2	Defining the mesh . . . . .	213
B.3.3	Beam parameters and heating . . . . .	215
<b>C KLEVER 2018 data conditioning</b>		<b>219</b>
C.1	Context . . . . .	219
C.2	$\gamma$ -CAL time drift stabilisation . . . . .	221
C.3	<i>e</i> -CAL time drift stabilisation . . . . .	223
C.4	<i>e</i> -CAL response linearisation and calibration correction . . . . .	228
<b>List of acronyms</b>		<b>233</b>
<b>List of figures</b>		<b>241</b>
<b>List of tables</b>		<b>243</b>

<b>Bibliography</b>	<b>245</b>
<b>Hall of Fame</b>	<b>261</b>

# Introduction

The electromagnetic interactions of the particles that cross crystals nearly aligned to the ordered distributions of atoms of the crystalline lattice – that is, the atomic planes and axes – undergo substantial modifications with respect to the processes that commonly occur in amorphous media. The lattice electromagnetic field experienced by the particles results from the coherent contribution of all the single atoms, which leads to several different effects: for instance, in the so-called channelling, the charged particles are forced into an oscillatory motion in transverse potential wells delimited by the atomic structures. Depending on the energy and incident beam-to-lattice angle, electrons and positrons emit characteristic electromagnetic radiation, either when channelled or, for instance, when periodically crossing multiple planes or axes – as in the so-called coherent bremsstrahlung radiation emission.

Moreover, at high energy, the relativistic length contraction makes the lattice atomic density appear significantly higher in the particle frame, and an extremely strong electromagnetic field is attained. At the multi-GeV scale, this field overtakes the critical field of quantum electrodynamics, which results in a dramatic enhancement of the cross sections of the hard photon emission by electrons/positrons and of the photon conversion into charged pairs. As a consequence, the electromagnetic showers in an oriented crystal develop faster than in an amorphous material or in a randomly oriented crystal, or, equivalently, the effective radiation length ( $X_0$ ) is reduced.

Nowadays, the study of the coherent interactions that occur in crystals at high energies is in its golden age. Indeed, the interest of the particle physics community in the aforementioned enhancement has grown dramatically stronger in recent years. The focus is twofold: to fully characterise these phenomena, in order to widen the knowledge of the interactions between particles and matter, and to exploit them for the development of next-generation tools for high-energy physics. Bent crystals with the same steering radius as magnetic fields of hundreds and thousands of tesla are used for beam collimation and extraction and for the high-precision measurement of the electric dipole moment of short-lived hadrons. Straight crystals are used



as high-performance radiators and photon converters. Furthermore, novel applications are frequently considered and tested.

The aim of this thesis work, which has been driven by this momentous interest, is also twofold. The first objective is to provide a comprehensive description of the coherent effects that occur in the multi-GeV regime in high- $Z$ , high-density, axially oriented straight crystals, and of the current status of the experimental studies on the subject. The second objective is to discuss three of the most interesting applications of axially oriented straight crystals to the next-generation particle accelerators and detectors: an optimised positron source for future lepton colliders, a high-efficiency photon converter to eliminate the electromagnetic component of a neutral hadron beam and an ultra-compact, high-performance electromagnetic calorimeter. In practice, the first two chapters define the general framework from both the theoretical and experimental standpoints. Chapter 1 lays the theoretical foundations of the lattice effects to the electromagnetic interactions in crystals. The main focus is put on the strong-field radiation emission and pair production processes, and on the resulting shower development acceleration. On the other hand, chapter 2 describes the beamline facilities – at CERN and DESY – and the experimental techniques exploited in all the measurements performed in the context of this work, as well as the simulation tools used to reproduce all the obtained results.

Each of the remaining three chapters is devoted to the discussion of one of the applications mentioned above and of the corresponding experimental investigation, with a special focus on the beamtests, on the analysis of the resulting data and on the development of the corresponding simulations. Together, these aspects represent the core of this thesis work.

In particular, in chapter 3, the innovative hybrid positron source scheme, which comprises two tungsten targets – one of which is an oriented crystal – is introduced. Moreover, both the experimental characterisation of the radiation emitted by 5.6 GeV in an oriented, 2 mm thick tungsten sample and the development of the simulations of the full-scheme setup currently considered for the FCC- $ee$  are presented. In chapter 4, the pair production measurements performed on a  $\gg X_0$  thick commercial tungsten crystal and their implications in the design of a compact photon converter for the  $K_L$  beamline of the HIKE experiment – currently under development at CERN – are described.

Finally, chapter 5 is devoted to strong-field studies in lead tungstate ( $\text{PbWO}_4$  or PWO), that is, one of the densest and fastest crystalline scintillators, which is frequently used in homogeneous electromagnetic calorimeters without taking its lattice orientation into account. This chapter summarises the extensive set of radiation and shower enhancement measurements performed

---

in recent years, mostly with 120 GeV electron beams, on increasingly thick oriented lead tungstate samples. The significant increase of the scintillation light emitted in the strong crystalline field of lead tungstate has been measured, as a function of the crystal thickness and of the beam-to-axis angle, for the first time worldwide. The goal of this chapter is to demonstrate the feasibility of innovative homogeneous calorimeters that would rival the current state of the art in terms of energy resolution while being more compact and having improved particle identification capabilities. Indeed, this pioneering concept is already considered for applications in both accelerator-based experiments (for instance, the HIKE Small Angle Calorimeter) and space-borne  $\gamma$ -ray detectors on satellites.



# CHAPTER 1

---

## Electromagnetic interactions in oriented crystals

The fact that the features of the interactions between particles and crystalline matter are non-trivially dependent on the orientation of the latter in space has been hypothesised since the beginning of the XX century, that is, soon after the first experimental evidences of the ordered-lattice structure of crystals coming from *X*-ray measurements. In particular, Stark firstly suggested in 1912 that some specific directions in a crystalline lattice should be more transparent than others to the passage of charged particles [1, 2]. The so-called channelling, which forces the trajectories of positively charged particles in between atomic rows, has then been firstly observed in 1963 in Monte Carlo simulations on the diffusion of low-energy heavy ions [3]: unexpectedly, the simulated trajectories that were close to atomic rows ranged macroscopic distances, resulting in a massive increase of the computational cost<sup>1</sup>. This result was soon validated by experimental observations [4] and, during the Sixties, an extensive theoretical framework for channelling was developed by Lindhard [5].

At the same time, extensive investigations were performed on the features of the electromagnetic radiation that electrons and positrons emit when cross-

---

<sup>1</sup>These simulations were performed to study the slowing down of ions at the keV scale in a crystalline lattice. The influence of the lattice orientation on the ion trajectories was expected to be small; on the other hand, a substantially larger penetration depth was observed in case of ions propagating almost parallel to the lattice rows [3].

ing a crystal, which are sensitive to the lattice orientation as well. Firstly, between the end of the Fifties and the beginning of the Sixties, coherent bremsstrahlung was studied theoretically [6] and experimentally [7, 8]. Since then, new effects of the crystalline lattice on the particle interactions have been observed, and theoretical models have been developed to describe them. This chapter provides a phenomenological overview of the theoretical description of the lattice-related effects to the interactions between particles and crystalline matter. After summarising the main features of the crystalline lattice and the corresponding electromagnetic fields and briefly discussing the general properties of channelling in the first half of the chapter, the focus is put on the processes that electromagnetic particles – namely electrons, positrons and photons – undergo across matter and on their modifications in oriented crystals.

## 1.1 Crystalline matter

Before delving into the characterisation of the interactions between particles and crystalline lattices, a description of the latter has to be provided. The following sections aim at laying down the basic crystal properties, briefly covering the general lattice structural and electrostatic features. Further details can be found in [1, 9].

### 1.1.1 Crystalline lattices

A crystal is a solid in which atoms are arranged in an ordered and symmetrical structure, namely, the crystalline lattice or Bravais lattice [1]. The most important symmetry in the lattice is the invariance by translation. In fact, the properties of a crystal are determined by the structure of the simplest non-periodic three-dimensional succession of atoms, the so-called unit cell, whose repetition along three mutually independent spatial directions constitutes the macroscopic lattice [10].

In practice, the unit cell can be described as a three-dimensional parallelepiped of sides  $(a, b, c)$  – the so-called lattice constants – and angles between them  $(a', b', c')$  [1]. Each vertex of this parallelepiped is called a node; the opposite vertices of the cell along any of its sides are occupied by the same atoms and constitute equivalent nodes [1]. Any invariance period  $\overline{\Delta r}$  in the lattice can be written as

$$\overline{\Delta r} = n_a a \hat{a} + n_b b \hat{b} + n_c c \hat{c} \quad (1.1)$$

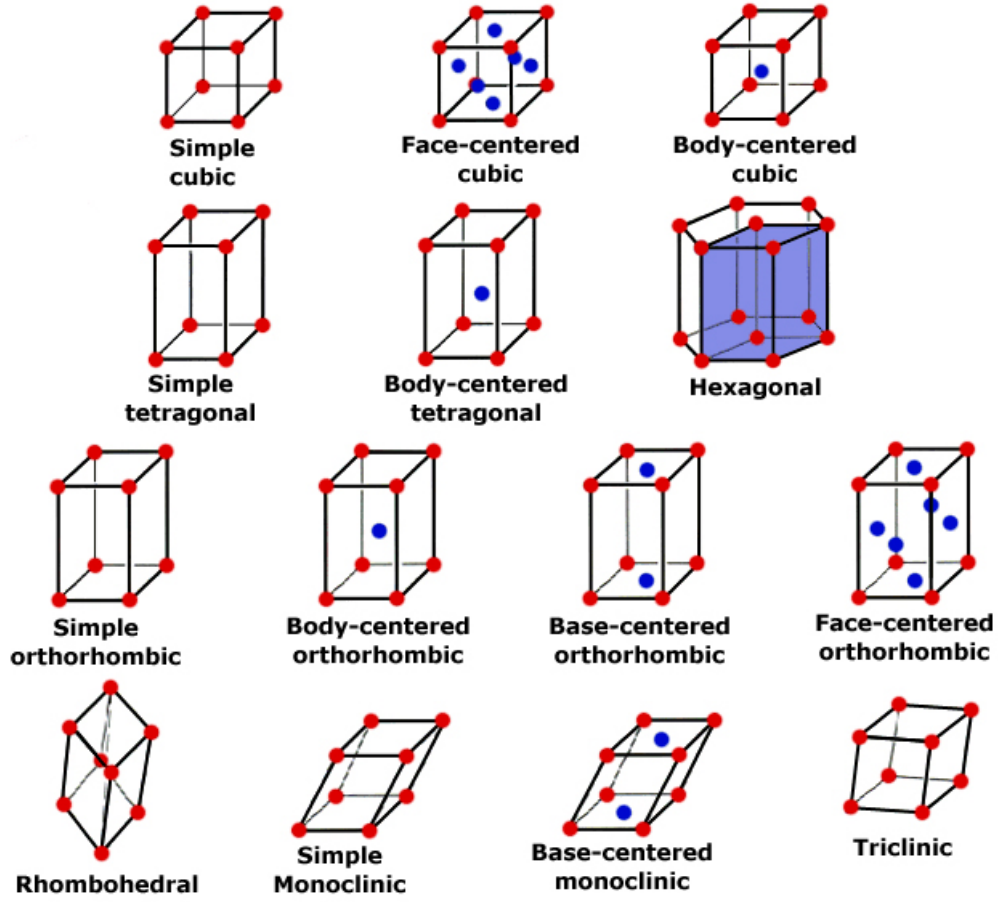


FIGURE 1.1: Types of Bravais lattices. The red (blue) points represent the atoms positioned in the cell nodes (inside the cell faces or body). From [11].

where  $\hat{a}$ ,  $\hat{b}$  and  $\hat{c}$  are the unit vectors that identify the directions of the unit cell sides and  $n_{a,b,c}$  are positive or negative integers, including zero, which address different nodes [1].

In addition to the aforementioned invariance by translation, a lattice can have other symmetries related to, e.g., rotations and reflections [1]. Different combinations of these symmetries come along with different conditions on  $(a, b, c)$  and  $(a', b', c')$ , i.e., different types of unit cells and, hence, of Bravais lattices [1]. Indeed, there are fourteen different types of Bravais lattices [1]. There are different visual representations of these lattice types; an example is provided in figure 1.1.

Each lattice features particular subsets of nodes which belong to a string – i.e., an axis – or plane [1]. In an ideal, infinite-size lattice there are axes and

planes in any orientation; however, their features in terms of, e.g., relative interatomic distances depends on the Bravais lattice type.

A quantitative naming scheme for mutually parallel axes and planes can be found. Planes, for instance, can be described by the equation [1]

$$\frac{n_a}{a_0} + \frac{n_b}{b_0} + \frac{n_c}{c_0} = 1 \quad (1.2)$$

where  $n_{a,b,c}$  are the numbers associated to any node in the plane as in equation 1.1 and  $a_0$ ,  $b_0$  and  $c_0$  are the coordinates of the intersections between the plane and the cell side directions  $\hat{a}$ ,  $\hat{b}$  and  $\hat{c}$  respectively, in units of lattice constants [1]. As  $n_{a,b,c}$  are integers, equation 1.2 is satisfied if  $1/a_0$ ,  $1/b_0$  and  $1/c_0$  are rational numbers, i.e., they can be written as [1]

$$\frac{\tilde{n}}{a_0} = h \quad , \quad \frac{\tilde{n}}{b_0} = k \quad \text{and} \quad \frac{\tilde{n}}{c_0} = l$$

where  $h$ ,  $k$ ,  $l$  and  $\tilde{n}$  are integers. Therefore, equation 1.2 becomes [1]

$$n_a h + n_b k + n_c l = \tilde{n} \quad (1.3)$$

which, for fixed  $h$ ,  $k$ , and  $l$  and different  $\tilde{n}$ , clearly defines all the mutually parallel planes. Conventionally,  $h$ ,  $k$ , and  $l$  are set to the lowest triad of values resulting in the same set of planes.

The numbers  $h$ ,  $k$ , and  $l$  are called Miller indices [1]. Planes are indicated with the notation  $(hkl)$ . On the other hand, the notation  $[hkl]$  addresses the mutually parallel axes that are orthogonal to the  $(hkl)$  planes, whereas the notation  $\langle hkl \rangle$  addresses all the sets of axes that are identical to  $[hkl]$  by invariance by rotation. In typical experiments on the coherent effects, mostly diamond-lattice crystals (e.g., diamond, silicon and germanium) and high- $Z$  metals with cubic lattice are probed. Figure 1.2 shows the Miller indices corresponding to the main axes and planes of the cubic lattice.

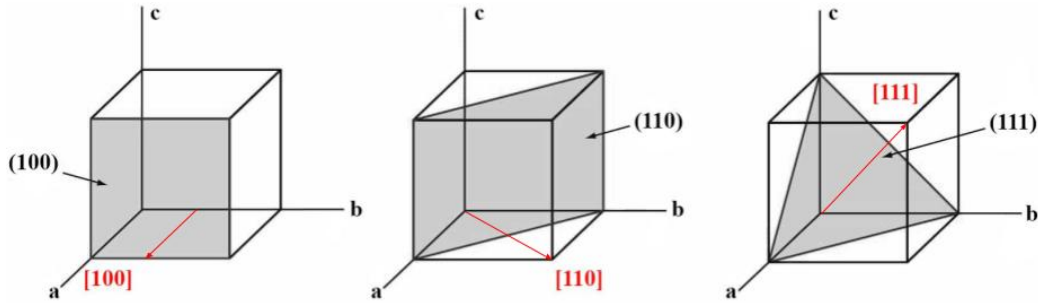


FIGURE 1.2: Miller-index notation for the most commonly studied axes (red) and planes (grey). Edited from [12].

The formalism of the Miller indices can be applied to any type of crystalline lattice. For instance, figure 1.3 shows a rather complex lattice – a two-element tetragonal structure, typical of, e.g., scheelite and lead tungstate – rotated to align different orientations to the page axis. In particular, in figure 1.3a, all the main axes and planes are oriented at a large angle with respect to the page axis. Despite the fact that in an ideal, infinitely wide lattice there are axes and planes in any direction, most of them have very high Miller indices, which in general corresponds to very low atomic density – i.e., these axes/planes are very weak – and overall the lattice appears and behaves almost like an unordered structure, namely, an amorphous medium. In practice, this condition is attained in most orientations: it is therefore typical to call it random orientation.

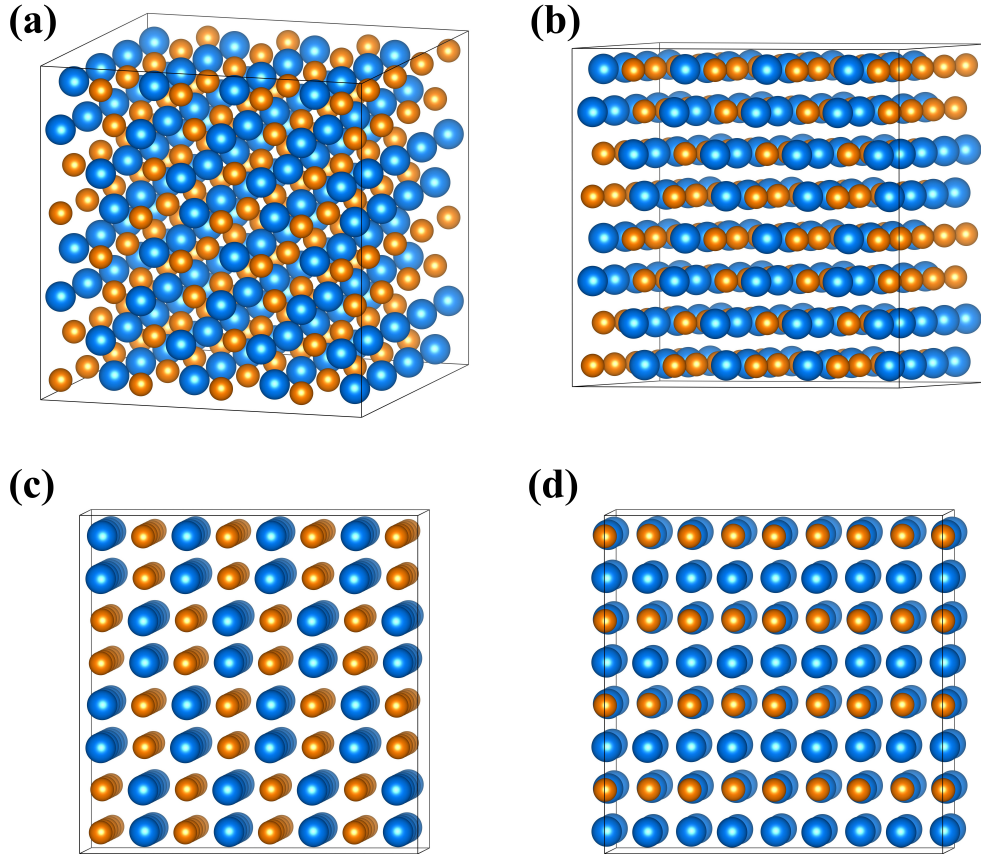


FIGURE 1.3: Lattice composed of two elements arranged in scheelite-like (i.e. tetragonal, two-element) structure, in different orientations: (a) amorphous-like, (b) in the (001) plane, (c) in the  $\langle 100 \rangle$  axis and (d) in the [001] axis.



In figure 1.3b, the (001) plane is orthogonal with respect to the page plane and none of the main axes – i.e., those with low Miller indices – is parallel to the page axis. Gaps in which the density of atomic nuclei is null are observed between neighbouring planes. Eventually, figure 1.3c and d show the axes  $\langle 100 \rangle$  and  $[001]$  respectively almost perfectly aligned with the page axis. In case of multi-element crystals, different kinds of axes can be observed: in the case shown in figure 1.3c atoms of different elements are arranged in separate strings, whereas in the case shown in figure 1.3d each string comprises atoms of all the elements involved.

Since the properties of all mutually parallel axes and planes are the same – typically, the features of the two different-element axes in figure 1.3c are averaged – and the Miller-index formalism addresses all of them with the same notation, it is convenient to adopt a representation of the lattice which only relies on its orientation and neglects the spatial position in it. This is the so-called crystallographic stereogram, i.e., a two-dimensional representation of the lattice in which two mutually orthogonal angles of view around a certain crystalline axis – namely, two misalignment angles  $\theta_x^{\text{mis}}$  and  $\theta_y^{\text{mis}}$  – are reported on the abscissas and ordinates, so that the axis is located in the reference system origin and all the planes including it are represented by lines crossing the origin. An example is shown in figure 1.4, in which the stereogram is superimposed on top of a lattice in perspective view, to qualitatively show the appearance the latter takes in each position  $(\theta_x^{\text{mis}}, \theta_y^{\text{mis}})$ .

### 1.1.2 Single-atom potential

In order to examine the electrostatic properties of lattice axes and planes, it is first necessary to describe those of the single atoms. Several different models of the single-atom potential  $V_{\text{atom}}$  experienced by an external charged particle exist. Let the external particle have a unitary electric charge in units of the electron charge  $e = 1.602 \times 10^{-19}$  C [13], i.e.,  $z = 1$ . A traditional and simple approach makes use of a Thomas-Fermi-like picture of the atomic potential, i.e., [1, 5, 14]

$$V_{\text{atom}}(r) = \frac{k_e Z e^2}{r} \phi\left(\frac{r}{a_S}\right) \quad (1.4)$$

where

- $k_e = 8.988 \times 10^9 \text{ Nm}^2/\text{C}^2$  is the Coulomb constant;
- $r = r(x, y, z) = \sqrt{x^2 + y^2 + z^2}$  is the distance from the atom centre ( $x, y$  and  $z$  being the three-dimensional Cartesian coordinates);

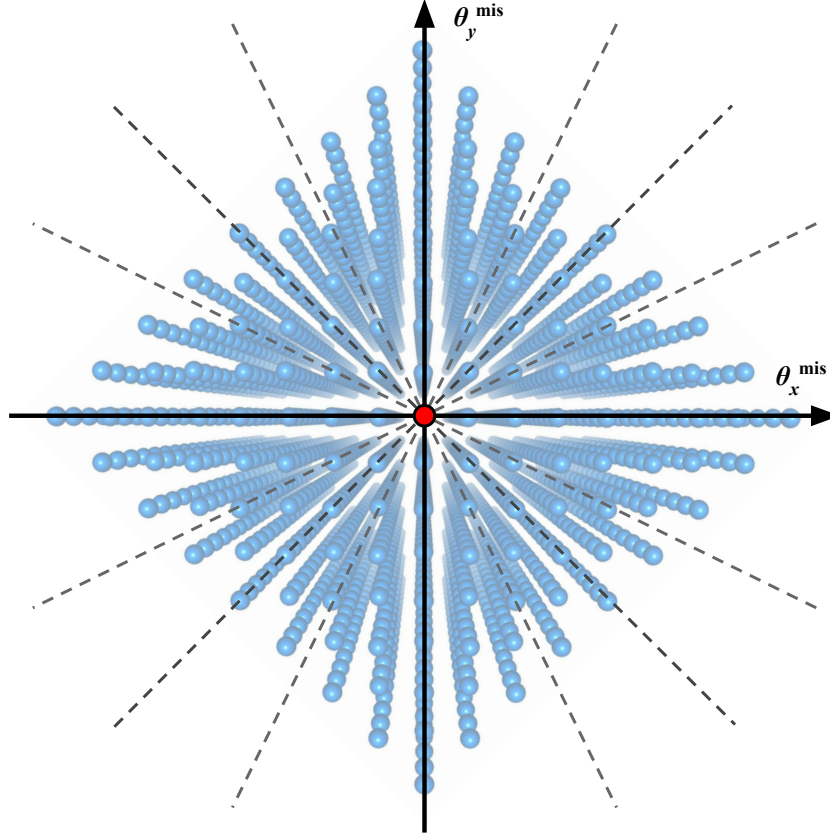


FIGURE 1.4: A crystallographic stereogram superimposed on a perspective view of the corresponding (body-centered cubic) lattice. The highest-density planes are highlighted with dashed grey lines (with the exception of those located along the plot axes), whereas the axis is indicated in red.

- $Z$  is the electric charge of the atomic nucleus in units of  $e$ ;
- $\phi$  is the screening function or Fermi function [1, 5, 14].
- $a_S \sim 0.8853a_0/\sqrt{Z^{2/3} + 1}$  [5, 14] is the screening distance and  $a_0 = 0.529 \text{ \AA}$  is the Bohr radius [13];

The first factor in equation 1.4 represents the total point-like charge, whereas  $\phi$  takes into account the spatial distribution of the charge, in which the screening of the central potential by the outer electrons is considered. Overall,  $V_{\text{atom}}$  only depends on  $r$  and is therefore spherically symmetrical. This dependence is made fully explicit by providing an expression for  $\phi$ . A frequently used approximation from Molière is [1, 14–16]

$$\phi(k) = \sum_{j=1}^3 a_j^{\text{M}} \exp(-b_j^{\text{M}} k) \quad , \quad (1.5)$$

where  $(a_1^{\text{M}}, a_2^{\text{M}}, a_3^{\text{M}}) = (0.1, 0.55, 0.35)$  and  $(b_1^{\text{M}}, b_2^{\text{M}}, b_3^{\text{M}}) = (6.0, 1.2, 0.3)$ .

Other models are often exploited when calculating the planar and axial potentials. Rather common choices are the Lindhard approximation of the screening function, [1, 5, 14]

$$\phi(k) = 1 - \frac{1}{\sqrt{1 + 3k^2}} \quad ,$$

and the Doyle-Turner model of the single-atom potential, [10, 14, 17]

$$V_{\text{atom}}(r) = 16\pi a_0 k_e Z e^2 \sum_{j=1}^4 \frac{a_j^{\text{DT}}}{(b_j^{\text{DT}}/\pi)^{3/2}} \exp \left[ \frac{-r^2}{(b_j^{\text{DT}}/4\pi)^2} \right] \quad ,$$

where  $a_j^{\text{DT}}$  and  $b_j^{\text{DT}}$  ( $j = 1, 2, 3, 4$ ) are tabulated in, e.g., [17]. All these atomic models lead to lattice potentials that are similar to one another in terms of shape and magnitude; for instance, all the resulting potential depth values differ from one another by less than 15% [10].

It has to be considered that atoms deviate from their equilibrium locations inside the lattice due to thermal vibrations [10]. This can be taken into account rewriting the potential as [10]

$$V_{\text{atom}}^{\text{th}}(r) = \int d^3r V_{\text{atom}}(|\bar{r} - \bar{\rho}|) w(\rho, u_1) \quad (1.6)$$

where  $u_1$  is the one-dimensional amplitude of thermal vibrations and  $w(\rho, u_1)$  is the probability of off-axis displacement by  $\rho$ , which can be assumed to have a Gaussian form, i.e.,

$$w(\rho, u_1) = \frac{1}{(2\pi u_1^2)^{3/2}} \exp \left( -\frac{\rho^2}{2u_1^2} \right) \quad .$$

Furthermore, it has to be noted that the screening radius varies in presence of thermal vibrations as well [10], i.e., the replacement  $a_{\text{S}} \rightarrow a_{\text{S}}^{\text{th}}$  might prove necessary to correctly model the particle-lattice potentials.

A more general and flexible model exploits the Fourier expansion of the potential described by equation 1.6, i.e., [10, 18]

$$\hat{V}_{\text{atom}}^{\text{th}}(\bar{q}) = \int_{\text{whole space}} d^3r V_{\text{atom}}^{\text{th}}(r) \exp(i\bar{q} \cdot \bar{r}) = \hat{V}_{\text{atom}}(\bar{q}) \exp \left( -\frac{u_1^2 q^2}{2} \right) \quad , \quad (1.7)$$

where  $i$  is the imaginary unit and  $\hat{V}_{\text{atom}}(\bar{q})$  is the Fourier transform of the potential calculated without taking into account the thermal vibrations. The form of  $\hat{V}_{\text{atom}}$  depends on the choice of the atomic model: for instance, the Molière approximation leads to the form [10]

$$\hat{V}_{\text{atom}}(\bar{q}) \propto \sum_{j=1}^3 \frac{a_j^{\text{M}}}{q^2 + (b_j^{\text{M}})^2} \quad .$$

## 1.2 Particle motion in an oriented crystal

The features of the coherent interactions experienced by particles impinging at a small angle with respect to the axes or planes of a crystalline lattice ( $\lesssim 1^\circ$  – see sections below) can be described by proper electrostatic potentials more effectively than by considering the potential of all the atoms involved separately. In particular, the effective axial and planar potentials can be defined with great simplification with respect to the case of separate single atoms: details on these effective potentials and on their effect on the incident particle dynamics are provided in the following sections.

### 1.2.1 Axial (and planar) continuous potential

According to the so-called continuum approximation, these potentials are independent on the spatial degrees of freedom over which the lattice structure under study expands [5, 19], i.e.,  $\hat{z}$  in case of an axis aligned with  $\hat{z}$  and  $\hat{y}$  and  $\hat{z}$  in case of planes orthogonal to  $\hat{x}$ .

A traditional and intuitive approach to the calculation of these effective potentials, introduced by Lindhard, consists in averaging the potentials of all the single atoms along the direction(s) belonging to the axis or plane [1, 5, 18]. In particular, the single-axis potential  $U_{\text{axis}}$  is obtained by integrating the single-atom potential over the whole axis, [5, 18]

$$U_{\text{ax}}(x, y) = U_{\text{ax}}(r_{\perp}) = \int_{-\infty}^{+\infty} \frac{dz}{d_{\text{ax}}} V_{\text{atom}}^{\text{th}} \left( \sqrt{r_{\perp}^2 + z^2} \right) \quad ,$$

where  $r_{\perp} = \sqrt{x^2 + y^2}$  is the distance from the string in the transverse plane and  $d_{\text{ax}}$  is the interatomic spreading of the string. Similarly, the single-plane potential  $U_{\text{plane}}$  is obtained as [1, 18]

$$U_{\text{pl}}(x) = n_{\text{atom}} d_{\text{pl}} \int_{-\infty}^{+\infty} dy \int_{-\infty}^{+\infty} dz V_{\text{atom}}^{\text{th}} \left( \sqrt{x^2 + y^2 + z^2} \right) \quad (1.8)$$

where  $n_{\text{atom}}$  is the volume density of atoms and  $d_{\text{pl}}$  is the interplanar spacing. These expressions can be made explicit by replacing, for instance, equations 1.4, 1.5 (for the Molière approximation) and 1.6 into the integrals. Finally, the overall lattice potential in the particular orientation under study results from an average over the contributions of neighbouring axes or planes [18]. In the more general approach based on the Fourier expansions (equation 1.7), the axial/planar potential can be obtained by summing up the potentials of the single atoms involved taking into account their locations inside the lattice [10]:

$$\begin{aligned} U_{\text{ax/pl}}(\bar{r}) &= \sum_j V_{\text{atom}}^{\text{th}}(|\bar{r} - \bar{r}_j|) \\ &= \frac{1}{(2\pi)^3} \int_{\text{whole space}} d^3 q \hat{V}_{\text{atom}}^{\text{th}}(\bar{q}) \sum_j \exp[i\bar{q}(\bar{r}_j - \bar{r})] \quad , \end{aligned}$$

where the summation index  $j$  is restricted to the sole atoms that belong to the axis/plane under study. In particular, in case of the  $[hkl]$  axis, the atoms to be summed over are the ones associated to the nodes for which equation 1.3 holds true with  $\tilde{n} = 0$  [10]. Together with equation 1.7, this results in [10]

$$U_{\text{ax}}(r_{\perp}) = \frac{1}{(2\pi)^2 d_{\text{ax}}} \int_{\text{transv. plane}} d^2 q_{\perp} \hat{V}_{\text{atom}}(\bar{q}_{\perp}) \exp\left(-i\bar{q}_{\perp} \bar{r}_{\perp} - \frac{u_1^2 q_{\perp}^2}{2}\right) \quad . \quad (1.9)$$

Starting from equation 1.9, an effective continuous potential experienced by the external particle under the influence of a single axis can be explicitly derived choosing an atomic model and a convenient, application-dependent set of approximations [10]. Since the value of  $r_{\perp}$  up to which the string potential is macroscopic is typically smaller than the string interspacing, axial interactions occur, to a good approximation, with one string at a time [19]. Therefore, this approach leads to satisfactory estimates of the main properties of the axis and of its effects on the particles impinging on it.

For instance, a good model of the potential of an axis in the whole space is provided by Baier, Katkov and Strakhovenko [10]:

$$U_{\text{ax}}^{\text{tot}}(r_{\perp}) \sim \frac{k_e Z e^2}{d_{\text{ax}}} \left\{ \ln \left[ 1 + \frac{(a_{\text{S}}^{\text{th}})^2}{r_{\perp}^2 + 2u_1^2} \right] - \ln \left[ 1 + \frac{(a_{\text{S}}^{\text{th}})^2}{1/\pi n_{\text{atom}} d_{\text{ax}} + 2u_1^2} \right] \right\}, \quad (1.10)$$

where, as already mentioned, the value of  $a_{\text{S}}^{\text{th}}$  depends on the crystalline medium and on the size of the thermal vibrations – some values are tabulated, e.g., in [10].

Figure 1.5 shows equation 1.10 applied to the case of the [111] axis of tungsten (main physical properties in section 2.1, chapter 2), with  $u_1 = 0.05 \text{ \AA}$  and  $a_{\text{S}}^{\text{th}} = 0.215 \text{ \AA}$ : as expected, the axial potential becomes weaker as the distance from the string centre increases. For instance, the value attained for  $r_{\perp} \sim 1 \text{ \AA}$  is  $< 10\%$  of the total potential barrier height. The latter can be evaluated as  $U_0 = U_{\text{ax}}^{\text{tot}}(0)$ , and is particularly important in computing the main properties of the axis.

The two kinds of multi-element axes shown in figure 1.3 should be dealt with differently from each other: in case of figure 1.3c, equation 1.10 should be used to evaluate the potentials of the different-element axes separately. On the other hand, in case of figure 1.3d, an average between the different single-atom potentials in the unit cell should be considered when computing

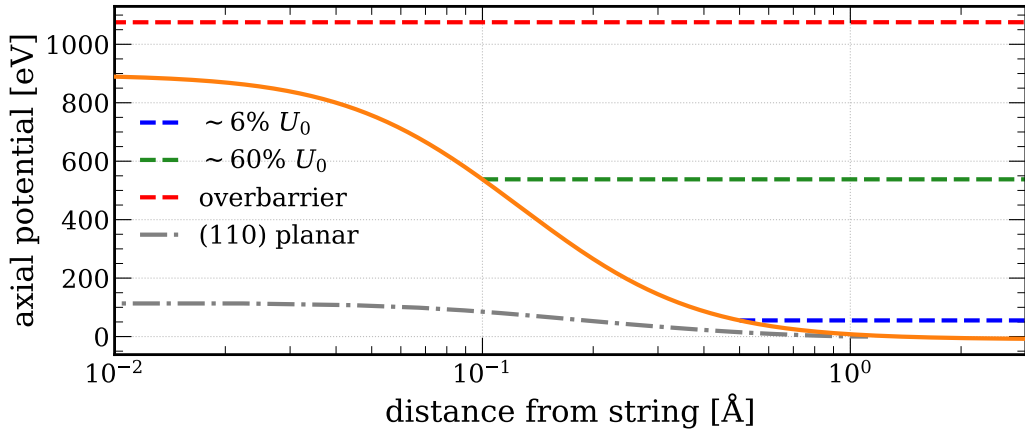


FIGURE 1.5: Estimate of the axial potential associated to the [111] axis of tungsten, obtained from equation 1.10 with  $u_1 = 0.05 \text{ \AA}$  and  $a_{\text{S}}^{\text{th}} = 0.215 \text{ \AA}$  (orange solid curve). The transverse energy of three different positive incident particles are superimposed as dashed lines: one has  $E_{\perp} > U_0$  (red), whereas the other two have  $E_{\perp} \sim 6\% U_0$  (blue) and  $E_{\perp} \sim 60\% U_0$  (green) respectively. For comparison, the potential associated to the (110) plane is also shown (dash-dotted grey).

$U_{\text{ax}}(r_{\perp})$  by means of equation 1.9. Lastly, it has to be noted that the potentials calculated above have been modelled on the case of positively charged external particles; they can easily be adapted to the case of negative particles by applying a global minus sign.

### 1.2.2 Particle dynamics in the lattice

The axial (planar) potentials obtained in section 1.2.1 can be used to calculate the total lattice potential, as the sum of the contributions of adjacent single strings (planes) [1]. The lattice potential is then used to describe the interactions the particles impinging on the crystalline medium undergo. Firstly, the dynamics of charged particles is considered, and the main focus is put on the case of an axially oriented lattice.

In the continuum approximation, developed by Lindhard [5], a complete separation between the longitudinal and transverse components of the incident particle motion is assumed [5, 19]. Moreover, in the limit of high particle momenta, the motion can be treated classically, since the particle De Broglie wavelength is small enough to prevent the formation of interference patterns and bound states are characterised by a large number of energy levels [14] – see section 1.2.3.

Let  $m$  be the mass of a particle elastically propagating at a small misalignment angle  $\psi$  with respect to a lattice axis oriented along  $\hat{z}$ . Since the axial potential does not depend on the position along the axis,  $z$ , the motion along  $\hat{z}$  is free, i.e., the particle propagates with constant longitudinal momentum  $p_z = \bar{p}\hat{z}$  and, hence, conserved longitudinal translational energy  $E_z = p_z^2/2m$  [19]. Since the interaction with the potential is elastic, the total particle energy  $E_0$  is conserved as well [19]. Therefore, the transverse energy [19]

$$E_{\perp} = E_0 - E_z = \frac{p_{\perp}^2}{2m\gamma} + U(r_{\perp}) \quad , \quad (1.11)$$

where  $p_{\perp}$  is the transverse momentum,  $\gamma = 1/\sqrt{1-\beta^2} = E_0/mc^2$  is the Lorentz factor,  $\beta$  is the speed in units on speed of light,  $c = 3 \times 10^8$  m/s [13] ( $v = \beta c$ ) and  $U = U_{\text{ax}}^{\text{tot}}$  ( $-U_{\text{ax}}^{\text{tot}}$ ) for positive (negative) charged particles, is conserved [19].

The rightmost side of equation 1.11 comprises two terms: the first one describes the kinetic contribution,  $E_{\perp}^{\text{kin}}$ , whereas the second one is merely the axial potential energy. It is useful to rewrite  $E_{\perp}^{\text{kin}}$  taking into account that  $p_{\perp} = m\gamma v_{\perp}$  and that  $p_{\perp} = p \sin \psi$  and  $v_{\perp} = v \sin \psi$ . Here,  $v_{\perp}$  is the transverse component of the speed. At small  $\psi$ ,  $\sin \psi \sim \psi$ , therefore [1, 20]

$$\begin{aligned}
E_{\perp}^{\text{kin}} &= \frac{p^2}{2m\gamma} \sin^2 \psi \sim \frac{p^2}{2m\gamma} \psi^2 \\
&= \frac{p_{\perp} v_{\perp}}{2} = \frac{pv}{2} \sin^2 \psi \sim \frac{pv}{2} \psi^2
\end{aligned} \tag{1.12}$$

and, in turn,

$$E_{\perp} = \frac{p^2}{2m\gamma} \psi^2 + U(r_{\perp}) \tag{1.13a}$$

$$= \frac{pv}{2} \psi^2 + U(r_{\perp}) \quad . \tag{1.13b}$$

The main features of the dynamics of the particle motion inside the lattice at different energy and angular ranges can be studied starting from equations 1.13a and b: they are summarised in the following sections.

### 1.2.3 Bound versus unbound motion

The most important classification criterion in the description of the motion of a particle in an oriented lattice is the amount of transverse kinetic energy. If  $E_{\perp}^{\text{kin}} < U(r_{\perp})$  for any value of  $r_{\perp}$ , or equivalently if  $E_{\perp} < U_0$ , there are parts of the crystal bulk in which the electrostatic potential is larger than the particle transverse kinetic energy and, hence, to which the particle cannot access.

The resulting phase space depends on the ratio between the transverse energy and  $U_0$ . Some sample trajectory sketches are shown in figure 1.6 superimposed to a sample axial potential contour plot, and the corresponding transverse energy values are shown in figure 1.5. Here, positive particles are considered. If  $E_{\perp} \ll U_0$  (blue curves), the particle might be trapped at the bottom of a potential well and oscillate in the transverse plane (rosette orbit [21]) – this condition is called hyperchannelling [22]. On the other hand, if  $E_{\perp} \lesssim U_0$  (green curves), the particle undergoes the so-called doughnut scattering [23], i.e., it ricochets off the potential peaks but can cross the saddle points located between neighbouring maxima, which results in a non-trivial phase space: for instance, the particle might be forced into a trajectory which is partly oscillating around a potential well, partly propagating across the adjacent strings. In both these cases, the particle is (completely or partially) bound to follow specific trajectories imposed by the lattice structure. Details on the resulting phenomenology are provided in section 1.2.4.

As already mentioned, in the continuum approximation, the description of the incident particle motion is purely classical for energies above 10–100 MeV,



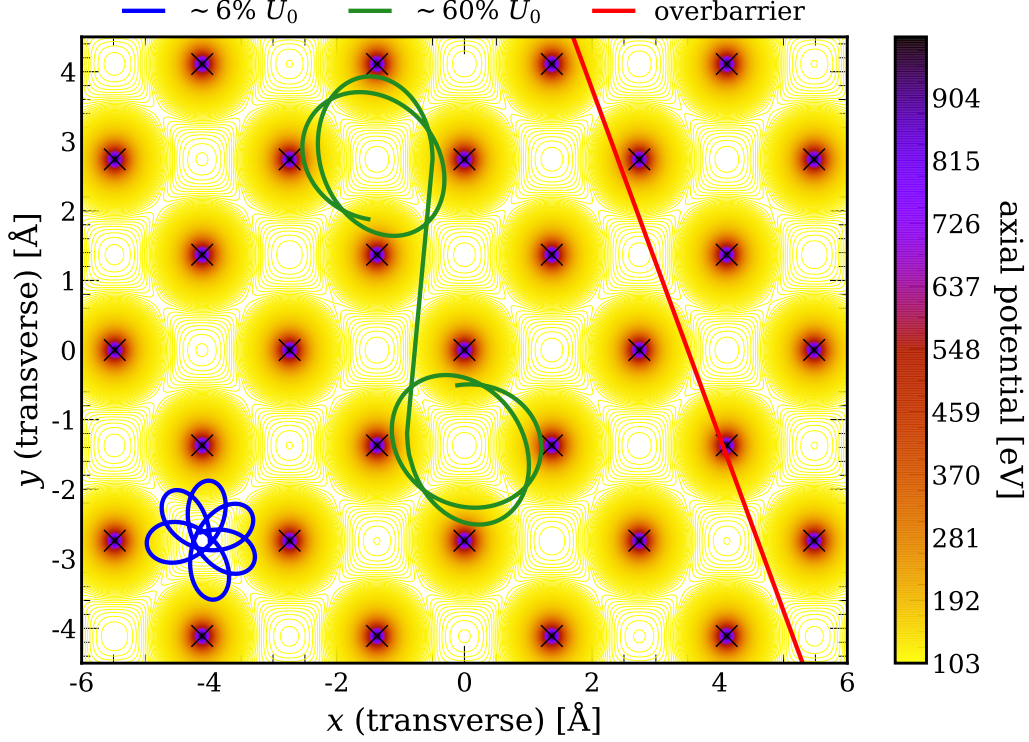


FIGURE 1.6: Contour plot of the axial potential associated to the  $[111]$  axis of tungsten in the transverse plane, obtained adding one instance of the leftmost term in equation 1.10 per string. The strings are indicated as cross markers. Different typical trajectories of positive particles are superimposed as solid lines for visualisation purpose; the color code is the same as in figure 1.5.

depending on the medium [20]. Indeed, the number of energy levels in the well is  $\propto \gamma \propto E_0$  [19, 20]. As a consequence, the higher the primary energy, the more adequate the classical picture is in describing the in-well motion [5].

Conversely, if  $E_{\perp} > U_0$  (red curves), the particle freely propagates above the lattice structure. This kind of motion is called unbound or over-barrier. Albeit it seems very similar to the motion of a particle in an amorphous medium, it can differ from it from the standpoint of the electromagnetic processes – details are provided in sections 1.3.4 and 1.4.

#### 1.2.4 Axial channelling

Channelling is the confinement of the motion of a charged particle impinging on a crystalline lattice into a trajectory that follows the direction of an axis or

plane due to the influence of its continuous potential [5, 19, 20]. In the axial case (sketch in figure 1.7), it encompasses all the in-well trajectories described in section 1.2.3, i.e., those for which  $E_{\perp} < U_0$ . In the following, the main properties of axial channelling by electrons and positrons are discussed.

#### 1.2.4.1 Critical angle

It is clear from equations 1.12 and 1.13b that the kinetic component of the transverse energy depends on the square of the misalignment angle,  $\psi^2$ . Therefore, a value of  $\psi$  can be found to mark the transition between the channelling regime and the unbound region of the phase space. When a positive particle is very close to the nearest atomic string, its transverse energy is [14, 19]

$$E_{\perp} \Big|_{\text{near}} \sim U_0 \quad . \quad (1.14)$$

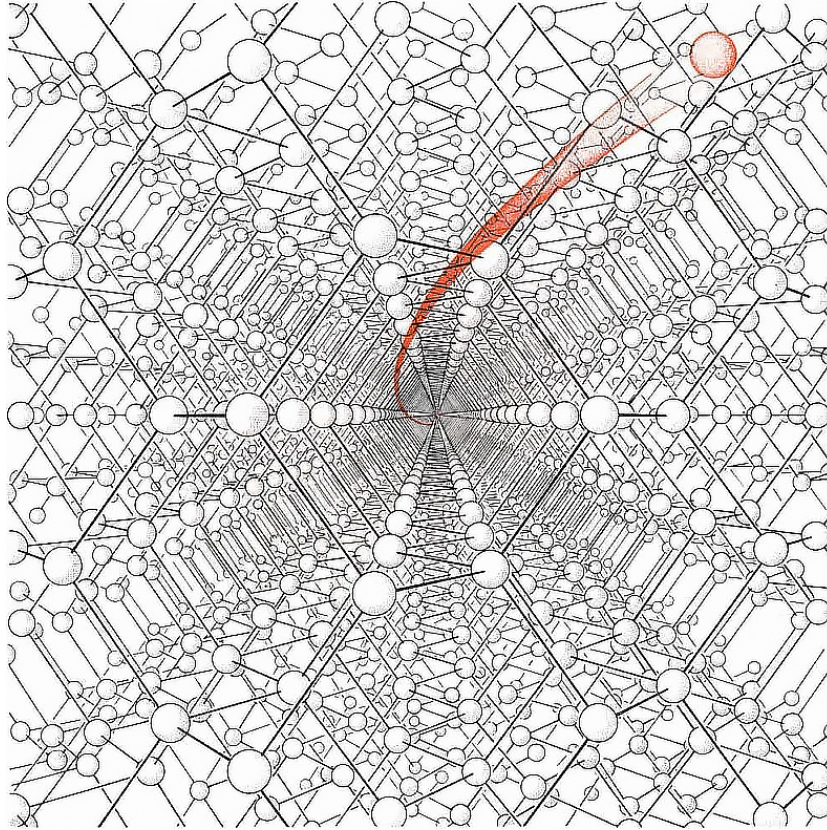


FIGURE 1.7: Sketch of the spiral trajectory typical of a positive particle channelled in a diamond-like axial well. From [24].

On the other hand, for  $r_\perp$  large, the transverse energy is [14, 19]

$$E_\perp \Big|_{\text{far}} \sim E_\perp^{\text{kin}} = \frac{pv}{2} \psi^2 \quad . \quad (1.15)$$

Since the transverse energy is conserved, equations 1.14 and 1.15 should be equalled. Solving for the misalignment angle leads to the value

$$\psi_L = \sqrt{\frac{2U_0}{pv}} \quad ,$$

i.e., the so-called Lindhard angle [1, 5, 10, 19, 20], which represents an estimate of the channelling angular acceptance. For ultrarelativistic particles  $v \rightarrow c$ ,  $pc \gg mc^2$  and therefore

$$\psi_L \xrightarrow{v \rightarrow c} \sqrt{\frac{2U_0}{E_0}} \quad . \quad (1.16)$$

It is clear from equation 1.16 that

- higher-potential axes feature a wider angular acceptance;
- the angular acceptance decreases as the energy of the incident particle increases.

Estimates are provided for tungsten and lead tungstate at different energies in section 2.1 (chapter 2). In general, in case of high- $Z$ , high-density crystals, values around 500  $\mu\text{rad}$  (100  $\mu\text{rad}$ ) are attained at a few GeV ( $\sim 100$  GeV).

#### 1.2.4.2 Electrons versus positrons

Figure 1.8 shows a sample axial potential for positive ( $x < 0$ ) and negative ( $x > 0$ ) particles. As already mentioned, the latter is simply obtained by applying a global minus sign to the former. It is clear that, at equal  $E_\perp$ , the area accessible to a positive particle is considerably larger than that accessible to a negative particle.

Indeed, if  $E_\perp \sim 50\% U_0$ , all the white and blue regions in figure 1.8 are accessible: the positive particles can propagate freely in most of the transverse plane, whereas negative particles are forced into narrow regions around a single atomic string, where they typically undergo rosette motion [21, 25] with numerous interactions with nuclei and core electrons which make them exit the channelling condition – see section 1.2.4.3.

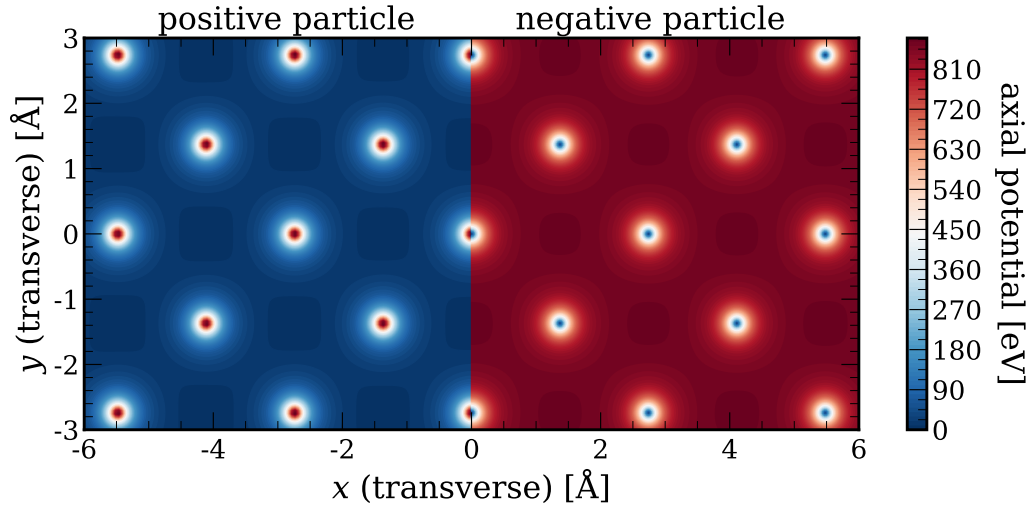


FIGURE 1.8: Comparison between the contour plots of the axial potential associated to the  $[111]$  axis of tungsten for positive ( $x < 0$ ) and negative ( $x > 0$ ) particles.

#### 1.2.4.3 Dechannelling

Scattering events inside the medium can break the conservation of the transverse energy [26]. Since, as shown in section 1.2.4.2, axially channelled positive particles have access to a much larger fraction of the crystal transverse section and propagate far away from the atomic strings, where the nuclei and most of the core electrons are, the size of this effect is significantly lower for positive particles than for negative particles [26].

The average length of the trajectories the channelled particles follow before dechannelling occurs can be estimated considering a beam of  $N_{\text{chan}}^{\text{front}}$  particles impinging on an crystal in perfect axial alignment [27, 28]. The number of particles at depth  $t$  can be estimated using a diffusion approach [1, 14, 27–29]:

$$N_{\text{chan}}(t) = N_{\text{chan}}^{\text{front}} \exp\left(-\frac{t}{\lambda_D}\right) ,$$

where  $\lambda_D$  is the so-called dechannelling length. The latter is roughly obtained as [27, 28]

$$\lambda_D \propto \frac{\psi_L^2}{\Delta\psi_{\text{MCS}}^2} \propto \frac{1/E_0}{1/E_0^2} = E_0 , \quad (1.17)$$

where  $\Delta\psi_{\text{MCS}}$  is the multiple Coulomb scattering (MCS) angle. In case of amorphous media, as estimate of the MCS is given by [30]

$$\Delta\psi_{\text{MCS}} = \frac{13.6 \text{ MeV}}{E_0} \sqrt{\frac{t}{X_0}} \left[ 1 + 0.038 \ln \left( \frac{t}{X_0} \right) \right] \quad , \quad (1.18)$$

$X_0$  being the material radiation length (see section 1.3.1); on the other hand, in case of crystalline media,  $\Delta\psi_{\text{MCS}}$  non-trivially depends on the position and orientation inside the lattice, and might get much smaller (larger) than the amorphous value when the particle moves in a region in which the density of scattering centres is lower (higher) [31]. Moreover, as shown in the leftmost side of equation 1.17, the dechannelling length is proportional to the incident particle energy [27]. Further details on axial dechannelling can be found, e.g., in [32].

#### 1.2.4.4 What about the planes?

As shown in equation 1.8, the average continuous potential for a plane only depends on one spatial coordinate, i.e., the position in the direction orthogonal to the plane itself. Therefore, planar channelling is significantly easier to attain than axial channelling, as the crystalline lattice has to be properly aligned in one direction only [28].

On the other hand, in general, the potential associated to low-index planes is much weaker than that associated to low-index axes [5]. Indeed, the ratio between the principal axial and planar potentials can be roughly estimated as  $\sim (20 \text{ eV})Z/(5 \text{ eV})Z^{2/3} = 4Z^{1/3}$  [5], i.e.,  $\sim 17$  for tungsten ( $Z = 74$  [13]) and  $\sim 10$  for much lighter elements such as silicon ( $Z = 14$  [13]). Moreover, the ratio between the corresponding critical angles is  $\sim 2Z^{1/6}$ , i.e., the critical angle for planar channelling is always 3–4 times smaller than that for axial channelling [5].

### 1.3 Electromagnetic radiation by a moving charged particle

It is well known that an accelerating charged particle emits electromagnetic radiation, and that the features of the latter are strongly dependent on the features of the dynamics that comes into play [33]. Clearly, this holds true for all the kinds of motion discussed in section 1.2.

In order to fully characterise the radiation emitted by an electron (or positron) crossing a properly oriented crystalline lattice in different energy regimes, it is useful to introduce the concept of spectral intensity, i.e.,

$$I(\omega) = \hbar\omega \frac{dN_{\text{single}}}{d(\hbar\omega)} \quad , \quad (1.19)$$

where

- $\hbar \sim 1.055 \times 10^{-34}$  Js [13] is the Planck constant;
- $\hbar\omega$  is the energy of the emitted radiation quantum;
- $N_{\text{single}}$  is the total number of emitted quanta;

In the quantum models of radiation emission such as bremsstrahlung,  $I(\omega) \propto \hbar\omega\Phi(\omega; E_0)$ , where  $\Phi(\omega; E_0)$  is the radiation emission differential cross section and  $E_0$  is the energy of the parent electron.

Typically, theoretical predictions are provided in the form of equation 1.19. On the other hand, the factor  $dN_{\text{single}}/d(\hbar\omega)$  is the radiation spectrum of frequencies, which, with proper normalisation, is tightly related to the experimentally observed spectra. In all the cases discussed in this work, multiple photons emitted by the same parent electron cannot be resolved by the detectors employed in the measurements; therefore,  $N_{\text{single}}$  is replaced by the total number of measured events  $N$  in all the spectra presented in the following chapters.

### 1.3.1 Bethe-Heitler bremsstrahlung

Bremsstrahlung is the emission of electromagnetic radiation resulting from the scattering of charged fast particles in the electric field of an atomic nucleus [34]. The standard bremsstrahlung theory, introduced by Bethe and Heitler [34], well describes the process of photon emission in amorphous media or randomly oriented crystals, in which successive interactions are independent on one another and the emitted radiation results from the contributions of all the single collisions adding up incoherently [5, 20].

In the high-energy Bethe-Heitler model, the cross section for the emission of a photon of energy  $\hbar\omega = h\nu = E_0 - E_1$ ,  $E_1 = E_1(\omega, E_0)$  being the final energy of the parent particle, is

$$\Phi(\omega; E_0) \propto \frac{\alpha Z^2 r_p^2}{\hbar\omega E_0^2} \left[ \left( E_0^2 + E_1^2 - \frac{2}{3} E_0 E_1 \right) \ln \left( \frac{183}{Z^{1/3}} \right) + \frac{E_0 E_1}{9} \right] \quad , \quad (1.20)$$

where

- $\alpha \sim 1/137.036$  [13] is the fine-structure constant,

- $r_p \propto (Z_p e)^2 / mc^2$  [13] is the classical particle radius and  $Z_p$  is its charge in units of  $e$ .

Several conclusions can be drawn from equation 1.20:

- the factor  $r_p^2 \propto 1/(mc^2)^2$  introduces a strong dependence on the particle mass, because of which the emission of bremsstrahlung radiation at the GeV-to-TeV scale is suppressed for any charged particle in the Standard Model but electrons and positrons<sup>2</sup>;
- the cross section is quadratically dependent on the atomic number of the nucleus,  $Z$ ;
- the global factor is inversely proportional to  $\hbar\omega$ , which gives to the bremsstrahlung radiation energy spectrum the characteristic trend shown in the theoretical curves in figure 1.9 and in the experimental amorphous spectra shown throughout chapters 3, 4 and 5.

Indeed, figure 1.9 shows the bremsstrahlung radiation spectral intensity as a function of the output photon energy for different materials and parent electron energies. In particular, all the curves but the dashed ones have been computed with the full, completely screened Bethe-Heitler cross section (equation 1.20), whereas the dashed curves have been obtained with a simplified model in which the screening is neglected. It is clear that the screening is more effective at high  $E_0$  – the difference between each solid curve and the corresponding dashed curve grows with  $E_0$  – and at low  $\hbar\omega$  – the divergence that is shown by the dashed curves for  $\hbar\nu \rightarrow 0$  is tamed in the solid curves. Most of the photons are emitted at small angle with respect to the parent electron trajectory [34]. An estimate of the average emission cone aperture angle is given by  $1/\gamma = mc^2/E_0$  [34], i.e., the higher the primary energy, the better collimated the output radiation is.

Equation 1.20 can be integrated over  $\omega$ . The result can be expressed as  $\Phi_{\text{rad}} = \Phi_{\text{rad}}(E_0)$  defined by [34]

$$\Phi_{\text{rad}}(E_0) E_0 Z^2 r_e^2 \propto - \left\langle \frac{dE_0}{dt} \right|_{\text{rad}} \rangle \propto \int_0^{E_0 - mc^2} d\omega \hbar\omega \Phi(\omega; E_0) \quad , \quad (1.21)$$

where  $r_e = 2.818 \times 10^{-15}$  m [13] is the classical electron radius.

Figure 1.10 shows  $\Phi_{\text{rad}}$  for different materials.  $\Phi_{\text{rad}}$  is compared to the average energy loss by electronic collision – properly normalised, according to the left

---

<sup>2</sup>Indeed, in case of the second lightest particle, i.e., the muon, whose mass is  $\sim 207$  times that of the electron [13], the bremsstrahlung cross section is  $\sim 1/43000$ .



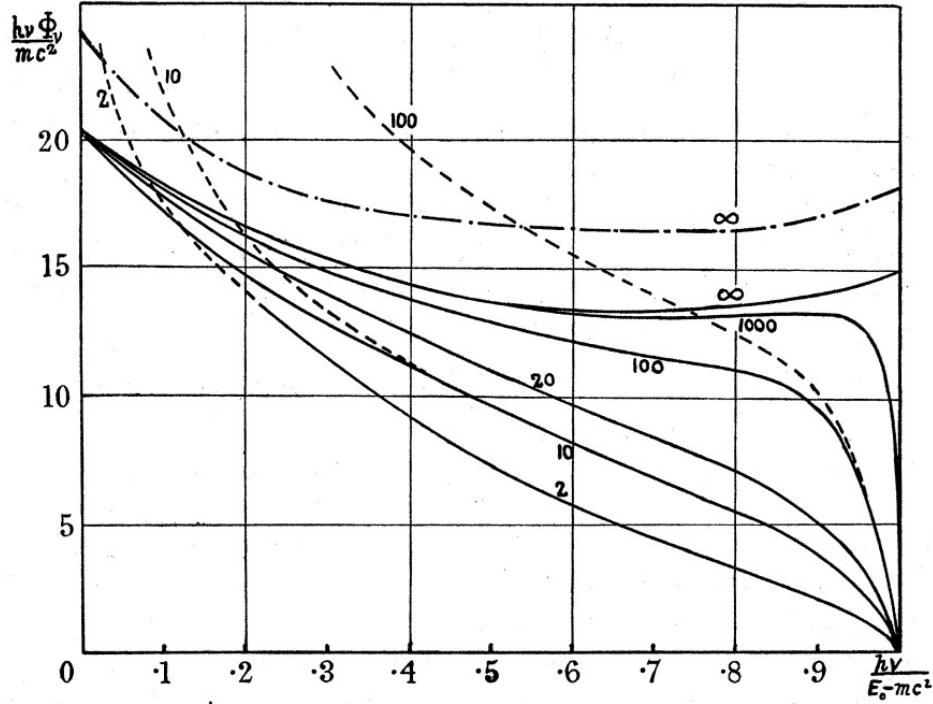


FIGURE 1.9: Spectral intensity of the standard bremsstrahlung as a function of the fraction of initial energy taken by the emitted photon, for lead with (solid lines) and without (dashed lines) the contribution of the screening and water (dashed-dotted line) and for different values of  $E_0$  (numbers affixed to the curves, in units of  $mc^2$ ). From [34].

side of equation 1.21: it is clear that the energy loss by collision dominates at low  $E_0$ , whereas bremsstrahlung sets on at high  $E_0$ . There is a medium-dependent critical value,  $E_c = E_c(Z)$ , defined as the energy in correspondence of which the energy loss contributions from radiation emission and collision equal each other<sup>3</sup>. An estimate of this critical energy is given, e.g., in [35]:

$$E_c = \frac{610(710) \text{ MeV}}{Z + 1.24(0.92)} \quad (1.22)$$

for solids (gases). Clearly, the higher the atomic number of the target, the lower the energy threshold for radiation emission to become dominant. Furthermore,  $\Phi_{\text{rad}}$  becomes independent on  $E_0$  when the latter is  $\gg E_c$ .

<sup>3</sup>Alternatively,  $E_c$  is often defined as the energy at which the ionization loss per radiation length is equal to the electron energy [30]; the two definitions lead to very similar results [30].



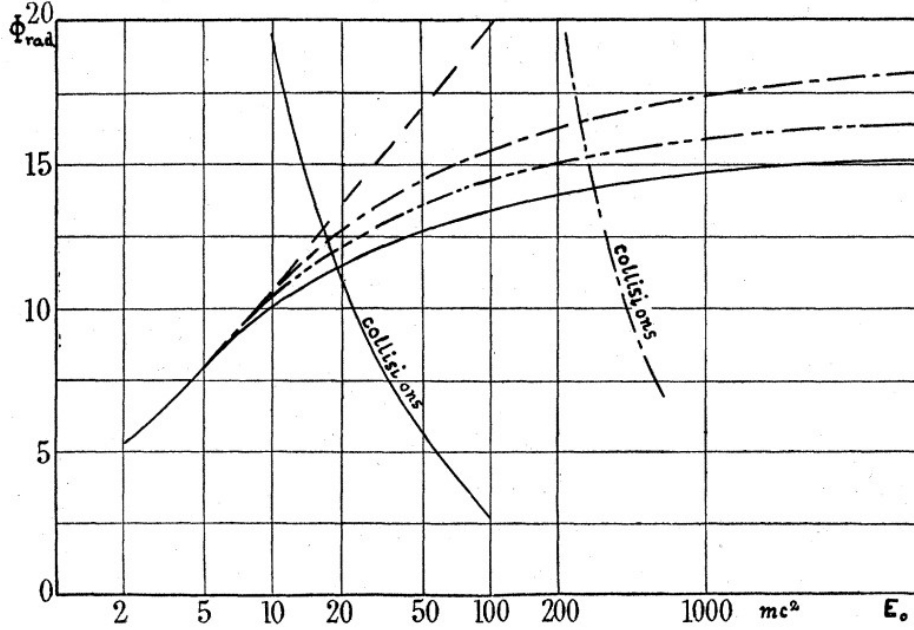


FIGURE 1.10: Integrated cross section of the standard bremsstrahlung as a function of the parent electron energy, for lead with (solid lines) and without (dashed line) the contribution of the screening, water (dash-dotted lines) and copper (dash-double dotted line). For comparison, the contribution resulting from the collisions is superimposed for lead and water. From [34].

Equation 1.21 also provides an estimate of the average energy loss by radiation emission [34]. Although this does not represent a proper estimate of the energy lost in a single electron-nucleus interaction, as the latter is affected by considerable straggling and thus may differ considerably from the average loss [34], useful statistical considerations can be made on its trend as a function of the penetration depth  $t$ . In particular, a scale of the penetration of an electron/positron through matter is given by [30, 35]

$$\left\langle \frac{dE_0}{dt} \right\rangle_{rad} = \frac{E_0}{X_0} .$$

$X_0$  is the so-called radiation length, i.e., the average distance over which an electron loses all but  $1/e$  of its energy by bremsstrahlung,  $e$  being the Euler number [30]. A rough estimate of the radiation length is provided by [35]

$$X_0 \sim \frac{(716 \text{ g/cm}^2) A}{\rho Z (Z + 1) \ln(287/\sqrt{Z})} ,$$

$\rho$  being the material density, and an extensive list of its value for various materials can be found, e.g., in [13, 30].

### 1.3.2 Radiation formation length

In case of electrons/positrons crossing a properly oriented crystal, the coherence between the periodic interactions with the lattice often leads to major modifications of the radiation spectrum shape with respect to that of standard bremsstrahlung [20, 36, 37]. This might seem counter-intuitive at a first glance, as, in the high-energy regime, the average distance between successive atoms in a string or plane (which is of the order of magnitude of the lattice constants) is much bigger than the electron De Broglie wavelength [20].

In fact, it takes a finite amount of time, and hence a finite distance for a photon to be generated by an accelerating electron: this distance can be much larger than the De Broglie wavelength [20, 36, 37]. More precisely, in order for the emitted photon to be considered fully formed and freely propagate, it has to be separated from the parent electron by at least one wavelength,  $\lambda = 2\pi c/\omega$ , which corresponds to a certain electron propagation distance [20, 36]. This can be seen as a consequence of the small momentum transfer between the parent particle and the scattering centre, which corresponds to a large uncertainty in the longitudinal spatial position by the Heisenberg uncertainty principle [30, 37].

The distance the electron has to propagate in order to attain full separation is called radiation formation length [20, 36, 37] or coherence length [20, 38]. Let it be  $l_f$ ; in order for the condition above to be verified, it shall be required that [20]

$$\frac{l_f}{v} = \left( l_f + \frac{\lambda}{2\pi} \right) \frac{1}{c} = \frac{l_f}{c} + \frac{1}{\omega} \quad ,$$

which, in the ultrarelativistic limit, where  $v \rightarrow c$  and hence  $\beta \sim 1 - (1/2\gamma^2)$ , results in

$$l_f = \frac{2\gamma^2 c}{\omega} \quad . \tag{1.23}$$

Equation 1.23 shows that higher-energy photons are formed over a shorter distance and that higher-energy electrons take a longer distance to emit a photon of the same energy. At very high energies (see section 1.4), the recoil imposed on the electron by the emitted radiation cannot be neglected [20]. Therefore, equation 1.23 becomes [20, 36]

$$l_f = \frac{2\gamma^2 c}{\omega'} \quad , \quad (1.24)$$

where  $\omega' = \omega E / (E - \hbar\omega)$ . Equations 1.23 and 1.24 can be obtained with several different approaches – a detailed summary is provided, e.g., in [20]. If the electron dynamics is affected by external factors within  $l_f$  – which might be orders of magnitude larger than the particle De Broglie wavelength [37] –, the features of the emitted radiation might vary significantly with respect to the standard case [20, 36, 37]. In particular, the overall photon yield and the relative intensity of single parts of the spectrum of  $\hbar\omega$  might increase or be reduced [20, 36, 37, 39, 40].

In practice, the presence of a finite radiation formation length affects all the radiation emission processes, starting from standard bremsstrahlung [40]. Indeed, the Bethe-Heitler model has to be corrected taking into account the LPM (Landau-Pomeranchuk-Migdal) effect, i.e., the suppression of the soft part of the bremsstrahlung spectrum that occurs when MCS disrupts the parent electron trajectory [40].

On the other hand, in crystals,  $l_f$  can be much larger than the interatomic spacing in an axis, especially at high energy. As a consequence, several different coherent mechanisms take place, depending on the energy scale and on the misalignment angle, that alter the radiation emission. Details are provided in the following sections.

### 1.3.3 Channelling radiation

The oscillations of a channeled electron or positron in the lattice potential well result in the emission of electromagnetic radiation – the so-called channelling radiation (CR), sketched in figure 1.11 [19] – whose features differ from those of standard bremsstrahlung. More precisely, this emission process can be seen as a consequence either of the coherence between the large number of successive soft scattering events with the atomic string [19] or of the bound-to-bound transitions within the potential well [20]. This coherent radiation component always comes alongside the incoherent one resulting from standard bremsstrahlung with randomly encountered scattering centres [19, 41].

Channelling radiation can be categorised by means of the spectral features attained at different values of  $E_0$  [20]. It is worth remarking that all the radiation emission processes described below are strictly related to channelling and, hence, require the incident  $e^\pm$  trajectory to meet the channelling requirements. In particular, for CR to be emitted, the incident particle has to

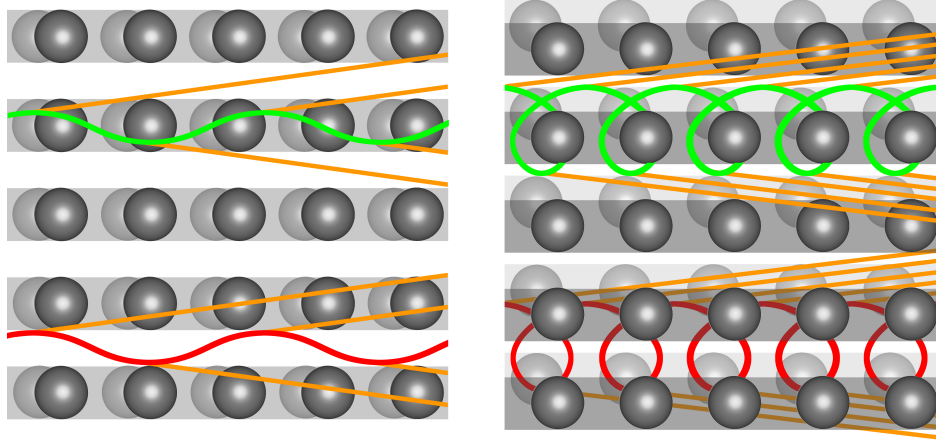


FIGURE 1.11: Sketch of channelling radiation emission (orange) by electrons (green) and positrons (red), in (*left*) planar and (*right*) axial alignment.

enter the crystalline lattice at a misalignment angle smaller than the Lindhard angle (equation 1.16), which becomes smaller for higher initial energy. At electron energies below about 100 MeV, the transverse potential well contains a limited number of states [19, 20]. In this case, the particle oscillating in the well can be treated like an electric dipole in the transverse plane, and the overall radiation spectrum clearly shows a general enhancement with respect to standard bremsstrahlung and peaks resulting from the quantisation of the well [19, 42]. Details can be found, e.g., in [42, 43].

On the other hand, between  $\sim 100$  MeV and a few GeV, the dipole approximation still holds, but the much higher number of energy states in the well (see section 1.2.3) makes a completely classical treatment of the process legitimate from the standpoint of both the particle motion and the radiation emission [20]. The dipole-like behaviour is attained because the angular excursion of the trajectory within the lattice channel, given by  $\psi_L \propto \sqrt{1/E_0}$ , is smaller than the radiation cone aperture ( $1/\gamma$ ) [14]. The resulting radiation is, in many respects, like that of a magnetic undulator [25, 44], i.e., a regularly spaced succession of dipole magnets of alternating polarity, which forces the particle into a small-amplitude oscillatory motion [45] – see blue curve in figure 1.12.

In an undulator, the oscillation wavelength is fully determined by the magnet succession pitch,  $l_0$ , and the emission occurs within an angle that is smaller than the typical radiation cone aperture,  $1/\gamma$  [46]. As a result, the radiation emitted in a dipole magnet stays within the acceptance of the downstream ones, and the radiation contributions from successive magnets sum up coherently [46]. Overall, this results in the emission of very intense, soft radiation

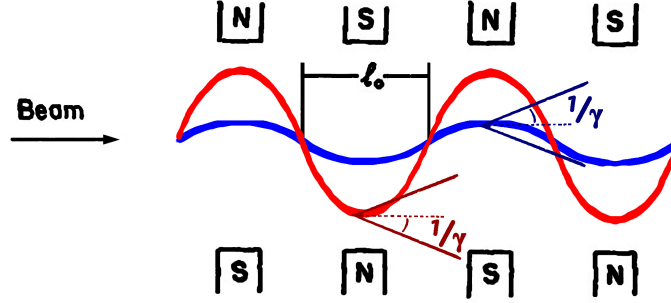


FIGURE 1.12: Scheme of a synchrotron insertion device, with the electron trajectory typical of an undulator (blue) and of a wiggler (red). The corresponding radiation emission cones are superimposed. Edited from [45].

with narrow peaks that comprise only the fundamental frequency and few higher-order harmonics, and a high angular collimation – i.e., within  $\sim 1/\gamma$  [46, 47].

Indeed, the mechanism of CR emission is similar to that of the magnetic undulator, and the intensity enhancement of the soft part of the radiation spectrum comes accordingly; on the other hand, since the shape of the lattice potential well is in general not exactly parabolic, the particle motion in it is not harmonic and the corresponding spectrum is less monochromatic than that of the undulator, especially in case of incident electrons [44].

At a few GeV and above, the dipole approximation cannot be applied anymore because relativistic effects that must be taken into account in the transverse motion also affect the longitudinal motion [20]. Moreover, the longitudinal motion is affected by the relativistic length contraction [19, 20]. In the particle frame, the atomic string appears shrunk: as a result, the axial field is boosted by a Lorentz factor [20].

Under the effect of such an intense field, the radiation emission typical frequency is shifted towards the harder part of the spectrum [20] and, in general, the spectrum is not monochromatic and significantly broader than the undulator-like one attained at lower primary energies [19, 48].

Similarly to the lower-energy case, the analogy between crystalline effects and synchrotron insertion devices can be considered to better characterise this effect. Contrary to the undulator case, in this energy range  $\psi_L > 1/\gamma$  [14, 19]. As a result, the transverse distance travelled by the electron/positron during the photon emission is smaller than the transverse field variation scale, and therefore the radiation is the same as that attained in a uniform field, i.e., synchrotron radiation [19, 33, 49, 50]. The latter is typical of, e.g., magnetic wigglers [33] – see the red curve in figure 1.12.

The energy spectrum of the high-energy synchrotron radiation emission is tightly related to the so-called universal synchrotron radiation function,  $S(\omega)$ , shown in figure 1.13 [33]. It is clear that the spectral intensity varies only slightly in a very broad wavelength range – i.e., from the infrared to the  $X$ -rays – [33] and features an exponential cutoff for radiation frequencies higher than the critical value [20, 30, 33]

$$\omega_c = \frac{3c\gamma^3}{2R} \quad , \quad (1.25)$$

where  $R$  is the curvature radius of the observed section of the parent particle trajectory. Moreover, synchrotron radiation is emitted in a broader angular range with respect to dipole-like radiation in the plane of the particle trajectory, whereas it is well collimated ( $\sim 1/\gamma$ ) in the orthogonal plane [33].

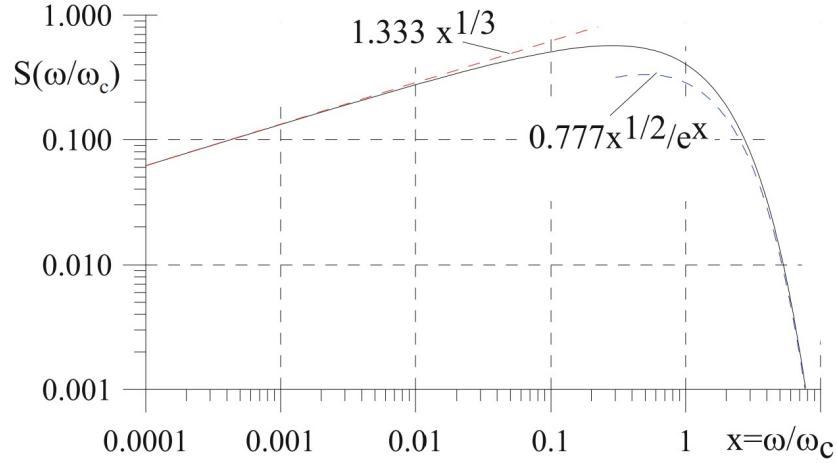


FIGURE 1.13: Universal synchrotron radiation function. From [33].

In case of the classical synchrotron radiation attained in crystals in the aforementioned energy and angular phase space, equation 1.25 becomes [20]

$$\omega_c = \frac{3eE_0^2\mathcal{E}_\perp}{2m^3c^4} \quad ,$$

where  $\mathcal{E}_\perp$  is the electric field exerted by the lattice transverse potential. In practice, the radiation spectrum is harder for higher parent  $e^\pm$  energy and for stronger crystalline axes. Above a few GeV, i.e., when, as mentioned in section 1.3.2, the electron recoil becomes non-negligible, a better estimate of critical frequency ( $\omega'_c$ ) is provided by [20]

$$\frac{\omega'_c}{E_0 - \hbar\omega'_c} = \frac{\omega_c}{E_0} \left( 1 - \frac{\hbar\omega_c}{E_0} \right)$$

$$\Rightarrow \omega'_c = \frac{\omega_c \left(1 - \frac{\hbar\omega_c}{E_0}\right)}{1 + \frac{\hbar\omega_c}{E_0} \left(1 - \frac{\hbar\omega_c}{E_0}\right)} . \quad (1.26)$$

### 1.3.4 Coherent bremsstrahlung

If its transverse energy is higher than  $U_0$ , the primary particle follows a straight trajectory crossing multiple adjacent lattice channels [19] – check the red line in figure 1.6. In particular, if the misalignment angle  $\psi$  is large enough for the particle to cross a set of neighbouring channels interspaced by a distance  $d_{\text{ch}}$ , then the particle experiences a periodic kick with frequency [1, 19]

$$\omega_{\text{ch}} = \frac{2\pi c\psi}{d_{\text{ch}}}$$

and emits electromagnetic radiation in the forward direction (i.e., within  $\sim 1/\gamma$ ) at each kick [1, 19]. This process, analogous to the Bragg-Laue  $X$ -ray diffraction [50], is the so-called coherent bremsstrahlung (CB) [8, 51] and is sketched in figure 1.14: it results in an enhancement of the overall radiation emission with respect to the incoherent component, especially in the soft part of the spectrum, if the  $e^\pm$  energy is high enough for the radiation formation length to span across multiple channels [1, 52]. Nevertheless, CB emission is harder than CR [53] since the period of the motion in channelling is larger than that of CB and, hence, the frequency is smaller.

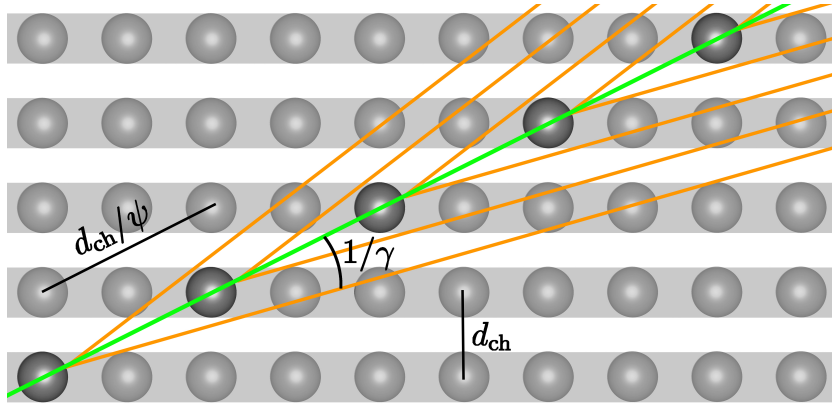


FIGURE 1.14: Sketch of coherent bremsstrahlung. The parent electron (emitted radiation) is drawn in green (orange).

Moreover, for fixed incident energy and misalignment angle, the spectrum shows sharp lines, defined by [1]

$$\frac{d_{\text{ch}}}{\psi} = 2\pi\tilde{n}l_f \Rightarrow \omega = \frac{4\pi c\gamma^2\psi}{d_{\text{ch}}}\tilde{n} \quad , \quad (1.27)$$

where  $\tilde{n}$  is a positive integer defining different-order harmonics. Equivalently, it can be stated that the CB cross section becomes mostly appreciable when the recoil momentum equals a vector of the reciprocal lattice, i.e., the Fourier transform of the crystalline lattice [20]. Similarly as in CR, the high-energy case requires a quantum treatment which takes into account the macroscopic recoil [1]: the Born approximation [54, 55] is used – details can be found, e.g., in [1, 20, 41, 56, 57].

As  $\tilde{n}$  increases in equation 1.27, the height of the corresponding peak decreases because of the reduction of the coherence length –  $l_f \propto 1/\omega \propto \tilde{n}$  [1]. Equation 1.27 shows that the spectral lines are harder for higher-energy parent particles. Clearly, there is an upper limit to the attainable photon energy, which has to be smaller than  $E_0$ : at high initial energy, the spectrum is broad and non-monochromatic, especially at large  $\psi$ . The strongest CB emission occurs within  $\sim 10 \psi_L$  [58, 59], and CB-related effects can be observed at up to  $\sim 1^\circ$  from the axis [50, 60]. Moreover, it shows the same features for both primary electrons and positrons [1, 59]. An example of CB measurement at the multi-GeV scale is shown in figure 1.15.

## 1.4 Crystalline strong field and shower enhancement

As already mentioned in section 1.3.3, when the parent  $e^\pm$  energy is sufficiently high, the relativistic length contraction sets in and the lattice potential experienced by the particle is enhanced by a factor  $\gamma$  [19, 20]. Since  $\gamma \propto E_0$ , there is no upper limit to the enhancement of the potential, and hence of the transverse electromagnetic field,  $\mathcal{E}_\perp$ , which typically has a value of  $\sim 10^{13}$  V/m.

In particular,  $\gamma\mathcal{E}_\perp$  can reach and even overcome the critical value [20, 61, 62]

$$\mathcal{E}_0 = \frac{m^2 c^3}{e\hbar} \sim 1.32 \times 10^{18} \frac{\text{V}}{\text{m}} \quad , \quad (1.28)$$



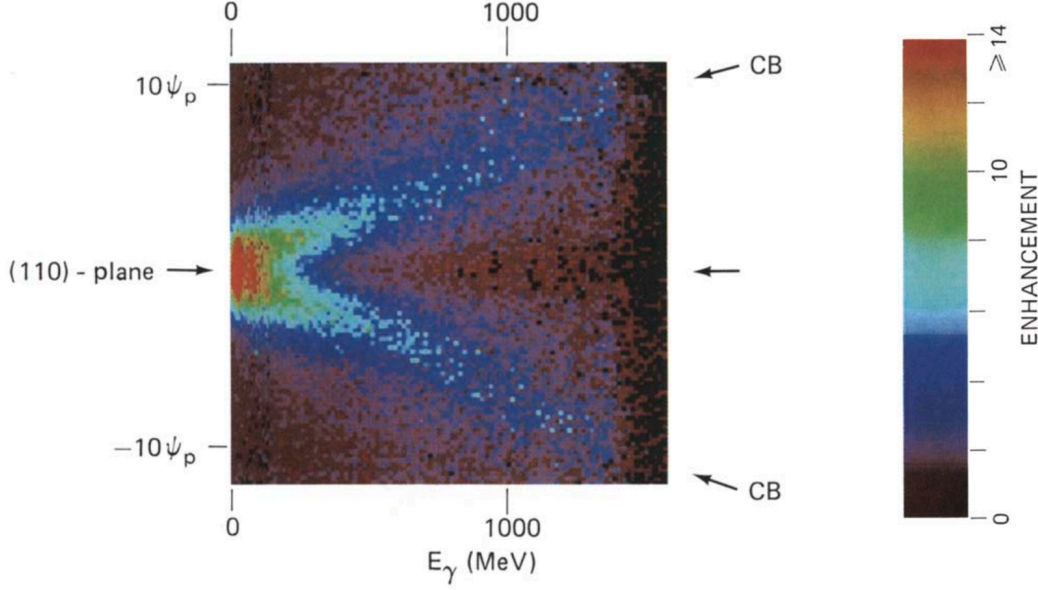


FIGURE 1.15: Measurement of the CB-related enhancement, with respect to the random case, of the radiation emitted by 10 GeV/c positrons impinging on a silicon crystal oriented along the (110) plane, as a function of the radiation energy and of the positron misalignment angle. Here,  $\psi_p = 70 \mu\text{rad}$ . From [59].

i.e., the so-called critical field of QED (quantum electrodynamics) or Schwinger field<sup>4</sup>.  $\mathcal{E}_0$  corresponds to the limit above which the electromagnetic field becomes non-linear in vacuum [61, 63]. In practice, in presence of a field of strength  $\gtrsim \mathcal{E}_0$ ,  $e^+e^-$  pairs are produced spontaneously [20, 61]. Indeed, equation 1.28 can be rewritten as

$$\mathcal{E}_0 = \frac{mc^2}{e\lambda_C}$$

where  $\lambda_C = \hbar/mc$  is the so-called Compton reduced wavelength, i.e., the wavelength of a photon with energy equal to the electron mass [20, 61]. Since a produced  $e^+e^-$  pair becomes real if the condition  $e\mathcal{E}_\perp\Delta l > 2mc^2$  is met, where  $\Delta l$  is the spatial separation between the two leptons, this form highlights that  $\mathcal{E}_0$  corresponds to the field required to produce a real pair separated by  $2\lambda_C$  [20, 62]. Fascinating electromagnetic processes occur in

<sup>4</sup>The Schwinger field is naturally obtained combining four fundamental constants of QED, which also highlight its main features: it is related to the interactions of the electron/positron ( $m$ ,  $e$ ) in both the quantum ( $\hbar$ ) and relativistic ( $c$ ) regime [20].

this field regime, such as the spontaneous creation of real leptons from the vacuum and photon-photon interactions – details can be found, e.g., in [20]. In general, an electromagnetic field of strength comparable to  $\mathcal{E}_0$  or higher is called strong field (SF) [20]. Strong fields extending over macroscopic volumes are naturally observed only in astrophysical phenomena such as supernovae and pulsars [20, 61, 64, 65]. On the other hand, with the present technology, the SF condition is artificially attained at smaller spatial and time scales: studies are performed on SF in, e.g., high-intensity lasers [20, 61, 63], ion-ion collisions [20] and beamstrahlung in next-generation colliders [20].

The strong field attained in the high-energy interactions with a crystalline lattice in the incident particle frame proves an easy, stable and relatively large-scale probe to study supercritical QED [20]. Moreover, in presence of crystalline strong fields, the electromagnetic processes are significantly modified with respect to their standard counterparts occurring at lower energy and in amorphous media – not only radiation emission, but also pair production by high-energy photons, as discussed in section 1.4.3. This proves interesting in view of several technological applications in high-energy physics (HEP) [20] such as the ones described in this work.

### 1.4.1 The strong field regime in crystals

An estimate of the intensity of the strong field and, in turn, of the subsequent effects is given by [20]

$$\chi = \frac{\gamma \mathcal{E}_\perp}{\mathcal{E}_0} \quad ; \quad (1.29)$$

here,  $\mathcal{E}_\perp$  ( $\gamma \mathcal{E}_\perp$ ) is the transverse field in the laboratory (incident particle) frame. Clearly, in order for the strong field regime to be attained,  $\chi$  must be greater than 1 [10, 20]. However, SF-related modifications to the standard electromagnetic processes occur down to  $\chi \sim 0.1$  [10, 60, 66]. An estimate of  $\chi$  which explicitly shows its dependence on the lattice properties is given by [20]

$$\chi \sim \frac{U_0 \gamma \hbar}{m^2 c^3 a_S} \quad . \quad (1.30)$$

Equations 1.29 and 1.30 show that the SF effect intensity linearly depends on

- the lattice potential ( $U_0$ ) and field strength;
- the incident particle energy ( $\gamma$ ).

A material-dependent energy threshold,  $\hbar\omega_t$ , can be defined<sup>5</sup>. Starting from equation 1.29, setting  $\chi = 1$  and roughly assuming  $\mathcal{E}_\perp \sim U_0/\sqrt{2}eu_1$  leads to [20]

$$\hbar\omega_t \sim \frac{\sqrt{2}u_1 m^2 c^4}{U_0 \lambda_C} . \quad (1.31)$$

However, as pointed out in [20], equation 1.31 represents a rather crude estimate and the resulting values represent an underestimate with respect to the predictions provided by the more detailed calculations described in [10]. Another simple approach consists of solving equation 1.30 for  $\gamma$ , setting  $\chi = 1$  and estimating  $a_S$  properly. This leads to

$$\hbar\omega_t = \frac{a_S m^2 c^4}{U_0 \lambda_C} , \quad (1.32)$$

which seems to provide more reliable results.

### 1.4.2 Strong field radiation

The extremely intense field is approximately constant over long sections of the particle motion inside the crystalline lattice. As a result, in the so-called constant field approximation [10, 20, 67–69], the particle propagates in the same way as under the effect of a uniform magnetic field, i.e., like in a synchrotron [20] and its trajectory comprises circular stages. A sketch of this motion is shown in figure 1.16.

The condition of transverse energy conservation between the beginning and the end of a single circular motion stage equation can be written, according to equation 1.13b, as [20]

$$\frac{p^2}{2m\gamma}\psi^2 = \frac{p^2}{2m\gamma}(\psi + \Delta\psi)^2 - U_0$$

which, assuming  $\psi \gg \Delta\psi$ , i.e., that the misalignment angle variation along this trajectory stage is small with respect to the initial angle, leads to

$$\Delta\psi = \frac{U_0}{\gamma m c^2 \psi} .$$

Indeed, if [10, 20]

$$\psi < \Theta_0 = \frac{U_0}{m c^2} \quad (1.33)$$

---

<sup>5</sup>This peculiar notation is due to the fact that the SF energy threshold was originally defined in the context of the SF pair production – see section 1.4.3.2 and [10].

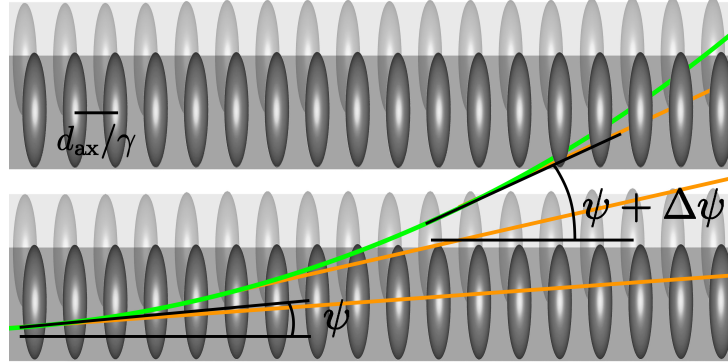


FIGURE 1.16: Sketch of the radiation emission in a strong crystalline field. The lattice is shown in the particle frame. The parent electron (emitted radiation) is drawn in green (orange).

then the trajectory curvature radius is small enough for the particle to exit the cone of aperture  $1/\gamma$  associated to the radiation emission of this part of the motion. As already discussed in section 1.3.3, this is the condition for the output radiation to be synchrotron-like [20].

It has to be noted that  $\Theta_0$  is independent on the initial energy and, on the other hand, strongly depends on the lattice potential. Comparing it with the critical angle for channelling (equation 1.16) leads to

$$\frac{\Theta_0}{\psi_L} = \frac{1}{mc^2} \sqrt{\frac{E_0 U_0}{2}} \quad ,$$

i.e., the higher the incident particle energy and the stronger the crystalline potential, the more dominant the SF effects are over channelling. Indeed, in case of heavy crystals and at  $\gtrsim 10$  GeV, the acceptance of the latter is several times smaller than that of SF [20] – see, e.g., section 2.1 (chapter 2). Moreover, at this very high energy regime, the radiation output from the motion in SF is of the same kind as that from channelling, described in section 1.3.3, i.e., synchrotron-like radiation emitted with significant recoil of the parent electron. The latter makes a quantum formulation the most suitable to describe this emission process, therefore the quantum descriptions of, e.g., the formation length (equation 1.24) and the spectrum endpoint frequency (equation 1.26) should be used.

In general, the total radiation spectrum, i.e., the energy spectrum of the radiation emitted by all the processes occurring inside the crystal, comprises the contributions of all the effects described in this chapter with different relative yields, depending on the initial energy and on the misalignment angle. In

particular, at high energy, the threshold defined in equation 1.33 can be considered as the division line between the synchrotron regime described above ( $\psi < \Theta_0$ ) and the dipole regime ( $\psi > \Theta_0$ ) in which coherent bremsstrahlung dominates<sup>6</sup> – see section 1.3.4. As already mentioned, coherent effects set in at up to  $\psi \sim 1^\circ$  [50, 60].

### 1.4.3 Strong field and photons

The creation of an  $e^+e^-$  pair by a high-energy photon incident in matter, i.e., the so-called pair production (PP), is intimately related to the emission of electromagnetic radiation by electrons/positrons at the same energy range. The Feynman diagrams associated to these two processes are shown in figure 1.17. Indeed, keeping in mind that a positron can be seen as an electron that travels backwards in time [70], it can be easily observed that the diagram of bremsstrahlung (right) is obtained by means of a simple counterclockwise rotation from that of PP (left)<sup>7</sup>.

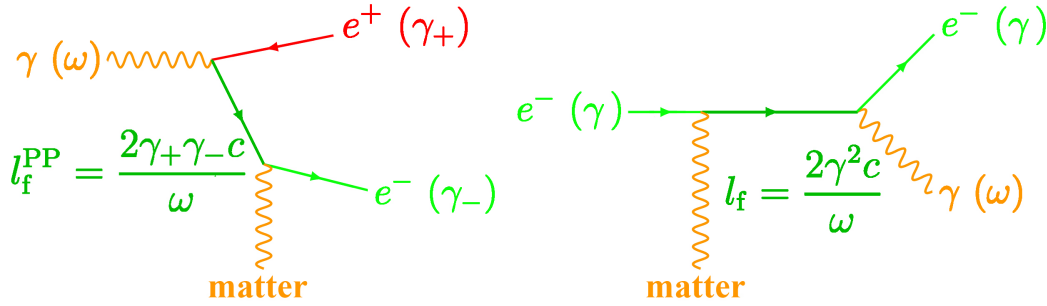


FIGURE 1.17: Feynman-like diagrams of (*left*) pair production and (*right*) bremsstrahlung. The corresponding formation lengths are reported as well.

Since bremsstrahlung is heavily affected by the presence of the crystalline lattice, it is natural to speculate about whether PP in crystals experiences any modification with respect to the amorphous case as well. This might seem rather counter-intuitive, as photons do not carry an electric charge and, hence, do not interact with the electromagnetic field.

<sup>6</sup>It is worth noting that the description of the behaviour around  $\Theta_0$  is puzzling; in particular, the CB model breaks at particularly high energies and low misalignment angles [41]. As it is typical of the literature on the topic, further details are provided when discussing the crystalline effects in pair production, in section 1.4.3.2.

<sup>7</sup>In truth, the two diagrams sketched here differ by the inversion between the two vertices involving the matter electromagnetic field and the input/output photon respectively. The interactions are symmetric with respect to this inversion.

In practice, PP is affected by the interactions with external fields while the pair is created, i.e., in the dark green section of the diagram in figure 1.17 left – see, e.g., [40, 71]. Modifications to the standard PP in oriented crystals are therefore possible [19, 20, 67, 68, 72], and are described in the following.

#### 1.4.3.1 Bethe-Heitler pair production

Before discussing the influence that the crystalline lattice has on pair production, it is useful to briefly summarise the general features of the process. The Bethe-Heitler model (introduced in section 1.3.1) provides a description of it in an amorphous medium [34]. Indeed, as shown below, the quantitative features of the latter are very similar to those of standard bremsstrahlung [30].

The cross section for the production of an electron of energy  $E_-$  and a positron of energy  $E_+$  by a parent photon of energy  $\hbar\omega = h\nu = E_- + E_+ \gg mc^2$  can be written as [34]

$$\Phi^{\text{PP}}(E_-; \omega) \propto \frac{\alpha Z^2 r_e^2}{(\hbar\omega)^3} \left[ \left( E_-^2 + E_+^2 + \frac{2}{3} E_- E_+ \right) \ln \left( \frac{183}{Z^{1/3}} \right) - \frac{E_- E_+}{9} \right] , \quad (1.34)$$

where  $E_+ = \hbar\omega - E_-$  and hence only two degrees of freedom are needed. Equation 1.34 applies to the case of high-energy incident photons; on the other hand, it is trivial that PP only occurs if  $\hbar\omega > 2mc^2 \sim 1.22$  MeV, whereas there is no lower threshold for radiation emission to set in [30, 34]. Nevertheless, the similarity between PP and bremsstrahlung is clearly observed once more comparing equation 1.34 with equation 1.20.

It is evident from the cross section expression and plot (figure 1.18) that PP is symmetrical with respect to the swap between electron and positron [34]. Moreover, figure 1.18 shows that at very low energy ( $\lesssim 25$  MeV) the energy spectrum for both the output particles is peaked at  $\sim 50\%$   $\hbar\omega$  whereas at higher energies two different peaks appear: at a few GeV or higher, one of the two particles typically takes most of the available energy. The asymmetry between  $E_-$  and  $E_+$  is bigger, the higher the parent photon energy.

The differential cross section for PP can also be calculated with respect to the angle between one of the emitted leptons – say, the electron – and the parent photon, i.e., [34]

$$\Phi^{\text{PP}}(\Delta\psi_-^{\text{PP}}, E_-) \propto \frac{\Delta\psi_-^{\text{PP}}}{1/\gamma_-^2 + (\Delta\psi_-^{\text{PP}})^2} , \quad (1.35)$$

where  $\gamma_- = E_-/mc^2$  is the Lorentz factor of the output electron. It is clear from equation 1.35 that the preferred emission direction for the electron (po-

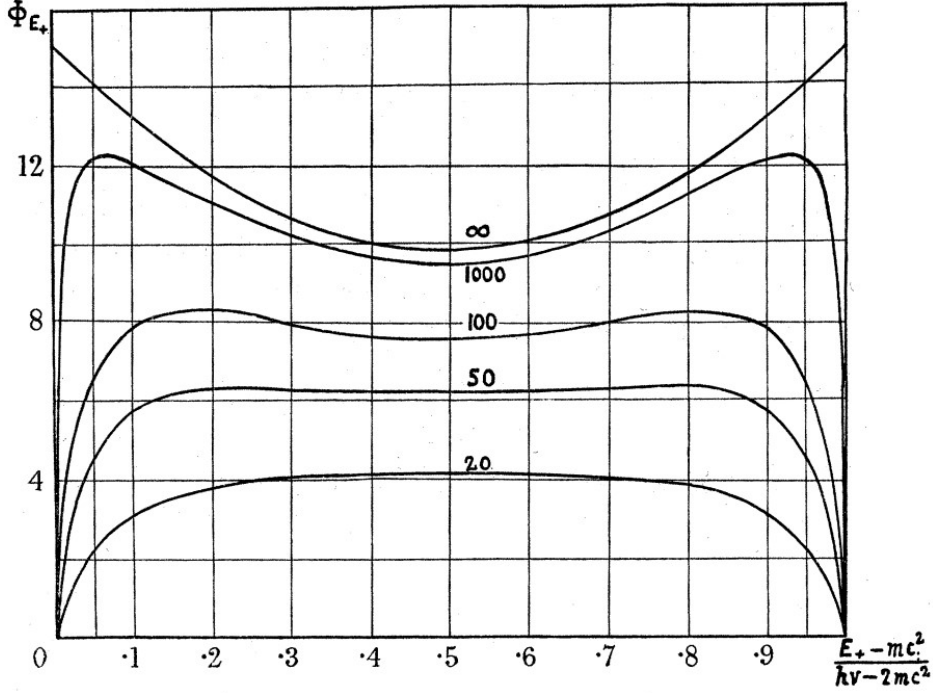


FIGURE 1.18: Cross section of standard pair production in lead as a function of the output positron energy in units of the parent photon energy, for different values of the latter (numbers affixed to the curves, in units of  $mc^2$ ). From [34].

positron) is at  $1/\gamma_-$  ( $1/\gamma_+$ ) from the parent photon trajectory [34]. Therefore, on average, high-energy output leptons are created in the forward direction [34].

An estimate of the number of photons that undergo pair production in a target of thickness  $t$  is provided by [35]

$$N^\gamma(t) = N_0^\gamma \left[ 1 - \exp\left(-\frac{7t}{9X_0}\right) \right] , \quad (1.36)$$

where  $N_0^\gamma$  is the number of incident photons. In other words, PP is characterised by a mean free path of  $(7/9)X_0$  [30, 35].

Finally, it is worth noting that the integral high-energy cross section [34]

$$\Phi_{\text{tot}}^{\text{PP}} \propto \alpha Z^2 r_e^2 \left[ \frac{28}{9} \ln\left(\frac{183}{Z^{1/3}}\right) - \frac{2}{27} \right]$$

is proportional to  $Z^2$  and is independent on the primary photon energy.

### 1.4.3.2 Lattice-induced effects

As already mentioned, differently from bremsstrahlung, pair production occurs only if  $\hbar\omega \gtrsim 1.22$  MeV [30, 34]. At the same time, rather high photon energies are required for coherent effects to manifest in the PP process [19, 20, 72]: a kinematic threshold can be easily estimated as [19, 72]

$$\hbar\omega_{t,\text{kin}} \sim \frac{2m^2c^4}{U_0} \quad .$$

However, for the coherent effects to attain a yield that is comparable with that of standard PP, considerably higher energies are required [19, 72], whose minimum value is better estimated by equations 1.31 and 1.32. In other words, pair production is affected by the crystalline lattice only around the SF energy scale or higher.

In general, above threshold, the PP yield undergoes a macroscopic enhancement with respect to the purely incoherent case [19, 20, 72]. This enhancement can be categorised into two different regimes, depending on the photon misalignment angle – the separation value being  $\Theta_0$  defined in equation 1.33, similarly to the SF radiation regime acceptance limit [10, 19, 20, 72].

Indeed, for  $\psi \lesssim \Theta_0$  the constant field approximation can be applied in the same way as in treating the synchrotron-like radiation case described in section 1.4.2 [67, 68], and the so-called strong-field pair production (SFPP) regime is attained. On the other hand, for  $\psi \gg \Theta_0$ , the perturbative approach based on the Born approximation [41, 73, 74] is valid, i.e., the same approach at the foundation of the coherent bremsstrahlung theory – see section 1.3.4. Indeed, the latter process is called coherent pair production (CPP) [8, 51].

The probability of coherent pair production has a maximum at  $\psi \propto 1/\omega \neq 0$ , i.e., at a misalignment angle inversely proportional to the energy of the parent photon [67, 68]. Therefore, the CPP model proves unsuitable in describing pair production in crystals at very high energy, because the angle corresponding to the maximum PP probability becomes  $< \Theta_0$  [10, 67, 68]. In practice, forcing a description of the coherent mechanisms of pair creation based on CPP out of its range of validity leads to unphysical results concerning the PP yield, like a major growth at very high energy and a suppression at  $\psi = 0$  [41]. More general descriptions that encompass both the models and, hence, are reliable for any misalignment angle and initial energy have been developed – details can be found, e.g., in [10, 41, 67, 68, 75–77].

An analog of the radiation formation length (section 1.3.2) can be defined for pair production as [20]



$$l_f^{\text{PP}} = \frac{2\gamma_+ \gamma_- c}{\omega} \quad , \quad (1.37)$$

where  $\gamma_{\pm} = E_{\pm}/mc^2$ . In a classical picture,  $l_f^{\text{PP}}$  can be interpreted as the required length to separate a created pair transversely by two Compton wavelengths when the pair is emitted with an opening angle  $1/\gamma_{\text{PP}}$ , where  $\gamma_{\text{PP}} = \hbar\omega/mc^2$  [20].

Equation 1.37 has the same form of equations 1.23 and 1.24, which further highlights the similarity between PP and bremsstrahlung [20]. However, the radiation formation length dramatically grows as the parent charged particle energy grows, whereas the pair formation length is inversely proportional to the incident photon energy (and directly proportional to the energies of the output leptons) [20]. This behaviour reflects the fact that the higher the initial photon energy, the shorter the propagation of the virtual  $e^+e^-$  pair before becoming real is. Moreover, it provides further proof of the inapplicability of the CPP model at high energy, i.e., when  $l_f^{\text{PP}}$  becomes small with respect to the spacing between successive planes/axes along the photon trajectory. For  $\chi$  of the order of a few units, the SFPP yield is roughly proportional to the pair formation length [20]. As a consequence, differently from standard pair production (figure 1.18), the pair creation yield as a function of the fractional energy taken by, say, the electron features one broad peak centered at  $\hbar\omega/2$  [19, 20]. On the other hand, at very high energy, the spectrum becomes more similar in shape to that of standard PP [20].

#### 1.4.4 Compact electromagnetic showers

If an electron/positron (photon) impinges on a multi- $X_0$  target with sufficiently high energy, the photon (lepton pair) resulting from its electromagnetic interaction with the latter will still have enough energy to undergo PP (radiation emission) [30, 78]. Multiple steps of this process, i.e., the so-called electromagnetic shower, can occur, generating more lower-energy secondary particles at each step, until the single-particle energy is approximately lower than the critical energy  $E_c$  defined in equation 1.22 and each particle dissipates the remaining energy by non-radiative interactions [30].

Recalling that the typical spatial scale is  $X_0$  for radiation emission and  $(7/9)X_0$  for PP, it is convenient to study the longitudinal shower development in terms of the number of radiation lengths, i.e.,  $\kappa = t/X_0$  [30]. Several analytical and numerical models exist. For instance, the average energy deposit of a shower as a function of  $\kappa$  is well described by [30, 35, 79]

$$\left\langle \frac{dE}{d\kappa} \right\rangle = \frac{(b^\dagger \kappa)^{a^\dagger - 1} \exp(-b^\dagger \kappa)}{\Gamma(a^\dagger)} E_0 b^\dagger \quad , \quad (1.38)$$

where  $\Gamma(k)$  is the Gamma function defined for any real  $k \neq 0, -1, -2, \dots$  as [80]

$$\Gamma(k) = \begin{cases} \int_0^\infty d\zeta \exp(-\zeta) \zeta^{k-1} & k > 0 \\ \frac{\pi}{\Gamma(1-k) \sin(\pi k)} & k < 0 \end{cases}$$

and  $a^\dagger$  and  $b^\dagger$  are parameters that depend on the total energy, on the target material and on whether the primary particle is a lepton or a photon, obtained fitting simulation data [35, 79].

According to the model described by equation 1.38, the number of secondary particles generated as the shower develops grows with  $\kappa$ , and so does the number of secondary charged leptons. At the same time, since the average energy per secondary particle decreases after each electromagnetic interaction, more particles go under threshold as  $\kappa$  grows, thus ceasing to contribute to the shower mechanism. As a result, the energy deposit attains a maximum at approximately [30, 35]

$$\kappa_{\max} = \frac{a^\dagger - 1}{b^\dagger} = \ln \left( \frac{E_0}{E_c} \right) + \tilde{\kappa} \quad , \quad (1.39)$$

where  $\tilde{\kappa} = -0.5$  ( $0.5$ ) for leptons (photons). Moreover, the rightmost equality in equation 1.39 can be solved for  $a^\dagger$ , since it is reasonable to set  $b^\dagger = 0.5$  [30].

It is worth remarking that this model is inadequate to describe the shower development in about the first two radiation lengths [30]. Nevertheless, the shower global and average behaviour is correctly reproduced [30].

Moreover, in general, the total shower length is not estimated correctly [30]; a better estimate is given by [35]

$$\kappa_{95\%} = \kappa_{\max} + 0.08Z + 9.6 \quad .$$

For instance, for primary electrons of up to  $\sim 300$  GeV, a thickness of  $\sim 25 X_0$  reduces the longitudinal leakage at the rear end of the target to  $\ll 1\%$  [35]. The MCS of secondary electrons and positrons away from the primary particle incident direction results in a transverse spread [35]. The scale of the

transverse size of a shower is given by the so-called Molière radius,  $R_M$ , an approximation of which is given by [35]

$$R_M \sim \frac{(21 \text{ MeV}) X_0}{E_c} .$$

$R_M$  represents the average lateral deflection experienced by electrons of energy  $E_c$  crossing  $1 X_0$  of matter, and is independent on  $E_0$  [35]. On average,  $\sim 90\%$  of a shower is contained in a cylinder of radius  $1 R_M$  [35].

Figure 1.19 shows a comparison between sketches of an electromagnetic shower initiated by a high-energy electron and developing in a crystalline medium in random orientation (top) and in axial alignment (bottom). Owing to the enhancement of bremsstrahlung and PP, when on axis, the shower is more compact along the longitudinal direction: in particular, it is clear that

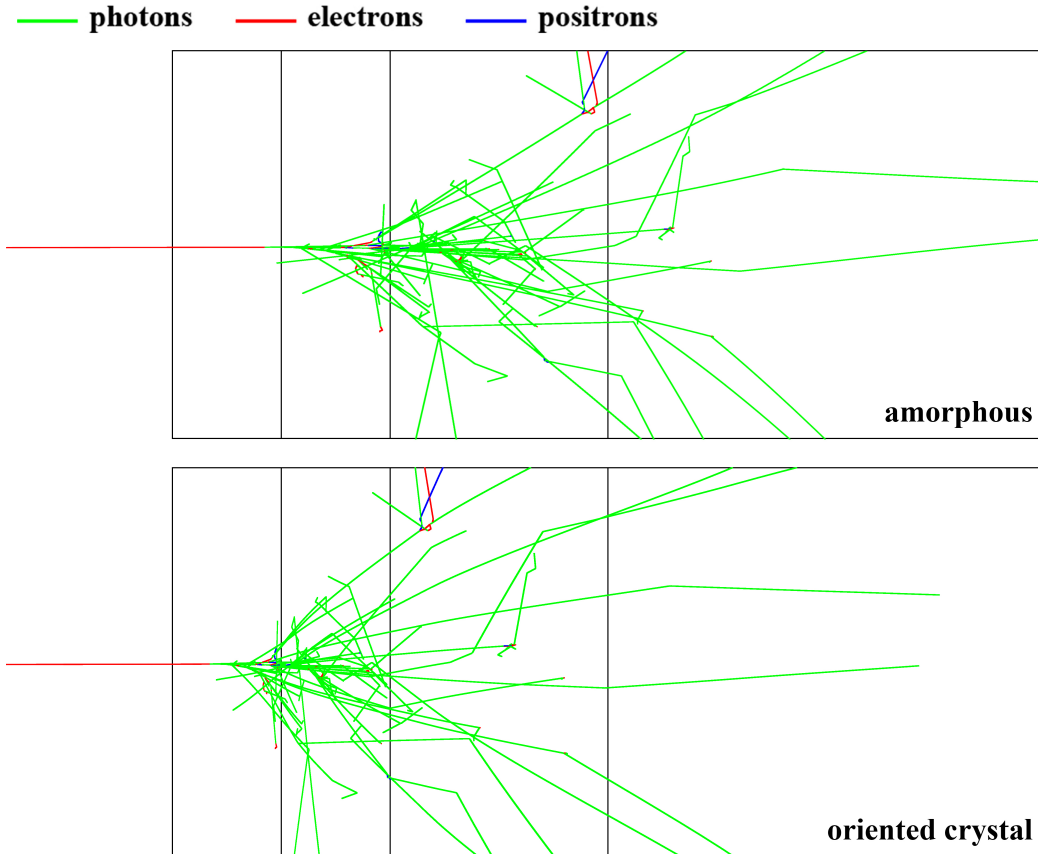


FIGURE 1.19: Sketch of the development of an electromagnetic shower in (*top*) an amorphous medium and (*bottom*) an oriented crystal.

- the shower endpoint, i.e., the right end of the two rightmost photon tracks, is contained in the target thickness only when the latter is axially oriented;
- the shower peak, i.e., the region of highest density of photon tracks, is located significantly closer to the target front when the latter is axially oriented.

The reduction of the shower length in crystals can be seen as the reduction of the effective radiation length values with respect to the standard values obtained in case of amorphous or randomly oriented media [50, 81]. This reduction is not uniform along the target depth: the enhancement of the electromagnetic processes is the strongest in the first interaction of the primary particle; already after the first shower interaction, secondary particles are generated with an energy lower than  $E_0$  and with an angle with respect to the shower axis, which results in a reduction of the coherent effect strength. As a consequence, the shower generation features the most significant enhancement in the first radiation lengths and becomes similar to the case of amorphous-like media in the downstream part.

Moreover, as shown in equation 1.39, the standard shower peak position depends on  $\ln(E_0)$ . This dependence is significantly weaker in axially oriented crystals, because the enhancement of bremsstrahlung and PP grows stronger as  $E_0$  increases, which compensates for the increase of  $\kappa_{\max}$  [81, 82].

### 1.4.5 Behaviour at extremely high energies

The maximum pair production enhancement with respect to the Bethe-Heitler yield can be estimated as [10, 20]

$$\eta_{\max}^{\text{PP}} = \frac{mU_0a_{\text{S}}d_{\text{ax}}}{3(Z\alpha\hbar)^2 \ln(183/Z^{1/3})} \quad . \quad (1.40)$$

The latter attains values that range from a few tens to a few hundreds. Owing to the fact that  $\eta_{\max}^{\text{PP}}$  is directly proportional not only to  $U_0$ , but also to  $d_{\text{ax}}$ , and features an inverse dependence on  $Z^2$  and  $\ln(Z^{1/3})$ , the stronger the crystalline axis, the lower is the SF energy threshold but also the maximum enhancement [20].

Equation 1.40 can also be used to roughly estimate the radiation enhancement with respect to the purely incoherent case [20]. It has to be noted that other estimates of the maximum enhancement attained by SFPP and SF radiation emission, performed by means of Monte Carlo (MC) simulations, are

lower than those found with equation 1.40 – see, e.g., section 2.4 (chapter 2) and [41].

The maximum values for both the processes are attained at  $\sim 100$  times the SF threshold energy  $\hbar\omega_t$ , which typically corresponds to several TeV or higher, i.e., significantly above the current energy scale of state-of-the-art electron and photon beams [20]. At even higher energies ( $\chi \gg 1$ ), the coherent mechanisms saturate [20, 41].

# CHAPTER 2

---

## Experimental techniques

On the wave of the recent and fast advancements in the development of the theory of coherent effects in crystals, experiments have been performed in the last decades, both to validate the theoretical predictions and to expand the already available knowledge with new empirical observations. In particular, the experimental characterisation of high-energy coherent interactions goes hand in hand with the construction of more powerful particle accelerators. The first experimental evidences of a modification to the features of the electromagnetic radiation emitted by electrons in crystals as a function of the lattice orientation came in 1959–1960. Firstly, coherent bremsstrahlung was observed [7, 8, 51, 83]. Only a few years later, in 1968, channelling radiation was measured for the first time at a few tens of MeV [42, 43]. Similarly, the first observation of coherent pair production (CPP) dates back to 1960 [84].

On the other hand, experimental investigations of strong field (SF) effects – that is, at tens of GeV or more – only started in the early 1980s [20] for both pair production (PP) [85, 86] and radiation emission [87] in germanium and diamond crystals respectively. Measurements on high- $Z$ , high-density crystals, such as tungsten and silicon, have been performed starting from the 1990s. Most of these studies were driven by the need to test the feasibility of an intense positron source [88, 89] and to develop a compact photon converter, a device to separate the photon and neutral hadron beam components with minimal absorption or scattering of the latter [66, 72] – this was needed by the NA48 experiment at CERN (Conseil Européen pour la Recherche Nu-

cléaire, today Organisation Européen pour la Recherche Nucléaire – Geneva, Switzerland), and featured samples with a thickness of  $\lesssim 1 X_0$  or, in the case of a few studies limited to the sub-strong field energy range, slightly thicker ones [82].

Nowadays, several novel applications of coherent effects at very high energy and/or in multi- $X_0$  crystalline targets are considered, as the ones discussed in this work. This chapter describes the framework of the experimental activity of these R&Ds. Particular attention is put on the experimental configuration of the beamtests, to which, since 2017, the author has participated, designing and installing the setup and performing the online characterisation of the detectors.

## 2.1 The AXIAL/ELIOT/STORM project

The INFN (Istituto Nazionale di Fisica Nucleare) collaboration that studies coherent effects in crystals<sup>1</sup> is a worldwide leader on experimental tests and MC simulations. Since 2016, the team has been carrying on a research line on electromagnetic particles – i.e., electrons/positrons and photons – impinging on high- $Z$ , high-density crystalline materials. The aim is twofold:

- to characterise the lattice effects in a wide range of energies (from hundreds of MeV to hundreds of GeV);
- to find and test the feasibility of potential applications of these effects to novel, high-performance technology for HEP – namely, accelerator components and detectors.

This research line has evolved into two major branches, which differ from each other in terms of the probed crystalline media: heavy metals and inorganic scintillators. Firstly, studies on tungsten crystals for intense radiation and positron beam generation were performed in 2017–2018 in the framework of the AXIAL project<sup>2</sup>. At the same time, AXIAL also dealt with the development of compact photon converters and the preliminary feasibility tests of innovative particle detectors based on oriented scintillating crystals. All these studies were expanded in the context of the ELIOT (ELectromagnetic

---

<sup>1</sup>Experimental teams from the INFN sections of Ferrara and Milano Bicocca and from Laboratori Nazionali di Legnaro are involved in this collaboration.

<sup>2</sup>The study of innovative radiation and positron sources based on oriented heavy crystals only constituted half of the AXIAL physics programme; the other half was focused on continuing the long-standing tradition of the INFN Ferrara team of studies of bent silicon and germanium crystals for beam steering – see, e.g., [90–92].

processes In Oriented crysTals) project, which was carried on in 2019–2020, and later, until very recently (2021–2022) of the STORM (STrOng cRystalline electroMagnetic field) project, in which a particular focus was put on the applications of the coherent effects and of the related concepts to next-generation hardware for HEP.

### 2.1.1 Heavy metals

Heavy metals such as tungsten (W) and iridium (Ir) feature the strongest lattice potentials – up to  $\sim 900$  eV [82] – among all the materials that have crystalline allotropes. Therefore, despite their rather poor crystalline quality, which in general results in lower channelling efficiency values, they prove to be excellent probes in studying the over-barrier coherent effects. Moreover, they are the most appealing option to be considered in the design of radiators or photon converters in which two of the most important parameters to be traded off between one another are the strength of the electromagnetic field in the target and the input angular acceptance: a higher crystalline potential corresponds to a larger angular acceptance, and the resulting field is very strong despite the rather large mosaicity<sup>3</sup> – typically  $\gtrsim 100$   $\mu\text{rad}$  in tungsten; moreover, a large mosaicity corresponds to an increase of the angular acceptance even further.

Currently, the STORM team is carrying out two projects focused on lattice effects in tungsten: the design of a high-intensity, low-emittance positron source based on an oriented radiator [93], and the development of a high-efficiency oriented photon converter to clean the photon background in the HIKE (High Intensity Kaon Experiments) neutral hadron beam [94]. Both of them are presented in this work, in chapters 3 and 4 respectively.

The main physical properties of tungsten are listed in table 2.1. Owing to its strength, radiation hardness, and short radiation and nuclear interaction lengths, it is widely exploited in experimental HEP – in particular, in the design of beam collimators, radiation shields, beam absorbers, targets for beam-dump experiments, electromagnetic radiators, and photon converters [82]. Moreover, tungsten foils with a thickness of  $\lesssim X_0$  can be easily manufactured and prove ideal as passive absorber layers in sampling calorimeters<sup>4</sup>; similarly, thin tungsten foils have been used in space-borne  $\gamma$ -ray telescopes, such as in the AGILE (Astro-rivelatore Gamma a Immagini LEggero) [95–

<sup>3</sup>The mosaicity of a crystal is the spread of the axis orientations in the individual crystallites that make up the macroscopic sample.

<sup>4</sup>A calorimeter is a block of instrumented material in which particles to be measured are fully absorbed and their energy is transformed into a measurable quantity [35] – further details on the subject are given in chapter 5.



	W	PWO
$Z/A$	74/183.84	0.41315
$\rho$ [g/cm <sup>3</sup> ]	19.3	8.3
Standard $X_0$ [mm]	3.504	8.903
Standard $R_M$ [mm]	9.327	19.59
$E_C$ for $e^-$ [MeV]	7.97	9.64
$E_C$ for $e^+$ [MeV]	7.68	9.31
Nuclear collision length [mm]	57.19	121.2
Nuclear interaction length [mm]	99.46	202.7
Pion collision length [mm]	69.36	152.1
Pion interaction length [mm]	113.3	240.4

TABLE 2.1: Physical properties of tungsten and lead tungstate [13, 30].

97] and Fermi LAT (Large Area Telescope) [98] trackers, to convert incoming photons into  $e^+e^-$  pairs [82].

The tungsten crystalline structure (figure 2.1 left) is simple: it features a body-centered cubic (BCC) scheme with a lattice constant  $a = 3.1652$  Å [82]. The two main axes are  $\langle 100 \rangle$ , which corresponds to the side of the unit cell, and the one crossing the body diagonal,  $[111]$ , which has an interatomic distance of  $\sqrt{3}a/2 = 2.7411$  Å. The main properties of both of them are listed in table 2.2 and their potentials are shown in figure 2.1 right as a function of the distance from the atomic string, calculated including thermal vibrations with an amplitude of 0.05 Å.

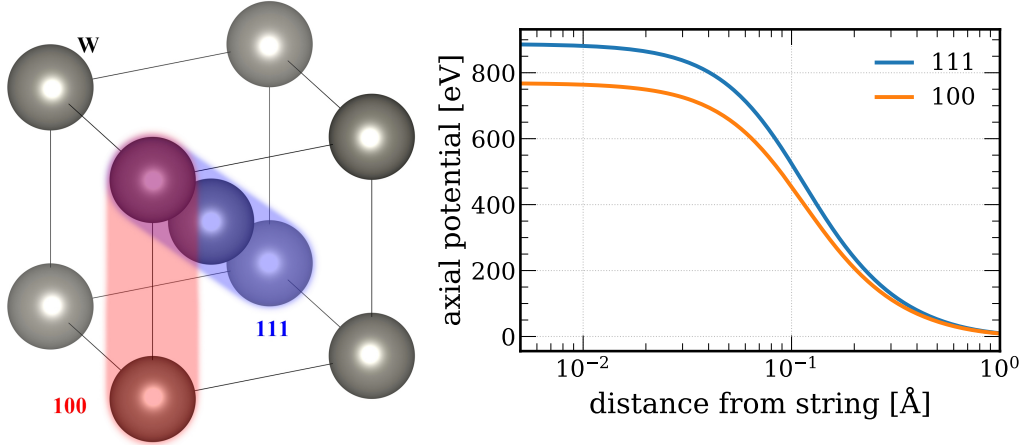


FIGURE 2.1: Crystalline tungsten unit cell (*left*) and axis potentials as a function of the distance from the atomic string (*right*). The two strongest axes, i.e.,  $[111]$  and  $\langle 100 \rangle$ , are considered.

	W		PWO	
Axis	111	100	100	001
$d_{\text{ax}}$ [Å]	2.7411	3.1652 [82]	5.456 [99]	12.020 [99]
$U_0$ [eV]	887	769	464	420
$^*\hbar\omega_t$ [GeV] ( $u_1 = 0.1$ Å)	10.74	12.39	20.54	22.69
$^{**}\hbar\omega_t$ [GeV] ( $a_S = 0.215$ Å $\cdot \sqrt[3]{Z/74}$ )	16.33	18.84	23.45	25.90
$\chi$ ( $E_0 = 5.6$ GeV, $a_S = 0.215$ Å $\cdot \sqrt[3]{Z/74}$ )	0.34	0.30	0.24	0.22
$\chi$ ( $E_0 = 120$ GeV, $a_S = 0.215$ Å $\cdot \sqrt[3]{Z/74}$ )	7.35	6.37	5.12	4.63
$\eta_{\text{max}}^{\text{PP}}$ ( $a_S = 0.215$ Å $\cdot \sqrt[3]{Z/74}$ )	20.62	20.64	83.59	166.69
$\Theta_0$ [mrad]	1.736	1.505	0.908	0.822
$\psi_L$ [mrad] ( $E_0 = 5.6$ GeV)	0.563	0.524	0.407	0.387
$\psi_L$ [mrad] ( $E_0 = 120$ GeV)	0.122	0.113	0.088	0.084

TABLE 2.2: Properties of the strongest axes of tungsten and lead tungstate. The values of  $\hbar\omega_t$  in the line above (\*) have been obtained from equation 1.31 with  $u_1 = 0.1$  Å and should be intended as rough (under)estimates [20]; on the other hand, the values in the line below (\*\*) have been obtained from equation 1.32 with  $a_S = 0.215$  Å  $\cdot (Z/74)^{1/3}$ , as well as the values of  $\chi$  and  $\eta_{\text{max}}^{\text{PP}}$  – for PWO, the average  $Z$  has been used. Details in section 1.4.1 (chapter 1).

### 2.1.2 Inorganic scintillating crystals

Owing to their high- $Z$  and density, which results in a short  $X_0$ , and to their light output in response to the passage of high-energy particles, inorganic scintillators are extensively used in the development of homogeneous electromagnetic calorimeters – details in chapter 5.

As of today, despite their crystalline nature, the influence of the lattice orientation on the electromagnetic processes inside the calorimeter bulk has been ignored in both the simulation and construction of all the state-of-the-art detectors [50]. On the other hand, the possibility of significantly reducing

the effective radiation length as compared to the standard one, evaluated in case of unaligned lattice, might prove appealing for the development of ultra-compact electromagnetic homogeneous calorimeters that would challenge the performance of the current state-of-the-art detectors [50].

Among the most commonly used crystalline scintillators in HEP, standard (undoped) lead tungstate ( $\text{PbWO}_4$  or PWO) features the highest density [30] and the shortest  $X_0$  and  $R_M$  [30] (values in table 2.1). Its average atomic number is  $Z = (82 + 74 + 4 \cdot 8)/6 = 31.33$  [13]. Moreover, it proves a very good scintillating medium – especially when properly doped, as in its latest generations; details are provided in section 5.2 (chapter 5).

The PWO crystalline structure (figure 2.2 left) is significantly simpler than that of most of the other inorganic scintillators commonly exploited in HEP. It is a scheelite-type structure of tetragonal symmetry and unit-cell parameters  $a = b = 5.456 \text{ \AA}$  and  $c = 12.020 \text{ \AA}$  [99]. The properties of the  $\langle 100 \rangle$  and  $[001]$  axes are listed in table 2.2, and their potentials as a function of the distance from the string, computed assuming a thermal vibration amplitude of  $0.05 \text{ \AA}$ , are shown in figure 2.2 right.

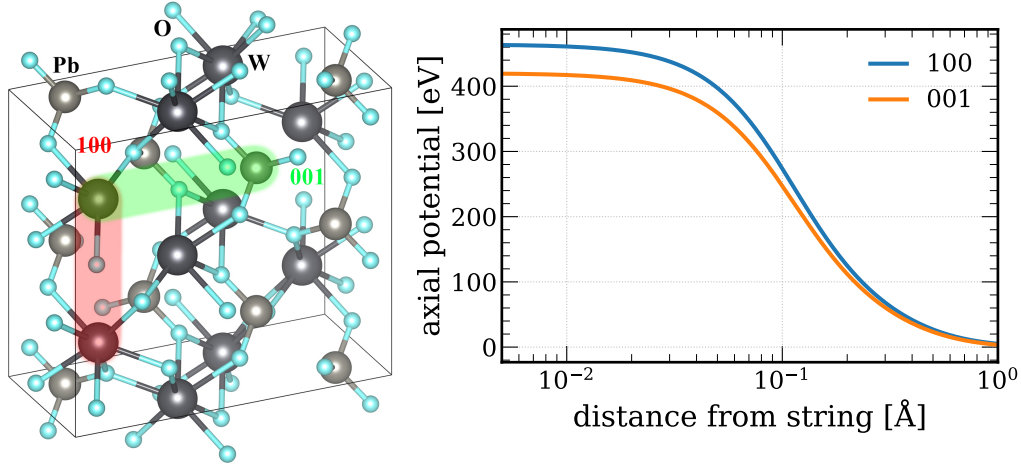


FIGURE 2.2: Lead tungstate: lattice structure (*left*) with two of the main axes ( $\langle 100 \rangle$  and  $[001]$ ) highlighted, whose potentials are also plotted as a function of the distance from the atomic string (*right*). For a clear visualisation of the lattice structure, two neighbouring unit cells have been drawn.

The strongest axis is  $\langle 100 \rangle$ , which features the shortest interatomic distance; lead and tungsten atoms are arranged in separate strings that alternate with each other in the transverse plane. On the other hand, considering the  $[001]$  axis, each string features an alternating sequence of lead and tungsten nuclei. In computing the potentials shown in figure 2.2 right, an average between

the fields of single lead and tungsten atoms has been used, which leads to the exact potential value for the  $[001]$  axis and proves a reasonable approximation for the  $\langle 100 \rangle$  axis – see section 1.2.1 (chapter 1).

Moreover, table 2.2 shows that the potential maxima and SF critical angles for PWO are approximately half those of pure tungsten. On the other hand, the roughly estimated SF critical energies are doubled with respect to the values obtained for tungsten. It can therefore be inferred that, despite their impressive strength, lattice axes in inorganic scintillators cannot rival those of purely metallic crystals from the standpoint of the intensity of the coherent effects.

In recent years, the STORM team has performed extensive studies on the coherent effects in oriented PWO, with particular focus on the SF energy regime [50, 60, 81, 100]. The ultimate goal of this R&D is to test the feasibility of an ultra-compact, high-performance electromagnetic calorimeter that would prove appealing in future forward detectors and source-pointing space-borne  $\gamma$ -ray telescopes [60]. This project is presented in chapter 5.

## 2.2 The experimental facilities

In order to experimentally characterise the coherent electromagnetic interactions that occur in oriented crystals, it is necessary to perform measurements with focalised particle beams. In particular, the STORM team exploits several international facilities to perform beamtests with electron/positron and photon beams in a wide range of energies. In the context of this work, several measurements were performed

- with 5.6 GeV electrons on the T21 beamline of the DESY (Deutsches Elektronen-Synchrotron – Hamburg, Germany) beamtest facility [101];
- with 120 GeV (and 100 GeV) electrons and positrons and with bremsstrahlung photons of up to  $\sim 100$  GeV on the CERN North Area (NA) beamlines [102, 103].

In the following, details on both these experimental facilities are provided. Some complementary measurements of channelling radiation and irradiation have been performed with 855 MeV electrons at the MAMI (MAInzer MIkrotron – Mainz, Germany) B experimental hall [104] – details can be found in appendix B. Moreover, crystalline lattice quality measurements have been performed with  $X$ -rays on the ESRF (European Synchrotron Radiation Facility – Grenoble, France) beamlines [105, 106]; they are referenced to throughout the following chapters.

### 2.2.1 DESY T21

T21 is one of the experimental areas of the DESY II Test Beam Facility – figure 2.3 [101]. DESY II is an electron synchrotron which typically operates at 6.3 GeV and with a two-pulse cycle of 160 ms [101].

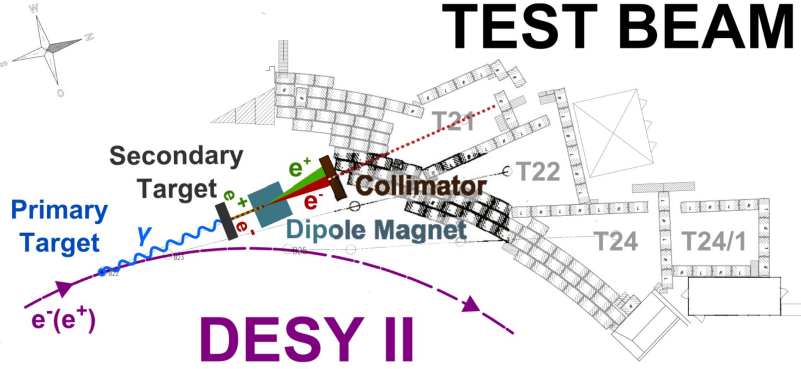


FIGURE 2.3: Layout of the DESY II Test Beam Facility. From [101].

All the electron (and positron) beams at the beamtest facility are obtained by double conversion from the primary electron beam circulating in the synchrotron rather than directly extracted from it [101]: bremsstrahlung photons are generated in a carbon fiber strip positioned in the synchrotron pipe and impinge on a secondary target, in which in turn electrons and positrons are created. The charge sign and momentum of the resulting beam are then selected with a dipole magnet.

The choice of the secondary target thickness and material and the setting of some lead collimators allow to control the beam intensity in the experimental areas [101]. The absolute particle rate also heavily depends on the beam intensity in DESY II, on the position of the carbon fiber inside the synchrotron pipe and on the selected beam momentum [101]. The latter can be set to up to  $\sim 6$  GeV/ $c$ ; intensity variations of more than a factor of 10 are observed in all the areas as a function of the selected momentum, with a maximum at  $\sim 2$  GeV/ $c$  [101]. It has to be noted that, albeit appealing in view of studying crystalline effects as close as possible to the SF energy threshold, choosing a momentum of 6 GeV/ $c$  would have resulted in too low a statistics collection rate; therefore, the momentum has been set to 5.6 GeV/ $c$  in all the physics runs performed in this facility.

Figure 2.4 shows the T21 experimental area. It is divided into two parts, separated by the Big Red Magnet [101] – a horizontal bending magnet with a longitudinal length of 1 m, an opening of  $1.5 \times 0.35$  m<sup>2</sup> and a vertically

oriented magnetic field of up to 1.35 T. The area upstream with respect to the magnet (figure 2.4 left) is rather small, with  $\lesssim 1$  m free room for the detector installation along the beam direction.



FIGURE 2.4: Experimental hall of the T21 beamline at DESY, upstream (*left*) and downstream (*right*) with respect to the Big Red Magnet.

The downstream part (figure 2.4 right) is several metres long and allows for the installation of all the detectors that measure the crystal output particles on multiple DESY tables. Moreover, it has room for the DAQ (section 2.3.1.4) and pre-alignment (section 2.3.2) systems.

Figure 2.5 shows the angular distributions of the T21 5.6 GeV/ $c$  electrons, measured in 2019 with the INSULab Telescope – see sections 2.3.1.1 and 2.3.3. This beam has a divergence of 776  $\mu\text{rad}$  (637  $\mu\text{rad}$ ) in the horizontal (vertical) plane, i.e.,  $\lesssim 50\%$  the SF critical angle for tungsten.

### 2.2.2 The CERN NA beamlines

The CERN North Area (NA – scheme in figure 2.6) is an experimental facility with high-performance, highly flexible beamlines that can adapt to both long-standing fixed-target experiments and beamtests [103].

The particle beams are provided by the Super Proton Synchrotron (SPS), which accelerates protons up to 450 GeV (and heavy ions up to 400 $z$  GeV,  $z$  being the ion charge in units of  $e$ ) [103]. Protons are slow-extracted from the SPS and impinge on three beryllium targets; different-particle beams are obtained starting from all the particles that result from the interactions in the targets, in two different ways [102, 103]:

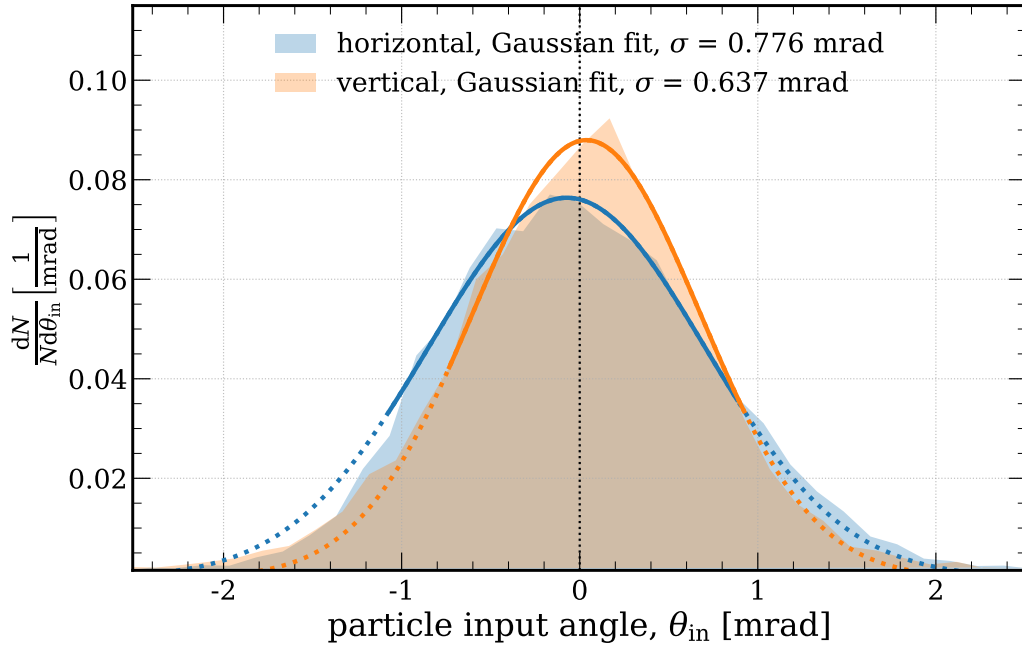


FIGURE 2.5: Angular distributions of the DESY T21 5.6 GeV/ $c$  electron beam.

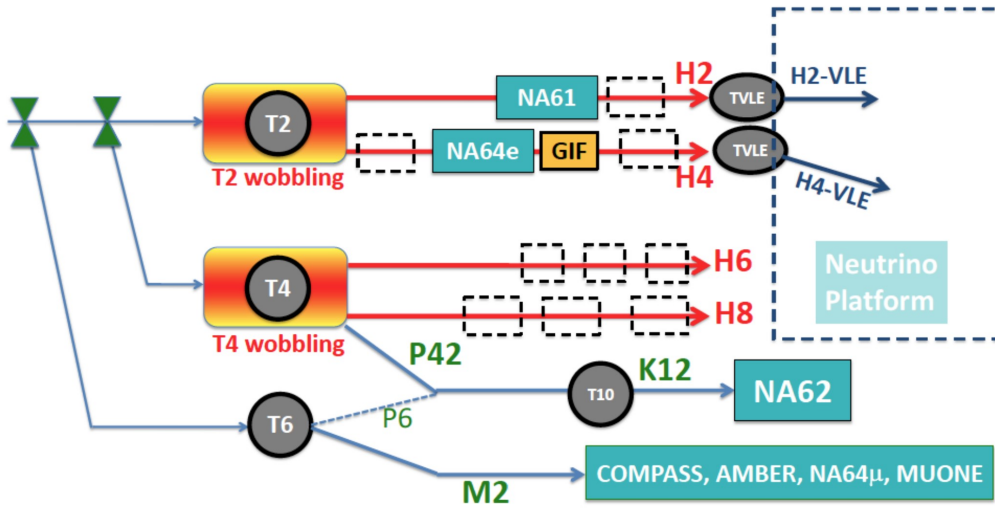


FIGURE 2.6: Scheme of the CERN North Area beamlines. From [103].

- secondary beams are generated capturing and properly manipulating the particles directly emerging from the targets. It is the case of, e.g., the pion and kaon beams [107].

- tertiary beams result from the in-flight decay of secondary particles and/or the interaction of the latter with secondary targets. It is the case of, e.g., the electron beams, which are mainly produced by conversion of photons from  $\pi^0$  decay [103].

Secondary and tertiary beams are delivered to the experimental areas, which are located in two surface halls (EHN – Experimental Hall North – 1 and 2) and one cavern (ECN – Experimental Cavern North – 3) [103]. While EHN2 and ECN3 are devoted to large permanent experiments – the main ones at the moment being COMPASS (COmmon Muon and Proton Apparatus for Structure and Spectroscopy) [108] and NA62 [109, 110] respectively –, EHN1 is mainly devoted to hardware R&D and small-scale physics measurements; it hosts four general-purpose beamlines – H2, H4, H6 and H8 [103].

As shown in figure 2.6, both the H2 and H4 beamlines exploit secondary and tertiary beams originating from the T2 target. In the H2 (H4) beamline, secondary beams of momentum up to 360 GeV/ $c$  (330 GeV/ $c$ ) are available, with a maximum momentum bite  $\Delta p/p = \pm 2\%$  ( $\pm 1.4\%$ ) [102, 103]. As for the electron/positron beams, they are available in both beamlines with highly variable purity – up to 99.5% [111], but it can drop to  $\lesssim 70\%$  at 120 GeV/ $c$  and to even lower values at higher momentum if working in parasitic mode with respect to users of the other beamline requiring special beam conditions – and with a momentum of up to a few hundreds of GeV/ $c$  [112]. The electron beams have a maximum intensity of  $10^6$  ( $10^5$ ) particles/spill in H4 (H2) [103] and are expected to feature slightly higher momentum bite values than the corresponding secondary beams.

Figure 2.7 shows the PPE172 experimental area of the H2 beamline, i.e., the area devoted to beamtests [103]. The latter is divided into two separate sections (figure 2.7 top and bottom) by a large superconducting vertical bending magnet, M1 [113], which has not been used in the measurements performed in this work. When performing electromagnetic radiation measurements (section 2.3.3), the horizontal bending magnet used to separate photons and  $e^\pm$ , a MBPL [102], has been placed right upstream with respect to M1.

Figure 2.8 shows the angular distributions of the 120 GeV/ $c$  electron beam in the H2 beamline, measured during the 2021 beamtest with the INSULab Telescope – see sections 2.3.1.1 and 2.3.3. Divergence values of 85  $\mu\text{rad}$  (94  $\mu\text{rad}$ ) in the horizontal (vertical) plane were measured, i.e., significantly lower than the SF critical angle values computed for the strongest axes of both tungsten and PWO – see table 2.2.

Most of the measurements performed with electrons in the SF regime within the framework of this work have been performed on the H2 beamline. How-



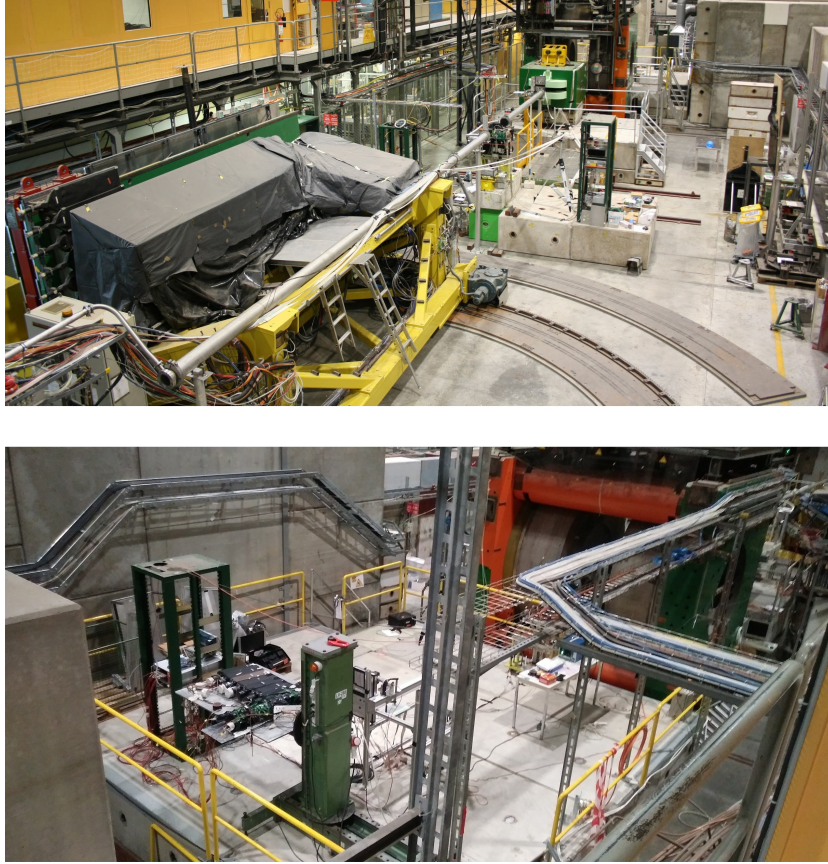


FIGURE 2.7: PPE172 experimental area on the H2 beamline at CERN, upstream (*top*) and downstream (*bottom*) with respect to the M1 superconducting magnet.

ever, beamtests have also been performed on the H4 beamline – see, e.g., the comparison between the radiation spectra obtained with 120 GeV/ $c$  electrons and positrons, in section 5.3.4.2 (chapter 5). In particular, these measurements have been performed in the PPE134 experimental area (figure 2.9). The beam divergence has been observed to be similar to that quoted for H2, i.e., 0.102 mrad (0.084 mrad) in the horizontal (vertical) plane for electrons and 0.098 mrad (0.095 mrad) for positrons.

## 2.3 SF (and sub-SF) measurements

The characterisation of the SF effects in the interaction of the beam with oriented crystals described in the previous section requires a dedicated ex-

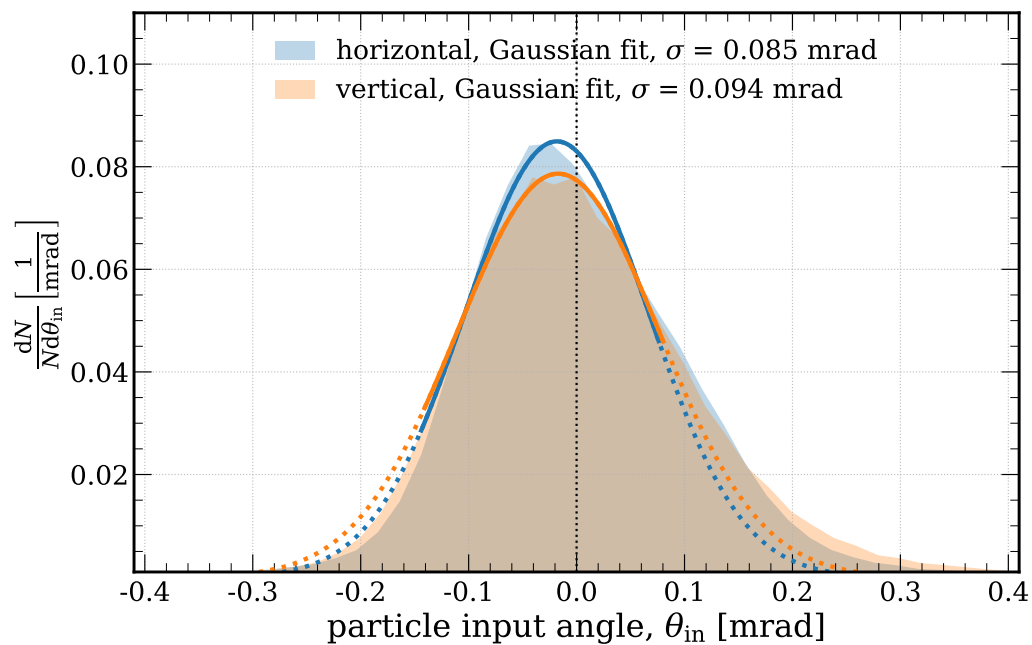


FIGURE 2.8: Angular distributions of the CERN H2 120 GeV/c electron beam.



FIGURE 2.9: PPE134 experimental area on the H4 beamline at CERN.

perimental apparatus with a specific sensitivity and performance. Among the general requirements, it is of paramount importance to have

- an input tracking system that has a high resolution on both the misalignment angle and the position of the particle hit at the crystal surface;
- detectors that are sensitive to the output multiplicity, for both charged particles and, taking into account the intrinsically random nature of PP (see section 2.3.1.3), photons, and in particular to multiplicity variations as a function of the misalignment angle;
- an electromagnetic calorimeter to measure the energy of the crystal output particles;
- a data acquisition system that works on an event-by-event basis, in order to study the correlation between all the quantities mentioned in the previous items;
- a remote-control goniometer for the precise spatial and angular alignment of the lattice with respect to the beam nominal path.

The measurements on the electromagnetic radiation features require also a strong bending magnet to sweep the charged particles away from the beam path and isolate the photons; details are provided in section 2.3.3. Moreover, in order to study the scintillation light in PWO, a dedicated photodetection system has to be exploited; details are given in section 5.3.1.2 (chapter 5).

### 2.3.1 The detectors

In the following sections, a description of all the individual detectors and of the DAQ (Data AcQuisition) system is provided. Depending on the measurements of interest in each beamtest, several experimental setups have been used, which exploit different configurations of the detectors: all these configurations are discussed later in the chapter, starting from section 2.3.3.

#### 2.3.1.1 The tracking system

The tracking system was developed by the INSULAb team at Università degli Studi dell'Insubria (Como, Italy). It is modular, i.e., the tracking layers can be installed independently on one another in any position along the beamline, which makes it highly versatile [114]. Each module features one double-sided or two  $xy$  single-sided silicon microstrip sensors ( $Z = 14$ ). Two different types of tracking modules are available, each one with different specifications.

### The INSULAb Telescope modules

Developed in the Nineties as test detectors of the BaBar Silicon Vertex Detector [115, 116], the INSULAb Telescope [116–118] modules (figure 2.10) are based on double-sided silicon microstrip sensors manufactured by CSEM. Each sensor has an active area of  $1.92 \times 1.92 \text{ cm}^2$  and features a junction side and an ohmic side, in which the strips are obtained by means of  $p^+$  and  $n^+$  implants respectively – a detailed description of the electrical properties can be found in [116–118]. The strips of the two sides are mutually orthogonal. Each sensor is assembled on a fiberglass support together with the printed circuit board (PCB) that hosts the readout ASICs (Application-Specific Integrated Circuits) [107, 117]. Three VA2 ASICs per vista are used [116, 117].

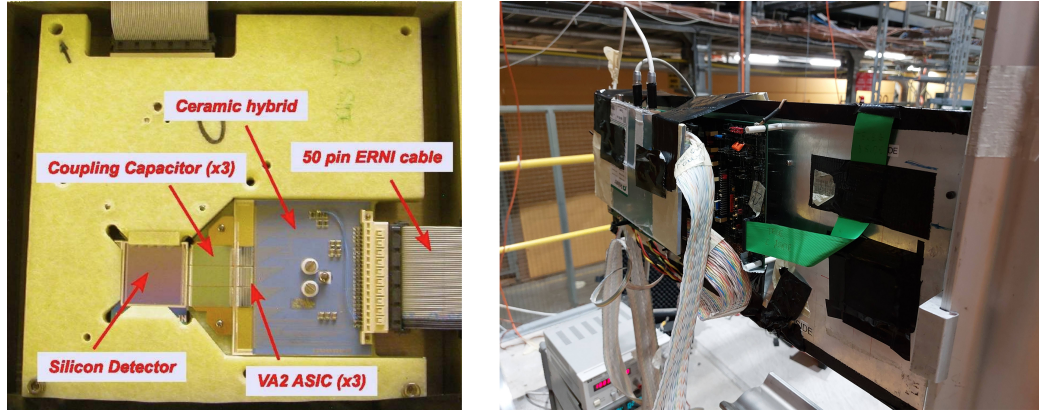


FIGURE 2.10: An INSULAb Telescope module: (*left*) detail of the sensor and ASICs assembled on the fiberglass support, and (*right*) fully assembled module installed at a beamtest.

The junction side has 768 strips with a physical pitch of  $25 \mu\text{m}$  [117] and features the floating strip scheme, i.e., one strip every two is read out: therefore, the sensor has 384 readout channels and a readout pitch of  $50 \mu\text{m}$  [117]. Overall, owing to the capacitive coupling between adjacent strips and to the analog readout [95–97, 107, 116], a resolution of  $4\text{--}5 \mu\text{m}$  is attained [116]. The ohmic side has 384 strips with a physical pitch of  $50 \mu\text{m}$  [116, 117] and no floating strip scheme. As a consequence, the spatial resolution is approximately 2–3 times worse than that of the junction side [116, 117]. The ohmic side has 384 strips with a physical pitch of  $50 \mu\text{m}$  [116, 117] and no floating strip scheme. As a consequence, the spatial resolution is approximately  $\sim 2$  times worse than that of the junction side [116, 117].



In general, the presence the downstream silicon sensor of the input tracking pair (see section 2.3.3) affects the overall angular resolution of the latter due to the MCS, which is given by equation 1.18 (chapter 1). In case of the INSULAb Telescope sensors, which are  $300\text{ }\mu\text{m} \sim 0.0032\text{ }X_0$  thick [116, 117], equation 1.18 results in  $\Delta\psi_{\text{MCS}} \sim 601\text{ }\mu\text{rad}/E[\text{GeV}] \sim 107\text{ }\mu\text{rad}$  ( $5\text{ }\mu\text{rad}$ ) at 5.6 GeV (120 GeV).

### The Silicon Beam Chambers

Each Silicon Beam Chamber (SiBC) features two single-sided silicon microstrip sensors (figure 2.11 left) with the strips mutually rotated by  $90^\circ$  around the beam direction, installed together in an aluminium box (figure 2.11 right). The sensors have been manufactured by Hamamatsu for the AGILE detector [96, 97].

The AGILE sensors have an active area of  $\sim 9.29 \times 9.29\text{ cm}^2$  [107], i.e.,  $\sim 25$  times larger than the INSULAb Telescope modules, and a thickness of  $410\text{ }\mu\text{m} \sim 0.0044\text{ }X_0$  [107], which results in an overall  $820\text{ }\mu\text{m}$  of silicon per module. Details on the electronic properties of these sensors can be found, e.g., in [95]. The strips are coupled to TA1 and TAA1 ASICs, three per sensor [107].

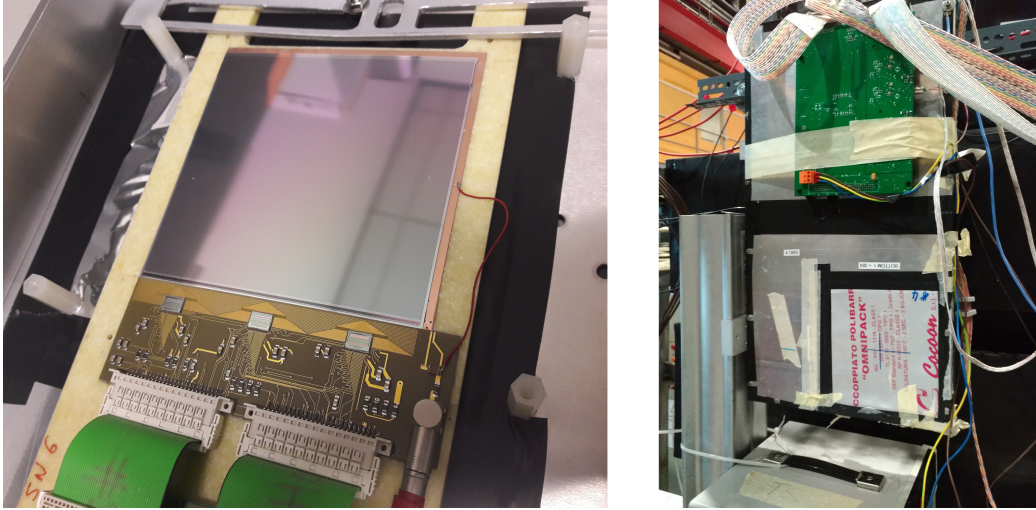


FIGURE 2.11: A Silicon Beam Chamber: (*left*) detail of the inside of the box, with one of the AGILE sensors coupled to the ASIC PCB and assembled on the fiberglass support, and (*right*) fully assembled module installed at a beamtest.

The strips have a physical pitch of  $121\text{ }\mu\text{m}$  [96, 97, 107] and the floating strip scheme is used, which results in an overall readout pitch of  $242\text{ }\mu\text{m}$  and in

a total of 384 channels per sensor [96, 97, 107]. The single-hit resolution is  $\lesssim 40 \mu\text{m}$  [96, 107].

In general, the contribution of the overall  $0.0087 X_0$  thickness of each module to the MCS is non-negligible and should be taken into account. Equation 1.18 leads to  $\Delta\psi_{\text{MCS}} = 1.04 \text{ mrad}/E[\text{GeV}] \sim 187 \mu\text{rad}$  ( $8.7 \mu\text{rad}$ ) at 5.6 GeV (120 GeV).

Larger-area tracking modules, featuring  $2 \times 2$  arrays of AGILE sensors, have also been exploited in the beamtest performed on the CERN H2 beamline in 2018 to test the KLEVER photon converter – see chapter 4. In this configuration, the two sensors placed one next to the other (with a 2 mm non-sensitive gap in between) along the strip length are strip-by-strip bonded together, and overall one strip every four is read out [119]. This allows to cover a surface of  $\sim 18.6 \times 18.6 \text{ cm}^2$  with  $\sim 60 \mu\text{m}$  spatial resolution [119].

### 2.3.1.2 The electromagnetic calorimeters

Several different electromagnetic calorimeters have been exploited in the beamtests to measure the energy of the photons and  $e^\pm$  exiting the crystals. They are described in the following. Each one of these detectors requires dedicated procedures for the ADC-to-GeV signal calibration and, in case of multi-channel devices, for the equalisation of the channels – details on some of these procedures are provided in appendix A.

#### Stefi

The Stefi calorimeter (sketch in figure 2.12) has been used at CERN, in the beamtests performed on the H4 beamline in 2016 [120] and 2017 [50]. It consists of a  $3 \times 3$  matrix of lead tungstate crystals, spare pieces of the endcap calorimeter of the CMS experiment at CERN [107, 121, 122], in random alignment.

Each  $\text{PbWO}_4$  block is trapezoidal, with a front section of  $2.86 \times 2.86 \text{ cm}^2$ , a rear section of  $2.96 \times 2.96 \text{ cm}^2$  and a length of 22 cm ( $24.7 X_0$ ) and is wrapped in a Tyvek sheet to increase the light yield [107]. Each block is contained in an aluminium box with a plastic plug for the coupling to the photodetector and the whole matrix is held together by a frame made of Bosch strut profiles [107]. Each crystal is read out by a monolithic  $2 \times 2$  array of SiPMs by FBK-irst – details can be found in [121].

The net half-size of the active volume, i.e., the half-size of the detector measured without taking into account the intra-channel gaps, is  $\sim 4.35 \text{ cm} \sim 2.22 R_{\text{M}}$  ( $R_{\text{M}} = 1.959 \text{ cm}$ ), therefore the contribution of lateral leakage is, in principle, negligible. However, as already mentioned, there is a few-mm gap

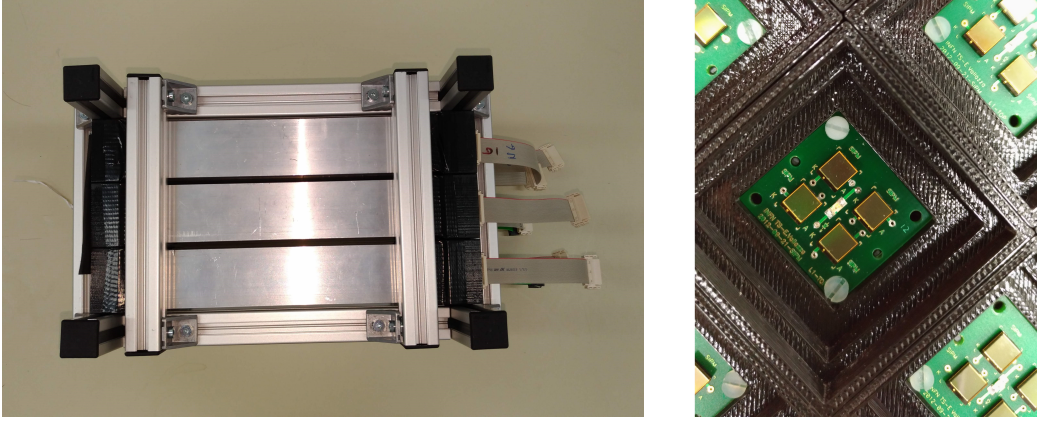


FIGURE 2.12: The Stefi calorimeter: pictures of (*left*) the fully-assembled detector and (*right*) the SiPM board and frame.

between the neighbouring blocks due to the mechanical frame, which results in the loss of part of the shower energy out of the active volume and thus negatively affects the detector energy resolution [107]. Overall, an energy resolution of

$$\frac{\sigma_E}{E} \sim \sqrt{\left(\frac{11.88\% \sqrt{\text{GeV}}}{\sqrt{E}}\right)^2 + \left(\frac{500 \text{ MeV}}{E}\right)^2} \quad (2.1)$$

has been measured [121].

### Genni

The Genni calorimeter (figure 2.13) has been exploited at CERN, in the beamtests performed on the H2 beamline in 2021 and 2022, and in all the beamtests performed at DESY. It is a  $3 \times 3$  matrix of BGO (bismuth germanate,  $\text{Bi}_4\text{Ge}_3\text{O}_{12}$ ) crystals, spare pieces of the PADME (Positron Annihilation into Dark Matter Experiment) calorimeter. The PADME crystals have been obtained by cutting the bigger trapezoidal crystals of the L3 endcap calorimeter and have an approximate dimension of  $2.1 \times 2.1 \times 23 \text{ cm}^3$  [107, 123, 124]. They are placed one next to the other with very good adherence between neighbouring channels, the gaps (irreducible, due to the paint of each block) being thinner than 1 mm [107]. Each crystal is coupled to a Photonis XP1912 PMT [125]. An energy resolution of



FIGURE 2.13: The Genni calorimeter: pictures of (*left*) the crystal matrix and (*right*) the PMT matrix.

$$\frac{\sigma_E}{E} \sim \sqrt{\left(\frac{3.73\% \sqrt{\text{GeV}}}{\sqrt{E}}\right)^2 + (2.43\%)^2} \quad (2.2)$$

has been measured – see [107]. Indeed, this detector shows a significantly better resolution than Stefi (equation 2.1), mainly due to the absence of large air gaps between the neighbouring channels. However, attention should be paid to the lateral leakage, as  $R_M = 2.259$  cm [13, 30] and the net half-size of the Genni active volume is only  $\sim 3.15$  cm  $\sim 1.39 R_M$ .

### The lead glass blocks

Since 2018, a battery of lead glass blocks (figure 2.14) has been exploited in several beamtests performed at CERN, arranged in arrays of different shapes. These blocks have been developed for the barrel electromagnetic calorimeter of the OPAL (Omni-Purpose Apparatus at LEP) experiment [126].

Each block is made of Schott SF57 glass with 76% of lead glass – a Cherenkov emitter. It is 37 cm  $\sim 29 X_0$  ( $X_0 = 1.265$  cm [13]) long and trapezoidal, with a front (rear) section of  $\sim 10 \times 10$  cm<sup>2</sup> ( $\sim 11 \times 11$  cm<sup>2</sup>). Moreover, it is covered with Tyvek and plastic sheets to increase the light yield and minimise the noise induced by external light sources in the PMT – a Hamamatsu R9880U-110 [127].

The transverse half-size of the active volume is  $\sim 5.5$  cm  $\sim 2.13 R_M$  ( $R_M = 2.578$  cm [13]), which makes the lateral leakage practically negligible. A single-block energy resolution of



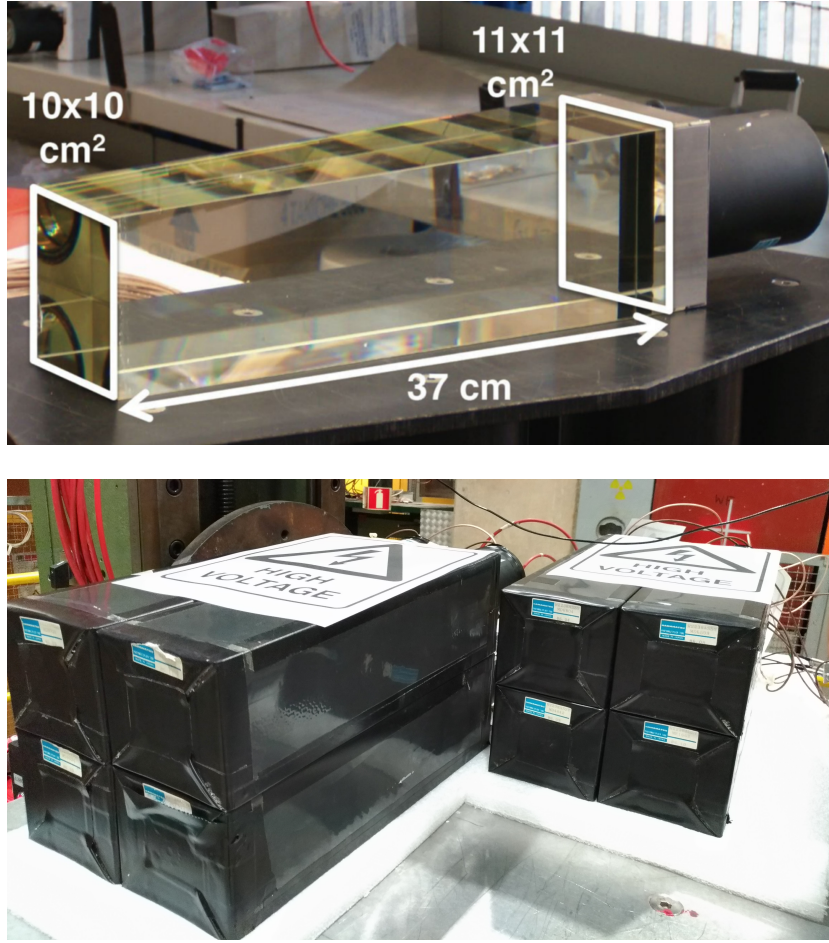


FIGURE 2.14: Lead glass blocks: (*top*) single block without the outer cover (from [126]) and (*bottom*) battery arranged in the setup of the AXIAL 2018 beamtest on CERN H2.

$$\frac{\sigma_E}{E} \sim \sqrt{\left(\frac{17.67\%\sqrt{\text{GeV}}}{\sqrt{E}}\right)^2 + \left(\frac{56.13 \text{ MeV}}{E}\right)^2} \quad (2.3)$$

has been measured during the 2022 beamtest on CERN H2, as shown in section A.3.1 (appendix A). During the data taking session performed in 2018 on the HIKE/KLEVER photon converter (see section 4.2, chapter 4) time stability and linearity issues affected the performance of some of the blocks; details are provided in appendix C.

### 2.3.1.3 The active photon converter

A custom detector, namely, the active photon converter (APC), has been developed to provide a spectrum of the number of  $e^+e^-$  pairs resulting from the conversion of the high-energy photons emerging from the crystalline samples under study, and ultimately insight on the number of radiated photons. Of course, since the process of pair production is intrinsically random, it is impossible to obtain an event-by-event measurement of the number of photons without a high-granularity calorimeter. However, information on the photon multiplicity can be inferred by measuring the  $e^+e^-$  multiplicity spectra obtained exploiting the setup described below with the results obtained from the beamtest full simulations – see section 2.4.

A sketch of the detector concept and a picture of its first instance are shown in figure 2.15. It is installed along the photon beam path, i.e., downstream with respect to the bending magnet when measuring the output radiation – see section 2.3.3. The first stage consists of a plastic scintillator to veto the events in which the photons convert before reaching the APC (in air, in an upstream multiplicity counter or in the scintillator itself). Then, a copper layer causes some of the photons to undergo PP. The thickness of this layer, and hence the conversion probability, can be selected by adding or removing  $450\text{ }\mu\text{m} \sim 0.03\text{ }X_0$  copper foils; typically, an overall thickness of  $0.2\text{ }X_0$ , corresponding to seven foils, is chosen. Eventually, the output  $e^+e^-$  pairs are measured by another scintillator, namely, the Downstream Counter (DC).

In case of radiation measurements on crystals of thickness  $\ll X_0$ , the number of output charged particles is small, which makes the detection of the lattice axis and surrounding planes particularly hard due to the poor contrast with

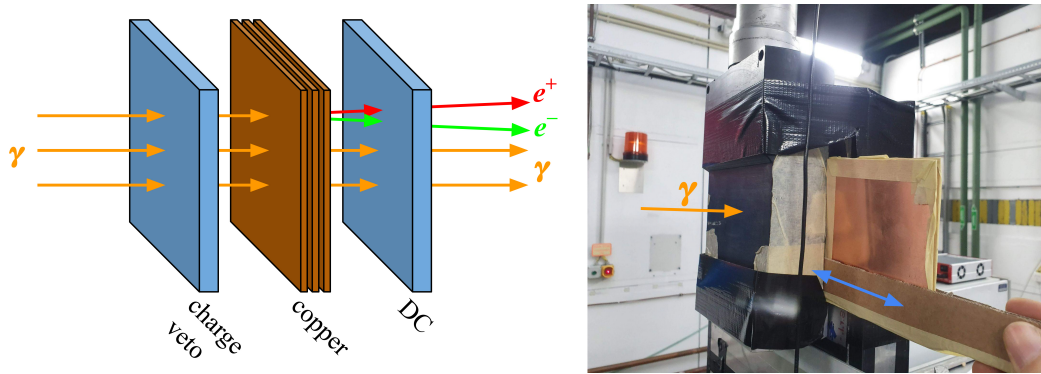


FIGURE 2.15: APC, (*left*) sketch of the concept and (*right*) picture of the detector installed on DESY T21 in 2019. The blue arrow indicates the way the copper layers can be inserted/removed without disassembling the detector.

respect to the random alignment. The APC has the additional purpose of providing better contrast, thus easing the sample alignment procedure, given the fact that it operates with output photons, which are more abundant than second-order electrons and positrons.

#### 2.3.1.4 The DAQ system

All the measurements presented in this chapter are performed on an event-by-event basis, i.e., the particles impinging on the crystalline sample are measured individually in correlation with the corresponding crystal output. Due to the Poissonian nature of the particles in the beams, multi-particle events up to a certain fraction, which depends on the beam intensity, cannot be avoided and are excluded offline.

In all the experimental configurations described in this section, the tracking system is read out by the high-performance INSULAb electronic chain. A scheme of the chain is shown in figure 2.16 and a detailed description is given in [107, 116].

The first element of the chain is the repeater, a PCB that amplifies the multiplexed analog output of the ASICs, provides the power and the configuration signals to the latter and delivers the bias to the silicon sensor [107]. Each tracking view features a repeater [107, 117]; in case of the silicon telescopes, an optocoupler board shifts the input and output signals of the ohmic side to match the DC level of the sensor bias [117]. The repeaters are coupled to an ADC board for the digitalisation of the multiplexed analog signal [107]. Depending on the number of tracking modules and on the distance between them, one or more VME crates host the last part of the chain, i.e., the VRBs (VME Readout Boards – one per tracking module), which [107]

- read the ADC output data during the spill, store them in a dedicated RAM (Random Access Memory) and transfer them to the DAQ PC during the interspill period;
- generate the hold for the sampling of the strip signals (details in [116]) and the clock for their multiplexing;
- manage the configuration of the ASICs and ADCs.

Moreover, the crate(s) hosts the trigger board and a SBS Bit3 620 bus adapter [128]; the latter connects the DAQ to the PC from which it is controlled via optical fiber [107].

The tracking system can be read out in both normal and zero suppression mode. In the former, the output of the ADCs is demultiplexed and all the

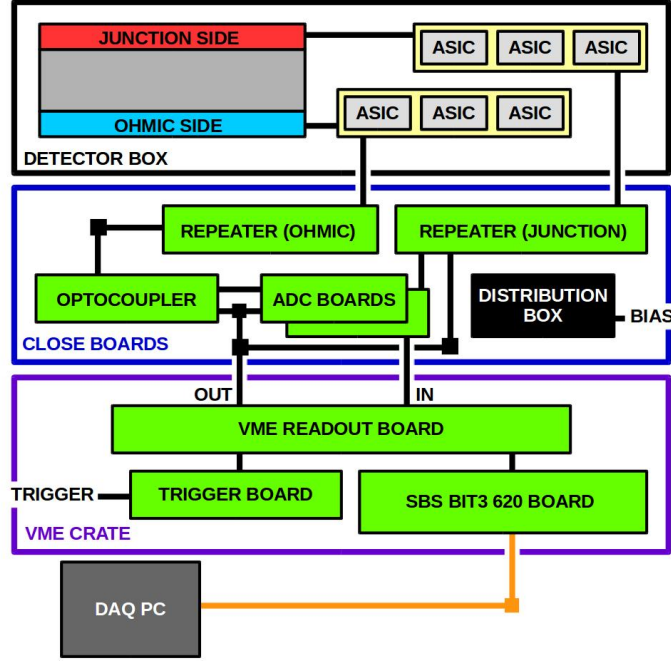


FIGURE 2.16: Scheme of the electronic chain that reads the silicon telescopes. The same logic applies to the case of the SiBCs, albeit with the repeaters hosted inside the module box and without the optocoupler board. From [117].

channels (i.e., 384 per vista, with 2 vistas per module) are stored in the RAM; the number of events per spill is limited to 4096 [107]. On the other hand, when in zero suppression mode, only the strips whose signal is above threshold value are stored in the RAM; the maximum number of strips that can be stored per layer per event is limited to 16 due to the hardware configuration, and the number of events per spill is limited to a few tens of thousands of events [107]. The choice of the readout mode affects the overall acquisition rate, the zero suppression mode being significantly faster.

All the other detectors (i.e. the scintillating multiplicity counters, the APC and the calorimeters) are read out by CAEN digitisers. Depending on the beamtest session, different models have been exploited, a rather common choice being the CAEN V1720 waveform digitiser – details can be found in [129].

The overall acquisition rate depends not only on the tracking system read-out mode, but also on the clock frequency and on the number of VRBs and digitisers in the system [107]. Typically, an experimental setup for the mea-

surement of SF effects features between two and four tracking modules and between one and three digitisers. Assuming that the zero suppression mode is chosen, a conservative estimate [107] leads to typical rate values in the (0.8, 1) kHz range.

### 2.3.2 Sample (pre-)alignment

In order to characterise all the crystalline effects as a function of the misalignment angle – i.e., the relative angle between the sample lattice axis and the nominal beam path – it is important to know the latter with a precision  $\ll \Theta_0$  (see section 1.4.2, chapter 1). The crystal-to-beam alignment is performed in separate stages.

Firstly, the relative alignment between the lattice and the crystalline sample faces is found. The miscut (i.e., the angle between the lattice axis of interest and the axis of the face) and the misflat (i.e., the angle between the lattice planes and the face edges) are characterised via *X*-ray techniques – either with the HRXRD (high-resolution *X*-ray diffraction) in the INFN Ferrara laboratory or with the *X*-ray high-quality beams at the ESRF synchrotron facility [105, 106]. This can be done with a precision of a few tens of  $\mu\text{rad}$ .

One or multiple samples are then mounted on a mechanical holder, which in turn is installed on top of a high-precision goniometer that allows the remote control of the sample spatial and angular orientation with a precision of  $\sim 5 \mu\text{m}$  and  $\sim 5 \mu\text{rad}$  respectively [100, 130, 131]. Five independent goniometer motors are available, each one moving a specific degree of freedom (DOF), and can be installed on top of one another as shown in figure 2.17 left: overall, there are three linear stages (one vertical and two horizontal – one with a bigger range than the other) and two angular stages (rotational and cradle, which govern the angular motion in the horizontal and vertical planes respectively). In most cases, in order to attain a higher range in the vertical translations, a XSCA scanning table [132] is used instead of the goniometer vertical motor, which spans only 2.5 cm.

A mirror is installed on the holder alongside the crystalline samples (figure 2.17 right) and the relative alignment of the mirror front surface with the front surface of all the samples is measured with high precision. In addition, an optical laser system is installed in the experimental area, in order to provide a reference for the nominal beam trajectory: once the system is aligned, the laser beam is at the same height as the particle beam and is parallel to it. A pentaprism is placed along the laser beam path at the same longitudinal position as the sample holder, which is rotated by  $90^\circ$  towards it: the laser beam crosses the pentaprism and impinges on the mirror front face, which reflects it back across the pentaprism and towards the laser gun.

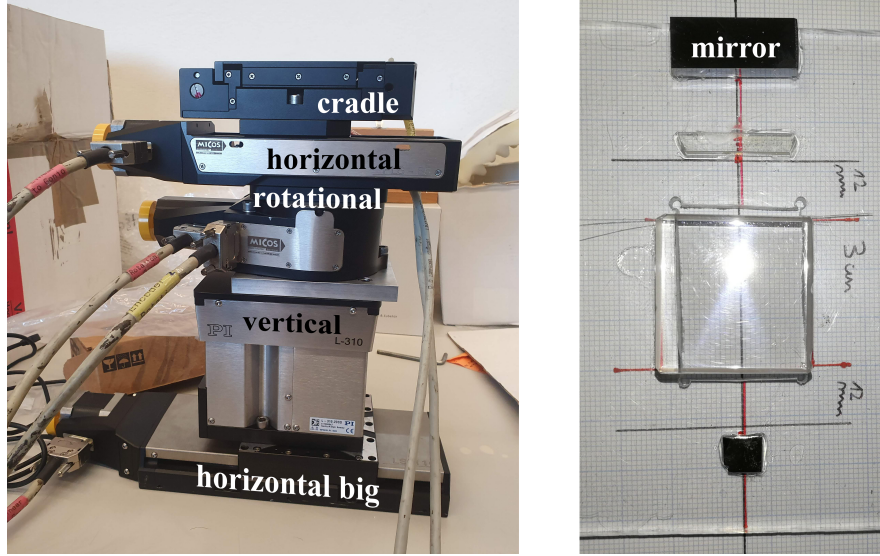


FIGURE 2.17: Elements of the pre-alignment system: (*left*) the goniometer installed in the laboratory with all the five DOFs, and (*right*) a holder housing three crystals (two PWO samples and a tungsten sample) and a mirror.

When the laser beam propagates back to its origin, the precise alignment of the mirror, and hence of the holder with all the crystals, with respect to the nominal particle beam path is found with an overall precision of  $\sim 100 \mu\text{rad}$ . This procedure, which is sketched in figure 2.18, is completed by correcting the goniometer angular DOFs applying the offsets found with the  $X$ -ray techniques.

The fine alignment is performed with the particle beam: the correlation between the particle incident angles, reconstructed by the input tracking system, and the output multiplicity counters (MCs) – i.e., SiBCs, plastic scintillators and, in case of thin crystals, the APC (see section 2.3.1.3) – is studied as a function of the goniometer DOFs, and the lattice axis corresponds to the position in which the multiplicity enhancement with respect to the amorphous case is maximum. Moreover, as discussed in section 5.3.3 (chapter 5) and in [133], the axial alignment in PWO can be found by studying the enhancement of the scintillation light yield measured with the SiPMs.

### 2.3.3 Measurement of the electromagnetic radiation

Figure 2.19 shows a sketch of the experimental apparatus for the measurements of the electromagnetic radiation resulting from the coherent interactions of electrons inside the crystalline samples.

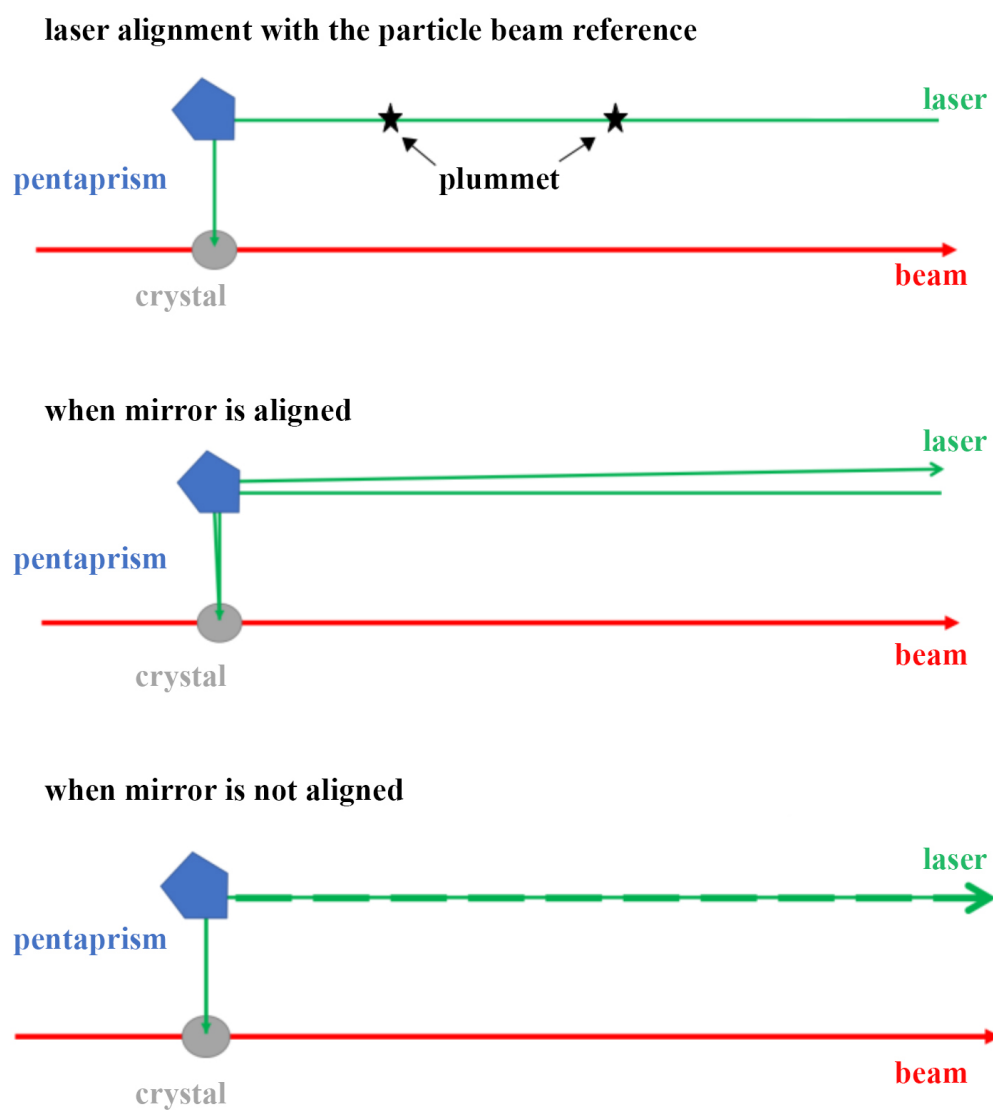


FIGURE 2.18: Sketch of the laser pre-alignment procedure. Edited from [133].



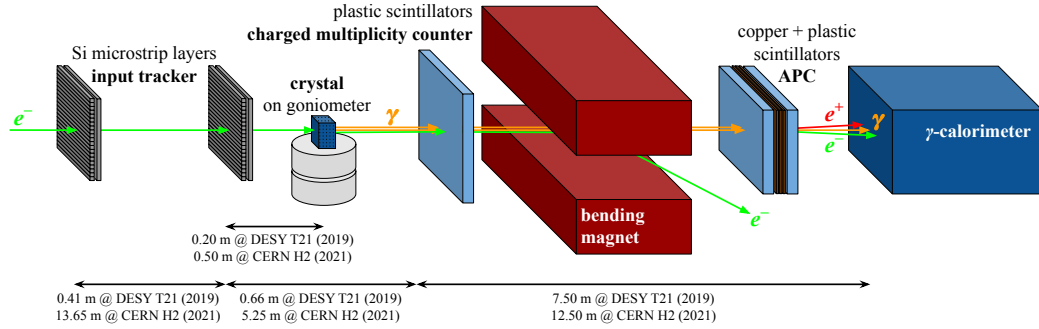


FIGURE 2.19: Sketch of the beamtest setup for radiation measurements. The relative positions of the different elements are indicated for the DESY (T21) 2019 and CERN (H2) 2021 cases; the corresponding values for the run on H2 in 2018 and for the previous runs on H4 (2016, 2017) are similar to those of 2021.

The input electrons (or positrons) impinge on a pair of INSULab Telescope modules that measure their trajectory. A bending magnet positioned downstream with respect to the goniometer and the multiplicity counters separates the charged particles and the photons exiting the crystalline sample. The APC and the electromagnetic calorimeter are placed along the photon path, several metres downstream with respect to the magnet, in order for the transverse separation between photons and electrons/positrons to be large enough for the charged particles to be entirely out of the acceptance of the photon detectors – typically a separation of a few tens of centimetres is enough.

This setup is used in the beamtests at both the CERN NA – i.e., with 120 GeV electrons (and positrons) – and on DESY T21 – i.e., with electrons in the few-GeV scale. As indicated by the numbers in figure 2.19, the detectors are positioned at different distances from one another along the beam axis in order to handle the different-energy and -divergence beams. In the runs at the CERN North Area, vacuum pipes are positioned on the beamline in all the gaps upstream with respect to the bending magnet.

The input tracking system has a lever arm of  $\sim 40$  cm ( $\sim 14$  m) on DESY T21 (at the CERN NA), which, conservatively assuming  $\sigma_{\text{res}} \sim 10$   $\mu\text{m}$  (see section 2.3.1.1), results in an intrinsic angular resolution  $\sim 25$   $\mu\text{rad}$  ( $\sim 0.7$   $\mu\text{rad}$ ). This is equal to  $\sim 3.5\%$  ( $\sim 1\%$ ) of the corresponding beam divergence (i.e., the average between the horizontal and vertical divergence) and to  $\sim 1.5\%$  ( $\sim 0.05\%$ ) of the SF critical angle for the [111] axis of tungsten ( $\Theta_0 \sim 1.74$  mrad). It has to be noted that, albeit good, the angular resolution on DESY T21 is not as satisfactory as that obtained at CERN. This is due to



the limited space available in the experimental hall upstream with respect to the bending magnet (see section 2.2.1).

The distance between the crystalline sample and the electromagnetic calorimeter significantly affects the angular acceptance of the latter, which in turn naturally introduces a cutoff to the soft part of the photon energy spectrum, since lower-energy electromagnetic radiation is emitted in a wider opening cone, as discussed in section 1.3.1 (chapter 1). For instance, the Genni calorimeter (section 2.3.1.2) has been used in both the beamtests performed on DESY T21 in 2019 and on CERN H2 in 2021; the corresponding angular acceptance values were  $\sim 8.17$  mrad and  $\sim 3.77$  mrad respectively. These values should be compared with the quadratic sum of the aperture of the electromagnetic radiation emission cone and of the angle of MCS experienced by the electrons across the target. As far as DESY T21 is concerned, in which a  $0.65 X_0$  tungsten sample was tested (section 3.2, chapter 3), this corresponds to  $\sim 2$  mrad, which is dominated by the MCS term, much smaller than the calorimeter angular acceptance.

In case of multi- $X_0$  crystals, the limited angular acceptance of the electromagnetic calorimeter proves a fundamental constraint to the overall hermeticity of the apparatus. The MCS contribution dramatically increases a large number of low-energy secondaries resulting from the shower development exit the sample. Therefore, if the calorimeter is too far away from the crystalline target, a non-negligible fraction of secondaries – either photons or electrons/positrons – will be emitted at a large angle with respect to the incident beam direction, with a significant energy loss out of the apparatus acceptance. Section 2.3.5 describes the improvements that are needed to hermetically measure the energy of the output particles in case of thick crystals.

### 2.3.4 Measurement of the pair production

Figure 2.20 shows a sketch of the experimental setup for the studies of the coherent effects in pair production by high energy photons, performed on crystalline tungsten in 2018 (section 4.2, chapter 4). It essentially comprises the same primary beam as in the other beamtests performed on the H2 beamline, i.e.,  $120 \text{ GeV}/c$  electrons (section 2.2.2), and the same components as the apparatus for the radiation measurements (section 2.3.3) rearranged as follows:

- the crystal has been moved downstream with respect to the bending magnet, where the separation between electrons/positrons and photons has already swept the charged particles of up to  $120 \text{ GeV}/c$  out of the

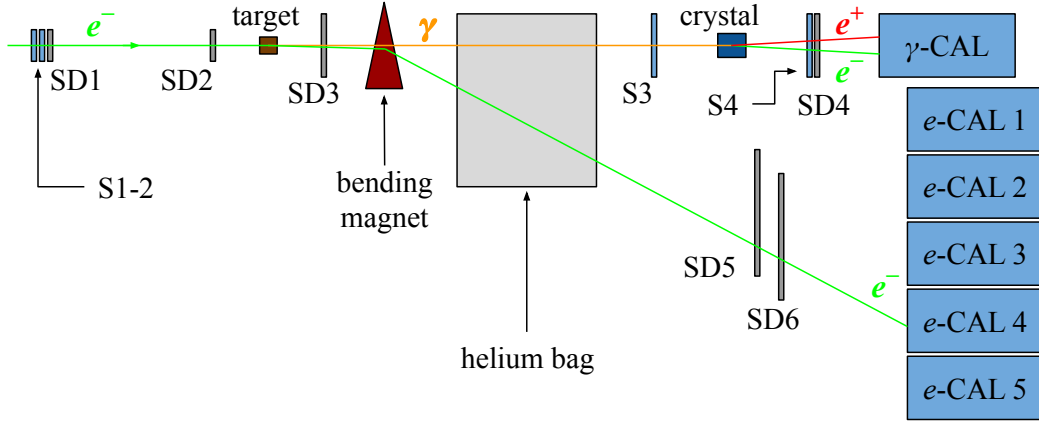


FIGURE 2.20: Sketch of the beamtest setup for pair production measurements installed for the KLEVER 2018 run. SD1–2 are silicon telescope modules; SD3–4 are SiBCs; SD5–6 are large-area SiBCs; S1–4 are plastic scintillators.

acceptance of the electromagnetic calorimeter ( $\gamma$ -CAL) placed on the neutral beam path – figure 2.21 left.

- A 1 mm thick copper target has been placed downstream with respect to the primary beam tracking system, i.e., between the SD2 silicon telescope module and the SD3 SiBC, for the generation of the photon beam via bremsstrahlung. The distance between the copper target and the crystalline sample was 17.1 m.
- An indirect measurement of the photon energy, which has a broad spectrum that extends from 0 to almost the primary beam energy and features the  $\propto 1/E$  trend typical of bremsstrahlung, has been provided by the photon tagging system. In practice, the energy of the primary electron after crossing the copper target and undergoing bremsstrahlung has been measured by a large-acceptance electromagnetic calorimeter, namely, the  $e$ -CAL, composed of an array of lead glass blocks – figure 2.21 left: the reconstructed photon energy is therefore

$$E_{\gamma\text{-tagged}} = 120 \text{ GeV} - E_{e\text{-CAL}} \quad . \quad (2.4)$$

- A large-transverse section helium bag (figure 2.21 right) has been placed downstream with respect to the bending magnet, in order to significantly reduce the MCS of the crystal output electrons, which would worsen the photon tagging performance, and the photon conversion in air. Moreover, two large-area SiBCs have been placed in front of

the  $e$ -CAL channels to measure the correlation between the electron momentum and output the trajectory induced by the bending magnet.

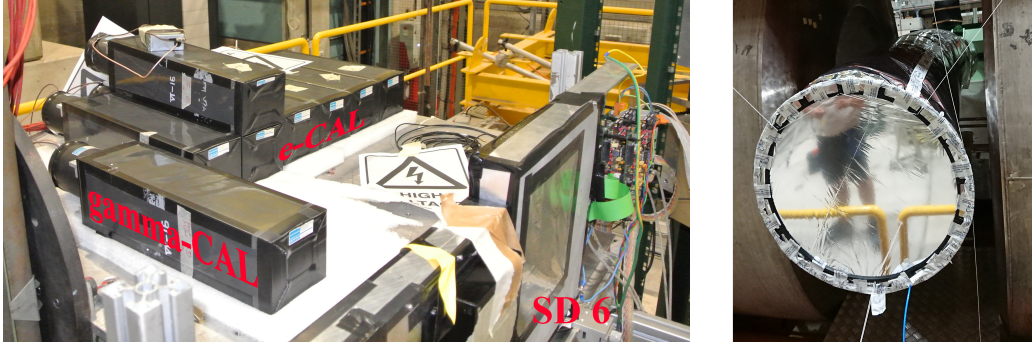


FIGURE 2.21: Downstream stage of the KLEVER 2018 beamtest: (*left*) calorimeters and SD6 tracking module, and (*right*) rear side of the helium bag.

This configuration allows the system to run in the so-called photon mode, in which the electron beam is swept away by the bending magnet and only the photons impinge on the sample under test. On the other hand, runs with the electrons directly impinging on the crystal or on the  $\gamma$ -CAL (or any  $e$ -CAL channel, provided that the DESY table on which all the lead glass blocks are positioned is properly moved) can be performed after moving the copper target out of the beam path and switching the bending magnet off.

Two scintillators, S3 and S4, are positioned upstream and downstream with respect to the crystalline target respectively. S4 is used to measure the charged particle multiplicity exiting the crystal. On the other hand, when in photon mode, S3 is exploited as a charged particle veto: events in which a signal is generated in it are excluded, as they correspond to photons converting upstream with respect to the target – either in the air or in any solid layer between the bending magnet and the scintillator, or in the scintillator itself. The correlations between the S3 peak time and its PH obtained with the bending magnet on and off are shown in figure 2.22: when the magnet is off, the primary beam directly impinges on the scintillator and a signal of several thousands of ADC is observed. On the other hand, when in photon mode, a much smaller signal from the charged products of the upstream conversion is measured. Limiting the offline physics analysis to the sole events in which

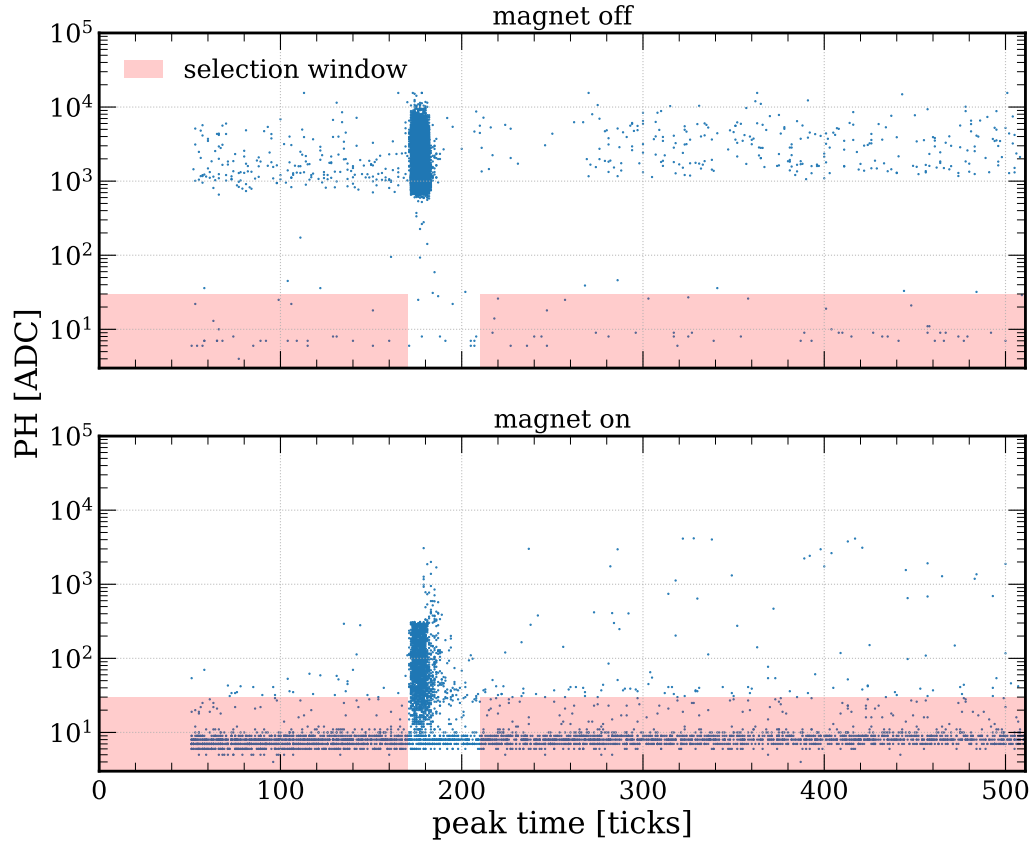


FIGURE 2.22: Correlation between the peak time and the PH of the charged particle veto counter, measured at the 2018 KLEVER beamtest with the magnet off (*top*) and on (*bottom*).

the S3 signal is off-time<sup>5</sup> guarantees that only events without any charged particle upstream with respect to the crystalline sample are considered.

### 2.3.5 Measurement of the total output energy

The measurement of the crystal output energy with improved hermeticity requires an improvement of the electromagnetic calorimeter acceptance, which is obtained by:

<sup>5</sup>For each event, the maximum of the digitalised waveform is written, together with its position in the acquisition time window: the particles always generate large signals within a short time window – here, between 170 and 210 ticks. On the other hand, when no particles cross the scintillating tile, the maximum baseline fluctuation is written, which features a low PH and a random peak time.

- choosing a wider calorimeter;
- reducing the distance between the calorimeter and the crystalline sample.

To perform this measurement there is no need to separate charged particles and photons with the bending magnet. Removing the magnet, the calorimeter can be placed arbitrarily close to the crystal rear side; moreover, the detection of all the output particles requires a considerably smaller-acceptance calorimeter, as all of them are contained in a comparatively narrow cone around the incident beam axis, regardless of their momentum.

Figure 2.23 shows a sketch of the setup installed on the CERN H2 beam-line in 2022 for the measurement of the energy deposit in  $\sim 4.6 X_0$  thick PWO samples (sections 5.3.5 and 5.3.6, chapter 5). The calorimeter has been moved upstream, its front face being at  $\sim 30$  cm from the crystalline sample. Moreover, as shown in figure 2.24, a large-area calorimeter, consisting of an array of 7 lead glass blocks arranged as a hibiscus, has been chosen – some details are provided in section A.3.2 (appendix A). With this configuration, a remarkable angular acceptance is attained for the electromagnetic calorimeter. The measurements performed with this setup are of particular interest when directly characterising the distribution of the energy deposit in scintillating samples by reading their light output.

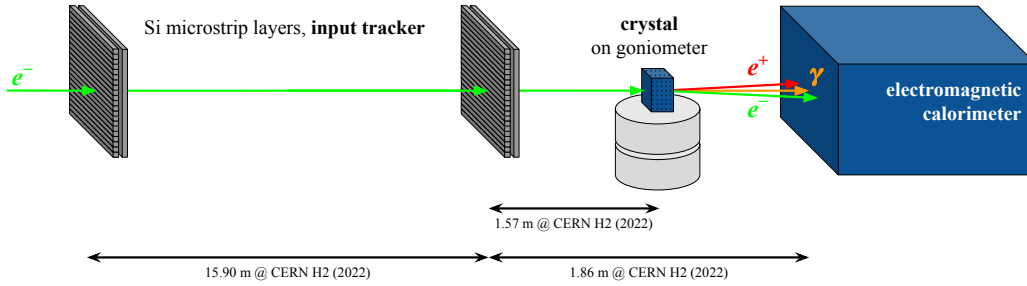


FIGURE 2.23: Sketch of the beamtest setup for the optimised measurement of the total energy.

## 2.4 Monte Carlo simulation tools

The development of comprehensive and reliable prediction tools based on the theoretical framework presented in chapter 1 proves fundamental for a full understanding of the data collected in all the aforementioned experiments.



FIGURE 2.24: Hibiscus-like array of lead glass blocks used as electromagnetic calorimeter in the STORM 2022 beamtest on CERN H2.

Although it may be possible to characterise the deterministic dynamics of the particles in crystalline potentials [134], this approach would prove inadequate in the description of several aspects of the particle-crystal interactions, such as the incoherent component of the scattering and, in the high-energy case, the intrinsically quantum nature of electromagnetic radiation emission (section 1.4, chapter 1).

It is therefore important to develop and validate MC tools that simulate the features of the interactions in oriented crystals. Many different simulation codes have been developed in recent years. Two different approaches have been exploited to reproduce the experimental results presented in this work: they are both based on the same code (presented in section 2.4.1) and differ from each other in the target thickness scale.

### 2.4.1 Sub- $X_0$ crystals

The simulation code used in this work to generate sets of data of realistic trajectories inside the averaged crystalline potentials has been developed by Prof. V.V. Tikhomirov at the Institute for Nuclear Problems of the Belarusian State University (INP BSU) [135] with L. Bandiera and A. Sytov of INFN Ferrara [14, 23, 41, 134, 136].

The features of the electromagnetic processes of high-energy particles in an oriented crystal are intrinsically semiclassical since, as discussed in chapter 1, the motion in the averaged potential is classical (i.e., non-quantum) [41] whereas the quantum recoil resulting from radiation emission is quantum [10, 93]. A convenient approach to combine these two facets consists in

exploiting the Baier-Katkov quasiclassical operator method<sup>6</sup>. Further details can be found, e.g., in [10, 14, 23, 41, 134, 137–139].

The trajectories of the radiation-emitting particles are calculated using the equation of motion in the axial potential at finite steps, with the random contribution of incoherent scattering at each step [41]. The simulated trajectories are used in an algorithm based on the Direct Integration of the Baier-Katkov formula (DIBK) [14, 23] to compute the radiation emission. PP can be simulated with the Baier-Katkov method as well, using an appropriate model of the cross section which takes the dependence on the primary energy into account [93]. These models should be valid for input energies down to  $\sim 200$  MeV; indeed, a threshold is set to 200 MeV, below which the standard electromagnetism formulae – i.e., those for amorphous matter – are used [93]. Moreover, a finite incident beam divergence can be taken into account.

In recent years, this simulation code has been used in the development of several applications – e.g., silicon-based crystalline undulators [41, 134, 140] and tungsten targets for high-energy positron sources [93]. This second case is discussed in detail in chapter 3, in which a validation of this simulation tool with experimental data is provided, and its integration in an optimisation study of the FCC- $ee$  positron source is described.

### 2.4.2 Multi- $X_0$ crystals

Exploiting the simulation program described in section 2.4.1 proves prohibitive when dealing with multi- $X_0$  crystalline samples, in which an electromagnetic shower is started by the incident particle, because the computation cost becomes too high [41]. In order to make its application feasible for the characterisation of the SF effects that occur in thick samples, a different use of this software has to be conceived.

To begin with, cost-effective simulations are performed on a very thin (10  $\mu\text{m}$ ) crystalline layer at different incident energies with the DIBK algorithm. In

<sup>6</sup> Using the formalism introduced in chapter 1, the Baier-Katkov formula in case of small radiation emission angles can be written as [14, 137]

$$\hbar\omega \frac{dN_{\text{single}}}{d(\hbar\omega)d\Omega} \propto \frac{\alpha}{8\pi^2} \frac{E_0^2 + E_1^2}{E_1^2} \omega^2 \left[ |\overline{I}_\perp|^2 + \frac{(\hbar\omega)^2}{\gamma^2(E_0^2 + E_1^2)} |J|^2 \right]$$

where,  $\Omega$  is the emission solid angle and, if  $\overline{\beta}_\perp(t)$  is the particle transverse velocity in units of  $c$  and  $\overline{\theta}$  is the emission direction with respect to the charged particle trajectory,

$$\left( \frac{\overline{I}_\perp}{J} \right) \sim \int_{-\infty}^{\infty} dt \left[ \frac{\overline{\beta}_\perp(t) - \overline{\theta}}{1} \right] \exp \left\{ \frac{i\omega E_0}{2E_1} \int_0^t d\tilde{t} \left[ \frac{1}{\gamma^2} + |\overline{\beta}_\perp(\tilde{t}) - \overline{\theta}|^2 \right] \right\} .$$

these simulation runs, only incident angles  $\psi_L \ll \psi \ll \Theta_0$  (see sections 1.2.4 and 1.4.2, chapter 1) are considered; in this way, the contribution of channelled particles, which is negligible in the SF regime and whose realistic-track characterisation would significantly increase the computation cost, is not included [41]. Moreover, limiting the integration to the aforementioned angular range guarantees that the resulting radiation emission and PP enhancement is as close as possible to the maximum value attainable with the lattice axis under study [41].

These energy scans allow to determine correction functions to the standard radiation intensity  $\mathcal{L}$  and pair production probability  $\mathcal{W}$ , in the form of relative enhancement as a function of the initial electron and photon energy respectively. For instance, figure 2.25 shows the correction curves obtained for PWO [001] [41]: as the SF regime is attained, the enhancement of both radiation emission and PP dramatically grows and saturates at several hundreds of GeV.

The correction functions are used to rescale the standard cross sections for bremsstrahlung and PP in the Geant4 toolkit [41, 81, 93], which is very powerful in simulating the electromagnetic shower development and the interactions in the experimental setup surrounding the crystalline sample. Therefore, this “modified” version of Geant4 is used to reproduce the measurements performed at very high energy on crystalline samples with a thickness  $\gg X_0$  and/or in case the full simulation of a beamtest focused on SF measurements is required.

Currently, the modified Geant4 toolkit is implemented in version 10.5 with the FTFP\_BERT reference physics list [141]. In the context of this work, it has been used to validate measurements of both PP and coherent radiation emission in SF – see chapters 4 and 5.



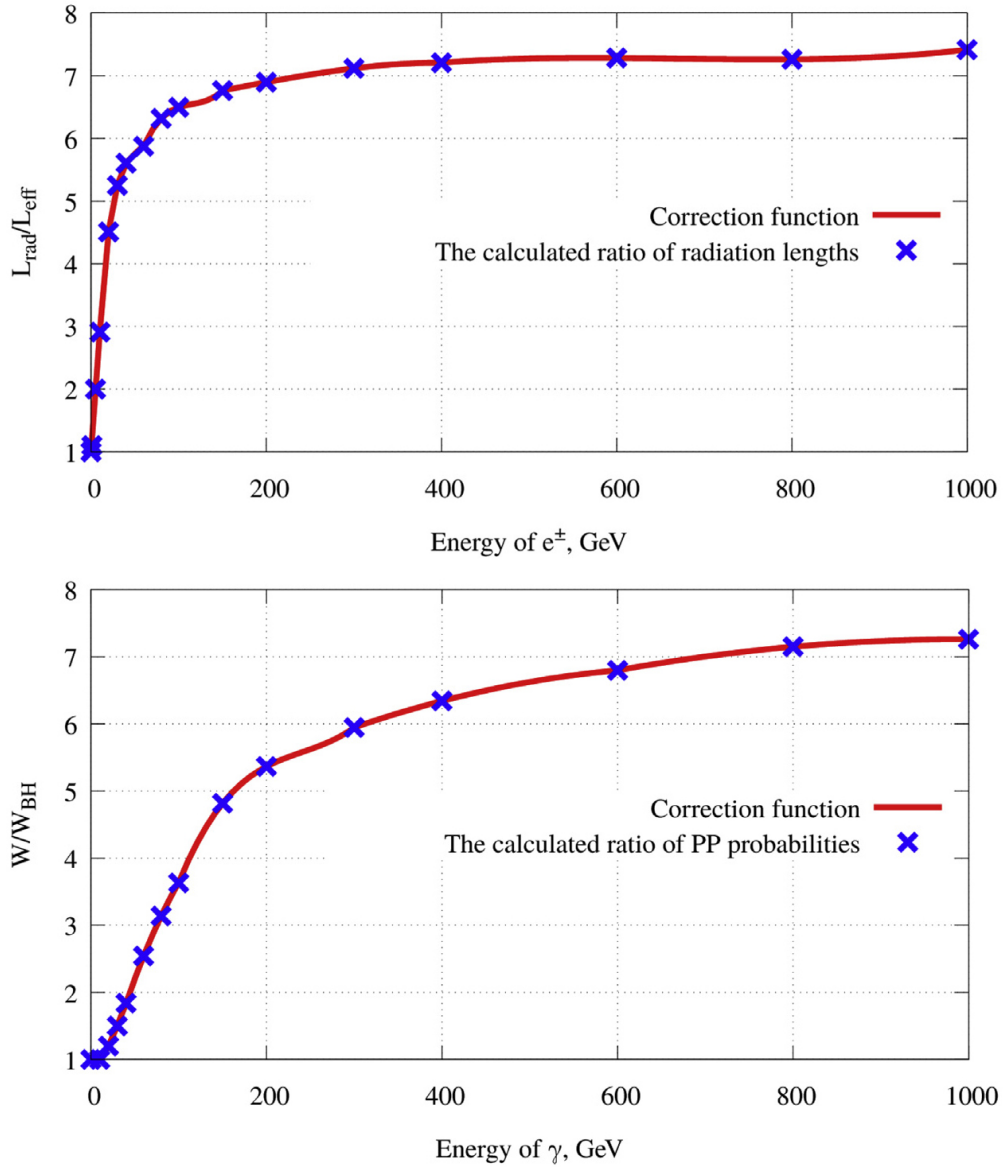


FIGURE 2.25: Relative increase of the standard Geant4 radiation intensity (*top*) and of the PP probability (*bottom*) in the modified simulation tool, for PWO [001]. From [41].

# CHAPTER 3

---

## An optimised positron source for next-generation lepton colliders

The generation of positron beams that could challenge the electron ones in terms of intensity and emittance has always proved one of the most important tasks in the design of a lepton accelerator. Differently from electrons, positrons cannot be obtained from ordinary matter. Therefore, dedicated setups have to be developed to produce positrons and accelerate them. Two options for positron production are feasible, that is,  $\beta^+$  radiation sources and pair production by photons in matter [78, 142]. The latter provides beams with a comparatively narrower angular distribution and intensity, energy and timing features that are tightly related to those of the parent photon beam, which make it considerably more suitable for application in HEP [142]. In particular, considering  $e^+e^-$  colliders, the beam from the electron source (typically a linac [78]) can be exploited to generate via bremsstrahlung the photons that are necessary for the positron production.

At present, all high-energy leptonic machines exploit the so-called conventional positron source scheme: a fraction of the electron beam impinges on a high- $Z$ , high-density, very thick (several  $X_0$ ) target, in which the first steps of the electromagnetic shower occur, resulting in the emission of photons, electrons and positrons [78, 93] which can then be easily separated by means of a magnetic system. Albeit simple and reliable, this standard concept cannot be exploited in the design of next-generation  $e^+e^-$  colliders such as the

FCC-*ee* (Future Circular Collider, electron-electron) and the ILC (International Linear Collider) as the beam intensity scale would result in serious target heating and radiation issues and the achievable emittance would not match the requirements [93, 142, 143].

Novel approaches to the design of low-emittance positron sources optimised for high-intensity beams are currently under study. This chapter presents the development of a next-generation positron source scheme which exploits oriented crystalline metals as compact photon radiators. In the first half of the chapter, the results obtained by the author analysing the experimental data on the electromagnetic radiation emitted by a tungsten crystal in different lattice configurations are presented and compared to the output of beamtest full simulations; the second half of the chapter focuses on the simulation-based optimisation of the aforementioned new positron source schemes, currently being performed by the author in collaboration with the IJCLab (Irène Joliot-Curie Laboratory) in Orsay (France).

### 3.1 Positron source schemes and features

In the following sections, only positron source (PS) concepts based on pair production by high-energy photons will be considered, as they represent the best option<sup>1</sup> for particle accelerators, due to the critical requirements of high intensity (typically  $\sim 10^{12} e^+/s$ ) and low emittance necessary to attain a high luminosity [142]. Nevertheless, the beams obtained with existing conventional positron sources (figure 3.1a), which represent the current state of the art, have an overall emittance which is orders of magnitude worse than the beams in high-brilliance electron sources due to the large divergence and momentum spread resulting from the shower development and the MCS in the target. [142].

Since the number of secondary particles in an electromagnetic shower increases with both the primary particle energy and the position along the direction of the cascade development, in order to get a large positron yield, high-energy incident electrons (at least multi-GeV [78]) and rather thick targets ( $3\text{--}6 X_0$  in current machines at the GeV scale or higher [142]) are needed [78, 93]. In particular, the ideal thickness should correspond to the maximum of the so-called transition curve, i.e., the output charged secondary yield trend as a function of the penetration depth inside the target [78, 93] – an example from a previous study is shown in figure 3.2. If the target is too thin, the shower develops towards the rear end in a few steps and the latter

---

<sup>1</sup>Recent studies such as [144] show that plasma-based positron acceleration is indeed promising, although its practical feasibility still remains to be proven [142].

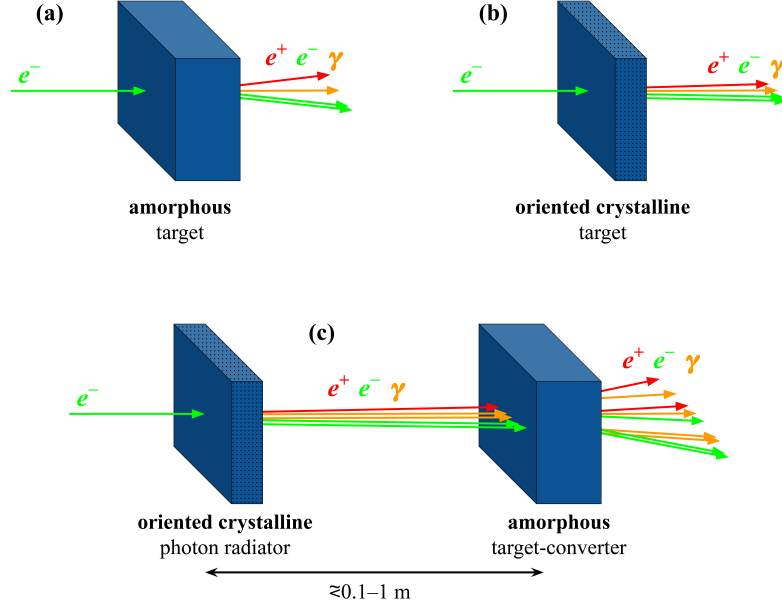


FIGURE 3.1: Comparison between different positron source schemes: (a) conventional, (b) single oriented crystalline target and (c) hybrid, with an oriented crystalline photon radiator and an amorphous converter – often referred to as “the target”.

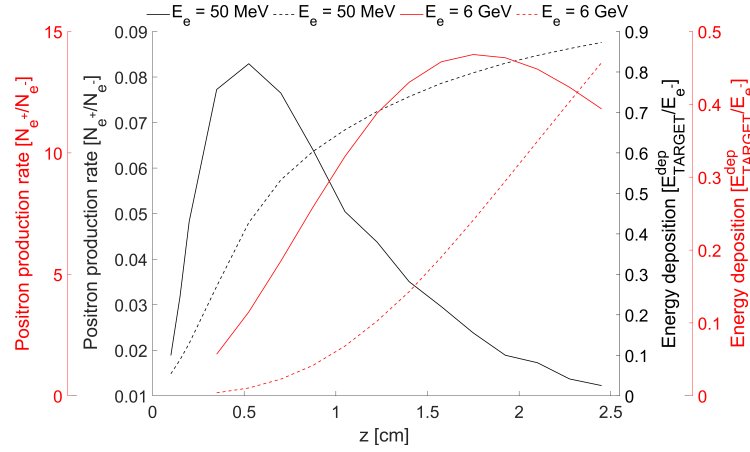


FIGURE 3.2: Transition curves (full lines) and average energy deposit per incident electron (dashed), for 50 MeV (black) and 6 GeV (red), as a function of the target thickness. Results from a conventional PS setup simulation with a tungsten target presented in [142].

is reached before the maximum number of secondaries is attained, whereas if it is too thick the average secondary-particle energy becomes too low and absorption sets on.

In practice, a trade-off has to be found between the  $e^+$  production rate, the output emittance – which has to be as small as reasonably achievable to match the spatial and angular acceptance of the magnetic selection and capture system [142] – and the energy deposit in the target. Indeed, the energy deposit is strongly non-homogeneous in the target volume, with a global maximum located along the beam axis at a few  $X_0$  from the front face [93]. This results in a strong temperature gradient and, in turn, in a large thermo-mechanical stress that, together with the large heating of the target, can alter its physical properties, and hence its positron generation yield [78, 142]. Moreover, these effects non-trivially depend on the time structure of the beam – see, e.g., [145].

Different quantities are typically used to describe the energy deposit:

- the average total energy deposited in the target per incident particle [143];
- the average energy density, i.e., the energy deposit per incident particle and per unit volume [78];
- the Peak Energy Deposition Density (PEDD), i.e., the average of the event-by-event energy density maxima [93, 146].

Generally, these quantities are determined in MC simulations for different incident beams and target shapes and materials. The integral nature of the average energy deposit and density makes both these variables easily accessible by summing all the processes that occur in the target volume. On the other hand, the evaluation of the PEDD is non-trivial and requires a scoring mesh to be defined on top of the target volume, i.e., a division of the target in a 3D matrix of voxels with independent sensitivity. This procedure has many caveats, which are discussed in detail in section B.3.2 (appendix B). For targets thinner than  $L_{\text{PEDD}}$ , where  $L_{\text{PEDD}}$  is the distance along the beam direction at which the electromagnetic cascade reaches its peak in energy deposit per unit depth, the PEDD value depends on the target thickness, whereas it is independent on the latter for thicknesses larger than  $L_{\text{PEDD}}$ . Moreover, the PEDD strongly depends on the beam spot size: for instance, it is shown in [143] that, in case of both 5 and 10 GeV electrons impinging on a 2 mm thick, axially oriented W [111] crystal, the PEDD is reduced by a factor  $\sim 6$  when increasing the incident beam spot size from 1 to 2.5 mm r.m.s.. A reasonable upper limit for the instantaneous PEDD in

tungsten was found to be 35 J/g [142, 143], whereas the stricter upper limit of  $\sim 10.5$  J/g per beam pulse is currently considered for the first configuration of the FCC- $ee$  [147].

The passage of high-intensity electron beams through matter might also result in high radioactivity. In fact, the secondaries that propagate out of the target have very broad angular and energy distributions: a fraction of them might fall out of the capture system acceptance and, therefore, heavily irradiate the surrounding environment [78]. This would result in the activation of the target itself and of all the materials in its vicinity – including the water in the magnet cooling systems [78]. Moreover, the production of ozone, which is a powerful oxidising agent and hence constitutes a potential danger for human health, would be enhanced in the area [78]. High radioactivity around the target would make maintenance and replacement activities challenging.

### 3.1.1 Novel concepts

In recent years, the increasing demand for higher-intensity positron beams has driven the R&D of novel PS concepts that would

- maximise the  $e^+$  production rate;
- minimise the output beam emittance;
- keep the energy deposit and activation at reasonable levels, ultimately avoiding the destruction of the target.

A feasible option to achieve the first and second items with a PEDD smaller than in the conventional scheme would be to split the single compact target into multiple stages, i.e., to replace it with a multi-target system [53, 143, 148].

Several different multi-target schemes have been studied. For instance, granular targets consist of 1–2 mm  $\varnothing$  tungsten spheres arranged in staggered rows. This system has two main advantages with respect to the conventional scheme [53]:

- better heat dissipation, given the fact that the contact surface between the target itself and the surrounding media (air, metallic holders, etcetera) is bigger. This feature improves as the sphere volume decreases.
- Lower energy density when equalising the output positron yield in the two cases.

Other designs can be exploited, in combination with or instead of granular targets, to develop novel PS concepts that would meet the requirements of future colliders and reduce the total amount of bulk material at the same time. In particular, crystal-based solutions are discussed in the following sections.

### 3.1.1.1 Exploiting crystals

The modifications to the pair production cross section that occur in oriented crystals described in chapter 1 – either channelling or over-barrier effects, depending on the kinematic phase space of interest – can be exploited to improve the PS design. For instance, the amorphous target could be replaced with a thinner axially-oriented crystalline target – figure 3.1b [93]: the latter would equal the positron production rate of the former with a smaller thickness and, hence, a smaller output emittance and energy deposit. However, it has to be pointed out that, for this configuration to achieve a positron yield that is competitive with that of well-optimised conventional schemes at high intensity, the crystalline target should still be thick enough for the strong temperature gradient to enhance thermal displacements and determine a gradual reduction of the quality of the lattice potential [93].

Another solution that allows to improve the output beam quality and to reduce the overall energy load even further consists in splitting the target into two separate stages: the input electrons interact in the first target (the photon radiator), whose thickness is of the order of one radiation length or slightly less, generating photons; the photons impinge on the second, thicker target (the target-converter, which is often simply referred to as “the target”), placed at a certain distance from the radiator, thereby undergoing pair production. This multi-target configuration, sketched in figure 3.1c, is called hybrid scheme [93, 149] and has several advantages with respect to the single-stage PS:

- the total energy deposited in the bulk is shared between the two stages, therefore each one of them receives a lower energy load [53].
- Since the radiator is just  $\lesssim X_0$  thick, the integral energy deposit in it and the PEDD are in general small [53]; furthermore, an oriented crystalline radiator can be made even thinner while attaining the same photon yield and angular aperture [93]. In this case, the reduced thickness of this stage limits the thermally-induced lattice quality degradation.
- The integral energy deposit and the PEDD in the target-converter can be reduced by increasing the distance from the radiator, thus cutting

the tails in the output of the latter off from the acceptance. Moreover, collimators or a bending magnet can be placed between the two stages [93]. The collimators (figure 3.3 top) further contribute to cut off the tails from upstream, whereas the magnet (figure 3.3 bottom) sweeps all the charged particles away from the target acceptance.

In practice, all the available options mentioned in the last item above differ from one another in several features such as input beam intensity tolerance, positron production rate, output emittance and radiation level in and around the two targets. Therefore, the choice of the optimal configuration mainly depends on the accelerator performance in terms of electron beam features (intensity, emittance, time structure, etcetera) and positron beam goal features.

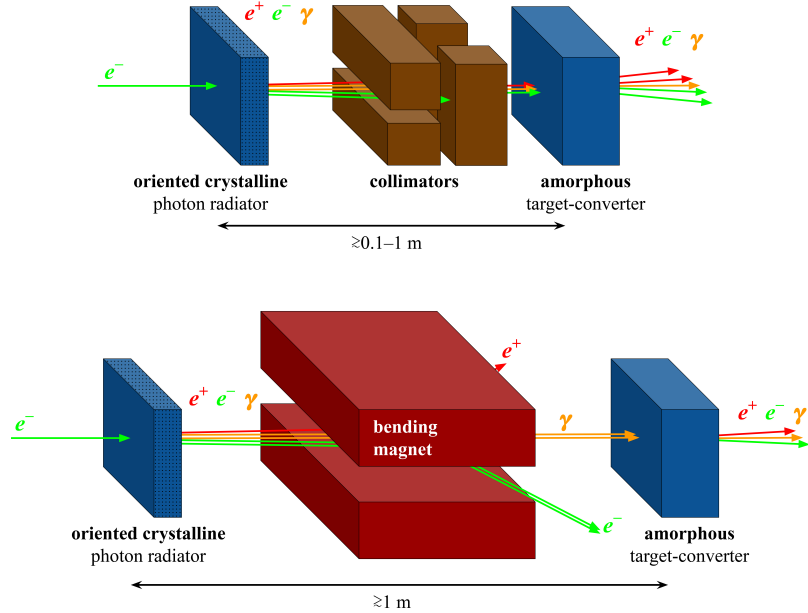


FIGURE 3.3: Optimised schemes for the positron source hybrid concept: a set of collimators (*top*) and/or a bending magnet (*bottom*) can be placed in between the crystalline radiator and the amorphous converter in order to stop all the large-angle particles and to sweep all the  $e^\pm$  away respectively.

### 3.1.2 The FCC- $ee$ requirements

The FCC- $ee$  is a next-generation  $e^+e^-$  collider currently under development at CERN. With its high luminosity, the cleanliness of the output states of



its (purely leptonic) interactions and its high and wide energy range, which encompasses the masses of the four heaviest fundamental particles currently known – the W and Z bosons, the Higgs boson and the top quark, this machine represents a powerful tool to perform precision measurements of the Standard Model. Moreover, it proves a solid starting point in the development of a 100 TeV hadron collider, in a synergic long-standing project that would reiterate that of the LEP/LHC (Large Electron-Positron Collider/Large Hadron Collider) [150], thereby allowing to investigate several scenarios beyond the Standard Model [142].

According to the present design, the FCC- $ee$  would significantly improve the performance of all present  $e^+e^-$  colliders. In particular, table 3.1 shows some of the key benchmark features of the FCC- $ee$ -Z, i.e., the FCC- $ee$  operated as a Z-factory – which will most likely be the first stage of operation of the FCC- $ee$  – and the corresponding requirements for the positron source; the same parameters are given for the two existing or past lepton colliders with the most performing PSs [142] – the Stanford Linear Collider (SLC) [151, 152] and the SuperKEKB [153] – and for the ILC, the future high-performance linear collider currently under study [154].

	SLC	SuperKEKB	ILC*	FCC- $ee$ -Z*
<b>Collider type</b>	linear	circular	linear	circular
<b>Luminosity</b> [ $10^{35}/(\text{cm}^2 \cdot \text{s})$ ]	$3 \times 10^{-5}$ [152]	8 [142]	0.135–0.49 [154]	23 [155]
<b><math>e^+</math> collision energy [GeV]</b>	50 [152]	4 [142]	125 [142]	45.6 [142]
<b>Repetition rate [Hz]</b>	120 [142]	50 [142]	300 [142]	200 [142]
<b>Bunches per pulse</b>	1 [142]	2 [142]	66 [142]	2 [142]
<b>Particles per bunch</b> [ $10^{10}e/\text{bunch}$ ]	5 [142]	6.25 [142]	3 [142]	2.1 [142]
<b>Beam intensity</b> [ $10^{12}e/\text{s}$ ]	6	6.25	594	8.4
<b>PS type</b>	conventional [142]	conventional [142]	TBD	TBD
<b>PS input <math>e^-</math> energy [GeV]</b>	30–33 [142]	3.5 [142]	3 [142]	6 [142]
<b>PS output hor. (ver.) emittance [<math>\mu\text{m}</math>]</b>	30 (2) [156]	100 (20) [142]	5 (0.035) [142]	24 (0.09) [142]
<b><math>e^+/e^-</math> ratio</b>	0.8–1.2 [142]	$\sim 0.6$ [142]	1.5 [142]	$\sim 0.5$ [142]
<b><math>e^+</math> flux [<math>10^{14}e^+/\text{s}</math>]</b>	$\sim 0.06$ [142]	0.025 [142]	2 [142]	0.06 [142]

TABLE 3.1: Features of the present and future (\*)  $e^+e^-$  colliders that exploit the most performing positron sources. The parameters related to the future machines correspond to the present benchmark and corresponding PS requirements. In particular, the PS-related values for the ILC refer to the conventional scheme under study as a backup solution.

It is clear from the data presented in table 3.1 that

- the FCC- $ee$  will strongly increase the luminosity with respect to the SuperKEKB, which currently holds the highest luminosity worldwide [157]. Overall, both the ILC and the FCC- $ee$  will significantly improve the performance of their predecessors currently in operation – the SLC and the SuperKEKB respectively.
- Circular colliders have higher luminosity than linear colliders but also higher emittance (see, for instance, the values at the PS output). FCC- $ee$  aims at a positron emittance comparable to that of SLC. Moreover, the beam intensities (evaluated as the product of pulse frequency, number of bunches per pulse and number of particles per bunch) are much higher for the linear machines.
- Both existing machines exploit a conventional PS, the SLC one being more efficient in positron production than that of the SuperKEKB.

As of today, several studies are being performed to determine the most suitable PS configuration for both the ILC and the FCC- $ee$ , which take into account the fairly different environments and requirements of the two machines. The extremely high electron beam intensity makes the choice of a solid-radiator source barely feasible for the ILC. Although the crystal-based hybrid scheme (optimised with magnets or collimators) and even the conventional scheme are currently being considered as a backup solution [142, 158], the most appealing option currently investigated consists of an undulator-based hybrid source, i.e., a source in which photons are generated by means of a magnetic undulator rather than via bremsstrahlung in a solid upstream stage [142].

Since setting up and operating an undulator-based source is considerably more challenging as opposed to the solid-radiator cases, mostly conventional and crystal-based hybrid options are currently under study for the FCC- $ee$ , whose beam intensity is considerably lower than that of the ILC. Extensive measurements are currently being performed on the features of the radiation resulting from coherent interactions by electrons of energy in the (2, 20) GeV range, which is particularly appealing for positron production from the standpoint of the yield [78] and relatively close to the energy of the collider primary electron beam – 6 GeV being the input electron energy foreseen in the FCC- $ee$  PS design (see table 3.1). At the same time, simulation studies are performed to improve both the PS conventional and hybrid scheme and to compare the performance of the two, in order to identify the best option for the FCC- $ee$  R&D.

## 3.2 The FCC– $ee$ hybrid source radiator: an experimental study

In recent years, several experiments have been performed on oriented crystals at the energies of interest for the FCC– $ee$  positron source, in order to test the feasibility of the crystal-based hybrid scheme. Most of these studies are focused on tungsten, which comes with a significantly high  $Z$  and short radiation length ( $X_0 = 0.3504$  cm). Other materials, like iridium ( $Z = 77$ ,  $X_0 = 0.2941$  cm [13]) and diamond, are currently under study: the former shows better features than tungsten but is scarcer and therefore more expensive [159], whereas the latter is expected to have strong crystalline potentials due to its tightly bound structure and low incoherent scattering contribution, but also narrower angular acceptance and high strong field (SF) threshold. Therefore, despite the appeal these options might have in terms of strength of the coherent effects, tungsten is currently the main candidate for this R&D.

The radiation produced by 5.6 GeV electrons impinging on high-quality crystalline tungsten has been studied at the DESY beam test facility (T21 beamline [101]) in 2019 [93]. An energy of 5.6 GeV has been selected instead of the actual PS design value of 6 GeV because of the larger intensity needed to collect enough statistics. The experimental setup is described in section 2.3.3 (chapter 2); in particular, it features the APC and the BGO-based Genni calorimeter. Both the spectra of the radiation energy and of the multiplicity of photons resulting from the interactions in the crystalline target have been investigated. The results presented in the following provide an excellent characterisation of these interactions, and the good agreement with the simulations prove the latter adequate in reproducing the features of the coherent effects in tungsten at the GeV scale.

### 3.2.1 The sample(s)

Figure 3.4 shows the transverse section of the sample under study at the DESY 2019 beamtest. It was manufactured by the Laboratory of Materials Science (LMS) of the ISSP RAS (Institute of Solid State Physics, Russian Academy of Science) [160]. It is  $2.25 \pm 0.05$  mm (i.e.,  $\sim 0.65 X_0$ ) thick and has a transverse section of  $\sim 7 \times 7$  mm<sup>2</sup> when oriented along the  $\langle 100 \rangle$  axis [93] – for which the corresponding SF critical angle is  $\Theta_0 \sim 1.5$  mrad.

It has to be noted that the energy of 5.6 GeV of interest for this study belongs to the range of limited SF ( $\hbar\omega_t \sim 18.84$  GeV and  $\chi \sim 0.3$ ) and corresponds to a Lindhard angle  $\psi_L \sim 524$   $\mu$ rad – see table 2.2, chapter 2. Moreover, the

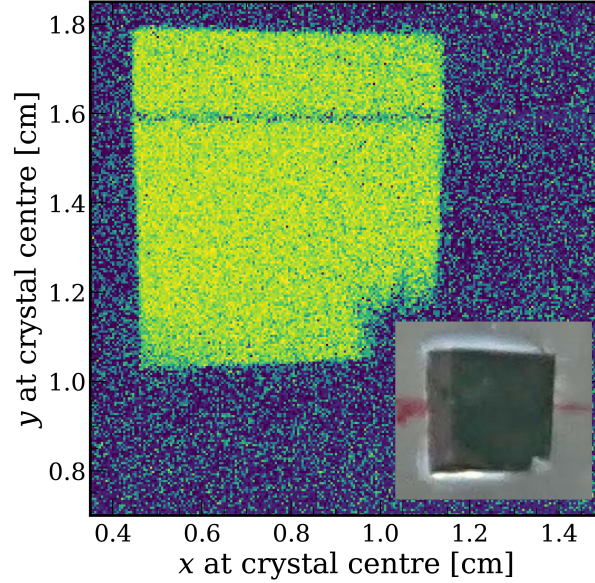


FIGURE 3.4: W  $\langle 100 \rangle$  sample probed at DESY. The crystal profile is highlighted by selecting the tracks which correspond to high multiplicity (more than 2 charged particles) at its output. A picture of the sample is superimposed for comparison.

measurements performed at the ESRF synchrotron facility (BM05 beamline [106]) showed that the sample has a significantly low mosaicity: most of the crystal surface presents values below  $60 \mu\text{rad}$ , and even the points with a worse crystalline quality (typically very close to small surface scratches, which most likely do not affect the lattice inside the bulk) show values below  $150 \mu\text{rad}$  [93]. Therefore, contributions to the coherent interactions from both under- and over-barrier effects are expected.

Thinner ( $\sim 1 \text{ mm}$  thick) commercial tungsten  $[111]$  samples have been studied with 855 MeV electrons at the MAMI B facility [104] in order to study the contribution of channelling radiation individually and determine how heavy irradiation by electrons affects the crystalline quality – details are given in section B.2 (appendix B).

### 3.2.2 Photon energy and multiplicity at 5.6 GeV

In the following sections, the strategy and results of the beamtest data analysis are discussed. The analysis framework has been developed using the software tools published in [161, 162]. These results have been recently published in [93].

### 3.2.2.1 Beamtest full simulations

Simulations have been performed to reproduce the experimental conditions of the beamtest on the DESY T21 beamline. In particular, the on-axis and amorphous-like cases have been simulated. As the sample thickness is  $< X_0$ , the code described in section 2.4.1 (chapter 2) has been exploited to simulate the interactions of the incident electrons in the axially-oriented crystalline sample.

The track-by-track output of the crystal simulation serves as a deterministic input for another code, based on standard Geant4, which reproduces the downstream part of the experimental setup [93] – the charge multiplicity counters, the bending magnet, the APC and the electromagnetic calorimeter. In the amorphous-like case, both the crystal stage and the apparatus downstream stage have been simulated with Geant4 [93].

### 3.2.2.2 Radiative energy loss

Figure 3.5 shows the spectra of  $E_{\gamma-\text{CAL}}$ , i.e., the energy of the electromagnetic radiation emerging from the crystalline target and detected by the photon calorimeter for each input electron. In particular, the measurements performed on the  $\langle 100 \rangle$  axis and at different misalignment angles up to  $\sim 28 \text{ mrad} \sim 1.6^\circ$  are presented in figure 3.5 top.

When on axis, the distribution of the energy at the calorimeter heavily differs from that typical of amorphous materials, showing a broad peak (at  $\sim 2.5 \text{ GeV}$ ) and a partial suppression of the softer component. The strength of these effects is approximately constant up to  $\sim 5 \text{ mrad}$  and decreases only slightly below  $\sim 10 \text{ mrad} \sim 0.6^\circ$ . As the misalignment angle grows, the soft component of the spectrum becomes comparatively more dominant over the hard one, with a fixed point at  $\sim 1.5 \text{ GeV}$  whose relative intensity does not seem to be affected by the lattice orientation. On the other hand, at  $14 \text{ mrad} \sim 0.8^\circ$  the energy distribution seems closer to the amorphous-like one.

Figure 3.5 bottom shows the same spectra as the plot at the top for the on-axis and simil-amorphous ( $28 \text{ mrad}$ ) cases, compared to the results of the beamtest full simulations. The simulated values have been smoothed by means of an interpolation with a B-spline function [163]. Overall, an excellent agreement between experimental and simulated data can be appreciated. It has to be noted that the endpoint of the random spectrum is at  $\sim 5.1 \text{ GeV}$ , i.e.,  $\sim 500 \text{ MeV} \sim 9 \%$  lower than the nominal input beam energy. As discussed in section 2.3.1.2 (chapter 2), this is mostly due to the lateral leakage of Genni.

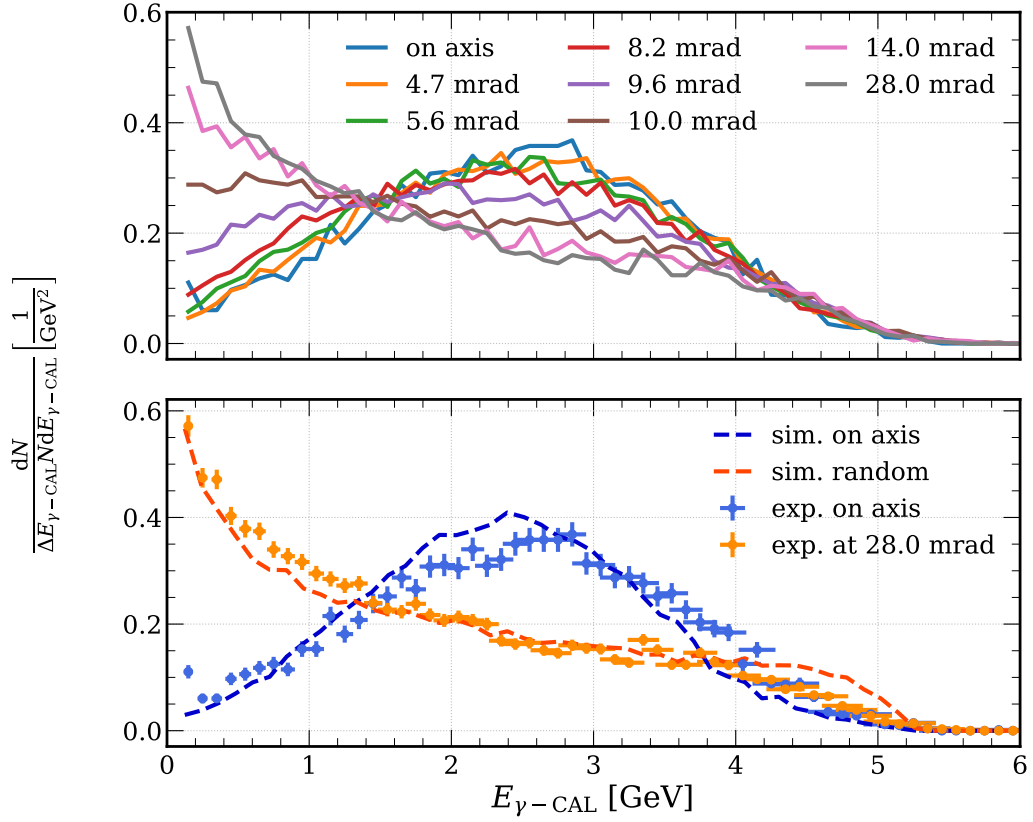


FIGURE 3.5:  $E_{\gamma\text{-CAL}}$  spectra (*top*) as a function of the misalignment angle and (*bottom*) comparison between experimental (points) and simulated (dashed curves) spectra.

### 3.2.2.3 Photon multiplicity

The experimental technique described in section 2.3.1.3 (chapter 2) has been exploited in the 2019 beamtest at DESY to investigate the distribution of the number of photons emerging from the crystalline sample per incident electron. Indeed, this observable proves extremely important for a full characterisation of the features of the coherent effects in real crystals, especially in view of their potential application as high-intensity electromagnetic radiation sources.

In order to compare the APC data to the simulation output, i.e., to the energy deposit in the DC plastic scintillator (in MeV), the APC-DC signal has to be calibrated. Figure 3.6 top shows the APC-DC energy deposit spectrum obtained by simulating a direct-beam run, i.e., a run in which no crystal is installed in the apparatus, the bending magnet is off and no copper is inserted

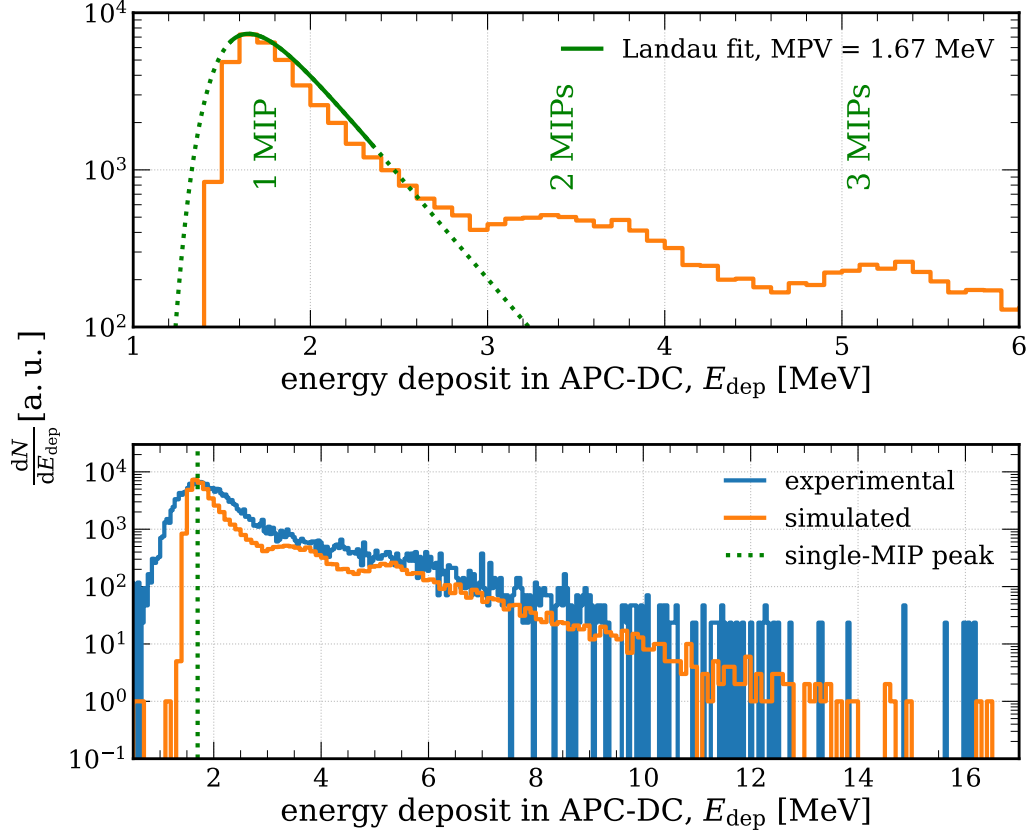


FIGURE 3.6: Direct-beam spectra of the APC-DC PH calibrated with the simulated energy deposit: (*top*) simulated spectrum with a Landau fit of the single-MIP peak and (*bottom*) comparison between simulated and (calibrated) experimental spectra.

into the APC. It is clear that most of the simulated events are characterised by a single electron (i.e., the one from the incident beam) crossing the DC scintillator, which results in a main, single-MIP peak centered at  $\sim 1.76$  MeV. A comparison between the simulated spectrum and the corresponding experimental calibrated spectrum is shown in figure 3.6 bottom: the experimental single-MIP peak is much larger than the simulated one and the double- and triple-MIP peaks are not visible at all due to the finite resolution of the DC light collection and readout (which is not reproduced in the simulation). However, the superimposition of these two distributions clearly highlights a trend compatibility that extends up to the spectra endpoint at  $\sim 16$  MeV  $\sim 9$  MIPs.

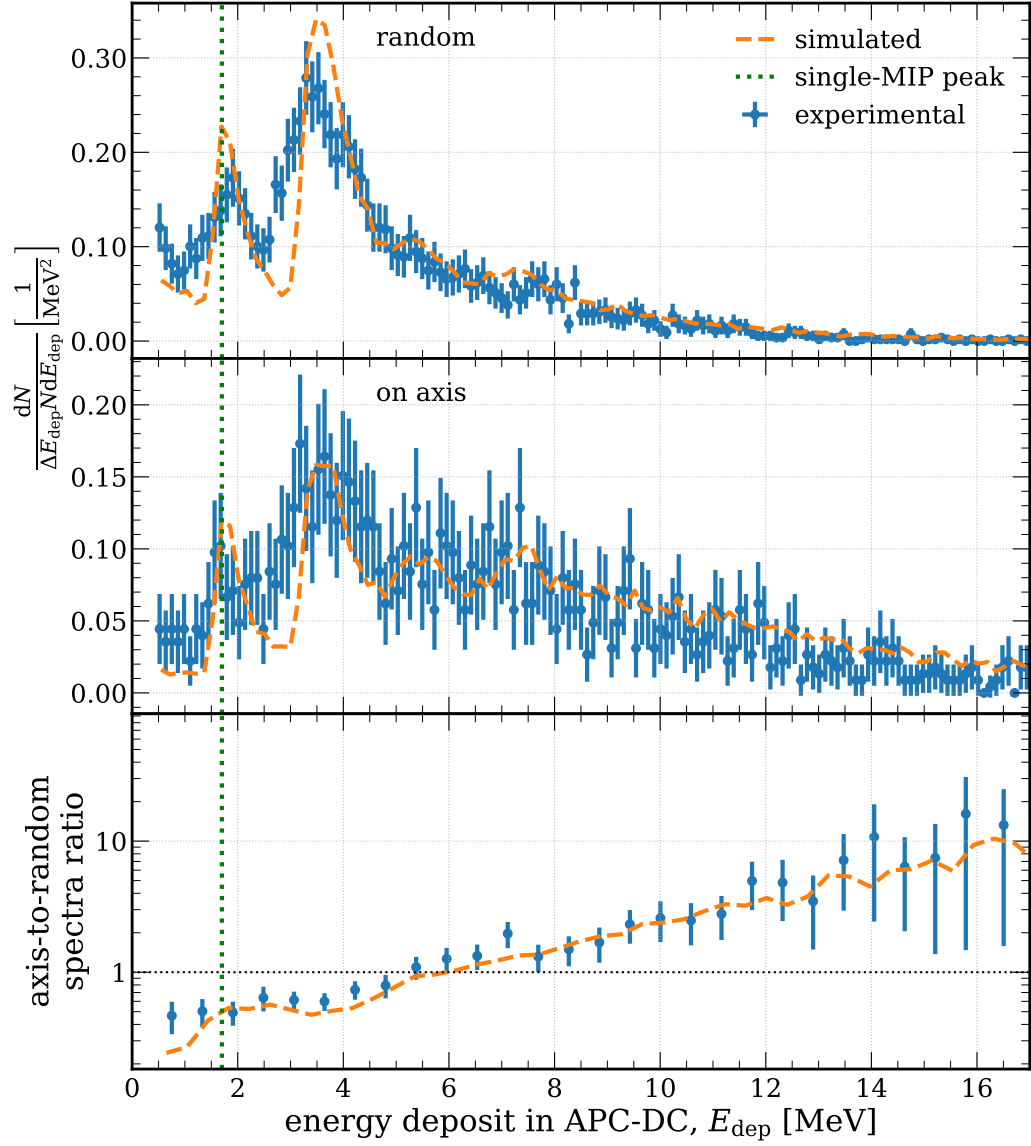


FIGURE 3.7: APC-DC signal spectra in random (*top*) and axial (*centre*) alignment configurations and axis-to-random ratio (*bottom*). Comparison between experimental data (blue) and simulation results (orange).



The results obtained in physics condition, i.e., with the crystalline sample installed on the beam, the magnetic field on and the copper inserted in the APC, are shown in figure 3.7 for the axial and random conditions. The energy deposit spectra shown at the top (random) and at the centre (axial) clearly demonstrate the compatibility between experimental and simulated data in the multi-MIP range; in particular, peaks are visible in the experimental spectra, as well as in the simulated ones (smoothed by means of an interpolation with a B-spline function [163]), corresponding to up to 4 MIPs. Moreover, the excellent compatibility between experimental results and simulation output in the whole range is evident from the ratio between on-axis and amorphous-like spectra, shown in figure 3.7 bottom. The ratio follows an exponential trend which is a function of  $E_{\text{dep}}$ , i.e., the energy deposit in the scintillator. As expected, for  $E_{\text{dep}} \lesssim 6$  MeV (corresponding to  $\sim 3.4$  MIPs) the random spectrum is more populated than the axial one, whereas for  $E_{\text{dep}} > 6$  MeV the axial spectrum dominates, showing a more-than-ten-fold enhancement with respect to the random case at  $\gtrsim 15$  MeV. This reflects the fact that, in general, more photons are generated when the coherent processes set in. As it can be observed in figure 3.8, the transition from the axial regime to that of standard incoherent bremsstrahlung is smooth and has a wide angular range, which reflects the results shown in section 3.2.2.2: an enhancement in the observed photon multiplicity is observed already at  $14 \text{ mrad} \sim 0.8^\circ$  from the axis.

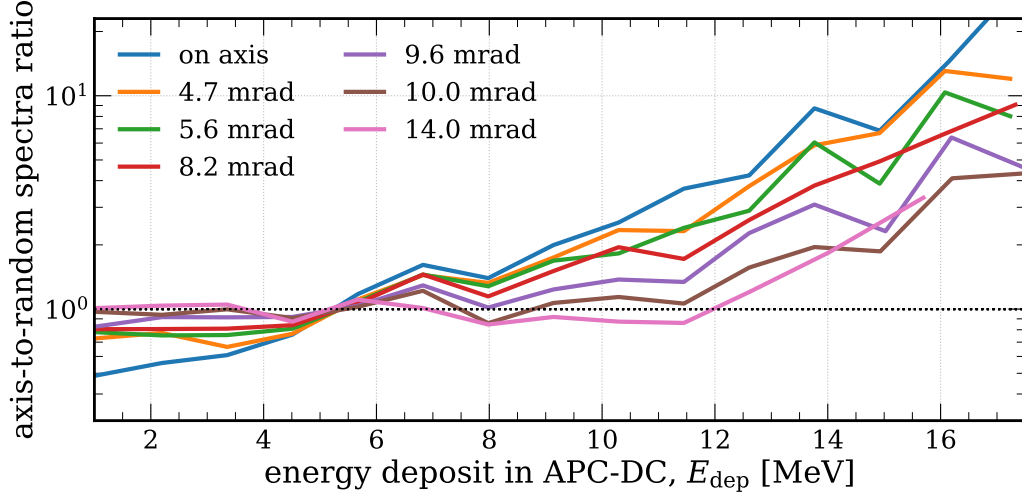


FIGURE 3.8: APC-DC signal spectra ratios as a function of the misalignment angle.

The results presented in this section demonstrate the feasibility of simulating the coherent interactions of the electrons at the GeV scale in oriented tungsten by means of the currently available simulation software. Information on many observables of interest which cannot be directly measured in experiments, e.g., the total number of photons generated in the interactions of each single electron with the crystalline lattice, can then be obtained from the simulations. Therefore, the simulation framework proves suitable for investigating the concept of crystal-based positron source in different configurations.

### 3.3 Towards the FCC-*ee* PS full simulation

The characterisation of the positron source is a fundamental item in the early stage of the FCC-*ee* design, as its features strongly affect the global performance of the collider. While experimental tests are being performed on the different components of the apparatus, it is of paramount importance to develop full simulations of all the feasible configurations, namely, the PS conventional scheme and several versions of the hybrid concept optimised in different ways, in order

- to compare them and to determine the best option;
- to obtain information on the features of the PS output particles that can drive the design of the downstream magnetic collection system [142].

The following sections present the results of the simulations performed on both the hybrid scheme, studied in several configurations, and the conventional scheme at the FCC-*ee* benchmark.

#### 3.3.1 The two-stage setup

The simulation of the full positron production chain in the hybrid configuration is performed in two separate stages, similarly to the scheme adopted for the simulations of the beamtest at DESY – section 3.2.2.1. Firstly, the interactions of the electron primary beam (modelled after the FCC-*ee* current design parameters) in the tungsten [111] crystalline radiator are simulated with the software described in section 2.4.1 (chapter 2), as the primary beam energy is 6 GeV and hence the dynamics is of the sub-SF type.

The track-by-track output of the crystalline stage is then exploited as an input for a standard Geant4 software, in which the tungsten amorphous target

environment (including the space, filled with vacuum, between the radiator and the target) is modelled. This stage was run with Geant4 version 10.7 and relies on the FTFP\_BERT reference physics list [141]. Several different configurations of this stage have been tested – the graphical representation of one of these configurations is presented in figure 3.9; all these simulation runs have been performed with the same crystal output file.

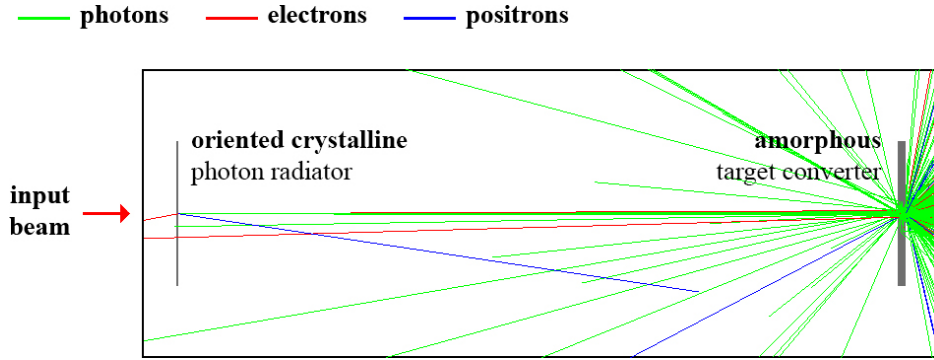


FIGURE 3.9: Rendering of the target stage of the hybrid PS Geant4 simulation, with 50 crystal output events displayed. The crystal bulk is not included in the simulation geometry and has been added here for the sake of visualisation. To be compared with figure 3.1c.

In order to guarantee that the results are fully comparable to those of the hybrid scheme, the simulations of the conventional case are performed with the same Geant4 code described above, in which the radiator-to-converter distance (here intended as the distance between the primary beam source and the converter) is set to zero. Furthermore, the same primary event population is used: the input tracks of the crystalline radiator program directly serve as input tracks of the Geant4 program. This ensures that the performance of the different PS configurations under study is probed with the same set of primary particles.

### 3.3.2 Crystalline radiator

A crystalline radiator with a thickness of 2 mm has been selected, as it provides a good photon yield while the output photon divergence and the integral energy deposit are moderate [93]. The [111] axis was chosen, as it features the strongest potential.

The primary beam is purely made of 6 GeV electrons, with a 500  $\mu\text{m}$  circular spot and a divergence of 100  $\mu\text{rad}$ .  $10^4$  primary electrons have been generated, which resulted into 175672 (61069) output photons ( $e^\pm$ ). Figure

3.10 shows the beam spots at the crystal front and rear sides. It is clear that the beam size is not macroscopically affected by the scattering inside the radiator, as the output distributions for both photons and electrons/positrons (both from the input beam and from the interactions inside the crystal) show the same shape and width as the input one.

On the other hand, the distributions of the output angles  $\theta_x$  and  $\theta_y$  (figure 3.11) for photons and for electrons/positrons heavily differ from each other and from the input one. Indeed, the output charged component of the beam has a divergence that is more than 8 times larger than the input one, which is due both to the primary electron recoil in the bremsstrahlung emission and to the MCS. The large- $\theta$  tails are mostly due to the bremsstrahlung recoil electrons that are left with a small fraction of their initial energy, as shown by the orange histogram (filled by tracks with a longitudinal momentum  $p_z > 1$  GeV) in figure 3.11 centre-right.

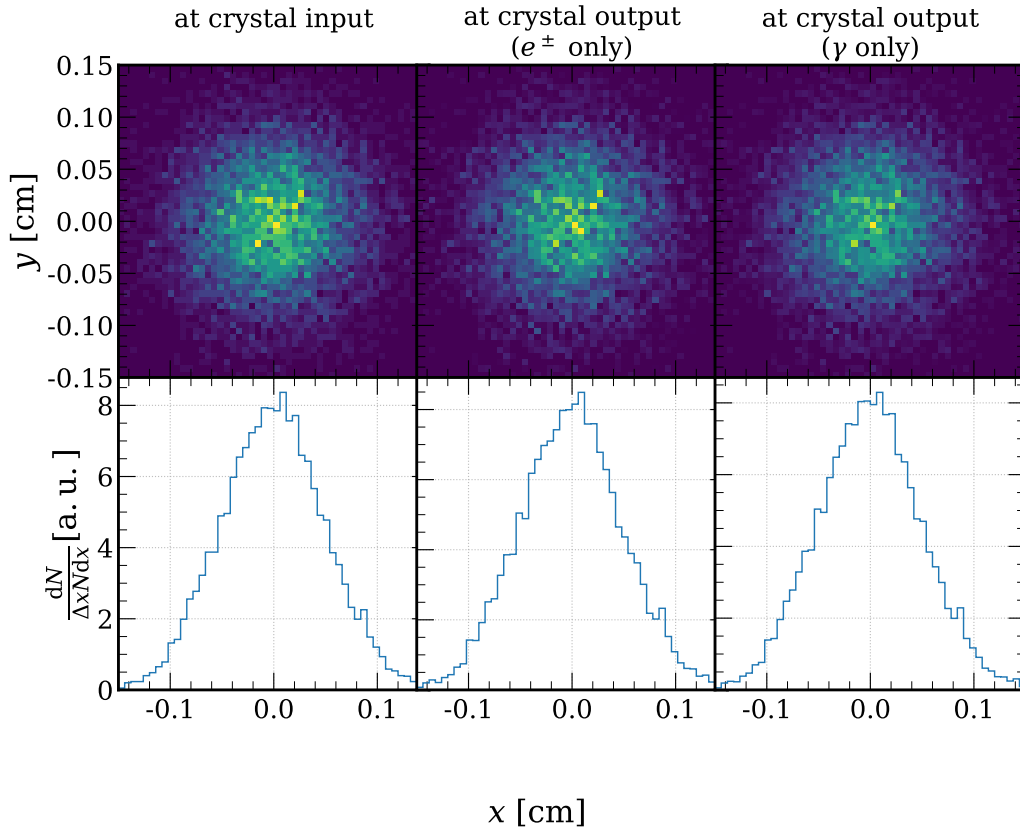


FIGURE 3.10: Beam spots at the crystal input (*left*) and output – for charged particles (*centre*) and photons (*right*).

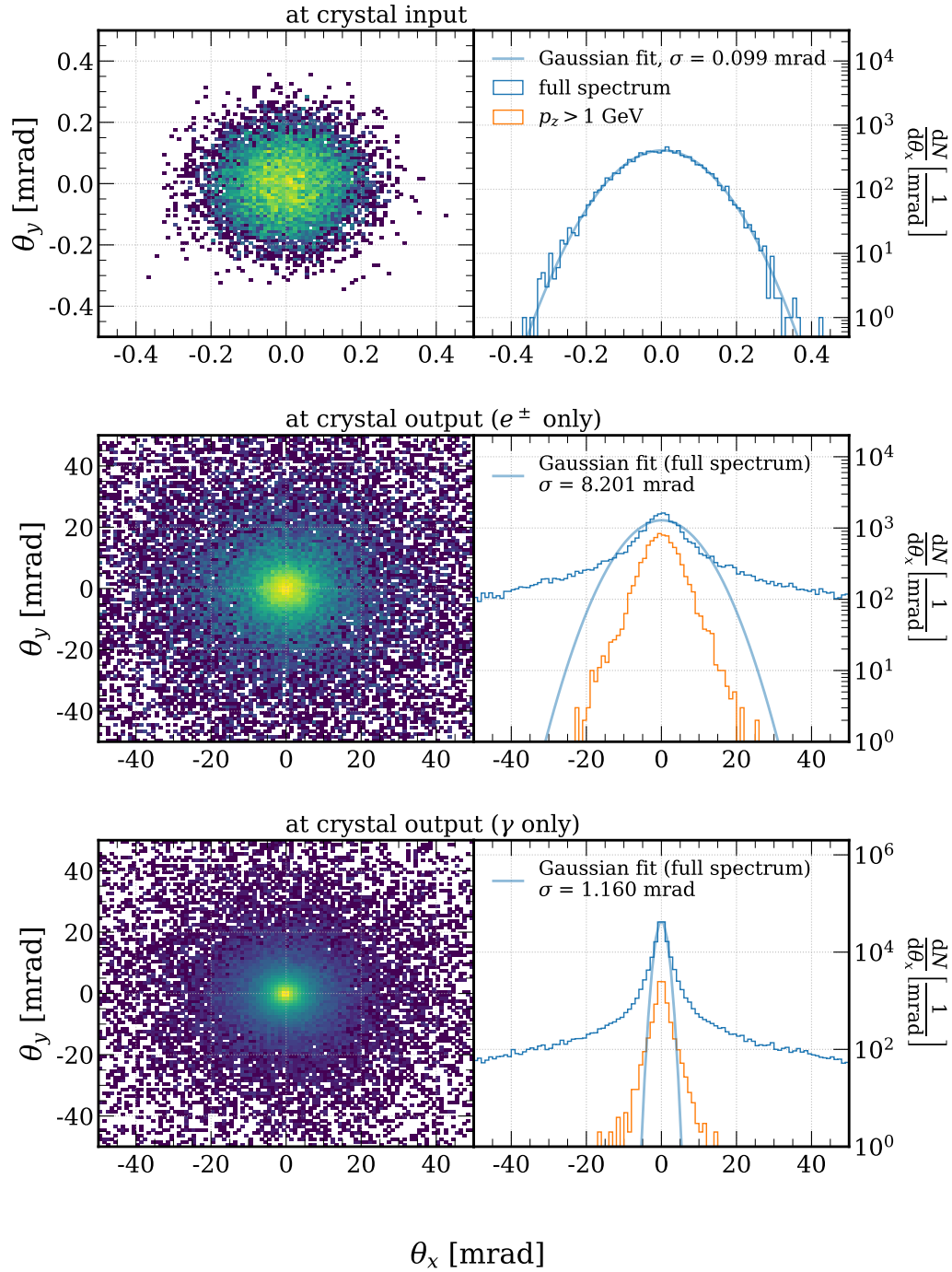


FIGURE 3.11: Beam angular distributions at the crystal input (*top*) and output – for charged particles (*centre*) and photons (*bottom*). Two-dimensional (one-dimensional horizontal) distributions are shown on the left (right). It has to be noted that the scale of the centre and bottom plots is 10 times the one at the top.

Conversely, photons emerge from the crystal with a small angle with respect to the primary trajectory. Indeed, the output photon divergence is just  $\sim 160 \mu\text{rad}$  larger than the input one, which accounts for the contributions of photons which are emitted by secondary electrons at slightly larger angles with respect to the primary beam aperture and of the radiation cone opening angle, i.e.,  $1/\gamma = 85 \mu\text{rad}$ . The orange curve in figure 3.11 bottom-right shows that, similarly as for charged output particles, higher-energy photons mostly contribute to the low-angle peak.

Finally, figure 3.12 presents the longitudinal momentum spectrum for output electrons/positrons and photons. It has to be noted that these are the spectra of the real output particle longitudinal momenta, which differ from the experimental radiation energy spectrum measured in the 2018 beamtest on DESY T21 (figure 3.5) because of, e.g., the limited acceptance of the setup of the latter.

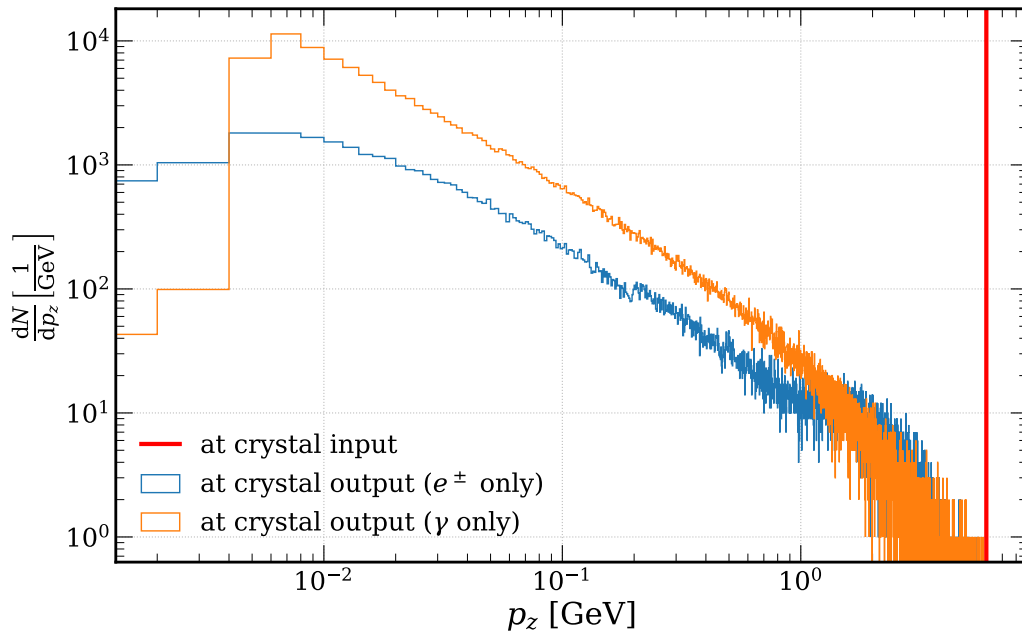


FIGURE 3.12: Output longitudinal momentum spectra.

### 3.3.3 Amorphous target optimisation

Several simulation runs have been performed for the target-converter stage in order to study how the PS output performance varies as a function of the distance between the crystal and the amorphous target,  $D$ , and of the thickness of the latter,  $L$ . On the other hand, the shape and transverse dimensions

of the target have not been varied: all the runs have been performed on a parallelepiped-shaped target with a  $199.75 \times 199.75 \text{ mm}^2$  square section. The choice of a very large target has been made to properly study the energy distribution inside its volume up to several units of Molière radius from the beam path.

Many different quantities are scored by the simulation software:

- the ID information (e.g., particle type) and kinematics (i.e., position, momentum, etcetera) of all the tracks at the Geant4 particle source (i.e., at the crystal rear face) and at the target rear face, by means of two dummy (i.e. made of the same material as the surrounding environment, and therefore transparent to the particle propagation) Geant4 sensitive detectors [164];
- the integral energy deposited inside the whole target volume, which is a sensitive detector as well;
- the integral energy deposit in each voxel of the mesh defined on top of the target volume.

### 3.3.3.1 Target mesh

A trade-off between precision of the results and computation resources has been found in a mesh with parallelepiped-shaped voxels of  $\Delta x = \Delta y = 250 \text{ }\mu\text{m}$  (transverse) and  $\Delta z = 500 \text{ }\mu\text{m}$  (longitudinal) – details can be found in section B.3.2 (appendix B). Overall, a matrix of  $799 \times 799 \times L[\mu\text{m}]/500 \text{ }\mu\text{m}$  voxels is considered. Both transverse directions account for an odd number of voxels, in order for the beam to hit the centre of the face of a voxel rather than its edge.

Figure 3.13 top presents a 2D representation of the central part of a sample mesh. The distance from the beam axis of each voxel is computed as  $r = \sqrt{x^2 + y^2}$ ,  $(x, y)$  being the position of the voxel centre. The two-dimensional plot is then filled with the voxel energy density as a function of  $r$  and  $z$ . As sketched in figure 3.14, the distribution of the values that  $r$  can assume is discrete (red lines), and the density of values grows with  $r$ , therefore the bin size in figure 3.13 top decreases as  $r$  grows. It can be clearly observed that the energy density pattern is strongly inhomogeneous, with a core starting from a depth of  $\sim 7 \text{ mm}$  (i.e.  $\sim 2 X_0$ ) along the beam direction and extending down to the target rear side. From the point of view of the transverse distribution, the energy density is halved already at  $\sim 500 \text{ }\mu\text{m}$  from the beam axis and is  $< 10\%$  at  $\sim 2 \text{ mm}$ .

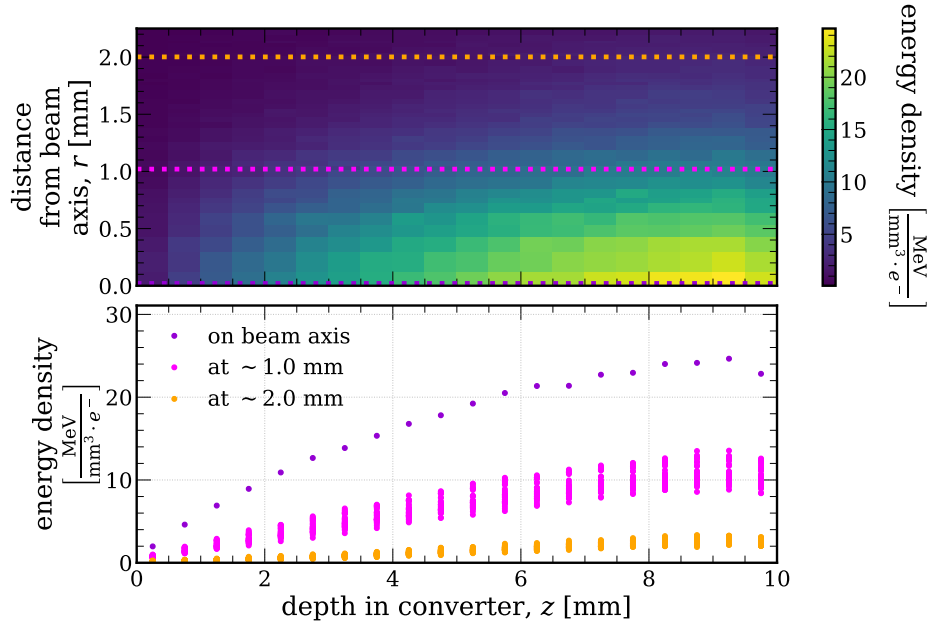


FIGURE 3.13: An example of mesh superimposed to the amorphous target, projected in a two dimensional view with radial versus longitudinal coordinates (*top*) and longitudinal profile of the average energy density at different distances from the central longitudinal axis (*bottom*). The beam impinges on the target from the left.

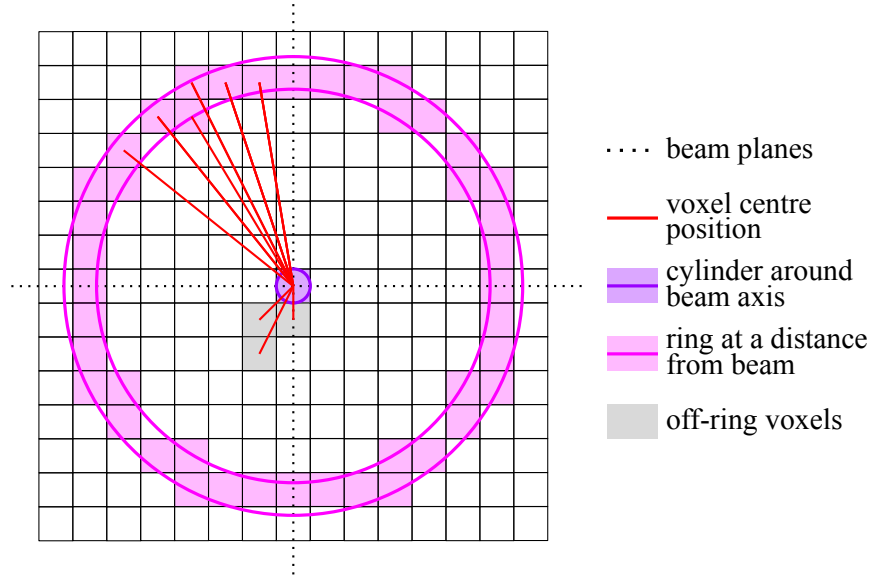


FIGURE 3.14: Sketch of the front view of a box-shaped mesh with reparametrisation into the cylindrical coordinates  $(r, z)$  in the transverse plane.



All these observations are confirmed by figure 3.13 bottom, which presents the longitudinal profile of the energy density at three different distances from the  $z$  axis – along the axis itself, at  $\sim 1$  mm and at  $\sim 2$  mm. Since, as already mentioned above,  $r$  results from a reparametrisation of the box-shaped transverse section of the mesh and is thus a discrete quantity, it is best to choose an interval rather than a single value: ring-shaped slices of width  $\Delta x$  are chosen and all the voxels whose centre is located inside the slice are considered. As a consequence, as illustrated in figure 3.14, all rings at a given distance from the  $z$  axis will comprise many values of  $r$  and thus many different energy density curves.

Overall, figure 3.13 clearly shows that the energy deposit maximum, which is significant for the evaluation of the PEDD in the target, is located on the beam axis. Care should be taken in case realistic bending magnets are implemented upstream with respect to the target: if the magnetic field is not intense enough or the target is too large, the remainder of the primary electron beam could hit the latter and hence strongly contribute to the integral energy deposit while introducing an off-axis component that might be much higher than the one given by photons propagating along the  $z$  axis.

### 3.3.3.2 Energy deposit, PEDD, positron production rate

In simulating the hybrid PS scheme, both  $L$  and  $D$  have been varied in a large phase space – (8, 13) mm and (10, 200) cm respectively. On the other hand, the conventional scheme was simulated with the optimal thickness value  $L = 17.6$  mm [93].

Figure 3.15 shows the results obtained from the target bulk sensitive detector as a function of  $D$  (abscissas) and  $L$  (different colours). The plot at the top shows the energy deposit averaged on all the particle tracks. As expected, the value grows with an approximately linear trend with the target thickness. On the other hand, all the curves depend on  $D$  only slightly. The curves for  $L = 8$  mm and 13 mm are shown superimposed on each other in figure 3.15 centre: a decrease of  $\sim 2$ –3% is observed as  $D$  is increased from 10 cm to 60 cm.

Moreover, the PEDD is computed by fitting the on-axis curve in figure 3.13 bottom with a parabola and taking the maximum. Trends of the latter are shown in figure 3.15 bottom. As the target is pulled away from the crystalline radiator, its angular acceptance decreases, thus cutting a larger fraction of the crystal output beam tails off. As a result, less particles impinge on the target – mostly those with the highest energy and hence the smallest angle, as shown in figure 3.11. On the other hand, as expected, a dependence on  $L$  is only observed for values smaller than the threshold depth  $L_{\text{PEDD}}$ ; from

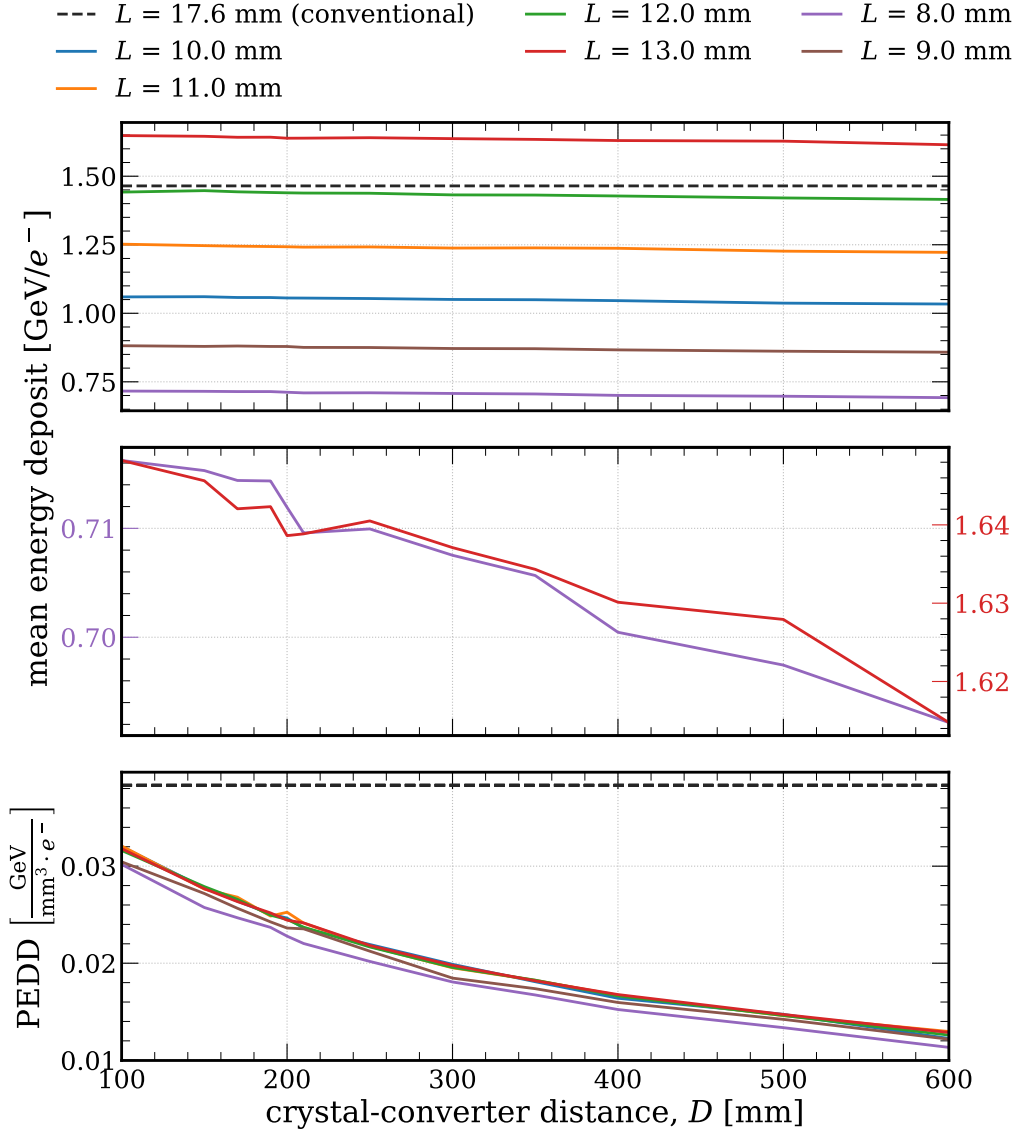


FIGURE 3.15: Integral bulk data from the hybrid PS target stage, as a function of  $D$  and  $L$ : energy deposit, for all the values of  $L$  (*top*) and only for the minimum and maximum case (*centre*), and PEDD (*bottom*). The corresponding values for the conventional PS scheme are shown as black dashed lines.

figure 3.13 it results that the energy density peak longitudinal position, and hence  $L_{\text{PEDD}}$ , is  $\sim 9.5$  mm. For every  $L > L_{\text{PEDD}}$  the energy density is lower than the one at the threshold depth, therefore the PEDD corresponds

to the energy density in  $L_{\text{PEDD}}$  independently on  $L$ ; on the other hand, for  $L < L_{\text{PEDD}}$  the PEDD always corresponds to the energy density value reached towards the rear end of the target.

The energy deposit resulting from the simulation of the conventional scheme (with  $L = 17.6$  mm – black dashed line) is similar to the value obtained in the hybrid case with  $L = 12$  mm. This reflects the fact that, although the target is thinner, several particles per primary electron impinge on it, with an average energy much smaller than the one of the incident beam. On the other hand, it is clear from figure 3.15 bottom that the PEDD in the hybrid case is considerably smaller than the one of the conventional case.

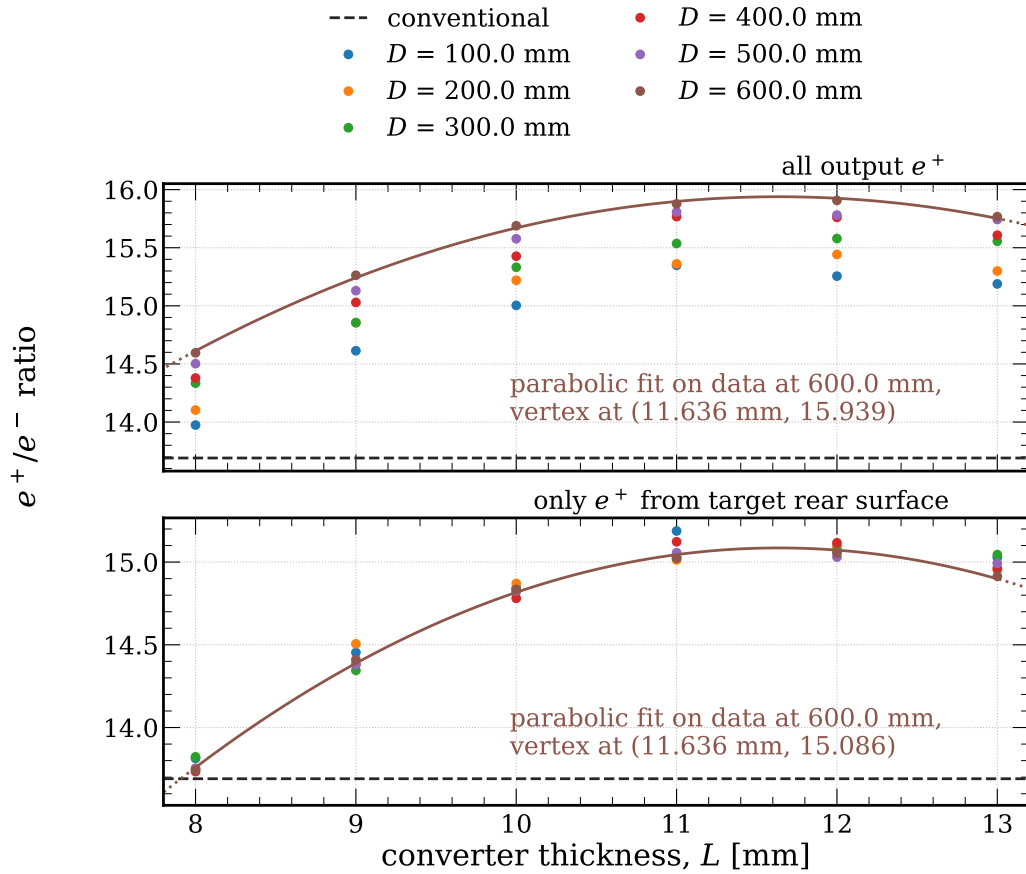


FIGURE 3.16: Output positron production rate from the hybrid PS setup, as a function of  $L$  and  $D$ ; all the positrons crossing a  $5 \times 5$  m<sup>2</sup> plane at the target rear end (*top*) and only those crossing the target rear face (*bottom*) are taken into account respectively. The corresponding values for the conventional PS scheme are shown as black dashed lines.

The integral energy deposit and the PEDD should be kept as low as possible, while trying to maximise the positron yield per incident electron at the PS output – namely, the positron production rate. The results obtained for the latter are shown in figure 3.16 as a function of  $L$  (abscissas) and  $D$  (different colours). These plots can be interpreted as transition curves, and can be compared with those shown in figure 3.2.

It is clear that each dataset (obtained at a different  $D$ ) shows a maximum in the positron production rate. The position of the maximum is independent on  $D$  and corresponds to  $L \sim 11.6$  mm. Furthermore, the  $e^+/e^-$  ratio does not show any clear dependence on  $D$ , whereas it grows with the output spatial acceptance: the comparison between figure 3.16 top and bottom, which account for all the positrons crossing the target rear plane in the whole simulation environment ( $2.5 \times 2.5$  m<sup>2</sup>) and inside the rear face only ( $\sim 20 \times 20$  cm<sup>2</sup> – closer to the acceptance of a realistic magnetic capture system) respectively, shows a rate reduction of  $\sim 5\%$ .

### 3.3.3.3 Output positron beam phase space

The simulation results presented in this chapter provide useful information for the design of the magnetic capture system that collects the positrons generated in the PS. In particular, the output beam kinematics (size, angular aperture, energy spectrum) should be investigated in detail for the acceptance of the downstream magnetic optics to match the features of the emitted positrons.

Figure 3.17 shows the Gaussian  $\sigma$  of the distributions of the positron output angle (top) and position at the target rear side (bottom). Both plots refer to the horizontal plane; the distributions obtained in the vertical plane show the same trends, given the cylindrical symmetry of the system around the beam axis. The positron divergence does not depend on  $D$  and depends only weakly on  $L$ ; moreover, there is no clear difference between the conventional and hybrid cases. On the other hand, the beam spot becomes larger as  $D$  grows and also, less clearly, as  $L$  grows. However, the beam size does not increase significantly with respect to the input value –  $\sigma \sim 1$  mm is obtained at 60 cm,  $\sim 1.2$  mm at 1 m and  $\sim 1.5$  mm at 2 m.

Finally, the features of the output positron energy spectra are presented in figure 3.18: the mean values and standard deviations are shown in the plot at the top and at the bottom respectively. Both these variables grow linearly as a function of  $L$  and are independent on  $D$ . Moreover the fact that the standard deviations are approximately twice the mean values reflects the broad shape of the distributions.

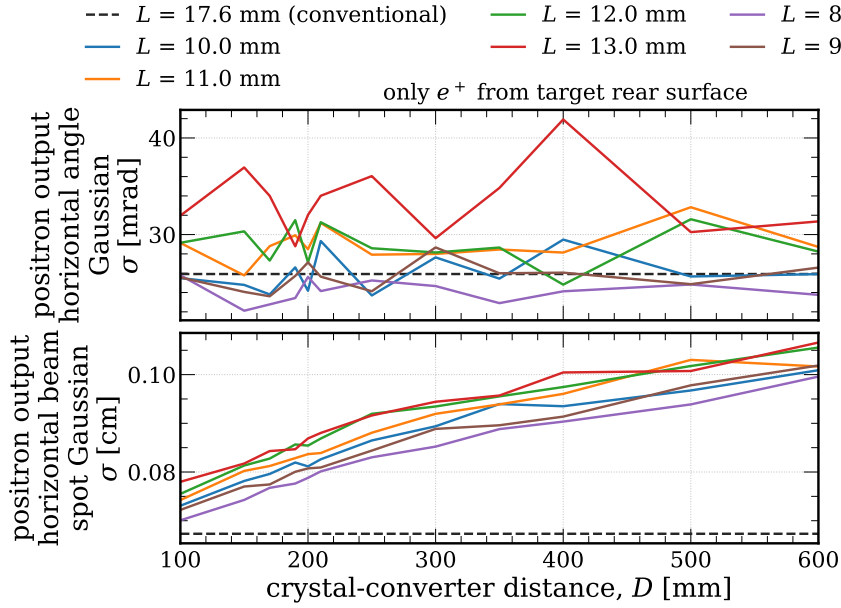


FIGURE 3.17: Output hybrid PS target positron beam angle (*top*) and beam spot size (*bottom*), as a function of  $D$  and  $L$ . The corresponding values for the conventional PS scheme are shown as black dashed lines.

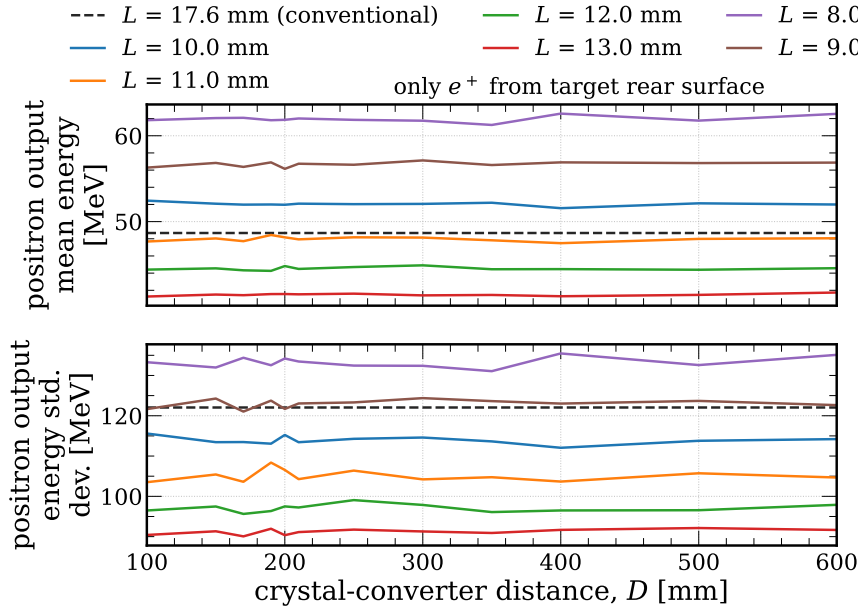


FIGURE 3.18: Output hybrid PS target positron energy, mean (*top*) and standard deviation (*bottom*), as a function of  $D$  and  $L$ . The corresponding values for the conventional PS scheme are shown as black dashed lines.

All the results presented in the previous section provide enough information to determine the optimal values of  $L$  and  $D$ . In particular,  $L$  should be 11.6 mm in order to maximise the positron production rate and  $D$  should be as large as possible while keeping the output beam spot from growing too much; ideally,  $D$  should be of the order of 60 cm or larger.

### 3.3.4 Collimator or/and magnet?

The performance obtained so far can be further improved by implementing a collimator or a bending magnet between the crystalline radiator and the amorphous target. Figure 3.19 shows the rendering of two Geant4 sample runs, with the collimator (top) and with the magnetic field (bottom).

The collimator consists of a 50 cm thick block of tungsten, of with transverse size  $2.5 \times 2.5 \text{ m}^2$  and a box-shape-sided aperture along the beam axis; it is located with its front face at 5 cm from the crystal rear face. A scan has been performed on the aperture size  $a$ , in the (0.5, 10) mm range, with  $L = 11.6 \text{ mm}$  and  $D = 60 \text{ cm}$ . Concerning the bending magnet, an ideal,

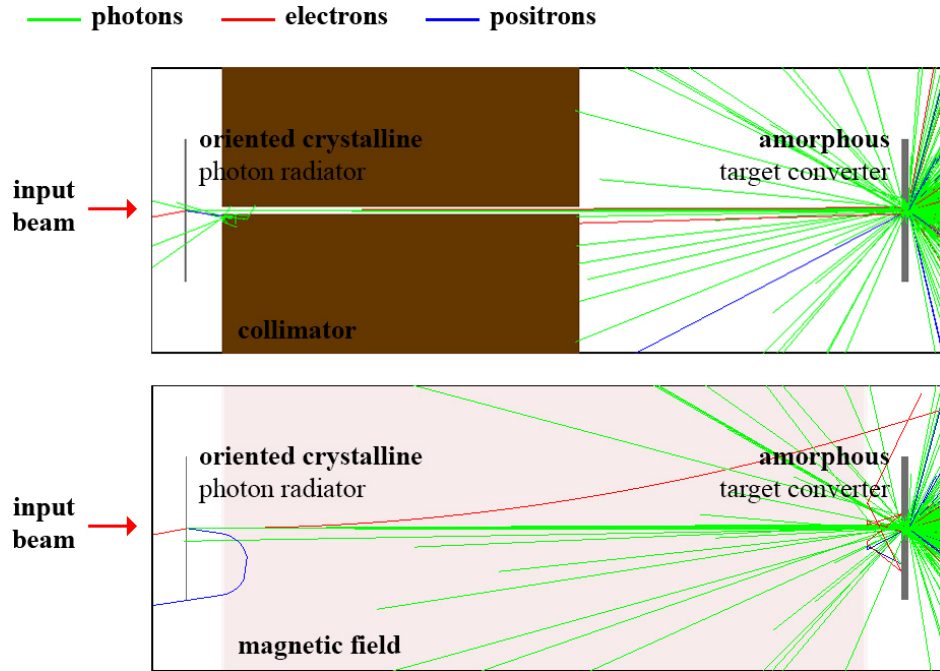


FIGURE 3.19: Rendering of the target stage of the hybrid PS simulation optimised by implementing a tungsten collimator (*top*) or a 2 T bending magnetic field (*bottom*), with 50 crystal output events displayed. To be compared with figure 3.3.

100 T magnetic field directed along the vertical axis has been implemented, with the aim of sweeping away all the charged particles from the crystal regardless of their energy. The field is uniform and spans in a 90 cm thick region centered at  $D/2$  from the crystal rear face. Single runs with  $D = 1$  m and 2 m have been simulated.

Figure 3.20 shows the results obtained from the target bulk sensitive detector as a function of  $a$  and in comparison with runs in conventional geometry (black dashed lines) and in hybrid geometry with no collimator and no field (red dashed lines) and with the field (green dashed lines) at different values of  $D$ . Moreover, figure 3.21 shows the positron production rate with the same colour code. Several observations can be made:

- for  $a \lesssim 2$  mm, all the values drop dramatically, which highlights the fact that a major fraction of the beam (whose total Gaussian width is, indeed,  $2\sigma \sim 2$  mm for  $D = 60$  cm) is stopped by the collimator.
- As  $a$  grows, all the curves asymptotically tend to the values obtained without the collimator.
- Despite the statistical fluctuations, it is clear that, for  $a \gtrsim 4$  mm, the PEDD is slightly lower than in absence of the collimator; a minimum is observed at  $\sim 7$  mm, with a reduction of 1% with respect to the no-collimator value. On the other hand, the PEDD obtained with the magnetic field instead of the collimator at  $D \geq 1$  m is consistently ( $\sim 30\%$ ) lower.
- For  $a$  in the (4, 10) mm range, the energy deposit is significantly ( $\sim 15\%$ ) lower than in the no-collimator case; the runs with the magnetic field lead to values that are similar to the latter.
- The positron production rate equals the result obtained with the conventional scheme at  $a \sim 5.5$  mm and it smoothly outgrows it for larger  $a$ . On the other hand, replacing the collimator with a bending magnet considerably improves the positron yield, whose value is almost the same as the one obtained without any optimisation device between radiator and target.

### 3.3.5 Result summary

Table 3.2 summarises all the main results obtained in the previous sections. All the variables of interest are provided for the most interesting PS configurations that have been investigated. All the selected cases except the conventional one feature  $L = 11.6$  mm, whereas three values of  $D$ , i.e., 0.6 m,

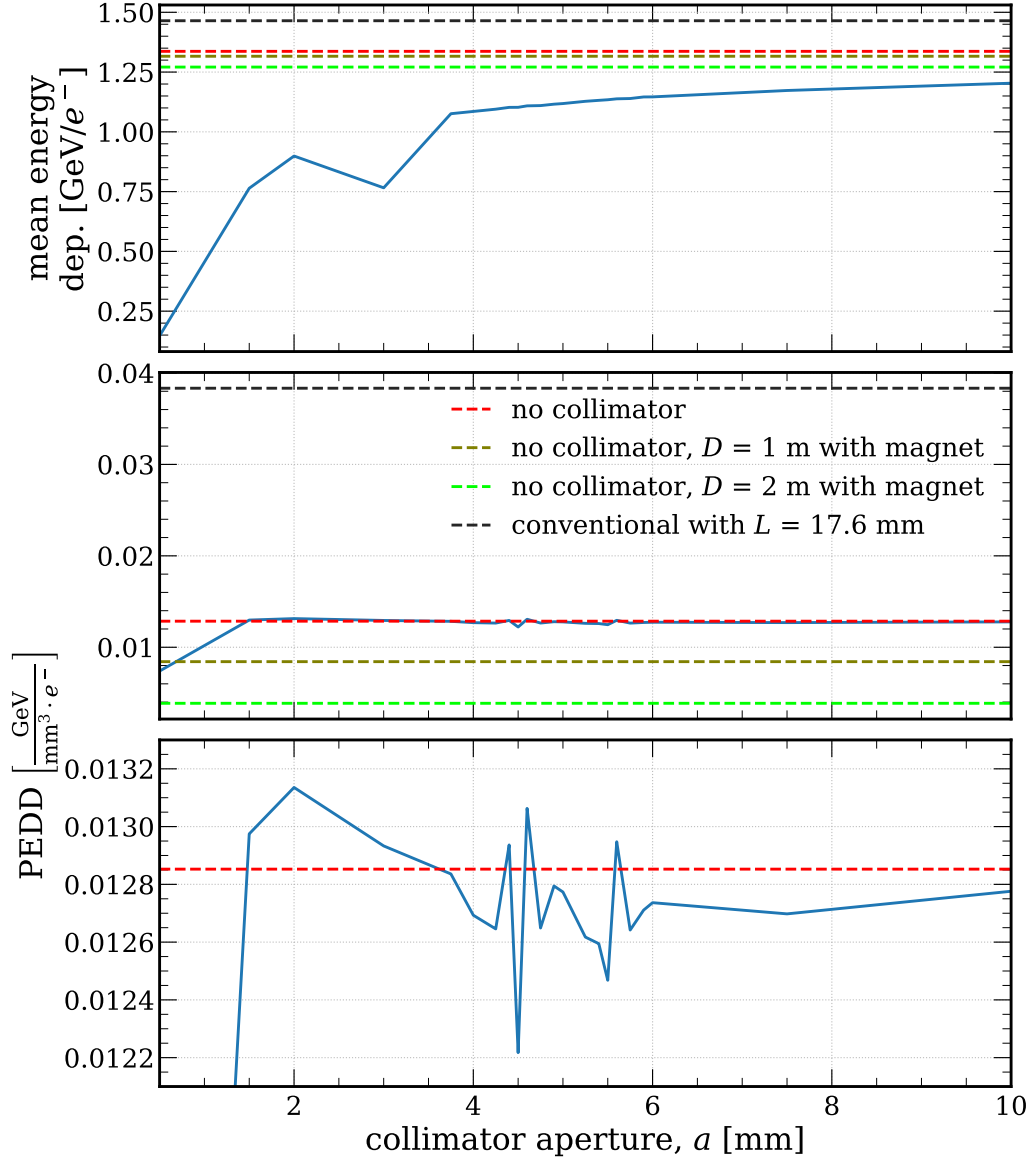


FIGURE 3.20: Integral bulk data from the hybrid PS target stage optimised with a collimator, as a function of  $a$ : energy deposit (*top*) and PEDD, with large range (*centre*) and zoomed around the collimator data (*bottom*). The corresponding values for the conventional PS scheme and for the setup optimised with a magnetic field are shown as dashed lines.



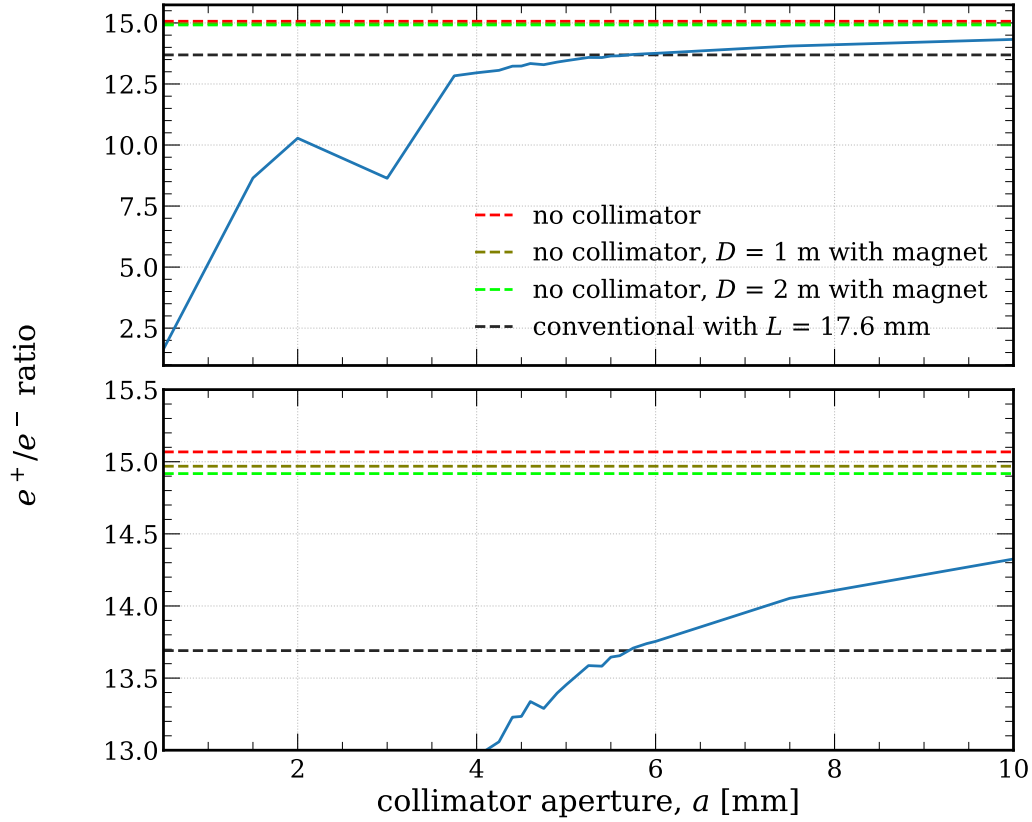


FIGURE 3.21: Output positron production rate for the hybrid PS setup optimised with a collimator, as a function of  $a$ . Only the positrons that cross the target rear face – with large range (*top*) and zoomed around the conventional value (*bottom*) – are taken into account. The corresponding values for the conventional PS scheme and for the setup optimised with a magnetic field are shown as dashed lines.

1 m and 2 m, have been selected for the hybrid scheme – the collimator and magnet options only being available for the latter two. Concerning all the collimator runs,  $a = 5.5$  mm has been chosen, as it results in the same positron production rate as the conventional scheme with significant (slight) reduction of energy deposit (PEDD) with respect to the no-collimator case. When implemented, the magnetic field is always set to the ideal value of 100 T.

In general, all the crystal-based hybrid scheme options significantly improve the performance of the conventional scheme from the standpoint of all the features of interest in the design of a PS system. In particular,

Scheme	conv.	hybrid						
$L_{\text{crys}}$ [mm]	–	2						
$D$ [m]	–	0.6	1			2		
$L$ [mm]	17.6	11.6						
Collimator?	no	no	no	yes	no	no	yes	no
Magnet?	no	no	no	no	yes	no	no	yes
$E_{\text{dep}}$ [GeV/ $e^-$ ]	1.46	1.34	1.32	1.13	1.32	1.27	1.11	1.27
PEDD [MeV/(mm <sup>3</sup> · $e^-$ )]	38.3	12.8	8.4	8.2	8.4	4.1	3.8	3.9
Out. $e^+/e^-$	13.7	15.1	15.1	13.6	15	14.9	13.7	14.9
Out. $e^+$ beam size [mm]	0.7	1.0	1.2	1.2	1.2	1.5	1.5	1.5
Out. $e^+$ beam div. [mrad]	25.9	27.4	26.8	27.7	28.9	29.2	25.6	27.1
Out. $e^+$ mean energy [MeV]	48.7	46.2	45.6	47.4	45.9	46.1	47.7	46.3
Out. $n/e^-$	0.37	0.31	0.31	0.27	0.29	0.29	0.26	0.30
Out. $\gamma/e^-$	299	310	308	270	307	301	268	301

TABLE 3.2: Summary of the fully-optimised PS full simulation results in different setup configurations.

- increasing the distance between the crystalline radiator and the amorphous target strongly reduces the PEDD, whereas the positron production rate slightly decreases and the positron beam size becomes slightly larger;
- implementing a collimator results in a major reduction of the integral energy deposit;
- implementing a magnetic field does not result in any significant improvement of the PS performance except a slight reduction of the PEDD (only observed with  $D = 2$  m);
- no clear dependence on the configuration is observed in the positron output divergence and mean energy;
- similarly, no major variation is observed in the numbers of neutrons and photons (of any energy) exiting from the target rear face per primary electron, which provide preliminary estimates of the amount of radiation in the environment surrounding the PS.

Starting from the PEDD per incident electron reported in table 3.2 in all the selected configurations, it is possible to calculate the corresponding values per beam pulse in the SI system. According to table 3.1, each pulse consists of two bunches of  $2.1 \times 10^{10}$  electrons, which results in  $4.2 \times 10^{10}$  electrons per pulse. Taking into account a density of  $19.25 \text{ g/cm}^3$  for tungsten leads to a PEDD per pulse of  $13.39 \text{ J/g}$  for the conventional scheme and of a range of values between  $4.47 \text{ J/g}$  ( $D = 60 \text{ cm}$ , no collimator, no field) and  $1.33 \text{ J/g}$  ( $D = 2 \text{ m}$  with collimator) for all the investigated hybrid scheme options. All these values are lower than the safety limit of  $35 \text{ J/g}$  empirically found for tungsten and all the values obtained with the hybrid schemes are significantly lower than the upper limit currently set for the first stage of the FCC- $ee$ ,  $\sim 10.5 \text{ J/g}$ .

# CHAPTER 4

---

## A highly efficient photon converter for the HIKE beamline

Differently from the electromagnetic processes, the hadronic interactions in crystalline matter are not affected by the orientation of the lattice due to their short range. In fact, the nuclear potentials have a spatial extension in the range of the femtometres, at least five orders of magnitude less than the typical distance between neighbouring nuclei in an atomic lattice. As a consequence, the ratio between the radiation length and the nuclear interaction length  $\lambda_I$ , which is the mean free path between two successive inelastic interactions with nuclei [35], is affected by the lattice orientation and becomes smaller the shorter the effective  $X_0$  is.

In particular, the reduction of the  $X_0/\lambda_I$  ratio is maximum in the strong field regime. As already discussed in chapters 1 and 2, the strong field (SF) critical energy is around  $\sim 10$  GeV or slightly more for heavy metals such as tungsten. At this energy scale, the aforementioned effect would prove perfectly suitable to solve a rather critical issue in the design of next-generation neutral kaon experiments, which are of indisputable interest in both the Standard Model precision testing and the search for New Physics.

Experiments on neutral kaon rare decays typically require a low-emittance, high-intensity  $K_L$  beam and a precise control on all the possible background sources in the detector. Given the way in which the  $K_L$  are generated, that is, by primary protons impinging on targets, and the fact that neutral particles cannot be separated from one another by means of magnetic fields,

the beams are contaminated by a high-intensity photon component coming from the primary target. These photons can be forced to convert into  $e^+e^-$  pairs, which in turn can be swept away by a dipole magnet. This conversion takes place in a thick, high- $Z$ , high-density target placed along the kaon beam path.

A standard target is made of amorphous materials, typically lead or tungsten. For the fraction of converted photons to be sufficiently high, the target has to be considerably thick, which also significantly affects the  $K_L$  beam features. On the other hand, an oriented crystalline photon converter would exploit the  $X_0/\lambda_I$  ratio reduction to enhance the photon conversion power with minimum effect on the kaon beam.

This chapter discusses an application of the concept introduced above, in the development of a high-efficiency photon converter for the beamline of the HIKE (High Intensity Kaon Experiments) experiment [165], currently under development at CERN. Particular attention is put on the data collected in 2018 at the CERN SPS on an oriented tungsten sample, analysed by the author and compared to the results of beamtest full simulations.

## 4.1 The HIKE experiment and beamline

HIKE [165] (logo in figure 4.1) is a next-generation experiment aimed at studying kaon rare decays. It is currently under development at the CERN SPS and it is expected to take place starting from the LHC Run 4 (expected from 2029). It continues the long-standing tradition of kaon experiments at CERN started with NA31 [166] (1986–1989), then including NA48 [167] (multiple phases between 1997 and 2004) and, since 2015, NA62 [109, 110], which is currently in operation. In the following sections, the scientific motivations at the foundation of the kaon experimental line and the HIKE requirements are presented.



FIGURE 4.1: Logo of the HIKE experiment. From [165].

### 4.1.1 Physics motivation

Although the Standard Model provides an exceptionally precise theoretical description of most of the interactions between particles measured so far, many experimental observations hint at its inconsistency with some of the latest results in HEP and cosmology [107, 165]. In fact, the SM might be an approximation of a more fundamental theory [165]. It is therefore extremely important and appealing to test the current theory with increasingly precise measurements, with the specific aims of characterising the SM better and looking for new deviations.

Among the currently considered descriptions of New Physics (NP) beyond the SM (BSM), two paradigms stand up [165]:

- the first one assumes that the NP would lie above the SM mass scale and would involve particles that undergo sizeable interactions but are significantly heavier than any currently known particle;
- conversely, the second one is based on the so-called feebly interacting particles (FIPs), i.e., particles within the SM mass range that only undergo very weak interactions – see, e.g., [168].

Not only both these families of models might treat the currently known discrepancies, but they also have the potential to provide explanations for several open questions in particle physics and even in other fields of modern physics, such as the nature of dark matter, the cosmological inflation, the source of neutrino masses and oscillations and the nature of the cosmological constant [165].

Quark-flavour physics proves a powerful tool to explore both the high-mass scale and the FIP domain [165], and strange, B and D meson decays represent an excellent probe to characterise flavour-based interactions [109, 165, 169]. In particular, FIPs could be produced in, e.g., unpredicted kaon rare decays [165].

On the other hand, already known rare kaon decays, such as, e.g., those of the form  $K \rightarrow \pi \nu \bar{\nu}$ , prove interesting as they are very clean (or “golden”) processes [109, 169, 170] that might unveil effects of NP at an energy scale above the limit of present and next-generation colliders [165]. In particular, the intrinsic cleanliness of the  $K^\pm \rightarrow \pi^\pm \nu \bar{\nu}$  and  $K_L \rightarrow \pi^0 \nu \bar{\nu}$  processes results from the following features:

- these processes are semileptonic rather than purely hadronic;
- the required hadronic matrix elements can be extracted, including isospin breaking corrections, from the data on the leading semileptonic  $K^+ \rightarrow \pi^0 e^+ \nu$  decay [94, 169];

- there are no contributions from intermediate photons [94];
- long-distance (i.e., low-energy) contributions and also higher-order electroweak effects are rather small in case of  $K^\pm$  and negligible in case of  $K_L$  [169] – equivalently, it can be stated that, since these processes are flavour-changing neutral currents (FCNCs) and, hence, the hard GIM (Glashow–Iliopoulos–Maiani) mechanism is at work [171], the contribution of the heaviest (i.e., the top) quark dominates, whereas the one of the up quark is always small [109] and the one of the charm quark is small (vanishes) in case of  $K^\pm$  ( $K_L$ ) [109, 171].

Beside the search for NP, the  $K \rightarrow \pi\nu\bar{\nu}$  processes are particularly appealing in

- characterising the top-related elements of the CKM matrix and the unitarity triangle – details can be found, e.g., in [94, 109, 169, 171–173];
- in case of  $K_L$ , investigating the direct (i.e., decay-related)  $CP$  violation – with a  $\lesssim 1\%$  contribution of the indirect (i.e., mixing-related)  $CP$  violation – [169, 174], whereas the charged decay channels are  $CP$ -conserving [169];
- improving the interpretation of the data from the recently observed lepton-flavour-universality-violating phenomena in the B meson sector [94, 175].

As already mentioned, several of the SM precision studies and the searches for NP discussed above can also be performed in the B and D sector. However, kaons can be obtained way more easily than heavier mesons: they are abundantly produced in hadronic inelastic scattering and have a relatively long lifetime, so that high-intensity and low-emittance kaon beams can be produced [165]. Moreover, theoretical predictions in the kaon sector are provided with relatively low uncertainties (1–2%) with respect to those of the B sector ( $\sim 10\%$ ) [169]. Finally, in view of the full picture of quark-flavour physics, the kaon sector proves complementary to that of B and D mesons explored by LHCb [165, 176] and Belle II [165, 177].

Over the past forty years, a series of high-precision kaon experiments (NA31 [166], NA48 [167] and NA62 [109, 110] – all hosted in the ECN3 cavern at the CERN SPS [103]) has been performed at the CERN North Area [165]. This long-standing tradition proved extremely successful: among the numerous results obtained by these experiments, the discovery of direct  $CP$  violation is widely quoted among the major achievements of CERN [165, 174].

The HIKE experiment is expected to continue this fortunate streak starting from LHC Run 4 [165]. It would exploit a kaon beam with an intensity increase by a factor 4–6 with respect to that of NA62 and cutting-edge detector technologies, thus having access to all the main aspects of rare kaon decays and searches accessible via kaon interactions, described above [165]. A particular focus is put on the quest for NP, which the experimental apparatus is designed to undertake both directly, i.e., looking for new particles and interactions, and indirectly, i.e., looking for deviations from the SM predictions in precision measurements [165]. The experiment would have access to a wide range of mass and coupling scales [165]. Moreover, the long decay volume and detector features make HIKE suitable to search for long-lived FIPs [165]. In practice, the HIKE programme is long-termed and consists of three phases, which share a major part of the detectors and infrastructures [165, 178, 179]:

- firstly, after increasing the beam intensity and upgrading some of the detectors currently in operation, a continuation of the  $K^+$  physics programme of NA62 is scheduled during Run 4 – phase 1.
- In phase 2, foreseen during Run 5, the experiment would operate in  $K_L$  mode with minor modifications to the detector layout, and would mainly address the study of several  $K_L$  rare decay channels, especially those involving charged particles in the final state.
- Phase 3, i.e., the so-called KLEVER ( $K_L$  Experiment for VErY Rare events) phase, is focused on the particularly challenging measurement of the  $K_L \rightarrow \pi^0 \nu \bar{\nu}$  branching ratio to  $\sim 20\%$  relative precision<sup>1</sup>. To optimise this measurement, major modifications of the experimental apparatus are foreseen. Some additional topics – mainly the measurement of very rare processes – could be studied in this configuration. KLEVER would run after phase 2 is completed, either before the end of LHC Run 5 or at the beginning of Run 6.

Some periods in beam-dump mode, i.e., dumping the beam upstream with respect to the experimental apparatus and measuring the beam absorber output state, are also foreseen during phases 1 and 2 [165]. Extensive details

---

<sup>1</sup>The KLEVER goal is to achieve a sensitivity of about 60 events at the branching ratio predicted by the SM with a signal-to-noise ratio of 1, which indeed corresponds to a relative uncertainty of about 20% [165]. The experiment would be able to observe a discrepancy with the SM predictions with a significance of  $5\sigma$  if the true branching ratio is more than twice or less than 25% of that of the SM, or of  $3\sigma$  if the true branching ratio is less than half of the SM prediction [165].



on the HIKE physics programme across the different phases can be found in [165].

Currently, the branching ratio of  $K_L \rightarrow \pi^0 \nu \bar{\nu}$  is under study by the KOTO ( $K_0$  at TOkai) experiment at J-PARC (Japan Proton Accelerator Research Complex) [94, 180, 181]. Recently, KOTO has set an upper limit to the value of the branching ratio to  $4.9 \times 10^{-9}$  at a confidence level of 90% [181] and, with the currently foreseen apparatus upgrades, should be able to reduce the 90% confidence level upper limit to the  $10^{-10}$  level by the mid 2020s [94].

However, more significant upgrades are needed in order to actually measure the branching ratio value and, hence, test the limitations of the SM [94]. Indeed, the HIKE experiment would face the challenge of developing the next-generation apparatus needed for the direct measurement of the branching ratio in the KLEVER phase [94, 165].

Moreover, the kaons exploited by the KOTO experiment have a peak momentum of 1.4 GeV/c [181]. On the other hand, the KLEVER kaon beam would have a mean momentum of  $\sim 40$  GeV/c, i.e.,  $\sim 30$  times higher than that of KOTO [94, 165]: the significantly stronger forward boost improves the rejection of background channels such as  $K_L \rightarrow \pi^0 \pi^0$  by facilitating the detection of the photons from the decay  $\pi^0 \rightarrow \gamma \gamma$  in the final state [94].

### 4.1.2 The HIKE experimental setup

Figure 4.2 shows a picture of the ECN3 cavern which currently hosts the NA62 experiment. As already mentioned, the latter is devoted to the study of rare  $K^+$  decays [109, 110]. Details on its experimental apparatus, which would essentially be left unchanged during HIKE phase 1, can be found, e.g., in [109, 110, 165].

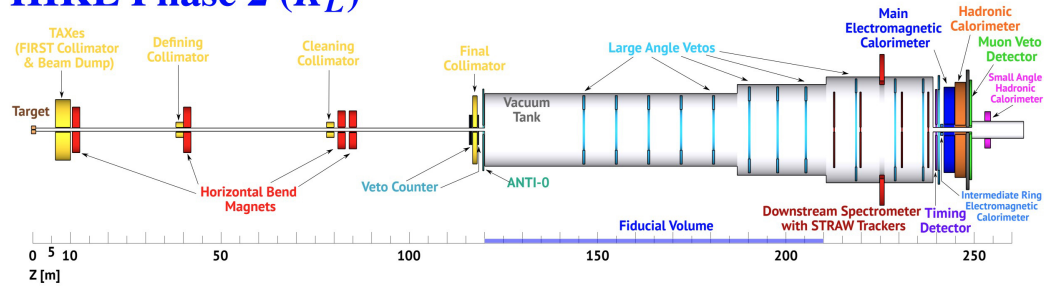
On the other hand, figure 4.3 shows the layout of HIKE phase 2 (top) and KLEVER (bottom) apparatus. It consists of a  $\gtrsim 100$  m long,  $\sim 3$  m  $\varnothing$  vacuum chamber, which serves as a decay tunnel for incident  $K_L$  and is mainly instrumented for [165]:

- the reconstruction of the kinematics of the decays of interest – performed differently, depending on the experiment phase, via the measurement of, e.g., the decay vertices position, the energy of the final photons and  $e^\pm$  and the momentum of all the final charged particles;
- the rejection of the background processes occurring in the beamline and inside the decay tunnel, obtained through highly hermetic veto systems and proper tuning of the beamline and experiment geometric features.



FIGURE 4.2: The ECN3 cavern and the NA62 experiment. The beam enters the cavern from the right. From [182].

### HIKE Phase 2 ( $K_L$ )



### HIKE Phase 3 (KLEVER)

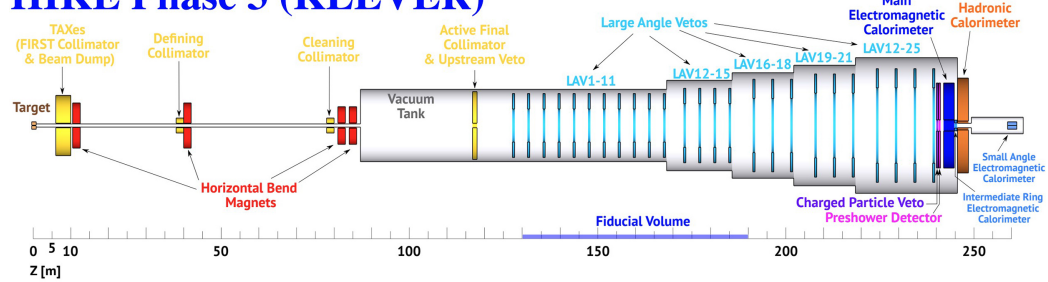


FIGURE 4.3: Layout of the HIKE experiment, phases 2 (*top*) and 3 (KLEVER) (*bottom*). From [165].

In the following sections, the focus is put on HIKE phase 2 and KLEVER, i.e., on the  $K_L$  modes, at which the work presented in this chapter is aimed.

#### 4.1.2.1 The experiment subsystems

The experimental apparatus comprises several subsystems. In the following, a very brief description of the main parts of the experiment and of their tasks is provided. A complete description with extensive details can be found in [165].

#### Hermetic photon and charged-particle veto

One of the main features of the HIKE setup is the highly efficient rejection of background channels with extra photons, such as  $K_L \rightarrow \pi^0 \pi^0 \rightarrow \gamma \gamma \gamma \gamma$ . As discussed in section 4.1.2.2, the effect of this decay channel – as well as of the other purely neutral channel  $\Lambda^0 \rightarrow n \pi^0 \rightarrow n \gamma \gamma$  – can be reduced by properly optimising the  $K_L$  beamline.

The rejection of the remaining fraction of  $K_L \rightarrow \pi^0 \pi^0$  is performed with photon veto detectors [165]. In particular, the whole fiducial volume is surrounded by ring-shaped arrays of lead glass blocks (such as the ones described in section 2.3.1.2, chapter 2), i.e., the so-called Large Angle Veto (LAV), which cover polar angles out to 100 mrad [165]. The LAV rejection efficiency depends on the position of the downstream limit of the fiducial volume with respect to the calorimeters, especially considering the sources of background of interest in the KLEVER configuration: extending the fiducial volume length downstream would increase the signal decay acceptance at the price of a worse background rejection power, therefore a trade-off has to be sought<sup>2</sup> [165].

Since the measurement of the  $K_L \rightarrow \pi^0 \nu \bar{\nu}$  decay proves particularly challenging due to the absence of charged particles and long-lived hadrons in the final state, it is particularly important to extend the acceptance of the photon veto system to small polar angle values in the KLEVER phase [165]. In this regard, a fundamental role is played by the Small Angle Calorimeter (SAC) [165], discussed below and in section 5.4.2 (chapter 5). Moreover, in this phase, events in which charged particles are detected in the dedicated systems – e.g., the scintillating Charged-Particle Veto (CPV) – or identified in any of the other detectors – e.g., the LAV – are rejected [165].

<sup>2</sup>It should be also taken into account that extending the fiducial volume would require an excavation to enlarge the ECN3 cavern, with a major impact on the experiment cost.

### Position-sensing detectors

The HIKE phase 2 apparatus comprises position-sensing scintillating detectors upstream (the Veto Counter – VC – and the ANTIcoincidence-0 – ANTI-0) and downstream with respect to the fiducial volume (the timing detector). These have the purpose of [165]

- providing information on the charged particle trajectories and timing, and
- vetoing the charged particles coming from upstream of the fiducial volume.

Moreover, a magnetic spectrometer instrumented with straw tracking modules is installed downstream with respect to the fiducial volume and upstream with respect to the calorimeters, for the reconstruction of the trajectory and of the momentum of the charged particles in the final state [165].

All the tracking systems would be removed in the KLEVER phase [165]. The vetoing of the upstream charged particles would be performed by other detectors such as the Upstream Veto (UV), i.e., an electromagnetic calorimeter positioned before the fiducial volume front [165].

### Calorimeters

Large-acceptance forward electromagnetic calorimeters with high energy resolution, time resolution and granularity prove essential in all the measurements of the HIKE physics programme on  $K_L$ , since they [165]:

- measure the energy of forward photons and are part of the photon veto;
- contribute to the charged-particle identification (thus providing additional background suppression) and measure the  $e^\pm$  energy;
- provide information on the event timing;
- contribute to locate the vertices of the decays involving photons – which, in KLEVER, is performed in synergy with the information provided by a PreShower Detector (PSD), i.e., a  $0.5 X_0$  converter followed by two tracking planes placed upstream with respect to the calorimeters.

The acceptance of the decay tunnel rear side is well covered by three different electromagnetic calorimeters [165]. The outermost and largest fraction of

the area is covered by the Main Electromagnetic Calorimeter (MEC), whose acceptance extends down to an inner bore of radius 12–15 cm [165]. The long-lived NA48 liquid-krypton (LKr) calorimeter [183, 184], which is currently used by NA62 and might be exploited by HIKE phase 1, would then be replaced by a new shashlik calorimeter made of alternating layers of lead and scintillator [165] – standard polystyrene proves sufficiently luminous, fast, and radiation resistant [165]; however, novel media such as nanocomposite scintillators are currently being considered [185, 186].

The region of intermediate polar angles is covered by the Intermediate-Ring Calorimeter (IRC) [165]. It consists of a shashlik calorimeter developed with a similar technology as that of the MEC but significantly smaller, with an inner bore of radius  $\sim 60$  cm placed at a transverse offset with respect to the centre and designed to precisely match the primary beam path: since the beams exploited in phase 2 and in KLEVER are slightly different from each other, two different detectors might be required for the two phases [165].

The innermost part of the apparatus rear end is covered by the Small Angle Calorimeter [165]. The SAC design proves one of the most challenging aspects of the experiment, because of the extremely high rates of neutrons and photons in the beam (see section 4.1.2.2): indeed, in the KLEVER configuration, they result in  $\sim 40$  MHz of photons of energy  $> 5$  GeV,  $\sim 440$  MHz of neutrons and  $\sim 130$  MHz of  $K_L$  impinging on this detector [165]. Since even higher rates are expected in phase 2, the SAC might not to be included in the experimental setup of this stage, of which this detector is not a crucial element [165].

The main purpose of the SAC is to detect photons from  $K_L$  decays that would otherwise escape via the downstream beam exit very efficiently, while remaining relatively transparent to the very high flux of neutral hadrons in the beam; in this way, small-angle background photons can be rejected efficiently while the experiment is not blinded by the random vetoes from the hadrons [165].

The work presented in this chapter has the goal of significantly reducing the photon component of the beam with minor effect on the emittance of the  $K_L$ , which proves particularly beneficial in the SAC design [165]. At the same time, R&D studies are currently being performed to develop a high-performance calorimeter that would meet the demanding needs of the experiment [165]. One of the most appealing options in the development of the SAC consists in exploiting the coherent effects that occur in axially aligned scintillating inorganic crystals to design a compact and highly granular homogeneous calorimeter [165]. The latter is the topic of the work presented in chapter 5, in which further details on the specific implementation of the SAC in the HIKE setup are discussed.

Finally, a system of hadronic calorimeters and (in phase 2) MUon Veto detectors (MUVs) is needed to perform the pion-muon identification and separation and to reject background from hadron interactions [165]. As for the electromagnetic calorimeters, the high beam intensity involved requires good timing performance [165]. Moreover, since the so-called catastrophically interacting muons, i.e., highly interacting muons which deposit all or a large fraction of their energy in the calorimeters, represent a major concern, some level of granularity in both the longitudinal and transverse direction is needed in order to distinguish the shapes of the showers generated by muons and by pions [165].

#### 4.1.2.2 The beamline

As the HIKE (High Intensity Kaon Experiments) acronym suggests, high-intensity beams are required to measure the rare processes in the physics programme with the expected uncertainty [165]. In particular, kaon beams with an intensity between 4 and 6 times that of the  $K^+$  beam currently exploited in ECN3 by NA62 are required [165, 178, 179]. Moreover, in the  $K_L$  stages, the beamline features play a major role in the control of some background channels, especially in case of the KLEVER configuration [165]. The HIKE  $K_L$  beamline is designed starting from the scheme of the neutral kaon beamlines already exploited by the NA31 and NA48 experiments [102, 165]. Firstly, the 400 GeV/ $c$  protons extracted from the SPS impinge on a beryllium<sup>3</sup> target, from which both charged and neutral particles of all sorts emerge [165]. The charged particles can be swept away by bending magnets and dumped in dump collimators (or TAXes – Target Attenuators for eXperimental areas), whereas the neutral particles –  $K_L$ , neutrons and photons, either directly from the target or generated by the  $\pi^0 \rightarrow \gamma\gamma$  decay – propagate in straight lines along the beam path [165].

The angle between the primary proton beam and the output component selected for the experiment is a key parameter in determining the overall  $K_L$  beam performance [165]. A smaller production angle increases the kaon flux and momentum, which facilitates the task of vetoing some upstream background channels with extra photons, e.g.,  $K_L \rightarrow \pi^0\pi^0 \rightarrow \gamma\gamma\gamma\gamma$  [165]. On the other hand, with higher-momentum kaons impinging on the experimental apparatus, less  $K_L$  and more  $\Lambda^0$  decay inside the fiducial volume [165]; similarly, the ratio between the numbers of  $K_L$  and neutrons in the apparatus

<sup>3</sup>Higher- $Z$  materials such as copper or tungsten are also considered for the primary target, as they would result in a reduction of the photon background; however, changing the target material would strongly affect its design, adding to the device cost and complexity [165, 187].

acceptance would be lower [94]. As the  $\Lambda^0 \rightarrow n\pi^0 \rightarrow n\gamma\gamma$  decay constitutes a dangerous background channel in the  $K_L \rightarrow \pi^0\nu\bar{\nu}$  measurement, a large angle should be chosen for the KLEVER phase, whereas a production angle as small as possible is preferred for phase 2, whose measurements are not affected by the background from  $\Lambda^0$  decays and neutron interactions [165]. A production angle of 2.4 mrad (8 mrad) seems likely in case of phase 2 (KLEVER) [165, 178, 187].

As shown in the sketches in figure 4.3, a series of collimators and magnets placed at the selected angle downstream with respect to the target cleans the beam from the charged components and defines the beam acceptance [165]. The latter should be set to  $\leq 400 \mu\text{rad}$ , which is necessary to measure the  $\pi^0$  transverse momentum with sufficient precision to reject background from the  $K_L \rightarrow \pi^0\pi^0$  decays [165]. The average kaon beam momentum should be 79 GeV/c (40 GeV/c) in phase 2 (KLEVER), which result in an average momentum of 46 GeV/c (27 GeV/c) for the  $K_L$  that decay inside the fiducial volume [165].

A high- $Z$  photon converter is positioned in the aperture at the center of the TAXes, along the beam path, and converts most of the high-energy photons ( $\gtrsim 5$  GeV) into charged pairs and lower-energy photons, thus reducing their flux by about two orders of magnitude [165]. In particular, beamline simulations performed with the FLUKA (FLUktuierende KAskade) MC tool [188] show that the rate of photons of energy  $> 1$  GeV ( $> 5$  GeV) is reduced from 27.9 GHz (14.6 GHz) to 6.1 GHz (0.47 GHz) by a 9.4  $X_0$  amorphous tungsten converter [165]. The effect of this converter on the neutron and  $K_L$  rates is negligible [165]. Overall, considering the KLEVER beamline, the combined effect of the photon converter and of the collimation system results in  $\sim 53$  MHz of photons of energy  $> 5$  GeV (corresponding to the SAC threshold for KLEVER),  $\sim 440$  MHz of neutrons and  $\sim 140$  MHz of  $K_L$  inside the fiducial volume [94, 165].

However, the  $K_L$  emittance is affected by the interaction with the converter: in tungsten, 9.4  $X_0$  correspond to  $\sim 58\%$  of a nuclear collision length ( $\lambda_C \sim 5.72$  cm) and  $\sim 33\%$  of a nuclear interaction length ( $\lambda_I \sim 9.95$  cm); therefore,  $\sim 35\%$  of the  $K_L$  in the beam interact in the converter and are scattered out of the nominal beam path [165]. As discussed in section 4.1.2.3, using an oriented crystal as photon converter would allow to reduce its thickness, and hence its hadronic interactions, while attaining the same conversion rate as in an amorphous converter [82, 165, 178].

#### 4.1.2.3 Coherent effects and hadrons: the oriented photon converter

As discussed in section 1.4 (chapter 1), high-energy photons impinging on a crystal within an angle of the order of  $\Theta_0$  with respect to a lattice axis experience higher probability of conversion into an  $e^+e^-$  pair; together with the enhancement of bremsstrahlung radiation emission, this corresponds to a reduction of the effective radiation length value with respect to the amorphous case. In other words, high-energy photons interacting in a crystal require a lower thickness to start an electromagnetic shower than in a randomly oriented target of the same material. As a consequence, a compact photon converter can be developed, which would attain the same conversion rate as the one implemented in the beamline simulations discussed above, while being thinner.

The hadronic interactions are not affected by the crystalline lattice orientation, as the nuclear potentials are short-ranged and only extend inside the atomic nuclei, i.e., at the scale of the fm [82, 165]. Therefore, in crystals, the values of  $\lambda_C$  and  $\lambda_I$  are independent on the lattice orientation. Equivalently, the ratio between, e.g.,  $X_0$  and  $\lambda_I$  is smaller at higher energy and in case of better beam-to-lattice alignment, i.e., when the SF effects are stronger. This makes the design of a photon converter with a good conversion rate and at the same time with minimum effect on the kaon beam emittance feasible.

This concept was already exploited by the NA48 experiment [72, 189]<sup>4</sup>. After testing different high- $Z$  crystalline samples [72], a 2.96 mm  $\sim 0.98 X_0$  iridium ( $Z = 77$ ,  $\rho = 22.42$  g/cm<sup>3</sup> [13]) crystal was eventually implemented in the experimental apparatus [189]. In this case, the crystal featured a very high crystalline quality and a thickness right below the standard radiation length value for iridium: when on axis, the effective thickness of the sample was slightly above 1  $X_0$  [189], which maximised the number of photons converted into charged pairs while keeping the generation of secondary photons as low as possible.

The HIKE experiment demands a larger angular acceptance for the coherent enhancement of the electromagnetic processes ( $\sim 400$   $\mu$ rad) and a much thicker converter (of several  $X_0$ , in order to exploit not only the conversion of the primary photon, but also the generation of secondary photons at lower energy which don't represent a dangerous component of the background and can easily be stopped inside the converter itself or by the beamline collimators).

---

<sup>4</sup>It is worth mentioning that the NA48 experiment also used a bent silicon crystal to generate simultaneous  $K_L$  and  $K_S$  beams – see [190].



Moreover, tungsten costs significantly less than iridium [159], therefore much thicker samples can be purchased at a very small fraction of the cost of the iridium ones. Commercial tungsten crystals are also considered: despite their rather poor crystalline quality, as opposed to research samples, which are much more expensive and difficult to replace, they compensate a general weakening of the coherent effect intensity with the possibility of developing thicker samples and with a larger angular acceptance of the effects, resulting from the large mosaicity values.

## 4.2 Pair production measurements in oriented tungsten

In 2018, a beamtest was performed on the H2 beamline at CERN [103] to characterise the coherent effects that occur in the interaction between high-energy photons (up to  $\sim 100$  GeV) and a commercial tungsten crystal in different orientations around the [111] axis. Details on the photon beam generation and on the experimental setup are provided in section 2.3.4 (chapter 2), whereas the crystal and the measurements are described below. All the results presented in the following sections have been recently published in [82].

### 4.2.1 The sample

This study was performed on a commercial tungsten sample, grown by Princeton Scientific [191]. It is approximately cubic, with a side (and hence a thickness) of  $1\text{ cm} \sim 2.85 X_0$ . All the measurements described below were performed around the [111] axis, which features the strongest crystalline potential and thus the largest angular acceptance – i.e.  $\Theta_0 = 1.736$  mrad; see table 2.2 (chapter 2). A mosaicity of  $\sim 3$  mrad was estimated from the combination of results of surface HRXRD and MC simulations; it corresponds to  $\sim 1.73 \Theta_0$  – particularly high, which reflects the commercial-borne nature of the sample.

When performing measurements with incident photons, it is particularly important for the sample to have a large transverse section, as reconstructing the input photon trajectories by means of a tracking system is impossible. In case of this beamtest, the crystal side was slightly smaller than the beam spot size at its longitudinal position – see its profile reconstructed with the electron beam directly impinging on it in figure 4.4 left.

However, it was observed that assuming that the bremsstrahlung photons originating from the copper target follow approximately the same trajectory as the parent electrons provides a good criterion to determine whether the photons hit the sample front side. Indeed, an estimate of the angular aperture of the secondary photon beam with respect to the primary one is given by the inverse of the Lorentz factor,  $1/\gamma$ : the latter is equal to  $\sim 4.26 \mu\text{rad}$  ( $\sim 25.55 \mu\text{rad}$ ) at 120 GeV (20 GeV), which corresponds to a transverse shift of  $\sim 73 \mu\text{m}$  ( $437 \mu\text{m}$ ) at the crystal – i.e.,  $< 1\%$  ( $\sim 4\%$ ) of the crystal edge. For comparison, the contribution of the MCS in the downstream silicon telescope module is  $\sim 6.11 \mu\text{rad}$  ( $\sim 36.69 \mu\text{rad}$ ). The transverse profile of the sample obtained in photon mode by propagating the electron trajectories from upstream with respect to the target is shown in figure 4.4 right.

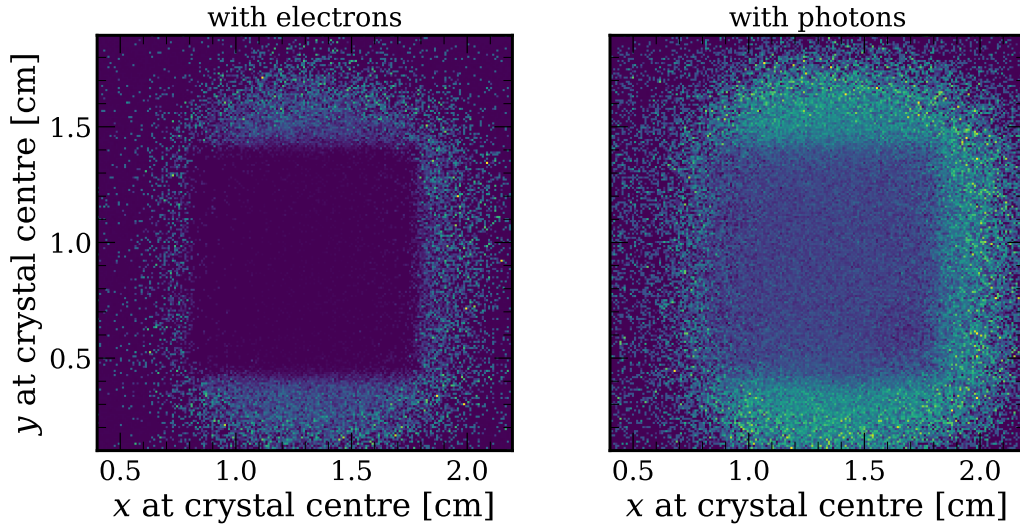


FIGURE 4.4: Profile of the W [111] sample probed during the KLEVER 2018 beamtest, obtained (*left*) with the electron beam directly impinging on the crystal and (*right*) with the photon beam, assuming that the photon propagation trajectory is that of the parent electron. They are highlighted by selecting the tracks which correspond to high output charged multiplicity.

#### 4.2.2 Analysis and simulation strategy and results

In the following, the physics results of the beamtest are discussed. The main focus is the study of the correlations, as a function of the sample lattice alignment with respect to the photon beam axis, between three different quantities, i.e., ideally,

- the total energy of the sample output particles;
- the energy of the incident photon;
- the number of charged particles at the sample exit.

The raw information that acts as a starting point for the study of the first two items consists of the measurements of the energy deposited in the  $\gamma$ -CAL and in the  $e$ -CAL channels. The spectra obtained after calibrating the detectors (see appendix A) and correcting for biases that affected the response of some of the channels (see appendix C) are shown in figure 4.5. The total output energy corresponds to the energy measured by the  $\gamma$ -CAL (figure 4.5 top), plus a component of missing energy due to the interactions with the crystalline sample and to the finite acceptance of the lead glass block. Similarly, the PH in the downstream multiplicity counter (S4 in figure 2.20, chapter 2) is expected to be proportional to the number of charged particles at the crystal output stage.

The primary photon energy can be obtained only indirectly. Starting from the total energy measured by the  $e$ -CAL, i.e.

$$E_{e\text{-CAL}} = \sum_{j=0}^4 E_{e\text{-CAL}}^j \quad (4.1)$$

where  $E_{e\text{-CAL}}^j$  are the energy values measured by the  $e$ -CAL single channels (figure 4.5 bottom), it is possible to compute the photon energy reconstructed by the tagging system,  $E_{\gamma\text{-tagged}}$ , by means of equation 2.4 (chapter 2). Furthermore, the missing energy in the photon branch can be evaluated as

$$E_{\gamma\text{-missing}} = E_{\gamma\text{-tagged}} - E_{\gamma\text{-CAL}} \quad .$$

It has to be noted that  $E_{\gamma\text{-missing}}$  results from the joint contribution of energy absorption or dispersion by the crystalline sample and limited acceptance of the  $\gamma$ -CAL. As discussed in section 4.2.2.1, the latter,  $E_{\text{bkg}}$ , can be estimated with the data collected in photon mode and without the crystal along the photon path. Thus,

$$E_{\gamma\text{-abs/disp}} = E_{\gamma\text{-missing}} - E_{\text{bkg}} \quad (4.2)$$

provides an estimate of the energy actually absorbed or dispersed by the tungsten sample.

The analysis software has been developed starting from the tools published in [161, 162]. Moreover, full simulations of the beamtest have been developed with Geant4. For the simil-amorphous case, standard Geant4 version 10.5

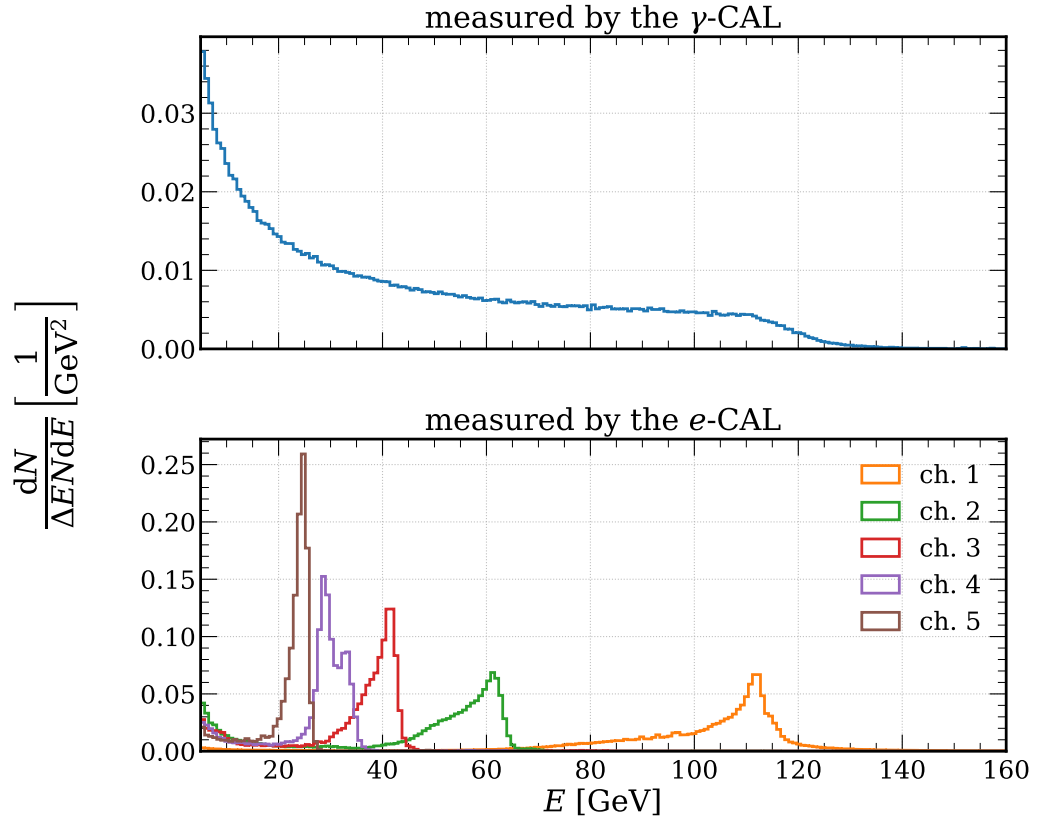


FIGURE 4.5: Energy spectra of the KLEVER 2018 calorimeters, measured in photon mode without the crystalline sample along the beam path by (*top*) the  $\gamma$ -CAL and (*bottom*) the  $e$ -CAL single channels.

has been used, with the FTFP\_BERT physics list [141]. On the other hand, given the fact that the sample thickness is  $\gg X_0$ , the software described in section 2.4.2 (chapter 2) proved the best option for the development of the on-axis simulation.

#### 4.2.2.1 Energy absorption

For each of the runs acquired in photon mode, both with the crystal in different orientations and without the crystal, the profile plot of the correlation between  $E_{\gamma\text{-CAL}}$  and  $E_{\gamma\text{-tagged}}$  is computed. This correlation is shown, for instance, for the random case in figure 4.6. In the following, only the events with  $E_{\gamma\text{-tagged}}$  between about 20 GeV and 100 GeV are selected: the subset of events with  $E_{\gamma\text{-tagged}} \lesssim 20$  GeV is excluded because of the effect

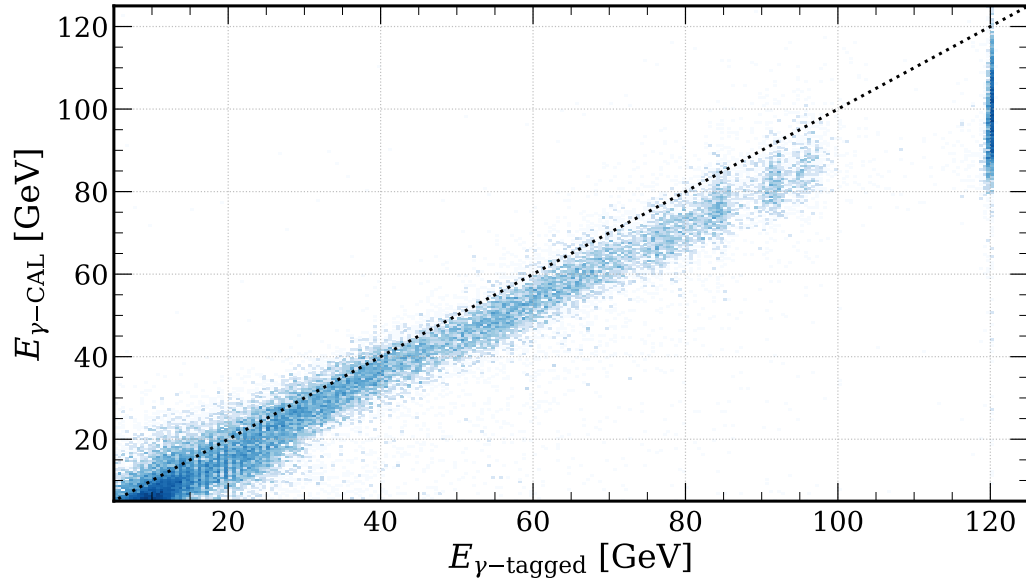


FIGURE 4.6:  $E_{\gamma\text{-CAL}}$  as a function of  $E_{\gamma\text{-tagged}}$  with the crystalline sample in random alignment.

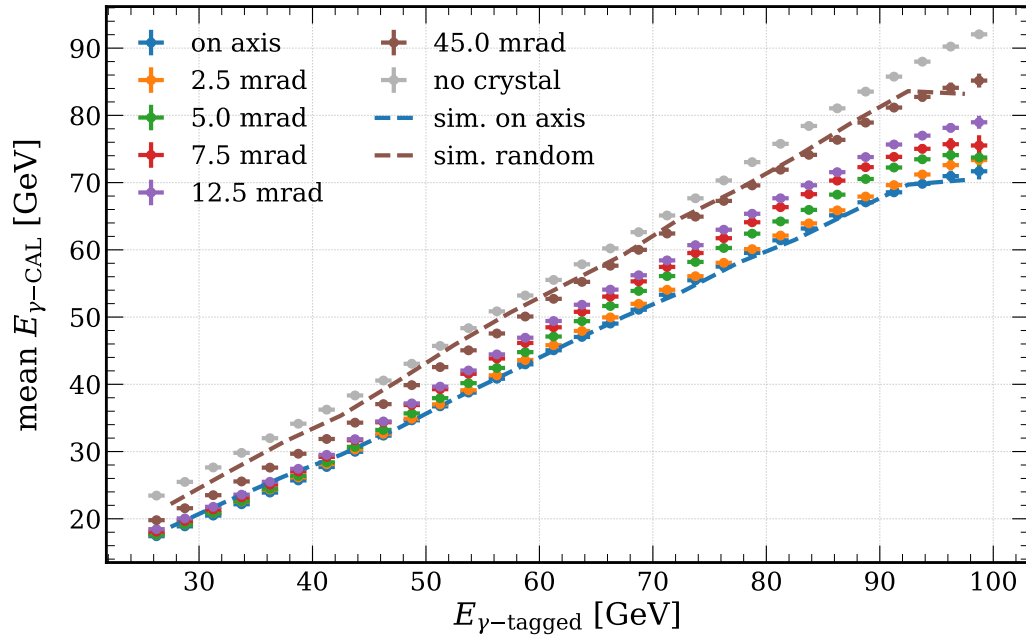


FIGURE 4.7: Profile plot of  $E_{\gamma\text{-CAL}}$  as a function of  $E_{\gamma\text{-tagged}}$  at different misalignment angles. Background data, i.e., with no crystal along the photon path, are also shown (grey). The points (dashed lines) represent the experimental data (simulation results).

of the  $e$ -CAL channel 1 response biases described in appendix C, whereas  $E_{\gamma\text{-tagged}} \sim 100$  GeV marks the tagging system acceptance limit. The resulting profile plots are shown in figure 4.7. The errors are computed taking into account the statistical uncertainty, the resolution of the detectors and the effect of the bias correction algorithms. Moreover, table 4.1 shows the values of  $E_{\gamma\text{-missing}}$  for three incident photon energies ( $\sim 39$  GeV,  $\sim 69$  GeV, and  $\sim 94$  GeV) and for different angles of incidence.

$\psi$ [mrad]	$E_{\gamma\text{-missing}}$ [GeV]		
	at 38.75 GeV	at 68.75 GeV	at 93.75 GeV
sim., on axis	11.78	17.78	23.76
exp., on axis	13.05 (0.75)	17.66 (0.81)	23.93 (0.96)
2.5	12.60 (0.75)	16.78 (0.80)	22.54 (0.93)
5.0	12.38 (0.75)	14.86 (0.80)	20.28 (0.94)
7.5	11.72 (0.76)	13.44 (0.80)	18.72 (0.98)
12.5	11.32 (0.76)	12.53 (0.80)	16.76 (0.91)
exp., random	9.07 (0.80)	8.75 (0.84)	11.00 (1.00)
sim., random	6.32	7.79	10.56
exp., no crystal	4.62 (0.75)	6.12 (0.76)	5.76 (0.79)

TABLE 4.1:  $E_{\gamma\text{-missing}}$  at different misalignment angles and for different values of  $E_{\gamma\text{-tagged}}$ . Errors on the experimental results are reported in parentheses.

Clearly,  $E_{\gamma\text{-missing}}$  is strongly enhanced when the beam is incident along the crystal axis with respect to the random case. The grey curve in figure 4.7 and the corresponding line in the table (“exp., no crystal”) represent an estimate of  $E_{\text{bkg}}$ , and can therefore be used to compute  $E_{\gamma\text{-abs/disp}}$  with equation 4.2. For a  $\sim 94$  GeV photon perfectly parallel to the axis,  $E_{\gamma\text{-abs/disp}} \sim 18$  GeV, as opposed to  $\sim 5$  GeV obtained for random orientation. Indeed, the amount of energy absorbed or dispersed by the crystal is seen to increase by about a factor of three. As clearly visible in figure 4.7, the maximum absorption power is stable up to about 2.5 mrad from the crystal axis and decreases as the angle grows. Nevertheless, at  $\sim 94$  GeV, the fraction of missing energy is still 1.5 times that for the random orientation even at an angle of incidence of 12.5 mrad. As expected, as the initial photon energy increases, the effective  $X_0$  decreases, and hence the amount of energy absorbed inside the crystal increases, so that the fraction of the initial photon energy absorbed is approximately constant over the whole photon energy range. The extremely broad angular range over which the macroscopic character of the enhancement in energy absorption is preserved can be ascribed to both the strength of the [111] axis and the high mosaicity of the sample.

The slight saturation of both the measured and the simulated trends for  $E_{\gamma\text{-tagged}} \gtrsim 90$  GeV has been carefully investigated. Figure 4.8 shows the true total energy of the crystal output particles as a function of the true energy of the incident photon, reconstructed by the simulations. The most notable difference between the measured and the true energy values is that the latter are independent on the detector acceptance. Indeed, the absence of a saturation for primary energies up to 120 GeV indicates that the saturation observed in figure 4.7 is due to the limited acceptance of the  $e$ -CAL.

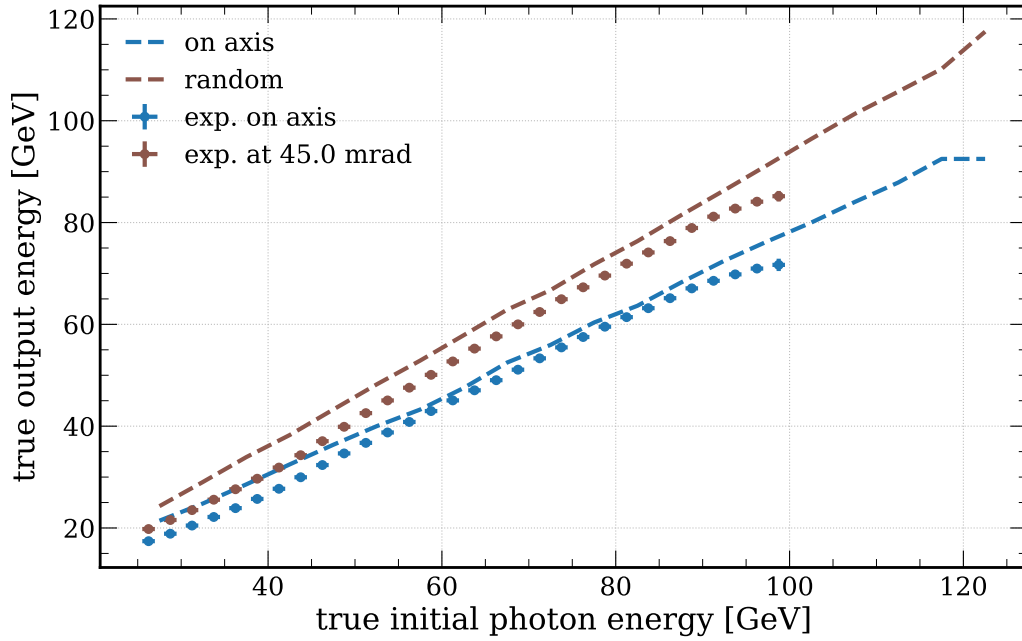


FIGURE 4.8: Profile plot of the total energy of all the particles at the crystal output as a function of the initial photon energy, resulting from the simulations of the random (brown) and on-axis (blue) configurations. The points represent the corresponding experimental data, added for comparison.

#### 4.2.2.2 Shower acceleration and charged multiplicity enhancement

The results presented in section 4.2.2.1 demonstrate the faster electromagnetic shower development due to the axial SF, with a resulting enhancement of the number of secondary particles. Each of these charged secondaries deposits considerably more energy inside the sample, resulting in a significant increase of total absorbed energy. This increase in the secondary production was also measured with the S4 scintillating multiplicity counter. A similar

approach as that discussed above for the  $\gamma$ -CAL data was adopted: the correlation between the signal of the output multiplicity counter and  $E_{\gamma\text{-tagged}}$  was studied in all the different run configurations (see, e.g., the random case in figure 4.9), and the corresponding profile plots are shown in figure 4.10.

As expected, the enhancement grows for decreasing misalignment angle and with the primary photon energy, i.e., at higher initial  $\chi$ . The corresponding ratios between measured values at different angles of incidence and in amorphous-like orientation range from 130–160% at  $\sim 30$  GeV, depending on the incoming photon angle, to  $\gtrsim 230\%$  at 100 GeV when on axis; indeed, even when off-axis by 12.5 mrad, the enhancement ratio is  $\sim 170\%$  for 100 GeV photons.

Moreover, figure 4.11 shows the true number of charged secondaries emerging from the sample rear side as a function of the true primary energy, as scored by the simulations. Again, the apparent saturation of the charged multiplicity enhancement for  $E_{\gamma\text{-tagged}} \gtrsim 90$  GeV is due to the  $e$ -CAL acceptance limit.

### 4.2.3 Final comments

The results of the 2018 beamtest demonstrate that an oriented crystal like the tested one would prove an excellent photon converter for the HIKE neu-

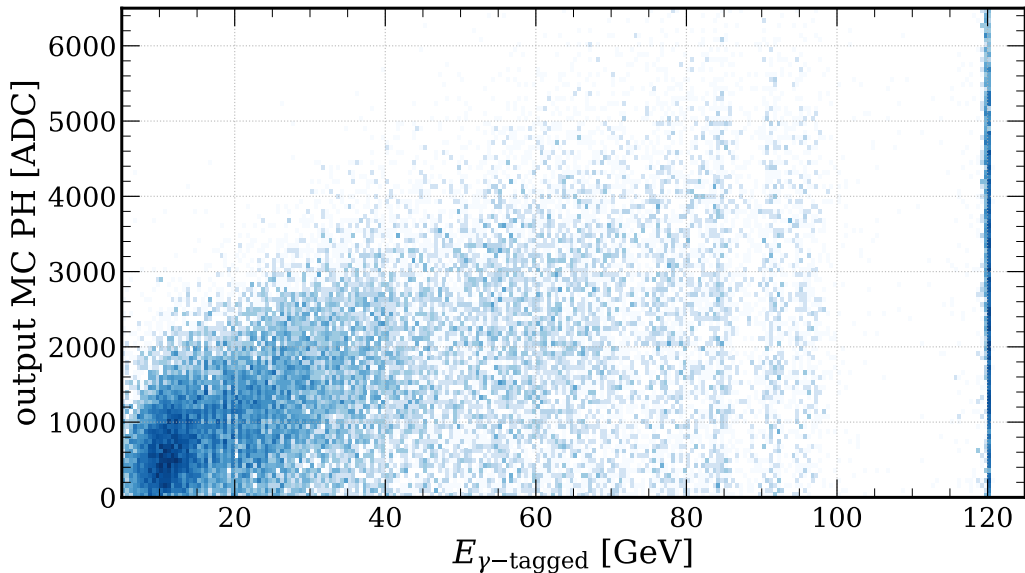


FIGURE 4.9: PH in the output MC as a function of  $E_{\gamma\text{-tagged}}$  with the crystalline sample in random alignment.



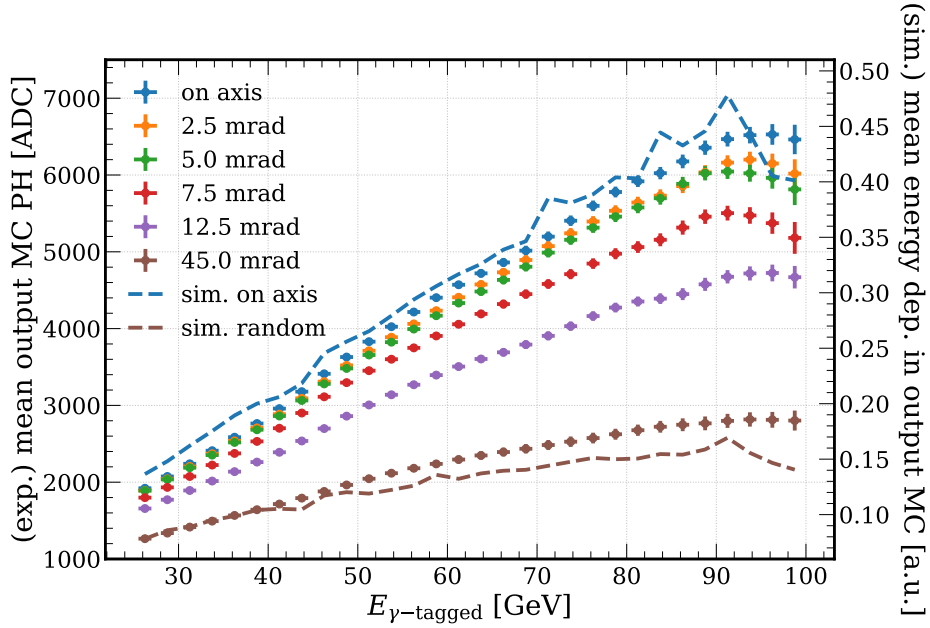


FIGURE 4.10: Profile plot of the signal in the output MC as a function of  $E_{\gamma\text{-tagged}}$  at different misalignment angles. Background data, i.e., with no crystal along the photon path, are also shown (grey). The points (dashed lines) represent the experimental data (simulation results).

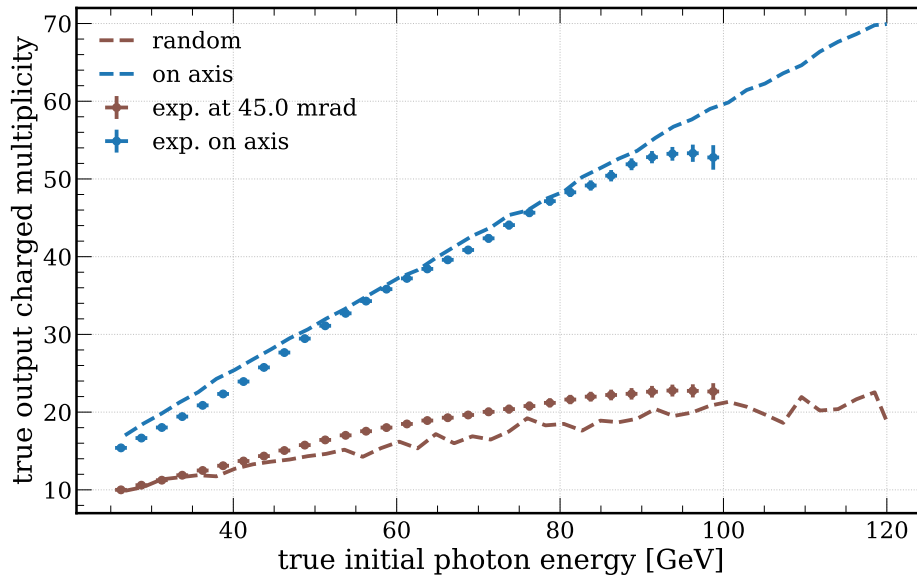


FIGURE 4.11: Profile plot of the charged-particle multiplicity at the crystal output as a function of the initial photon energy, resulting from the simulations of the random (brown) and on-axis (blue) configurations. The points represent the corresponding experimental data, added for comparison.

tral hadron beamline, thanks to the enhanced photon absorption and dispersion at large angle (section 4.2.2.1) and conversion into  $e^+e^-$  pairs (section 4.2.2.2). Moreover, it has been shown that a commercial crystal with rather poor crystalline quality – its mosaicity being  $\sim 3$  mrad – can rival higher-quality tungsten samples, like the much thinner one studied in [72] – a  $0.9 X_0$  thick sample with a mosaicity of  $\sim 300$  mrad, i.e., only 10% of the one tested in 2018 –, in terms of conversion enhancement.

At the same time, it has been demonstrated that the good photon absorption, dispersion and conversion performance reflects an acceleration of the shower development in the axial SF. The same simulation software that has proved able to reproduce the beamtest results with excellent agreement has been exploited to study the development of the shower initiated by perfectly parallel electron and photon pencil beams at different energies inside an ideal tungsten block in both the amorphous-like and axial (along the [111] axis) configurations. The fraction of primary energy deposited per radiation length is shown in figure 4.12 as a function of the penetration depth inside the block, in several different beam configurations. The block is a  $20 \times 20 \times 20$  cm<sup>3</sup> tungsten crystal, i.e., thick and wide enough to contain all the shower particles.

When on axis, the maxima of all of the curves are located approximately at the same depth, thus demonstrating that in case of axially oriented tungsten the position of the shower maximum is nearly independent on the initial energy between a few GeV and  $\sim 1$  TeV. For a 100 GeV photon impinging on the axially oriented crystal, the energy deposit at a depth of 1 cm  $\sim 2.85 X_0$  is about three times higher than in random orientation and corresponds to that of an amorphous target of length  $\sim 1.47$  cm  $\sim 4.19 X_0$ . Moreover, the same simulation code can be used to obtain an estimate of the radiation length effectively experienced by the primary photon: computing the fraction of incident 100 GeV photons that cross 1 cm of axially oriented tungsten without converting into  $e^+e^-$  pairs and using equation 1.36 (chapter 1), a value of 1.05 mm was obtained, i.e., 3.3 times the standard value ( $X_0 = 3.504$  mm).

#### 4.2.3.1 A different application: compact sampling calorimeters

The shower development acceleration in heavy crystalline metals might prove interesting for many applications in HEP other than compact photon converters. For instance, it can be exploited to improve sampling electromagnetic calorimeters.

A sampling calorimeter consists of several high- $Z$ , high-density passive layers, which force incoming electromagnetic particles to shower, interleaved with

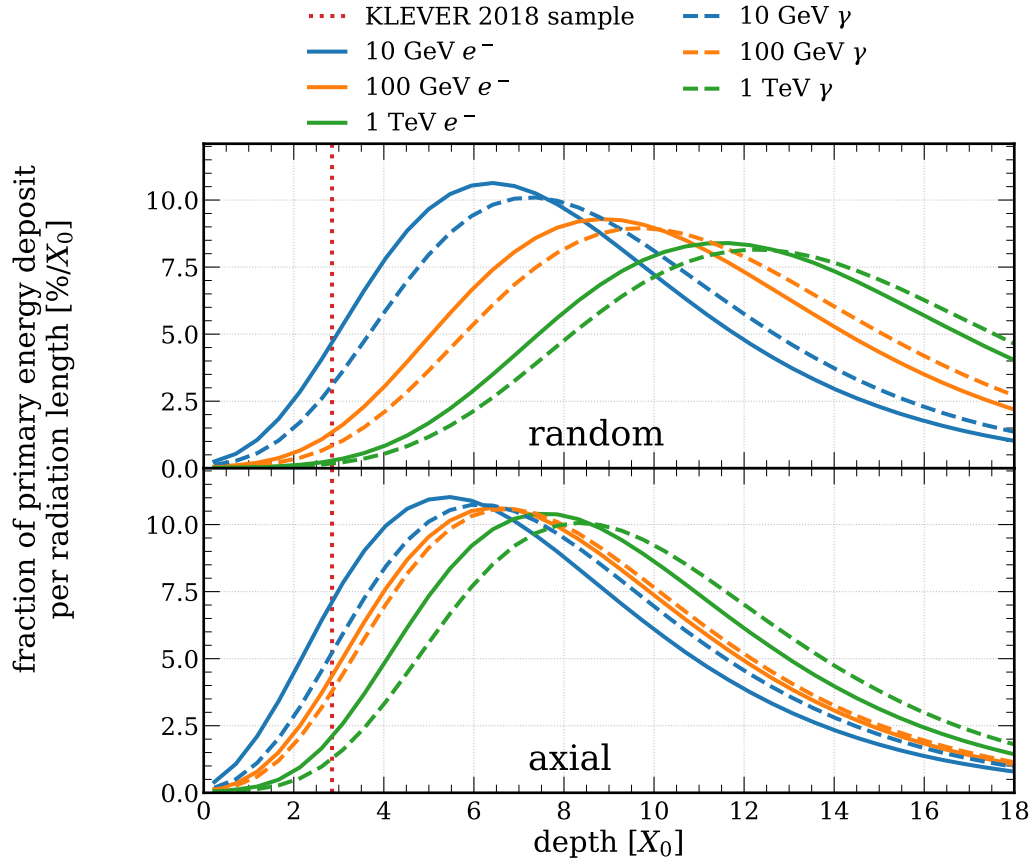


FIGURE 4.12: Fraction of energy deposit by the electromagnetic shower initiated by electrons (solid lines) and photons (dashed lines) per radiation length as a function of the penetration depth in (*top*) amorphous tungsten and (*bottom*) crystalline tungsten oriented along the [111] axis. The thickness of the sample under study at the 2018 KLEVER beamtest is superimposed (red dotted line).

active layers, typically made of plastic scintillator; in each of the latter, a signal proportional to the number of secondary particles crossing the scintillating layer is generated [35]. The total energy deposited in the calorimeter by an incident particle is proportional to the sum of all the ionisation tracks due to the charged particles in the shower, which in turn is proportional to their number [35].

The use of, e.g., oriented tungsten absorber layers instead of amorphous ones would allow for a reduction of the thickness of the passive part of the detector. Overall, as for homogeneous calorimeters (discussed in detail in chapter 5),

a sampling calorimeter could be developed with the same performance as the current state of the art but more compact, especially for applications at extremely high energies.

Furthermore, one of the key parameters in the definition of the performance of a sampling calorimeter is the so-called sampling fraction [35],

$$f_{\text{samp}} = \frac{E_{\text{MIP}}^{\text{act}}}{E_{\text{MIP}}^{\text{act}} + E_{\text{MIP}}^{\text{abs}}} \quad ,$$

where  $E_{\text{MIP}}^{\text{act}}$  and  $E_{\text{MIP}}^{\text{abs}}$  are the energies deposited by an incident MIP in the active and passive parts of the detector respectively. Indeed, the energy deposit by ionisation in a crystal should not be influenced by the strong crystalline field, as it should only be proportional to the length of the ionising particle track inside the material. As a consequence, reducing the thickness of the passive part should correspond to an increase of  $f_{\text{samp}}$ : this would result in an increase of the signal from the active volume and, hence, in a reduction of the noise term in the energy resolution (discussed in detail in section 5.1.1, chapter 5) with respect to a calorimeter with the same thickness but with thicker, randomly aligned absorber layers [35]. The stochastic term in the resolution would be reduced as well [192].



# CHAPTER 5

---

## Towards ultra-compact homogeneous calorimeters

As future particle physics experiments are conceived, both to better understand the Standard Model and to look for evidence of the existence of New Physics, increasingly demanding constraints are put on their design. The design of detectors that match the stringent requirements in terms of, e.g., precision, speed and compactness proves particularly challenging and, at the same time, is of paramount importance in marking the feasibility of these new experiments.

Electromagnetic calorimeters often prove to be the key elements in high-energy physics and astroparticle physics experiments. Despite their generally excellent performance, current state-of-the-art calorimeters are often very big and heavy. Several next-generation experiments would greatly benefit from a reduction of the electromagnetic calorimeter thickness, while attaining the currently achievable response performance. At the same time, it is particularly appealing for a calorimeter not only to measure the incident particle energy with an energy resolution as good as possible, but also to provide information on the incident particle type.

In this chapter, the possibility of developing compact calorimeters based on inorganic scintillators with excellent particle identification capabilities by properly orienting the crystalline active volume is discussed. The first part of the chapter provides a brief description of the working principles of calorimetry and of the properties of lead tungstate, a crystalline scintillator

of common use. The second part of the chapter presents the results obtained in the context of this thesis work from the data collected in several studies performed, since 2016, on oriented lead tungstate, from the standpoint of radiation emission, scintillation light emission and energy deposit. Both the full simulations of the beamtests and the analysis of the experimental and simulated data were performed by the author. At the end of the chapter, particular attention is put on the possible application of the observed effects to the development of a working detector and on its integration in physics cases of interest.

## 5.1 Homogeneous calorimetry

In homogeneous calorimeters, the electromagnetic shower initiated by the incident  $e^\pm$  or photon fully develops in the active medium, in which the whole energy of the primary particle is thus deposited and measured [35]. Among the available choices of detector material, inorganic scintillators prove the most appealing option in HEP, as they feature high density and  $Z$  and their signal in response to the passage of the ionising particles is easily read out [35].

Inorganic scintillators are crystalline materials, and the light emission is related to their crystalline structure [30, 35]. The energy deposited by the ionising particles incident in the medium excites the bulk electrons, thus promoting them from the valence band to the conduction band [35]. The subsequent electron de-excitation results in the emission of visible light [35]. The performance of inorganic scintillators as active media heavily depends on the features of the scintillation mechanism, which in turn depend on the chosen material [35]. In order to improve them – by, e.g., increasing the light yield, changing the light spectrum shape or speeding up the de-excitation process – crystals can be doped with a small amount of other elements, which results in the addition of impurities that create new activation bands in the gap between the valence and the conduction band [35].

In general, the main advantage of homogeneous calorimeters over sampling calorimeters, briefly discussed in section 4.2.3.1 (chapter 4), is a significantly better energy resolution [35]. However, the development of uniform-response arrays of scintillating crystals and the fine segmentation of the calorimeter volume (especially in the longitudinal direction) are typically challenging [35]. Moreover, inorganic scintillators often suffer from slow response [35] and ionisation-induced radiation damage [30], which poses limitations to the development of detectors for experiments which operate at high beam intensity. The calorimeter performances are discussed in the following sections, with

particular attention to the values attained by scintillating crystal calorimeters.

### 5.1.1 Energy resolution

In an ideal homogeneous calorimeter, considering infinite size in both the transverse and longitudinal directions, perfect uniformity and with no response degradation due to instrumental effects (non-hermetic coverage, distortions induced by the readout electronic chain, etcetera), the intrinsic energy resolution is due to the fluctuation of the total length of the tracks of the ionising particles in the shower [35]. Since the shower development is a merely stochastic process, the absolute uncertainty on the total track length is proportional to its square root, which results in a relative uncertainty on the measured energy of [35]

$$\frac{\sigma_E}{E} \propto \frac{\sqrt{E}}{E} = \frac{1}{\sqrt{E}} \quad . \quad (5.1)$$

The energy resolution of a real calorimeter can be modelled as [35]

$$\frac{\sigma_E}{E} = \sqrt{\left(\frac{a_{\text{calo}}}{\sqrt{E}}\right)^2 + \left(\frac{b_{\text{calo}}}{E}\right)^2 + c_{\text{calo}}^2} \quad , \quad (5.2)$$

where the first, second and third term under square root are called stochastic, noise and constant term respectively. Descriptions of these three terms are provided below, and a sample resolution curve is shown in figure 5.1.

Furthermore, typically, the calorimeters integrated in HEP experiments must provide a large dynamic range – typically of several orders of magnitude [35, 122]. As a consequence, a linear response and a good resolution over a wide range are requirements of primary importance in the development of a calorimeter [35].

#### Stochastic term

The stochastic term encompasses the fluctuations in the shower development inside the detector volume [35]. In homogeneous calorimeters, these fluctuations are particularly small, because the shower entirely develops inside the active volume and, hence, the initial energy is usually almost entirely measured [35]. The stochastic term corresponds to the intrinsic energy resolution (equation 5.1) weighted by a factor  $\ll 1$  – i.e., the so-called Fano factor [193] – and, hence, is very small: typical values of  $a_{\text{calo}}$  are of the order of a few



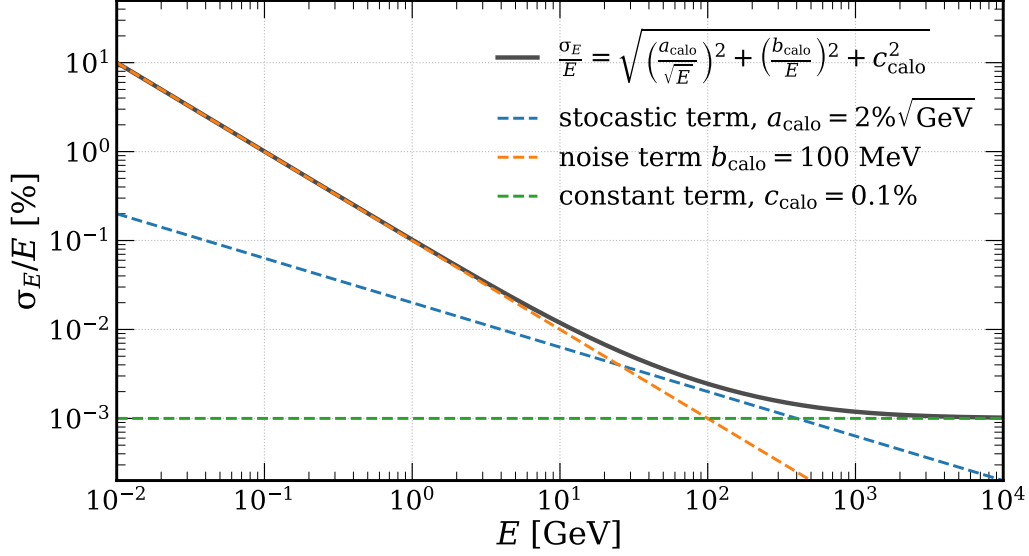


FIGURE 5.1: Example of an energy resolution curve (solid grey curve); the single terms are shown as dashed curves.

$\% \sqrt{\text{GeV}}$  [35]. For comparison, the latter is about one order of magnitude less than in state-of-the-art sampling calorimeters [35].

### Noise term

The noise term encompasses the contribution of the electronic noise and depends on the detector technique [35]. In particular, scintillation (and Cherenkov) detectors can achieve small levels of noise by properly choosing the photodetection system [35].

This term might have a major effect on the total resolution value, especially in the sub-GeV regime [35], as it is clear from figure 5.1. Therefore, it is typically required in the design of the detector electronic chain that  $b_{\text{calo}}$  is smaller than  $\sim 100$  GeV per readout channel [35].

### Constant term and other geometric effects

The constant term models the biases resulting from instrumental effects that cause non-uniformities in the detector response as a function of the primary particle impact position but not of its energy [35]. In particular, these non-uniformities can be due to irregular shapes of the detector elements, to imperfections in the mechanical structure (e.g., in case of scintillating calorimeters, in the single-channel positioning and in the coupling of the active volume to

the photodetectors), to age-, temperature- and radiation-related damage, etcetera [35]. These contributions affect the precision on the energy measurement especially when the incident particle hit points are distributed over a large area of the calorimeter acceptance [35].

As it is clear from figure 5.1, the constant term becomes dominant at very high energies [35]. Therefore, it becomes of particular concern as new experiments, which would operate in the multi-TeV regime, are developed for future accelerators [35]. This requires that a special care is taken in the technical design of next-generation calorimeters – especially of the homogeneous ones, in order not to compromise the excellent resolution they generally have due to their significantly small stochastic term [35]. In general,  $c_{\text{calo}}$  should be kept  $\lesssim 1\%$  [35].

At the same time, other geometrical features of the calorimeter should be kept under control at the stage of its design and integration in the experimental setup, i.e., for instance, transverse and lateral leakage and losses in hermeticity resulting from the presence of gaps between channels that align with the nominal trajectory of the incident particles [35]. These effects differ from those affecting the constant term because they determine a loss of information rather than its degradation. Similarly as with the contributions to  $c_{\text{calo}}$ , the presence of these imperfections should be avoided as much as possible in the development of a homogeneous calorimeter [35], since they introduce additional fluctuations to the measured energy values and, hence, determine an increase of the stochastic term.

### 5.1.2 Segmentation, spatial and angular resolution

One of the main challenges in the design of a scintillating homogeneous calorimeters is its segmentation [35]. Although, in general, crystal calorimeters feature some transverse granularity at the level of a few cm (worse than, e.g., noble-liquid calorimeters [35]), longitudinal segmentation is not implemented since the crystals are grown as high-aspect ratio parallelepipeds that are typically oriented with the long sides parallel to the nominal direction of the incident particles. This is due to many reasons:

- transverse cuts in the crystals (with enough room in between to host the mechanical holders and the photodetectors) might compromise the hermeticity of the detector active volume and result in a decrease of the energy resolution;
- reading the scintillation light out from the central channels would prove particularly challenging from the standpoint of the design of the photodetection system, which must be as compact as possible and must

not be affected by the high number of secondaries created as the shower develops;

- it would require a major machining work on the crystals, which are rather fragile, and might result in a degradation of their optical properties.

As a consequence, scintillating homogeneous calorimeters are typically sensitive to the impact position of the incident particles, albeit with rather poor spatial resolution, but not to the incident angle [194]. The latter is obtained with at least two samplings of the transverse profile of the shower at different depths inside the calorimeter volume [194]. This information completes the electron tracking performed by the tracking system and allows to reconstruct the direction of propagation of the photons, which often proves particularly important in the reconstruction of the interaction vertices [35, 194].

### 5.1.3 Particle identification

The spatial measurements mentioned above provide useful information to distinguish between different particle types [35]. The basic idea is that the energy deposited in the electromagnetic calorimeter by different particles is distributed differently in the detector volume [194]:

- the shower by  $e^\pm$  and photons is initiated very close to the calorimeter front and is peaked after a few  $X_0$ ;
- hadrons and hadron jets start a hadronic shower, thus depositing (part of) their initial energy after  $\sim 1 \lambda_I \gg 1 X_0$  and down to the rear end of the detector, and in a wider transverse area;
- charged hadrons leave a ionisation track upstream with respect to the hadronic shower start;
- muons do not initiate a shower and leave a ionisation track along the whole calorimeter thickness.

Moreover, a fine transverse granularity and the sensitivity to the incident particle angle in the upstream part of the calorimeter (the first  $\sim 5 X_0$ ) allow to resolve multiple  $e^\pm$  and photons impinging on the detector at the same time and small distance to one another [35]. It is particularly important to distinguish between single-photon tracks and couples of photons resulting from the decays of the  $\pi^0$ , which constitute a ubiquitous source of background in the study of interactions involving hadrons [35, 194].

Examples of other particle identification tools that might be exploited in electromagnetic calorimeters are the pulse shape discrimination [195] and the Cherenkov-scintillation light dual readout [196]. Moreover, the performance of all the aforementioned particle identification criteria could be further improved by combining the information provided by the calorimeter with that of the other detectors in the experimental setup [35, 197].

## 5.2 Scintillation in PWO

Among the eligible materials in the design of a homogeneous scintillation calorimeter, lead tungstate ( $\text{PbWO}_4$  or PWO) proves one of the best options among the fastest and densest inorganic scintillators [99]. The main physical and crystalline properties of PWO are discussed in section 2.1.2 (chapter 2), whereas its properties as a scintillating medium and their dependence on the choice of doping are described below.

In the last three decades, PWO-based calorimeters have been considered in the design of several experiments in a wide range of energies and geometries. As of today, two of the best performing PWO-based detectors are the CMS (Compact Muon Solenoid) ECAL (Electromagnetic CALorimeter) [122], operational since 2008 (figure 5.2), and the  $\bar{\text{P}}\text{ANDA}$  (antiProton ANnihilation at DArmstadt) EMC (ElectroMagnetic Calorimeter) [198], currently under development. PWO is also exploited by the ALICE experiment at CERN [199]. Moreover, it was considered for the electromagnetic calorimeter of the (then terminated) BTeV experiment at Fermilab [200] and is currently being considered in the preliminary design of the detectors for, e.g., the Future Circular Collider and the Electron Ion Collider [201].

The main properties of the scintillation mechanism of PWO are shown in table 5.1. First-generation PWO, or PWO-I, features good timing performance thanks to the strong thermal quenching [198, 204]. In particular, two separate light components are observed at a wavelength of about 420 nm, i.e., in the blue, with a decay time of  $\sim 10$  ns [30, 201] and  $\sim 30$  ns [30] for the faster and slower component respectively – or even slightly less, according to, e.g., [99, 198, 201], which quote an overall decay constant of 6–6.5 ns.

The blue scintillation band is the dominant one [198, 201]; on the other hand, the spectrum is rather broad and encompasses other colours of the visible spectrum [99, 204]. Overall, the scintillation spectrum of PWO is well matched to the photodetection efficiency of many photodetectors of common use [204]. The (two, owing to the birefringent nature of PWO [99, 204]) high refractive indexes,  $n_o = 2.242$  and  $n_e = 2.169$  [99], result in an additional, very prompt light component from Cherenkov emission [201].

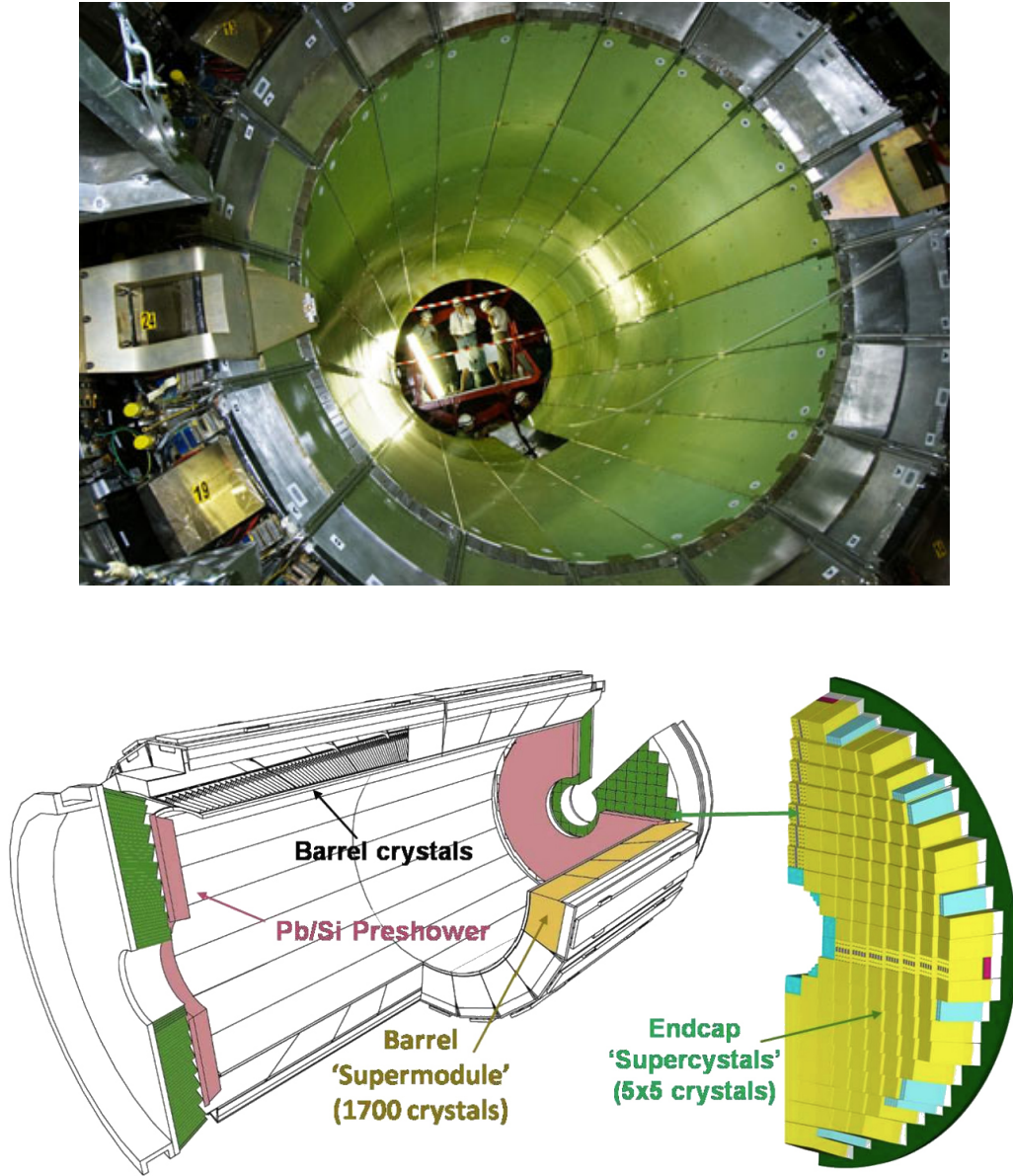


FIGURE 5.2: Picture (*top*) and scheme (*bottom*) of the CMS ECAL. From [202] and [203] respectively.

	PWO-I	PWO-II	PWO-UF
$\rho$ [g/cm <sup>3</sup> ]	8.28 [30]	8.28 [198]	8.27 [201]
Scintillation max. [nm]	420 [30]	420 [198]	420 [201]
LY [ph. $e^-$ /MeV]	8–12 [205]	17–22 [205]	7 [201]
LY rel. to NaI [%]	0.3 [30]	0.6 [198]	about 0.2
$\tau_{\text{decay}}$ [ns]	10–30 [30, 205] 6.5 [198]	10–30 [30, 205] 6.5 [198]	0.64 [201]
$-d\text{LY}/dT$ [%/°C]	2.5 [30]	3 [205]	about 0.4 [201]
$dk$ [1/m]	1.5 [205]	1 [205]	0.3 [201]

TABLE 5.1: Properties of the scintillation mechanism in different generations of lead tungstate.

Furthermore, differently from many other inorganic scintillators, PWO is radiation-tolerant<sup>1</sup> and non-hygroscopic [30, 99, 204].

On the other hand, PWO-I features a comparatively low light yield (LY) [30, 204] – only 0.077% (0.3%) that of NaI(Tl) (sodium iodide doped with thallium) considering the faster (slower) blue component [30]. Moreover, the light yield is temperature-dependent [99, 204]: an approximately linear dependence on the laboratory temperature with a slope of  $-1.8\%/K$  between 250 K and 300 K ( $\sim -2.5\%/^{\circ}\text{C}$  at room temperature) is quoted in [99] ([30, 198]).

In general, lattice doping at the growth stage has been performed since the first studies on PWO in order to attain better light yield, reduced light absorption, increased radiation hardness and better uniformity of the scintillation parameters [204]. Indeed, in recent years, the scintillating performance of PWO have been further improved with respect to the values discussed above by perfecting the doping techniques – details can be found, e.g., in [198, 201, 205–207] and in the following sections.

### 5.2.1 PWO-II

Originally, the search for an improvement of the PWO light yield has been driven by the need for a high energy resolution at the  $\lesssim 10$  GeV scale, which is of interest for experiments such as  $\overline{\text{PANDA}}$  [198, 206]. This led to the development of second-generation PWO, or PWO-II [205].

The increase of light output in PWO-II with respect to PWO-I is obtained with an improved structural perfection and with a better control on the

<sup>1</sup>However, it has to be noted that minor radiation-related issues such as afterglow, reduction of the optical transmission and slight modifications to the spectrum shape are occasionally observed [99, 206].

concentration of lanthanum and yttrium ions in the doping procedure [205]. Indeed, lanthanum and yttrium are typically exploited in the production of PWO-I as well, owing to the fact that their presence in the lattice suppresses point structure defects which slow down the scintillation mechanism [198, 201]. However, the significant performance enhancement in PWO-II is attained by keeping the ion concentration at  $\lesssim 50$  ppm and under strict control [198, 205], whereas typical values in PWO-I are highly fluctuating around  $\sim 100$  ppm [205].

As shown in table 5.1, PWO-II features approximately twice the light yield of PWO-I, and the same light spectrum shape [198, 205]. The optical transmission is also the same between the two generations [99, 206], as well as the decay times [198, 205] – although very recent studies show slightly shorter emission times, as shown in figure 5.3 left [201]. Furthermore, PWO-II features better radiation tolerance, which is shown, e.g., by the lower value of the radiation-induced absorption coefficient,  $dk$  [205, 208]. On the other hand, the light yield features a stronger dependence on the temperature ( $T$ ) than PWO-I; as a consequence, the light output can be further enhanced by cooling the crystals down to  $\lesssim 0^\circ\text{C}$  [198, 205].

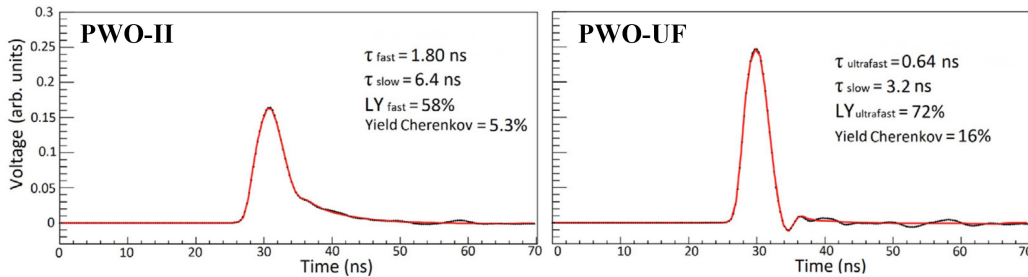


FIGURE 5.3: Scintillation pulses from 2 mm thick PWO-II (*left*) and PWO-UF (*right*) samples. From [201].

### 5.2.2 PWO-UF

The current demand for extremely fast detectors for next-generation, high-intensity HEP experiments drives the development of faster scintillators [201]. In particular, recent studies on the luminescence of PWO highlighted the presence of very fast (“ultrafast” or UF) scintillation components with sub-ns decay times [201]. High-precision doping techniques – i.e., increasing the concentration of lanthanum and yttrium to  $\sim 1500$  ppm and simultaneously solving the charge compensation problem showing up at a high number of dopant ions that replace the lead ions – allow to enhance these light com-

ponents and hence to obtain an overall  $\tau_{\text{decay}} \sim 640$  ps [201]. The timing performance can be seen in figure 5.3 right: the fraction of light in the fastest component is significantly higher than in PWO-II and even the slower components are more prompt. Moreover, the overlap between the scintillation leading edge and the Cherenkov pulse is bigger [201].

As shown in table 5.1, these excellent timing features are obtained at the price of a reduction of the light yield, whereas the shape of the emission spectrum is approximately the same as that of previous-generation PWO [201].

Although the overall light output dependence on the temperature is weaker than, e.g., PWO-II, the ratio between the yield of the ultrafast component and that of the slow component significantly drops as  $T$  decreases, and the slow part dominates below  $\sim 0^\circ\text{C}$  [201]. The radiation hardness is very good [201]. Moreover, interestingly, a slightly lower density value (by  $\sim 0.1\%$ ) with respect to standard PWO is obtained, which might result from the high-concentrations involved in the doping procedure [201].

### 5.3 Oriented detectors: preliminary studies with electrons

Despite the extensive use that has been made of inorganic scintillators in high-energy physics in the last decades, their crystalline nature and, in turn, the modification of their features that occur under particular orientations have always been ignored in the detector design [50].

Nevertheless, the reduction of the radiation length that occurs in the particle rest frame when the strong field (SF) regime (section 1.4.4, chapter 1) is attained could be exploited to develop innovative calorimeters based on oriented crystalline blocks, featuring a more compact design than the current state of the art while rivaling it in terms of the energy resolution [60]. Moreover, the reduction of the  $X_0/\lambda_1$  ratio with respect to the case of amorphous media, discussed in chapter 4, could prove useful in the design of a calorimeter that is relatively transparent to hadrons or, in synergy with a fine segmentation, provides highly efficient photon-hadron discrimination [165].

In recent years, the concept of an oriented crystal-based calorimeter has drawn the attention of part of the HEP community. In particular, this configuration proves appealing for applications with a well-defined and narrow angular spectrum. This interest has driven the experimental investigation presented in this chapter, which is focused on the characterisation of the coherent effects occurring in oriented PWO in the SF regime, especially from



the standpoint of the acceleration of the shower development and, in turn, of the enhancement of the scintillation light emission. As anticipated, several tests have been performed since 2016; however, the total data analysis and simulations have been performed in the context of this thesis work. In particular, the analysis has been performed with the software tools published in [161, 162].

### 5.3.1 The samples under test

Several different samples have been selected and tested, whose features are summarised in table 5.2. During the years, thicker and larger samples have been probed. The first measurements were performed on a  $0.45 X_0$  thick [001] strip with a transverse area of  $2 \times 55 \text{ mm}^2$  (profile in figure 5.4), produced by MolTech (Molecular Technology GmbH, Berlin, Germany) [209]. It has a low surface mosaicity,  $\sim 100 \text{ } \mu\text{rad}$ , measured via hard  $X$ -ray diffraction on the ESRF ID11 beamline [210]. Measurements of the axial radiation enhancement were performed on this sample with electrons (and positrons [120]) at different energies – in both the SF ( $\chi \sim 4.63$ ) and the sub-SF ( $\chi \sim 0.22$ ) regime – with the experimental setup described in section 2.3.3 (chapter 2). Moreover, the on-axis enhancement of the scintillation light was observed for the first time in this crystal [100, 211].

In 2021, two samples were probed:

- a  $1 X_0$  thick  $\langle 100 \rangle$  PWO-II block with a transverse area of  $\sim 30 \times 30 \text{ mm}^2$  and a surface mosaicity of  $\sim 250 \text{ mrad}$ , produced by the Institute for Nuclear Problems of the Belarusian State University (INP BSU) [135];

<b>Thickness [<math>X_0</math>]</b>	0.45	$\sim 1$	$\sim 2$	4.6
<b>Thickness [mm]</b>	4	9	18	41
<b>Transv. size [mm<sup>2</sup>]</b>	$2 \times 55$	$\sim 30 \times 30$	$9 \times 27$	$\sim 30 \times 30$
<b>Axis</b>	001	100	001	100
<b>Generation</b>	I	II	I	I
<b>Surface mosaicity [<math>\mu\text{rad}</math>]</b>	$\sim 100$	$\sim 250$	$\sim 350$ (hor.) $\sim 550$ (ver.)	$\sim 250$
<b>Tested on CERN H2/H4</b>	2016-2018	2021	2021	2022
<b>Tested on DESY T21</b>	2019	2019	no	no

TABLE 5.2: Features of the PWO samples probed on the SPS H2 beamline.

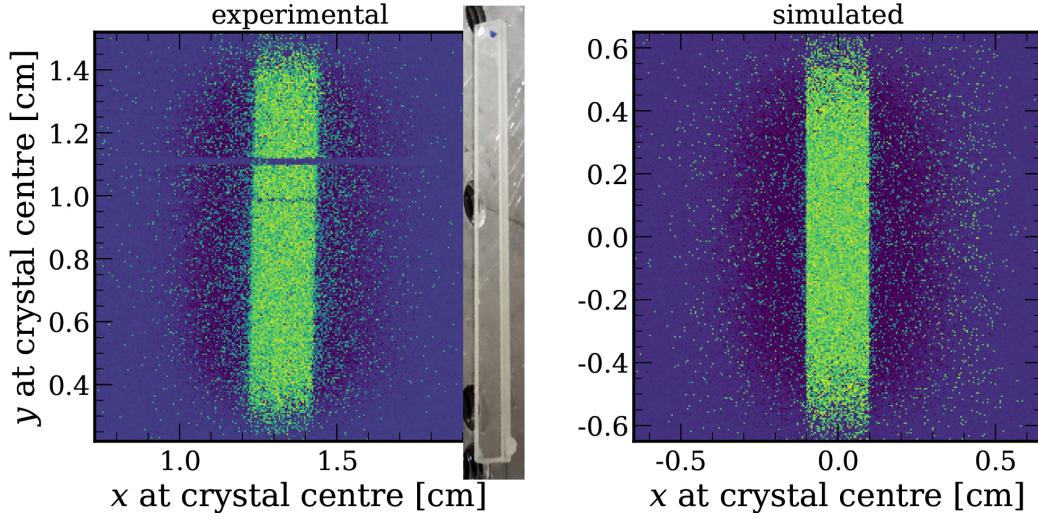


FIGURE 5.4: PWO [001]  $0.45 X_0$  sample probed at CERN. These plots show the data collected in 2018 (*left*) and the corresponding simulation (*right*). In the experimental (simulated) plot the crystal profile is highlighted by selecting the tracks which correspond to high PH in the SiPM (high energy deposit in the strip). A picture of the sample is superimposed for comparison.

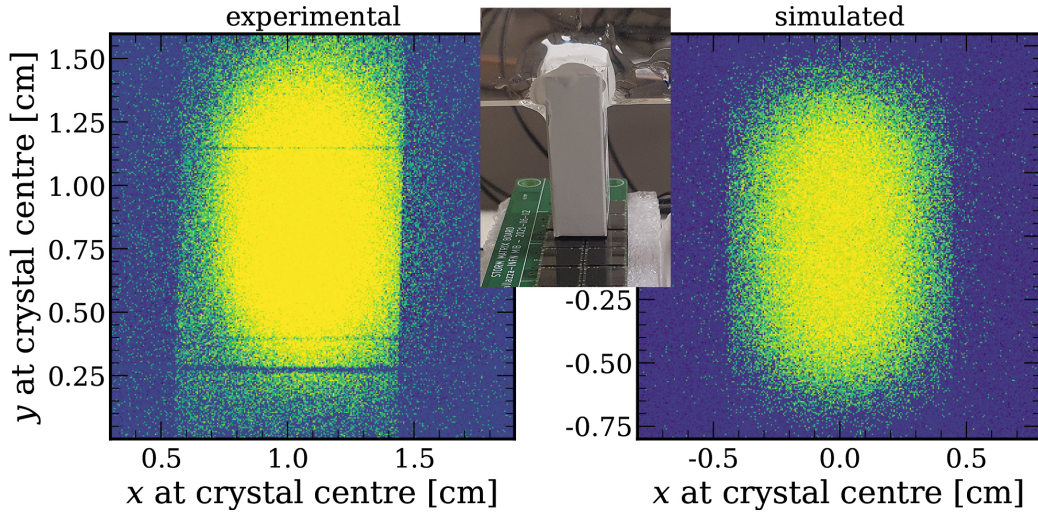


FIGURE 5.5: PWO [001]  $2 X_0$  sample probed at CERN, observed in the experimental data (*left*) and in the corresponding simulation (*right*). In the experimental (simulated) plot the crystal profile is highlighted by selecting the tracks which correspond to high PH in the SiPM (high energy deposit in the block). A picture of the sample is superimposed for comparison.

- a  $2 X_0$  thick [001] PWO-I block with a transverse area of  $\sim 9 \times 27 \text{ mm}^2$  (profile in figure 5.5) and a surface mosaicity of  $\sim 350 \text{ mrad}$  ( $\sim 550 \text{ mrad}$ ) in the horizontal (vertical) plane, produced by MolTech.

Measurements of radiation and scintillation spectra as a function of the misalignment angle were performed on both these samples with 120 GeV electrons ( $\chi \sim 5.12$  and  $4.63$  respectively) on the CERN H2 beamline [103]. The  $2 X_0$  sample was also probed at 100 GeV, whereas the  $1 X_0$  was also tested at DESY [101] with a 5.6 GeV electron beam.

Since 2022, the setup described in section 2.3.5 (chapter 2) is employed, in order to measure the energy deposited in multi- $X_0$  samples during the electromagnetic shower development. In 2022, two identical  $4.6 X_0$  thick  $\langle 100 \rangle$  PWO-I blocks were probed. They have a transverse area of  $\sim 30 \times 30 \text{ mm}^2$  and a surface mosaicity of  $\sim 250 \text{ } \mu\text{rad}$ , measured via HRXRD in the INFN Ferrara laboratory. They have been machined from a single, 15 cm thick spare crystal of the CMS ECAL. All the results related to  $4.6 X_0$  thick PWO presented in the following have been obtained with one of these samples.

### 5.3.1.1 Face polishing for optical coupling

After the crystal growing and machining into the required dimensions, in order to perform scintillation measurements (see section 5.3.1.2), it is necessary to polish the sample faces that have to be coupled to the photodetectors. Figure 5.6 shows two identical  $\sim 30 \times 30 \times 9 \text{ mm}^3$  samples installed on a tunable-weight holder instrumented to measure thickness variations with an error of  $\sim 1 \text{ } \mu\text{m}$ ; the samples are franked to the holder with wax. It is clear from the figure that the selected faces are opaque, with a roughness at the level of hundreds of  $\mu\text{m}$ .

The holder is placed on a lapping surface, i.e., a plate which rotates at a constant speed and forces the holder itself into a circular motion, thus guaranteeing a uniform lapping of the sample surface that is in contact with it. The lapping rate can be set by properly tuning the plate rotation speed, choosing its material (e.g., soft iron or ceramic) and adding an abrasive (e.g. aluminium powder or colloidal silica); multiple stages at different rates might be necessary, in order to optimise the polishing time while avoiding excessive abrasion of the surface and the creation of scratches that worsen the overall optical transparency.

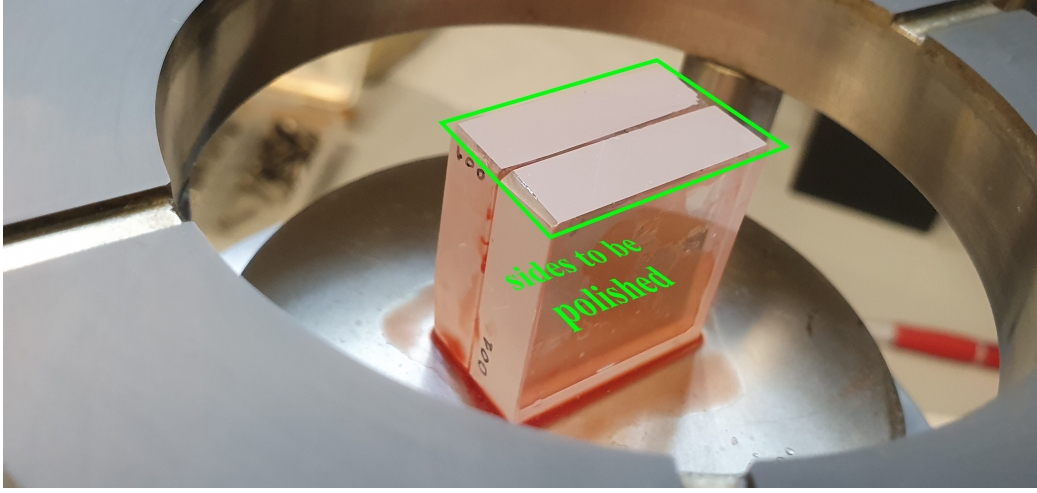


FIGURE 5.6: Setup for the polishing of side faces of the  $1 X_0$  PWO samples to be coupled to the photodetectors.

#### 5.3.1.2 Scintillation light readout

Since 2018<sup>2</sup>, all the studies performed at CERN on PWO samples have been completed by measurements of the scintillation light output. This required the development of a dedicated photodetection system. Several different systems have been developed and tested, which, as the samples under study have become bigger along the years, have scaled accordingly in terms of active surface and number of channels.

All the systems are based on silicon photomultipliers (SiPMs). A SiPM [212] consists of an array of Geiger-mode avalanche photodiodes (G-APDs) [213, 214] connected to a common output, each with its own quenching resistor [133]. The absorption of a photon triggers a Geiger avalanche and, hence, the flow of an inverse current between the diode sides; the latter results in a voltage drop across the quenching resistor, which in turn reduces the bias across the diode to a value lower than the breakdown limit [133].

Although the response of each G-APD is digital with respect to the photon detection, the common output signal is pseudo-analog, i.e., proportional to the number of pixels that are on and thus to the number of detected photons [133]. Indeed, the light intensity  $I_\gamma$  is related to the number of pixels turned on,  $n_{\text{G-APD}}^{\text{on}}$ , via [215]

<sup>2</sup>Preliminary studies on the subject, which hinted at several caveats a measurement of this kind generally has, have been performed already in 2017.

$$n_{\text{G-APD}}^{\text{on}} = n_{\text{G-APD}} \left[ 1 - \exp \left( -\frac{I_{\gamma} \text{PDE}}{n_{\text{G-APD}}} \right) \right] ,$$

where  $n_{\text{G-APD}}$  is the total number of pixels in the array and PDE is the so-called photodetection efficiency, i.e., the ratio between the number of detected avalanches and the number of incoming photons [214], typically calculated as a function of the input photon energy.

SiPMs feature excellent performance in terms of efficiency, bandwidth, gain, linearity and speed [133, 215]. Moreover, they are compact, require low bias voltage (typically a few tens of volts) and can operate in magnetic fields [215]. Their drawbacks are the generally rather strong dependence of the performance on the temperature and the relatively high dark count rate (DCR), i.e., the rate of pixels that turn on because of avalanches triggered by thermally generated electron-hole pairs and free electrons in the diode depletion region [215]. Typical DCR values range from a few kHz/mm<sup>2</sup> to a few MHz/mm<sup>2</sup>, depending on the temperature [133].

In the tests performed on the 0.45  $X_0$  strip in 2018, one of the smallest faces of the sample was coupled to a commercial photodetection chain based on the ASD-NUV4S-P SiPM by AdvanSiD [216]: its  $4 \times 4$  mm<sup>2</sup> square-shaped surface well matches the strip face, and its photodetection efficiency, which has a FWHM (full-width half maximum) of  $\sim 190$  nm that ranges in 380–570 nm and the peak sensitivity wavelength at  $\sim 420$  nm (NUV standing for Near-UltraViolet), matches the PWO scintillation spectrum perfectly [100]. The SiPM is coupled to the evaluation board via a dedicated socket [217]. The AdvanSiD ASD-EP-EB-N Evaluation Board [218] is used in order to provide easy interface to the digitiser (see section 2.3.1.4, chapter 2), current to voltage conversion and signal amplification [100]. This configuration is shown in figure 5.7.

Starting from 2021, a custom photodetection system has been employed. It is modular: each unit consists of an array of three  $2 \times 2$  SiPM matrices, model ARRAYC-60035-4P-BGA by onsemi [133, 219, 220]. Each matrix element is a 6 mm C-Series sensor, i.e., a low-noise, high-gain SiPM with squared pixels of size  $35 \times 35$   $\mu\text{m}^2$  and a PDE peaked in the blue [133, 220, 221]. The signals from the four sensors in the matrix are summed together, so a minimum of one channel per matrix (and, hence, three per unit) can be read out [133, 220]. The overall 12 SiPMs are mounted on a PCB as a ball grid array (BGA) [133, 220] as shown in figure 5.8. The PCB was designed at the INSULab laboratory and assembled by SCEN; it features a total surface of  $63 \times 23$  mm<sup>2</sup>, a thickness of 1.5 mm and a total active area of  $42 \times 14$  mm<sup>2</sup>. The efficiency of the PWO-SiPM system has been tested with cosmic rays (essentially muons) impinging on a  $\sim 10 \times 20 \times 30$  mm<sup>3</sup> PWO block with



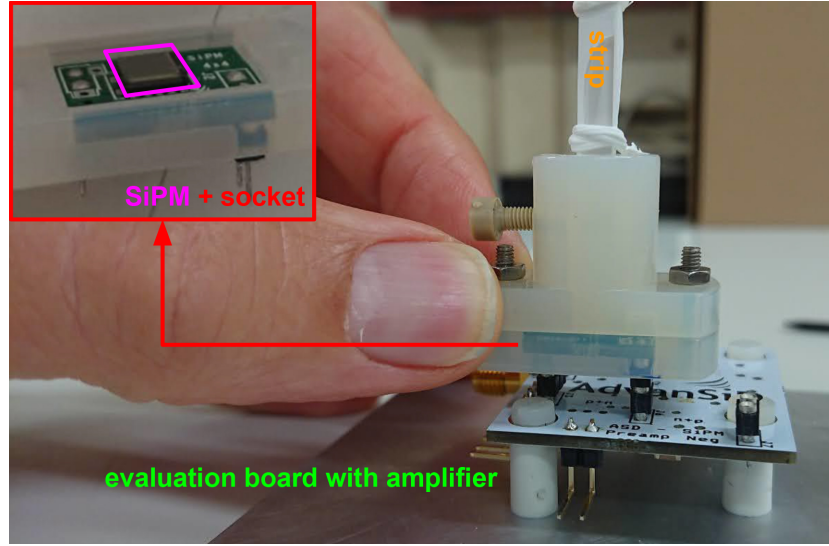


FIGURE 5.7: Fully assembled photodetection system exploited in the 2018 measurements at CERN: PWO strip (orange), SiPM (pink), socket (red) and evaluation board (green). Edited from [100].



FIGURE 5.8: INSULab custom SiPM boards.

random lattice orientation and the longest side orthogonal to the ground, and efficiency values higher than 80% have been measured. Further details on these preliminary tests, as well as on the system electronics, can be found in [133, 220].

In 2021, two single boards have been exploited to read the light output out from the two samples under study, i.e., the  $1 X_0$  and  $2 X_0$  ones. The faces that were coupled to the SiPM arrays were on the lower side of the samples and had a surface of  $\sim 1 \times 3 \text{ cm}^2$  (with the short side along the beam axis) and  $\sim 1 \times 2 \text{ cm}^2$  (with the long side along the beam axis) respectively. This configuration is shown in figure 5.9.

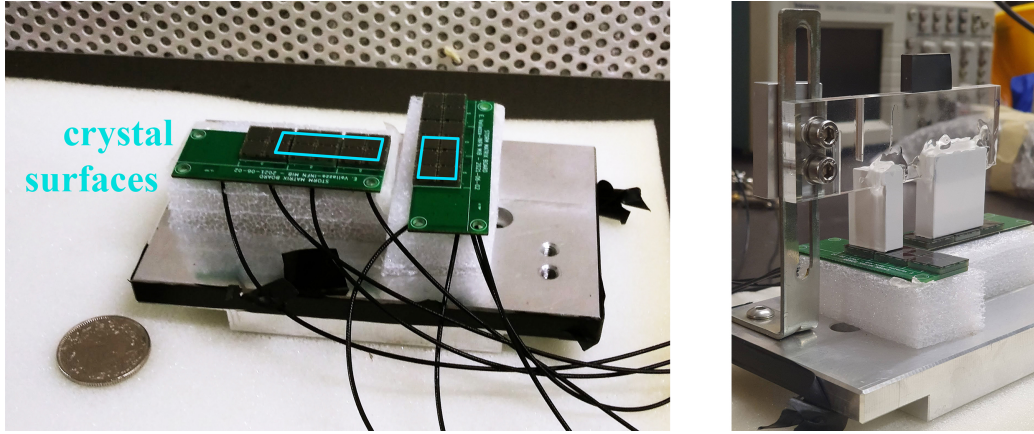


FIGURE 5.9: Photodetection system used in the 2021 measurements at CERN: (*left*) SiPM arrays alone, with the surfaces of the crystalline samples coupled to the sensors superimposed in light blue and (*right*) fully-assembled crystal-photodetector system.

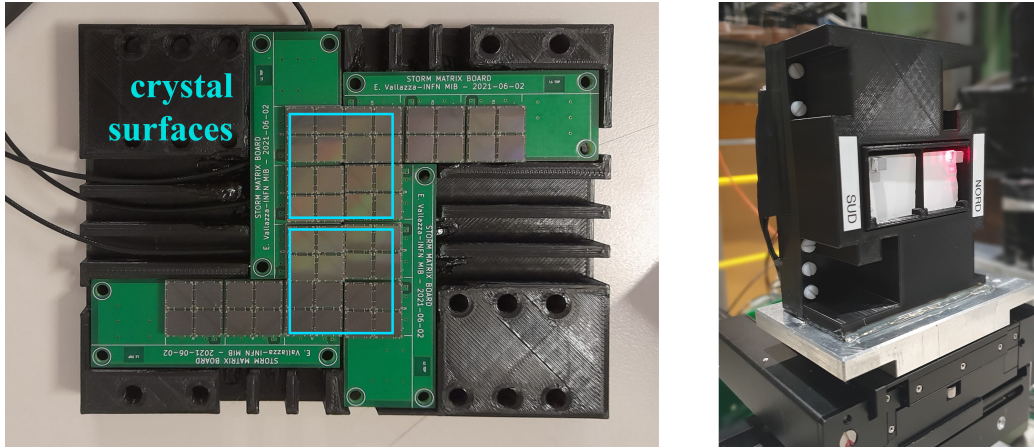


FIGURE 5.10: Photodetection system used in the 2022 measurements at CERN: (*left*) array of photodetection units alone, with the surfaces of the crystalline samples coupled to the sensors superimposed in light blue and (*right*) fully-assembled crystal-photodetector system installed on the goniometer at the beamtest.

On the other hand, in 2022, the two  $4.6 X_0$  samples were installed very close to each other on one side. Four photodetection units have been combined as shown in figure 5.10 left to accommodate the two  $3 \times 3 \text{ cm}^2$  square-shaped surfaces. This configuration is hosted in a dedicated hermetic plastic holder,

which also positions the crystals with the longest side along the beam path, i.e., with the SiPMs orthogonal to the beam; see figure 5.10 right.

### 5.3.2 Simulations

Simulations have been performed with Geant4, both to study the features of the shower development in an ideally large and thick crystal, and to reproduce the experimental results obtained in the beamtests. Geant4 version 10.5 has been used; for the random case, the QGSP\_BERT physics list was chosen [141], whereas the axial case was simulated with the framework described in section 2.4.2 (chapter 2). The correction coefficients to the standard electromagnetic processes have been calculated, as described in section 2.4.1, assuming an input divergence of 1 mrad.

#### 5.3.2.1 Shower development sampling

The simulated fraction of primary energy deposited per radiation length as a function of the penetration depth is shown in figure 5.11 in case of random orientation (top) and of the [001] axis (bottom). These simulations have been performed with monochromatic pencil beams impinging on a very long ( $> 20 X_0$ ) crystal.

Similarly to oriented tungsten (section 4.2.3, chapter 4), when the crystal is axially oriented, the shower develops faster, therefore the energy deposit peaks are in general closer to the front surface. Moreover, the maxima of the curves at 20 GeV and 120 GeV are much closer to each other than in random orientation. For instance, for 20 GeV (120 GeV) electrons, the shower peak is reached at  $\sim 6.8 X_0$  ( $\sim 8.7 X_0$ ) when randomly oriented and at  $\sim 5.8 X_0$  ( $\sim 6.8 X_0$ ) when on axis.

The integrals of the curves in figure 5.11, which represent the total fraction of the primary energy deposited in the crystal when the shower has reached a certain depth, are shown in figure 5.12. At 120 GeV (bottom), the difference between the axial and the random curves is significantly larger than at 20 GeV, which reflects the fact that the SF effect strength grows with the energy.

Figures 5.11 and 5.12 provide useful information for choosing the crystal thickness to study the shower development at different stages. In particular:

- in  $\lesssim 2 X_0$  thick samples, the energy deposit corresponds to a small fraction ( $\leq 1\%$ ) of the primary energy, the difference between the integral energy deposit attained on axis and in random configuration is small whereas the ratio between them is the largest – further details in section 5.3.5;



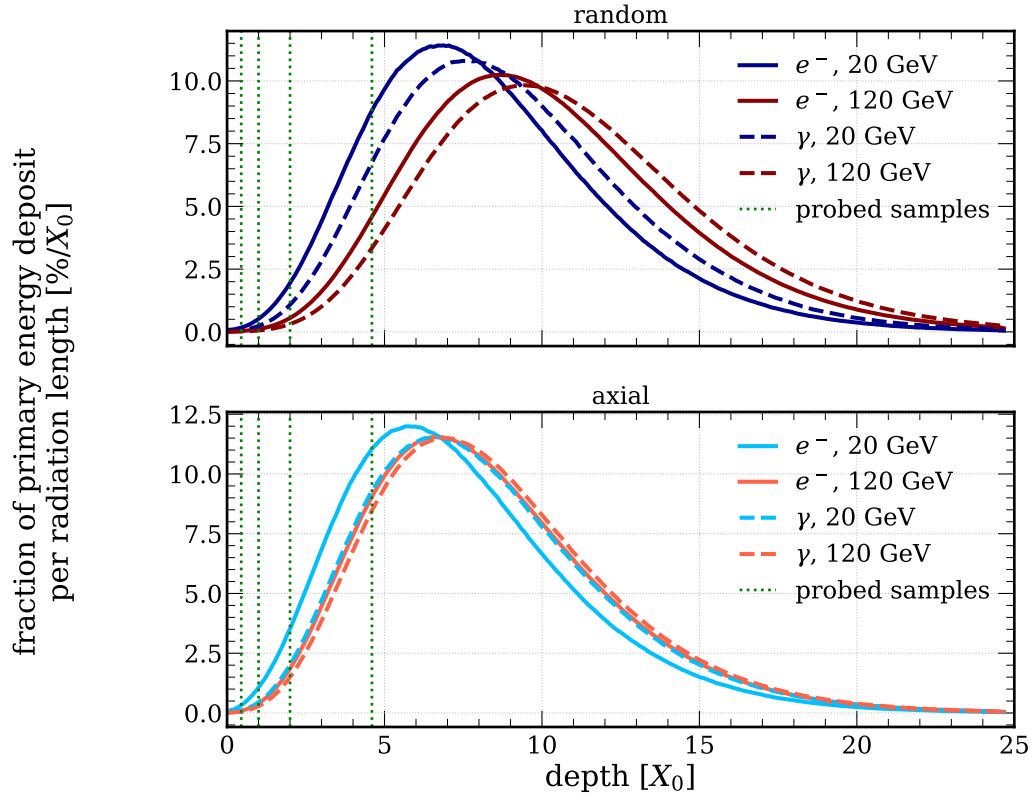


FIGURE 5.11: Fraction of energy deposit by the electromagnetic shower initiated by electrons (solid lines) and photons (dashed lines) per radiation length as a function of the penetration depth in (*top*) randomly and (*bottom*) axially ([001]) oriented PWO.

- between  $\sim 2 X_0$  and the position of the energy deposit peak in random ( $\sim 8.8 X_0$ ) the energy deposit per  $X_0$  corresponds to a major fraction of the primary energy and the difference between the axial and random integral energy deposit grows with the penetration depth;
- as the depth grows above the random energy deposit peak position, the axis-to-random difference decreases;
- at a thickness of  $\gtrsim 20 X_0$ , almost all the initial energy has been deposited in the crystal regardless of the lattice orientation.

The thicknesses of the experimentally tested PWO samples are indicated as green dotted lines.

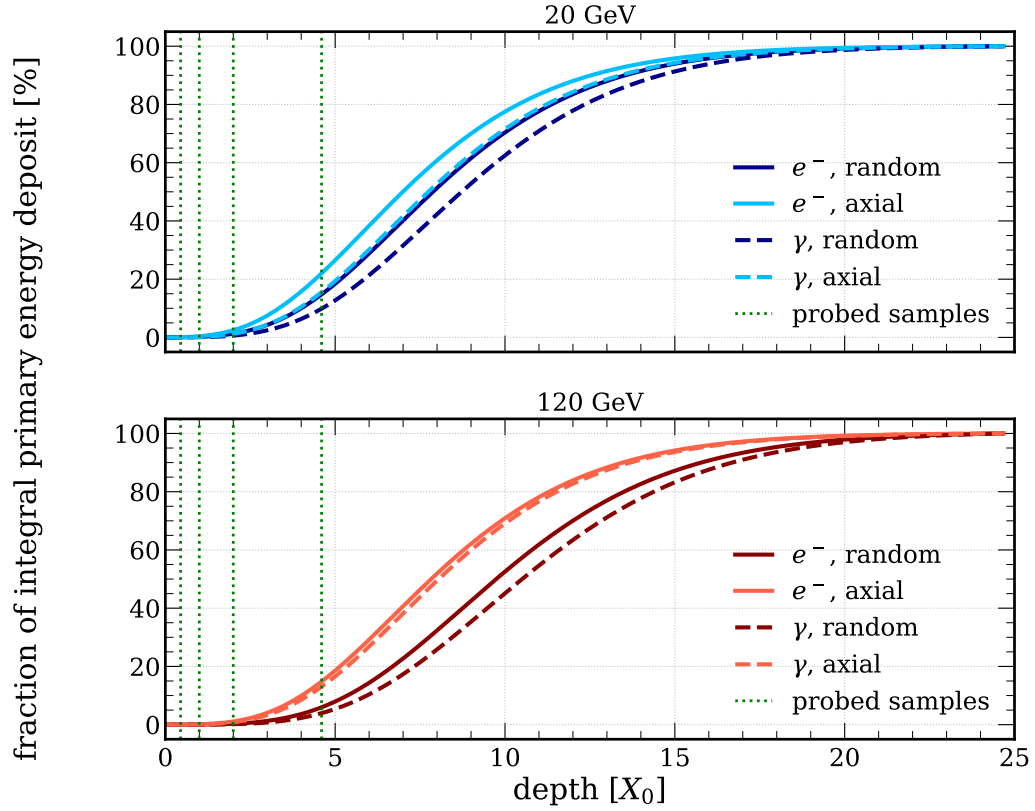


FIGURE 5.12: Fraction of energy deposit by the electromagnetic shower initiated by (*top*) 20 GeV and (*bottom*) 120 GeV electrons (solid lines) and photons (dashed lines) as a function of the penetration depth in PWO at different orientations. Each curve is the integral (over the depth across the sample) of the corresponding curve in figure 5.11.

### 5.3.2.2 Simulations of the beamtests at the CERN SPS

Full simulations of all the beamtests performed on the CERN H2 beamline between 2018 and 2022 have been developed, starting from the Geant4 template published in [222]. Modelling the energy distribution of the incident beam proved particularly critical in order to correctly reproduce the physics results. Figure 5.13 shows a comparison between the measured energy distributions of the beams directly impinging on the calorimeter and the corresponding distributions resulting from the full simulations. In 2018, the beam featured a sharp peak around 120 GeV, which could be adequately approximated by a Gaussian curve with 3.5% relative sigma. The beam used in the 2021 beamtest showed the same features.

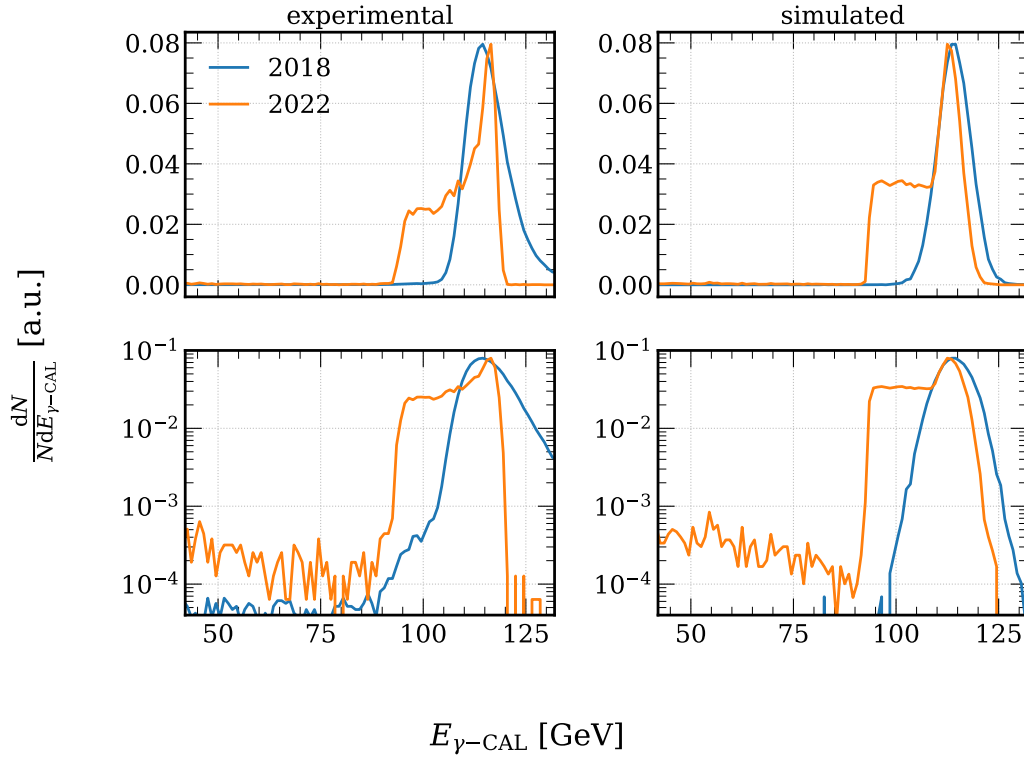


FIGURE 5.13: Beam energy distribution at the 2018 (blue) and 2022 (orange) beamtest on the SPS H2 beamline, directly measured with the forward calorimeter (*left*) and obtained in the corresponding simulations (*right*) with an electron beam of nominal momentum 120 GeV/ $c$ , in linear (*top*) and logarithmic (*bottom*) scale.

On the other hand, in 2022, the beam was heavily different. It comprised two electron components: a principal sharp peak around 120 GeV (with relative width  $\sim 2.5\%$ ) and a continuous edge between  $\sim 100$  GeV and the principal peak. Most likely, the latter component results from the interaction of the primary beam with some material positioned upstream with respect to the experimental area. Moreover, the beam contained a large number of pions, which result in a low-energy continuous component in the calorimeter spectra, clearly visible in the plots at the bottom of figure 5.13, at  $\lesssim 90$  GeV. As shown in figure 5.13 right, the experimentally measured beam energy distributions have been adequately reproduced in the simulations, with the following procedure:

- for each physics configuration of interest, three separate simulation runs have been performed, each with the same number of primary particles

(typically 10000–20000) and a different beam component – the electron peak, the electron edge and the pion peak. The components have been modelled as shown in figure 5.14: the peaks (edge) have been modelled with Gaussian curves (a flat distribution).

- Before merging the data obtained from the simulations of the different components, the energy spectrum of each component has been properly weighted, in order to reproduce the direct-beam experimentally measured spectrum. The populations of the three simulated samples have been descaled accordingly.
- Moreover, the energy value at which the spectra of the two electron components equal each other is found (dotted red line in figure 5.14): above (below) this value, only the electrons from the Gaussian (flat) component are selected, in order not to introduce non-physical discontinuities in the spectra.

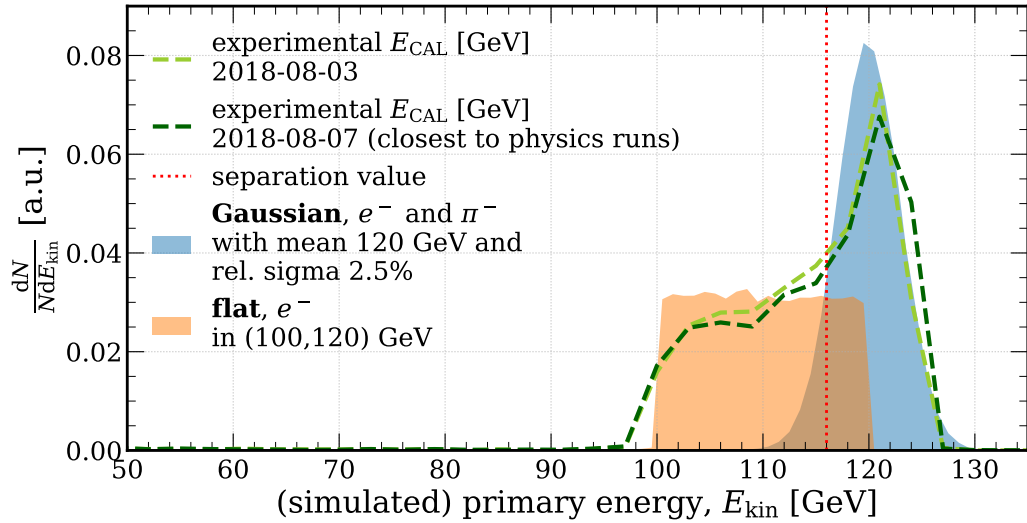


FIGURE 5.14: True primary energy of the beam particles in the simulations of the 2022 beamtest on the SPS H2 beamline. The corresponding direct-beam energy measured with the calorimeter in two different runs is superimposed (dashed green curves). The Gaussian (flat) energy component consists of electrons and negative pions (electrons).

### 5.3.3 Sample alignment

The pre-alignment procedures discussed in section 2.3.3 (chapter 2) are performed when the samples are installed in the setup. Then, scans over the goniometer angular degrees of freedom (DOFs) allow to align the beam to the lattice axis with high angular precision – about  $10 \mu\text{rad}$  or less. In order to detect the presence of planes and axes aligned with the beam path, variations in the response of different detectors as a function of the position of the goniometer DOF are sought.

Figure 5.15 shows a horizontal angular scan performed on the  $1 X_0$  sample tested in 2021 on the SPS H2 beamline, at a vertical angle of  $\sim 3 \text{ mrad}$  from the axis. The plot at the top shows the response of a plastic scintillator placed downstream with respect to the sample. This is the typical beam-to-axis alignment procedure in case of  $\gtrsim 1 \text{ mm}$  crystalline samples at high energy: as

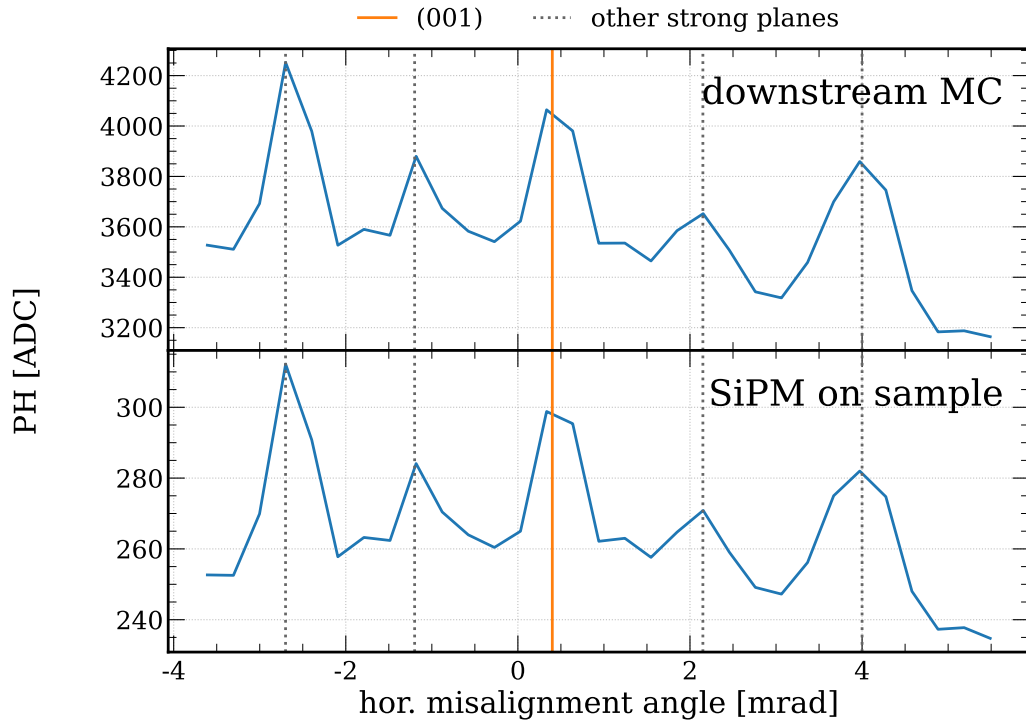


FIGURE 5.15: Goniometer scan on the horizontal misalignment angle of the PW0  $1 X_0$  sample. The response of a downstream MC (*top*) and that of the photodetection system (*bottom*) are shown as a function of the angle. The (001) plane (orange) and other higher-order skew planes (grey, dashed) are observed.

the angle between the beam and the axis of interest or neighbouring planes becomes smaller, the enhancement of the electromagnetic processes in SF becomes stronger, with a subsequent increase of the number of secondary charged particles at the crystal exit.

The plot at the bottom of figure 5.15 shows the response of the SiPMs as a function of the scan angle. As discussed in [133, 220], the signal of the SiPMs shows identical behaviour as that of the downstream MC: both the detectors highlight the presence of the (001) planes at approximately the centre of the scan (not precisely aligned with the axis, which is located at 0 mrad, due to the nonzero misflat of the sample) and of other strong skew planes around it. The planes are detected with the same contrast with respect to the signal attained in random alignment in the two cases.

Thanks to the fact that the scintillation light emitted inside the sample proves a powerful tool for the lattice alignment, no scintillating MC was installed between the crystal and the calorimeter in 2022. Figure 5.16 shows the goniometer angular phase space of the 4.6  $X_0$  sample reconstructed with the SiPM data collected in different DOF scans.

The large light yield of this PWO block and its good crystalline quality allowed to observe high-index peaks, whose effect on the electromagnetic

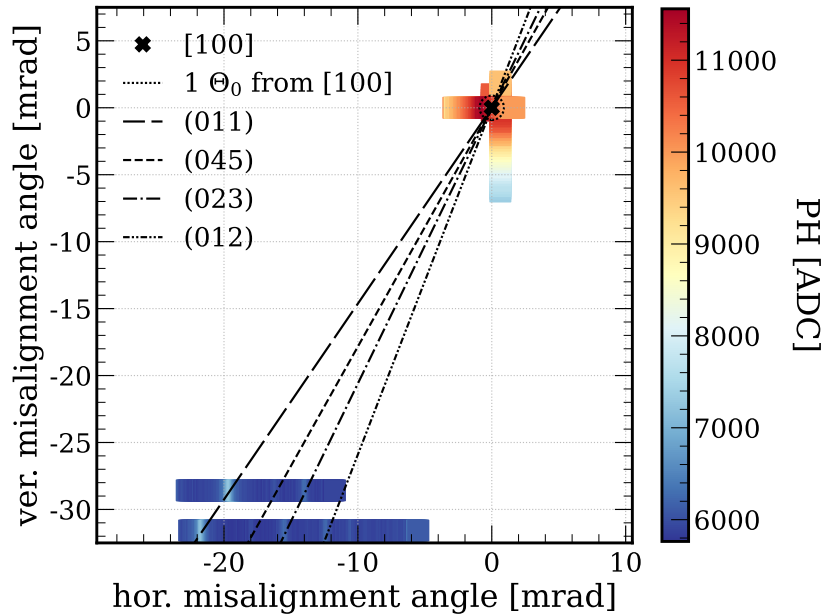


FIGURE 5.16: Crystallographic stereogram measured on the PWO 4.6  $X_0$  sample. Several skew planes are observed at different distances from the axis (black cross), and are highlighted with black lines.

processes is very small compared to that of the  $\langle 100 \rangle$  axis – like, e.g., the (045) plane –, thus reconstructing part of the crystallographic stereogram of this sample with impressive plane-to-random contrast. At a few  $\Theta_0$  or less from the axis, the signal of the SiPMs is significantly higher than in any other part of the stereogram, including the observed strong planes like, e.g., the (011) plane: in the latter, a PH about 75% of that measured in the axis is detected at a misalignment angle of  $\sim 2^\circ$ .

The high sensitivity of the scintillation signal to small angle variations around the lattice planes can be clearly observed in figure 5.17 top, which shows

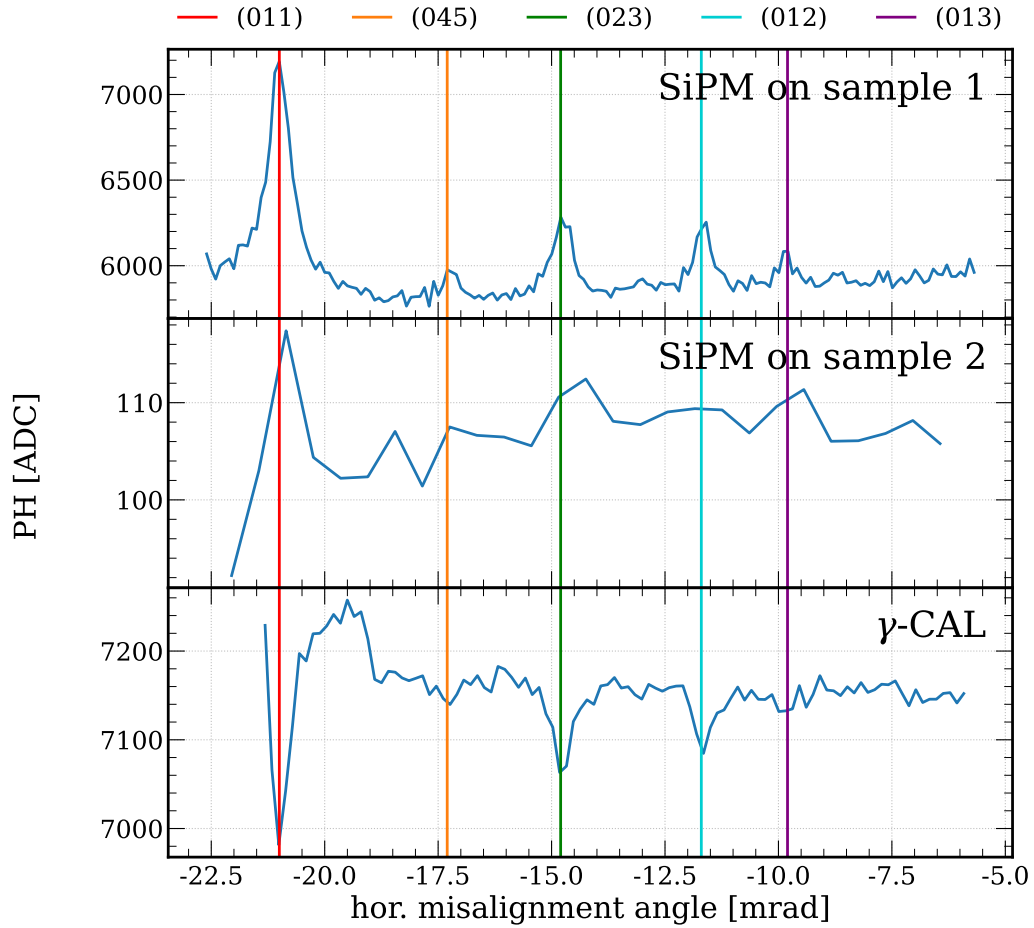


FIGURE 5.17: Goniometer scan on the horizontal misalignment angle of the PWO 4.6  $X_0$  sample. The response of the SiPMs coupled to the sample placed on the beam (*top*) and to the adjacent sample placed out of the beam path, at  $\sim 3$  cm (*centre*) and that of the  $\gamma$ -CAL (*bottom*) are shown as a function of the angle. Several skew planes are observed.

the SiPM signal as a function of the horizontal misalignment angle in a goniometer scan performed at  $\sim 30$  mrad from the axis in the vertical plane – i.e., the horizontal band at the bottom of figure 5.16. In case of the lowest-order planes, the shower development acceleration in the sample on the beam results in an increase of the signal of the adjacent sample (figure 5.17 centre) as well.

Moreover, as clearly shown in figure 5.17 bottom, in case of thick samples and of the experimental configuration optimised for the energy deposit measurement – described in section 2.3.5 (chapter 2) – the calorimeter is also highly sensitive to the lattice structure: in presence of a plane, the energy absorbed by the crystal increases and, in turn, the energy deposited in the calorimeter is reduced by approximately the same amount. This method shows almost as good a plane-to-random contrast as that obtained from the scintillation signal, and provides a feasible option for alignment in case no scintillation measurements are performed.

#### 5.3.4 Output radiative energy loss

The electromagnetic radiation emitted by high-energy electrons interacting in relatively thin ( $\sim 2 X_0$  or less) crystalline samples provides a clean measurement of the SF effects, which can be compared to the theoretical predictions and to the results of the simulations. This approach provides a powerful tool to evaluate the performance of the latter and prove them suitable to simulate the application-specific calorimeter prototypes.

In [50], the radiation spectra measured on the CERN H4 beamline [103] in 2017 with the  $0.45 X_0$  [001] sample have been compared to the results of preliminary simulations, developed with the simulation tool described in section 2.4.1 (chapter 2) without modelling the beamtest experimental setup. On the other hand, in this section, a comparison between the experimental data and the corresponding beamtest full simulations is shown. Figure 5.18 shows the spectra of  $E_{\gamma-\text{CAL}}$  – i.e., the energy of the output radiation measured by the photon calorimeter – obtained with the  $0.45 X_0$ ,  $1 X_0$  and  $2 X_0$  samples on the H2 beamline between 2018 and 2021. Data were collected both on axis and at several tens of mrad with respect to it, i.e., in random orientation – as well as at different angles in between (section 5.3.7).

A generally good agreement between the measured spectra and the ones obtained from the full simulations is observed. Moreover, several observations on the features of these spectra can be made:



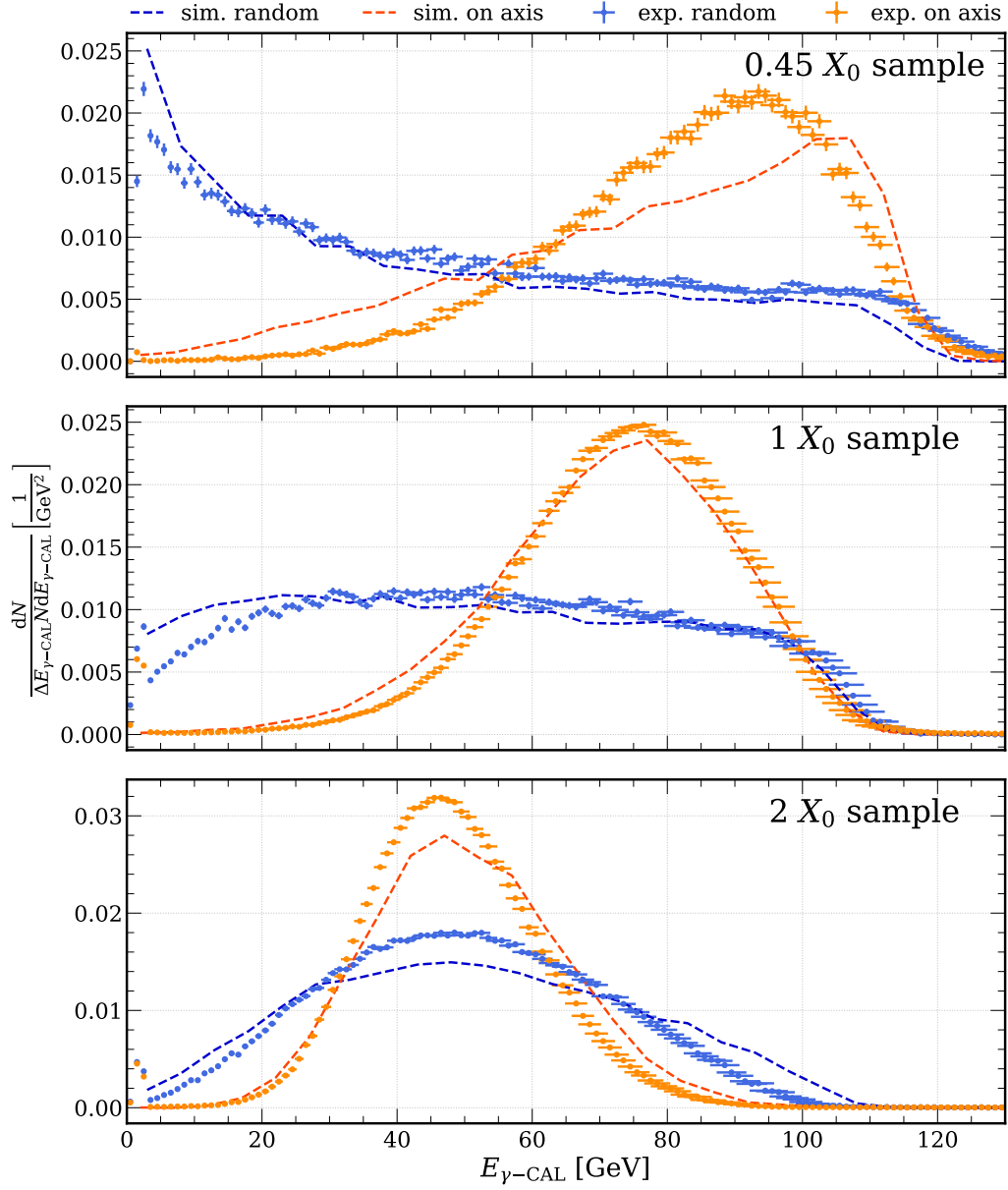


FIGURE 5.18:  $E_{\gamma\text{-CAL}}$  spectra obtained from the measurements (points), performed on different samples, and the corresponding simulations (dashed curves).

- the spectrum obtained from the  $0.45 X_0$  sample in random orientation clearly shows the features of the standard bremsstrahlung spectrum obtained with the Bethe-Heitler model (figure 1.9, chapter 1).
- As the thickness of the sample increases to  $\gtrsim 1 X_0$ , the soft part of the random spectrum is suppressed, due to the fact that more lower-energy photons are produced and absorbed inside the sample, emitted at large angle – i.e., out of the calorimeter acceptance – or stopped in the material between the crystal and the calorimeter. The thicker the sample, the stronger the suppression and the larger the range of suppressed energies are.
- Similarly, the hardest part of the spectrum is more suppressed as the thickness of the sample increases. Indeed, as the shower develops and more secondaries are generated, the average energy per secondary decreases; as a consequence, less photons with a major fraction of the primary energy emerge from the crystal.
- In general, the spectra obtained in axial orientation show the typical features of quantum synchrotron radiation, i.e., the strong suppression of the soft part of the spectrum and the presence of a comparatively narrow peak towards the high-energy part.
- As the thickness of the sample increases, the peak energy becomes smaller. This is due to the fact that the strength of the coherent effects decreases as the number of secondaries increases and, in turn, as their energy decreases and their angle with respect to the trajectory of the parent particle increases. In case of samples with a thickness of several ( $\gg 1$ )  $X_0$ , the random and axial spectra would become similar to each other, and asymptotically – i.e., at a thickness of tens of  $X_0$  – the radiation emission is fully suppressed in both cases, as the primary energy is almost entirely absorbed inside the crystal.

#### 5.3.4.1 Radiation enhancement at different energies

It is interesting to compare the results obtained measuring the radiation from the crystalline samples under study at different energies. In particular, the  $0.45 X_0$  and the  $1 X_0$  samples have also been probed at DESY, in the sub-SF regime – see section 2.2.1 (chapter 2). Indeed, figures 5.19 and 5.20 show the ratios between the spectra measured on axis and in random alignment at different energies, for these two samples, as a function of the fraction of initial energy measured by the  $\gamma$ -CAL.

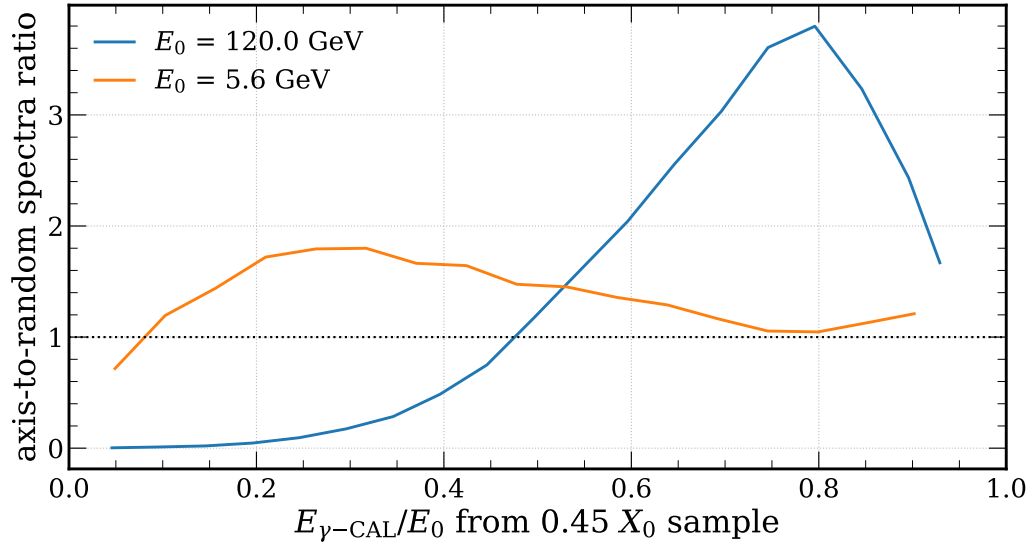


FIGURE 5.19: Ratio between the axial and random  $E_{\gamma\text{-CAL}}$  spectra obtained by electrons at different energies impinging on the PWO  $0.45 X_0$  sample probed on SPS H2 (120 GeV – blue) and on DESY T21 (5.6 GeV – orange).

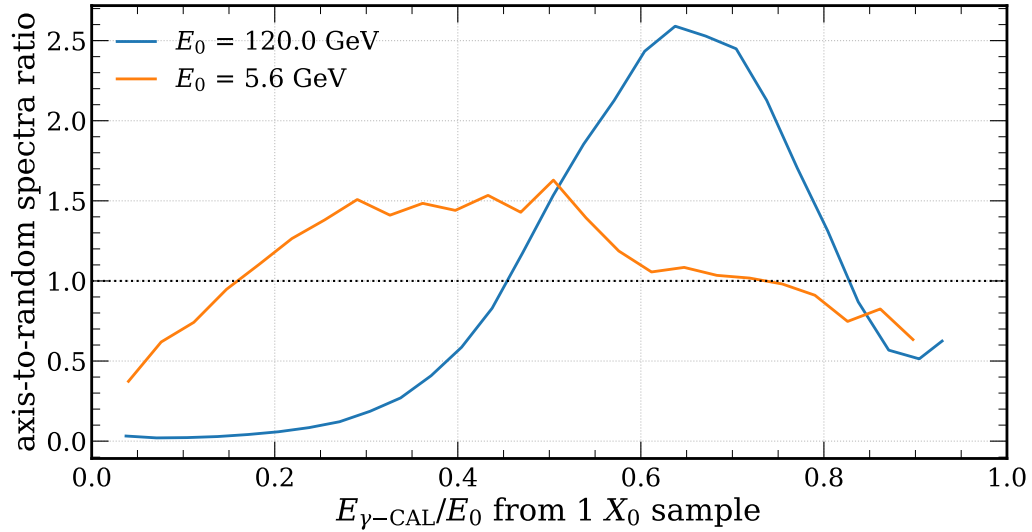


FIGURE 5.20: Ratio between the axial and random  $E_{\gamma\text{-CAL}}$  spectra obtained by electrons at different energies impinging on the PWO  $1 X_0$  sample probed on SPS H2 (120 GeV – blue) and on DESY T21 (5.6 GeV – orange).

Clearly, the spectrum component that is affected by the enhancement, thus featuring a ratio  $\gg 1$ , is harder at 120 GeV than at 5.6 GeV, which reflects the quantum synchrotron nature of the SF radiation discussed in section 1.4.2 (chapter 1). The strength of the enhancement is also strongly dependent on the primary energy: a maximum enhancement greater than  $\sim 350\%$  is attained in the  $0.45 X_0$  sample at 120 GeV, whereas values  $< 200\%$  are observed at 5.6 GeV.

Moreover, measurements were performed on the  $2 X_0$  sample at 120 GeV and at 100 GeV. They are shown in figure 5.21: as expected, when in the SF regime, even a comparatively small increase of the initial energy, and hence of  $\chi$ , results in the hardening of the radiation spectrum and in the strengthening of the enhancement.

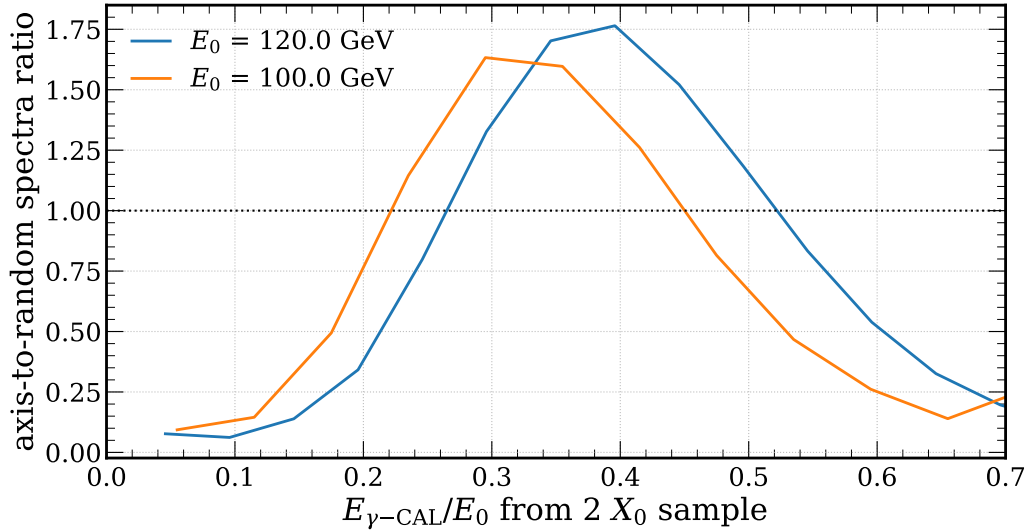


FIGURE 5.21: Ratio between the axial and random  $E_{\gamma\text{-CAL}}$  spectra obtained by electrons at different energies impinging on the PWO  $2 X_0$  sample probed on SPS H2 at 120 GeV (blue) and 100 GeV (orange).

Together, the curves referring to the data collected at 120 GeV (blue curves) in figures 5.19, 5.20 and 5.21 also show that the peak enhancement is affected by the sample thickness: the greater the latter, the lower the enhancement and the fraction of primary energy at which it occurs are.

#### 5.3.4.2 What about positrons?

It is important that the energy measurement performed by an electromagnetic calorimeter does not depend on whether the primary particle is an electron or a positron. Although the  $e^-$  and the  $e^+$  are identical from the point

of view of the electromagnetic interactions [223], it is worth studying their behaviour in oriented crystals, since, as discussed in section 1.2.4.2 (chapter 1), some of the coherent interactions – i.e., the ones that occur inside the lattice potential well – depend on the sign of the incident particle charge.

At the GeV scale and above, the SF regime is attained in heavy crystals such as PWO. Since the radiation mechanism is synchrotron-like in this regime (see section 1.4.2, chapter 1), no differences are expected in the radiation energy spectra between the cases of incident  $e^-$  and  $e^+$ . Indeed, dedicated measurements have been performed in 2016 on the SPS H4 beamline; the  $0.45 X_0$  crystal was probed with 120 GeV electrons and positrons. The resulting radiation spectra have been published in [120] and are shown in figure 5.22: as expected, the spectra obtained with the electron and positron beam are perfectly compatible to each other in both the simul-amorphous and on-axis configurations.

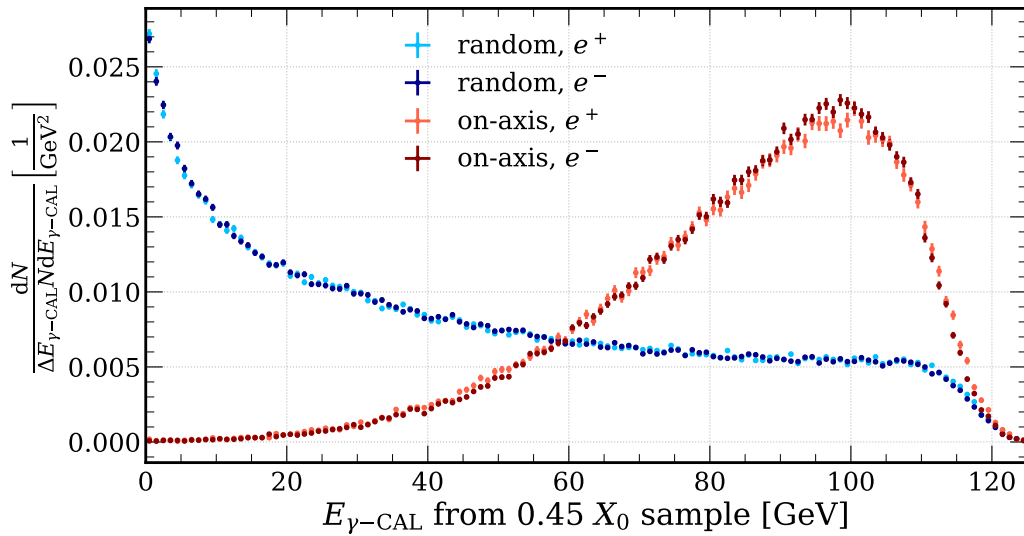


FIGURE 5.22: Comparison between  $E_{\gamma\text{-CAL}}$  spectra obtained with electrons and positrons impinging on the PWO  $0.45 X_0$  sample in amorphous-like (blue) and axial (red) alignment.

### 5.3.5 Scintillation light and energy deposit

In the following, the measured scintillation light spectra are presented. They are compared to the spectra of the energy deposit inside the crystals, resulting from the simulations. In particular, figures 5.23, 5.24, 5.25 and 5.26 show

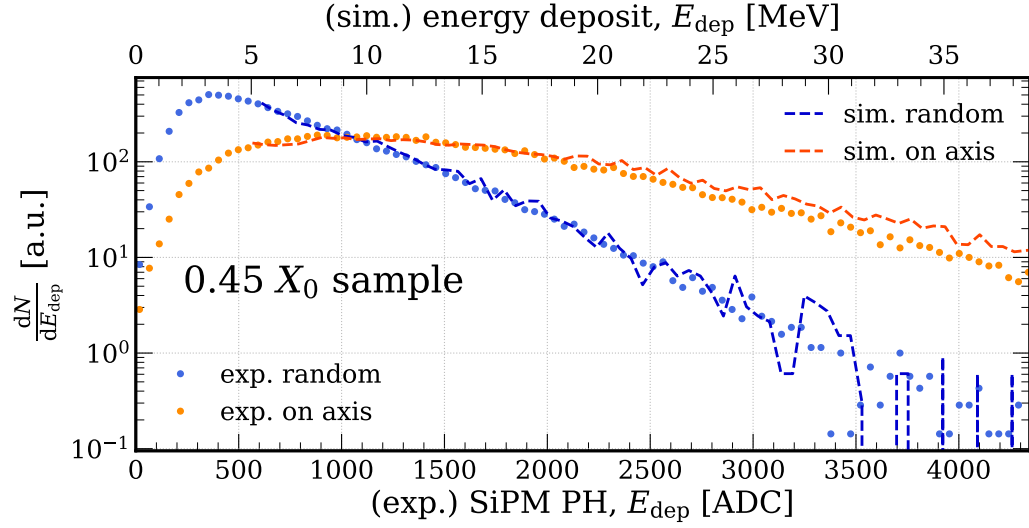


FIGURE 5.23: Scintillation light spectra measured by the SiPM on the PWO  $0.45 X_0$  sample (points), and the corresponding simulations (dashed curves).

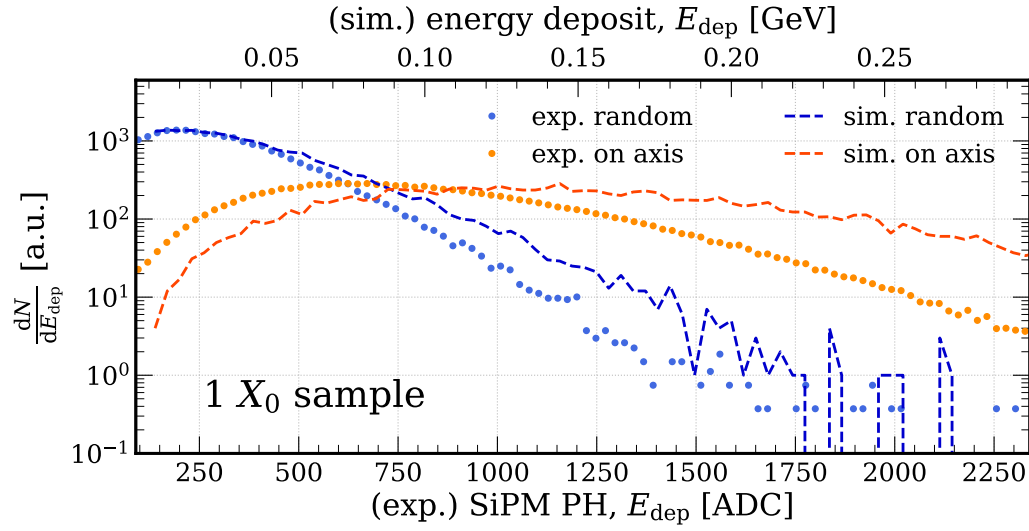


FIGURE 5.24: Scintillation light spectra measured by the SiPMs on the PWO  $1 X_0$  sample (points), and the corresponding simulations (dashed curves).

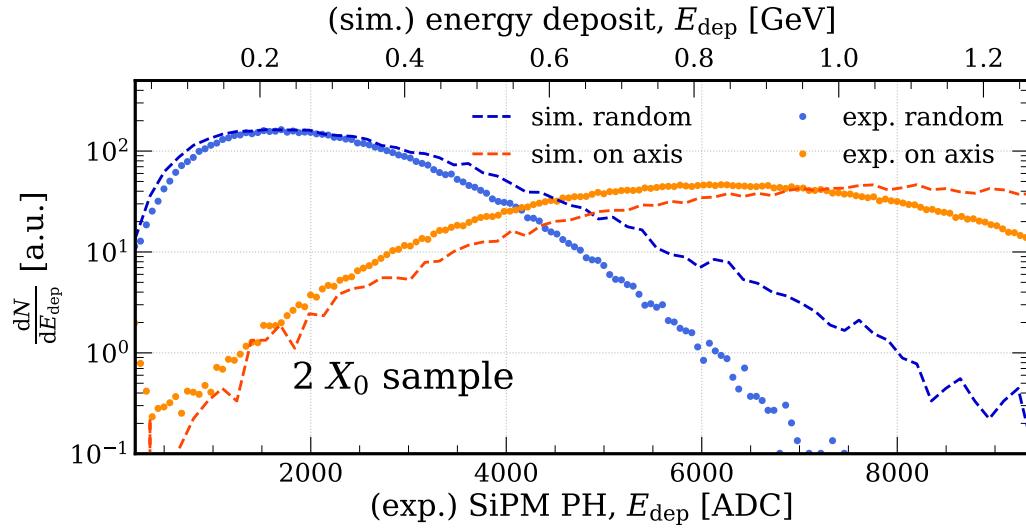


FIGURE 5.25: Scintillation light spectra measured by the SiPMs on the PWO  $2 X_0$  sample (points), and the corresponding simulations (dashed curves).

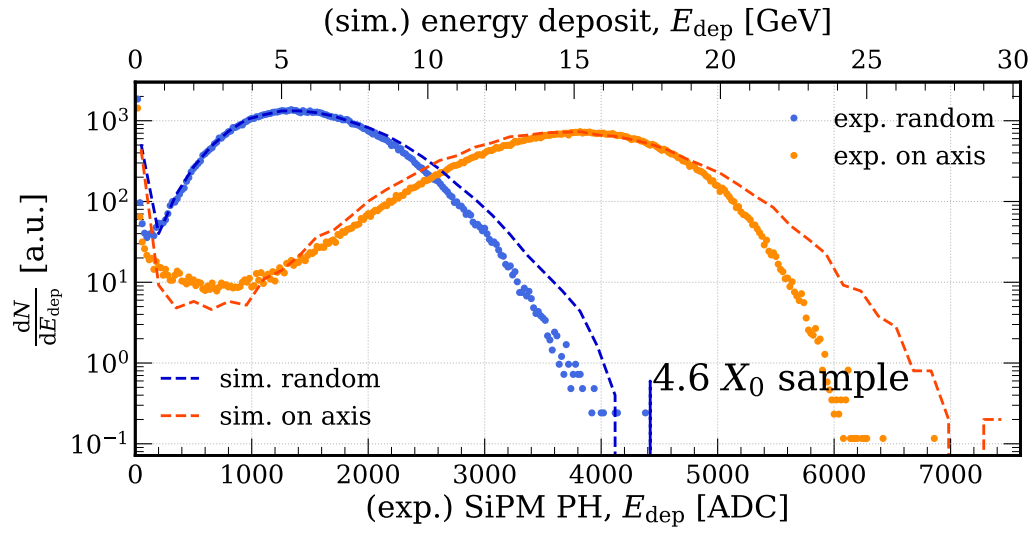


FIGURE 5.26: Scintillation light measured by the SiPMs on the PWO  $4.6 X_0$  sample (points), and the corresponding simulations (dashed curves).

the results obtained with 120 GeV electrons impinging on the  $0.45 X_0$ ,  $1 X_0$ ,  $2 X_0$  and  $4.6 X_0$  sample respectively.

The good agreement between the spectral shape of the experimental data and that of the simulations indicates that the scintillation light is proportional to the energy deposit in a wide range. All the most probable values (MPVs) of the random (axial) spectra,  $E_{\text{dep}}^{\text{rnd}}$  ( $E_{\text{dep}}^{\text{ax}}$ ), are shown in figure 5.27a (b), superimposed on the corresponding curves shown in figure 5.12 for 120 GeV electrons. In the experimental data, the ADC-to-GeV conversion has been performed equalising the experimentally measured random scintillation peak with the corresponding simulated energy deposit peak.

In simul-amorphous configuration,  $\sim 3.6$  MeV are deposited in case of the  $0.45 X_0$  sample and  $\sim 25$  MeV in case of the  $1 X_0$  sample. The value significantly grows in case of multi- $X_0$  samples: the spectrum is peaked at  $\sim 222$  MeV in case of the  $2 X_0$  sample and at  $\sim 5.6$  GeV – i.e.,  $\sim 4.6\%$  of the nominal beam energy – in case of the  $4.6 X_0$  sample. As expected, when on axis (figure 5.27b), the energy deposited inside the crystal significantly grows due to the SF effects. In case of the  $4.6 X_0$  sample, an impressive energy deposit of  $\sim 15.1$  GeV is attained, i.e.,  $\sim 12.6\%$  of the primary energy.

It is particularly interesting to study the difference between  $E_{\text{dep}}^{\text{ax}}$  and  $E_{\text{dep}}^{\text{rnd}}$  – figure 5.27c. In fact, the dependence of this difference on the sample thickness is very strong. At a thickness  $\lesssim X_0$ , this difference corresponds to a very small fraction of the nominal beam energy –  $< 0.05\%$ , i.e.,  $< 60$  MeV. On the other hand, the value dramatically grows at higher thickness values: a fractional difference of  $\sim 0.5\%$  (i.e.,  $\sim 600$  MeV) is attained at  $2 X_0$ , and a value of  $\sim 7.9\%$  (i.e.,  $\sim 9.48$  GeV) is attained at  $4.6 X_0$ .

Moreover, figure 5.27d shows the ratio between  $E_{\text{dep}}^{\text{ax}}$  and  $E_{\text{dep}}^{\text{rnd}}$ , which provides an estimate of the energy deposit enhancement obtained on axis with respect to the random case. As anticipated in section 5.3.2.1, the latter is the largest at a thickness below a few  $X_0$ . Indeed, the largest measured enhancement ( $\sim 378\%$ ) is attained with the  $2 X_0$  sample. The value obtained with the  $4.6 X_0$  sample,  $\sim 268\%$ , approximately equals that of the  $0.45 X_0$  sample,  $\sim 249\%$ . All the difference and ratio values computed from the experimental data are in good agreement with the simulated curves. Furthermore, the enhancement resulting for the  $0.45 X_0$  sample is in excellent agreement with the value of  $2.230 \pm 0.027$  obtained from a different simulation study, i.e., from ideal simulations of the scintillation light emitted by a 120 GeV electron pencil beam impinging on the PWO strip – see [211].

As shown in table 5.3, the average energy deposit increase attained when the sample is axially oriented corresponds to an enhancement of the average thickness effectively experienced by the particles in the shower. This effective thickness is evaluated as the thickness a randomly oriented crystal should



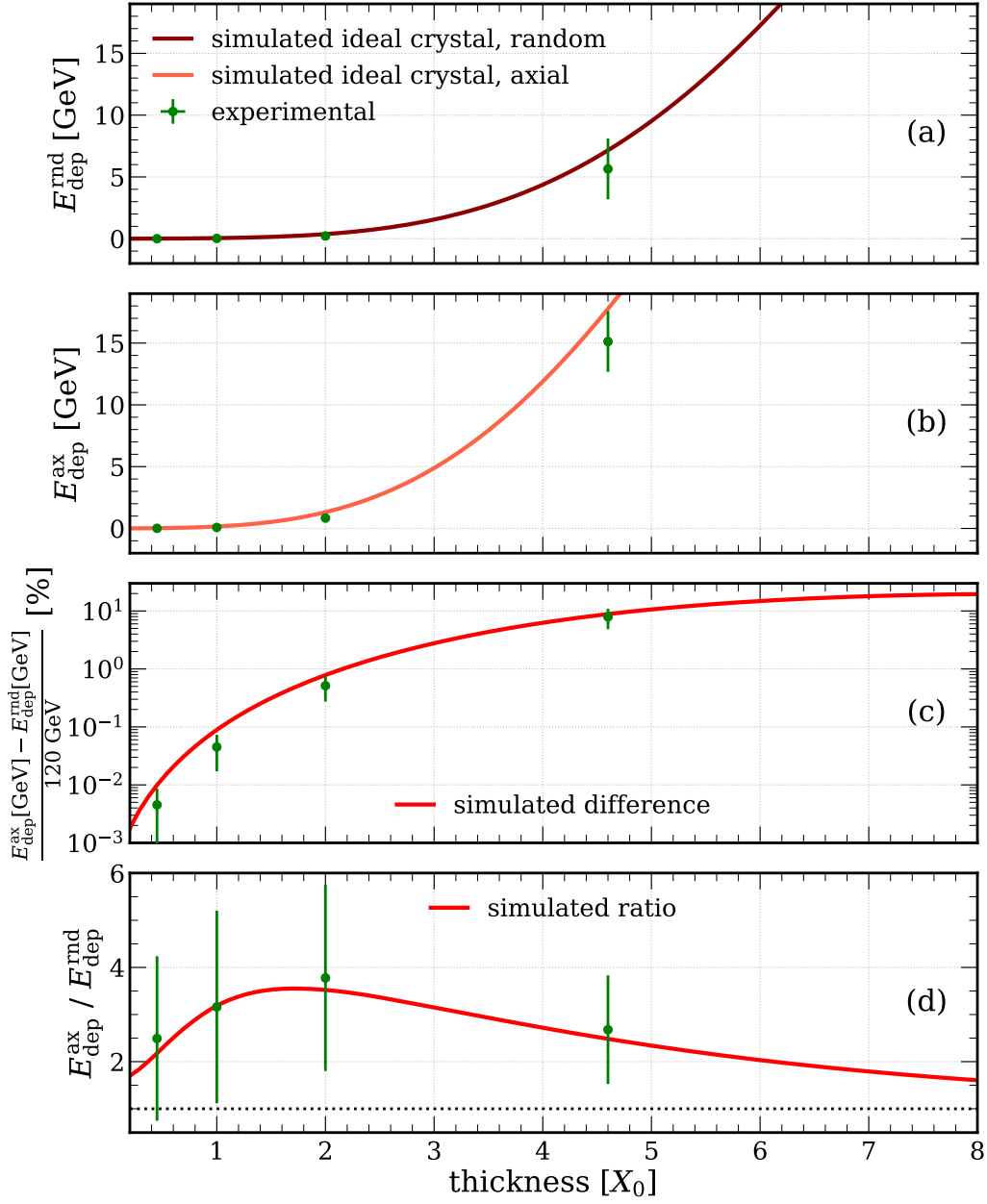


FIGURE 5.27: Measured energy deposited in different PWO samples in axial (a) and random (b) alignment, their difference (c) and their ratio (d), as a function of the sample thickness. The corresponding simulation curves, obtained from the curves shown in figure 5.12, are also shown.

Thickness [ $X_0^{\text{std}}$ ]	Eff. thickness [ $X_0^{\text{std}}$ ]	Thickness enh. [%]	$\langle X_0^{\text{app}} \rangle$ [mm]	$\langle X_0^{\text{app}} \rangle$ [ $X_0^{\text{std}}$ ]
0.45	$0.745^{+0.223}_{-0.301}$	$165.48^{+49.51}_{-66.97}$	$5.380^{+3.657}_{-1.239}$	$0.604^{+0.411}_{-0.139}$
$\sim 1$	$1.520^{+0.256}_{-0.324}$	$151.98^{+25.65}_{-32.43}$	$5.858^{+1.589}_{-0.846}$	$0.658^{+0.178}_{-0.095}$
$\sim 2$	$2.923^{+0.329}_{-0.397}$	$146.17^{+16.45}_{-19.84}$	$6.091^{+0.957}_{-0.616}$	$0.684^{+0.107}_{-0.069}$
4.6	$6.208^{+0.674}_{-0.711}$	$134.96^{+14.62}_{-15.45}$	$6.597^{+0.853}_{-0.646}$	$0.741^{+0.096}_{-0.072}$

TABLE 5.3: Measured thickness enhancement and mean apparent radiation length in the PWO samples probed on the SPS H2 beamline.

have to make the primary electrons lose the measured amount of energy deposited on axis. The measured values range from  $\sim 165\%$  in case of the  $0.45 X_0$  sample to  $\sim 135\%$  in case of the  $4.6 X_0$ , becoming smaller as the sample thickness increases. The latter is in agreement with the expectations, since, as the shower develops, the secondaries have lower average energy and larger angular aperture with respect to the direction of the primary electron, thus experiencing weaker SF-related effects.

The effective thickness values can be used to make an operative estimate of the apparent radiation length experienced on average by the shower  $e^\pm$  and photons across different oriented crystals,  $\langle X_0^{\text{app}} \rangle$ . It has to be noted that this value depends on the crystal thickness and on the particle energy, since the strength of the coherent effects decreases as the shower develops. Therefore, it should not be intended as an absolute redefinition of the radiation length in axially oriented PWO or as the value of radiation length effectively experienced by the primary electron impinging on the crystal, but rather as a merely practical estimate of the SF-related enhancement of the electromagnetic processes at a certain energy in samples of a certain thickness, up to a few  $X_0$ . Conversely, in case of thicker samples, most of the initial energy is deposited inside the crystal bulk regardless of the lattice orientation, and hence  $\langle X_0^{\text{app}} \rangle \rightarrow X_0^{\text{std}} = 8.903$  mm.

Table 5.3 provides an estimate of this mean apparent radiation length obtained with 120 GeV electrons impinging on the samples under study. The  $\langle X_0^{\text{app}} \rangle / X_0^{\text{std}}$  ratio (rightmost column in table 5.3) is  $\sim 60\%$  in case of the  $0.45 X_0$  sample and grows up to  $\sim 74\%$  in case of the  $4.6 X_0$ , meaning that, as expected, the radiation length reduction is less pronounced in thicker samples. The results obtained for the  $1 X_0$  and  $2 X_0$  samples are in excellent agreement with those presented in [133], obtained with a different analysis approach from the same experimental data. Moreover, the results of measurements performed on the  $1 X_0$  sample with incident photons and a setup

very similar to the one discussed in section 2.3.4 (chapter 2) [224] are also fully compatible with the ones presented in this section.

The size of the errors on the values listed in table 5.3 depends on the gradient of the red curves in figure 5.27: for instance, the errors on the thickness enhancement and on  $\langle X_0^{\text{app}} \rangle$  are smaller where the variation of  $E_{\text{dep}}^{\text{ax}}$  as a function of the sample thickness (figure 5.27b) is larger.

### 5.3.6 Total output energy and setup hermeticity

Figure 5.28 shows the energy spectra measured by the electromagnetic calorimeter positioned immediately downstream with respect to the  $4.6 X_0$  sample, in 2022. Differently from the electromagnetic radiation measurements shown in figure 5.18, these spectra comprise the energy of all the particles exiting the crystalline sample. It can be observed that:

- these spectra feature rather narrow structures, corresponding to a major fraction of the difference between the initial energy and the energy deposited in the crystal.
- As expected, the peak of the axial spectrum is at lower energy than that of the random spectrum. The reduction of the crystal output energy reflects the energy deposit enhancement discussed in section 5.3.5.

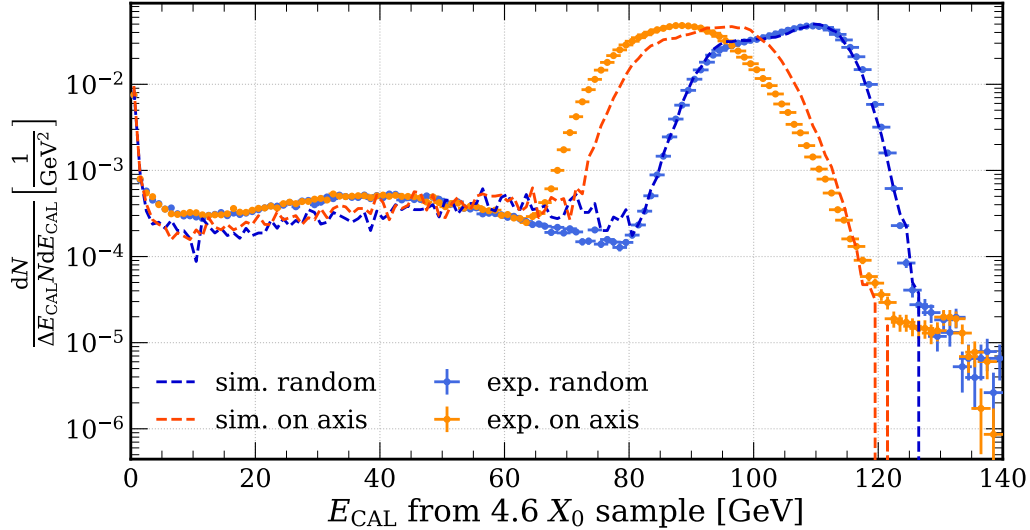


FIGURE 5.28:  $E_{\text{CAL}}$  spectra obtained from the measurements (points), performed on the  $4.6 X_0$  sample at the STORM 2022 beamtest, and the corresponding simulations (dashed curves).

- Both the random and axial spectra feature an edge extending down to a few GeV less than the peak. This reflects the incident beam structure – details can be found in section 5.3.2.2.
- The continuous component at  $\lesssim 80$  GeV ( $\lesssim 60$  GeV) in the random (axial) spectrum is due to the pions in the beam. This component represents a minor fraction of the collected statistics and is unaffected by the lattice orientation.

The spectrum measured in simul-amorphous orientation shows an excellent agreement with the corresponding simulation. On the other hand, albeit identical to the simulated spectrum in shape, the experimental axial spectrum is peaked at 7–8 GeV less. Since the scintillation light measurements and simulations are in excellent agreement with each other (figure 5.26), it is unlikely that this discrepancy is due to an issue with the simulation of the energy deposit inside the crystal.

Conversely, it is possible that, when the sample is in axial orientation, part of the secondaries generated as the shower develops in it exit at very large angle with respect to the beam direction, out of the calorimeter acceptance. This effect might not be correctly reproduced by the modified version of Geant4, in which MCS is not rescaled with respect to standard Geant4, like bremsstrahlung and pair production (PP) are.

The ratio between the energy deposited in the six lateral lead glass blocks and in the central block of the hibiscus-like calorimeter (see section 2.3.5, chapter 2) has been computed, in both the random and axial configurations. The resulting axis-to-random ratio obtained from the experimental (simulated) data is  $\sim 1.92$  ( $\sim 1.75$ ), which means that:

- as expected, the output particles have a significantly broader angular distribution when the sample is on axis, which reflects the fact that the shower at the crystal rear face is at a more advanced stage than in random orientation;
- the measurements feature a  $\sim 9\%$  larger axis-to-random ratio than the simulations, which indicates that the distribution of the output particle exit angles is broader in the experiment, so some of the lowest-energy secondaries might be emitted out of the calorimeter acceptance limit.

The second item of the list above might be closely related to a topic of utmost interest in the study of the SF-induced shower enhancement, i.e., the influence that the coherent effects might have on the Molière radius. As of today, this topic has not been discussed in literature, and dedicated measurements are envisaged in the next years.

### 5.3.7 Angular range

In view of the integration of oriented scintillating crystals into specific applications, it is important to characterise the dependence of the coherent effects on the misalignment angle. This characterisation is done by performing high-statistics runs at an increasing angular distance from the axis, along a direction that is chosen as far as possible from any strong planes.

The resulting variation in the response of the calorimeter and the photodetection system as a function of the misalignment angle is studied in the following sections. In all the contour plots below, the vivid vertical strips correspond to the actually measured spectra, whereas the shaded parts correspond to contour-plot interpolations [225]. The spectra obtained in simul-amorphous orientation are also shown, at a smaller distance from the axis than the actually selected one (the real misalignment angle typically being of several degrees), in the right side of the plot.

#### 5.3.7.1 From the calorimeter response

Figure 5.29 shows the radiation spectra measured by the  $\gamma$ -CAL on the 1  $X_0$  and 2  $X_0$  samples at different misalignment angles. Clearly, as the misalignment angle increases, the radiation spectrum becomes broader and more similar to the spectrum obtained in simul-amorphous configuration.

Considering the 1  $X_0$  sample, the features of the spectrum measured at 2 mrad from the axis are in between those of the spectra measured on axis and in random orientation. On the other hand, the spectra measured with the 2  $X_0$  sample show approximately the same features from the axis up to 2 mrad, hinting at a larger angular acceptance with respect to the thinner sample. This might partially reflect the fact that the 2  $X_0$  sample, which features a higher surface mosaicity than the 1  $X_0$  sample (table 5.2), has a higher internal mosaicity as well. Moreover, a higher number of lower-energy secondary particles is generated in thicker samples, which, recalling that the angular range of channelling and CB (i.e.,  $\psi_L$  and  $\sim 10 \psi_L$  respectively) grows as the particle energy decreases, might contribute to the observed direct relation between the acceptance of the coherent interactions and the sample thickness as well.

Figure 5.30 shows the spectrum of the output particle energy (both  $e^\pm$  and photons) as a function of the 4.6  $X_0$  sample misalignment angle in the measurements performed in 2022. Clearly, the total energy of the particles exiting the crystal grows with the misalignment angle. In particular, the spectrum MPV is  $\sim 88.5$  GeV on axis,  $\sim 96.5$  GeV at 2 mrad,  $\sim 105.5$  GeV at 17 mrad and  $\sim 109.5$  GeV in random (measured at  $\sim 70$  mrad): the reduction of the

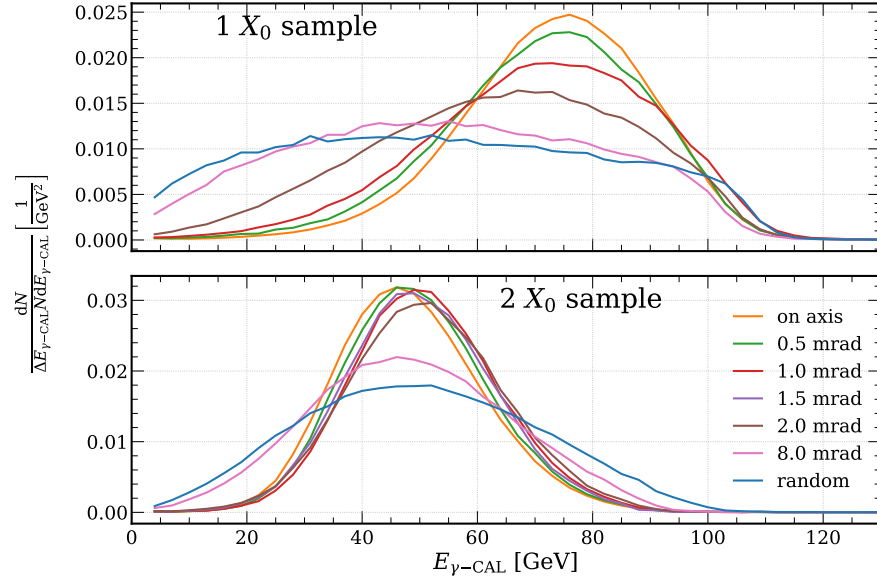


FIGURE 5.29:  $E_{\gamma\text{-CAL}}$  spectra as a function of the misalignment angle, obtained from the measurements performed on the 1  $X_0$  and 2  $X_0$  samples.

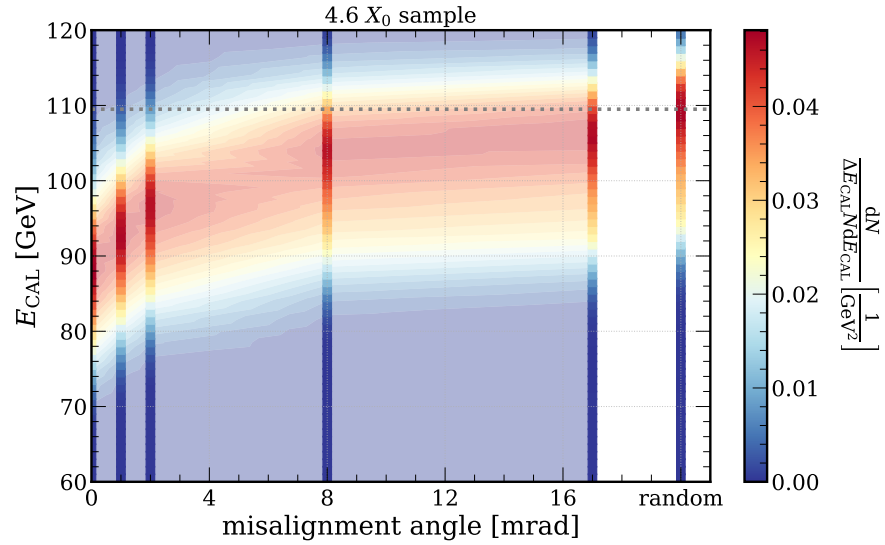


FIGURE 5.30:  $E_{\text{CAL}}$  from the PWO 4.6  $X_0$  sample as a function of the misalignment angle. The vivid (shaded) parts of the contour plot correspond to the actual data (graphical interpolation). The misalignment angle chosen to plot the random data is not to scale and the MPV of the spectrum measured in the latter is superimposed (dotted grey line).

output energy is particularly pronounced up to a misalignment angle of a few mrad, which is consistent with the fact that  $\Theta_0 \sim 0.908$  mrad for the axis under study, but a lower-strength effect is still attained at  $\gtrsim 17$  mrad  $\sim 1^\circ$ .

### 5.3.7.2 From the photodetector response

The SiPM data provide a more precise way than those of the photon calorimeter to evaluate the angular range of the measured coherent effects, since a change of the misalignment angle reflects a variation of the amount of energy deposited in the crystalline sample, which in turn corresponds to a shift of the scintillation spectrum MPV. This can be clearly observed in figures 5.31, 5.32 and 5.33, which show the dependence of the measured energy deposit spectra on the misalignment angle in case of the  $1 X_0$ ,  $2 X_0$  and  $4.6 X_0$  sample respectively.

All these cases feature a narrow peak centered on the axis. In each figure, the dashed green line represent the misalignment angle at which the difference between the mean energy deposited on axis and in random alignment is at 50% of its maximum. This value, which might be considered an op-

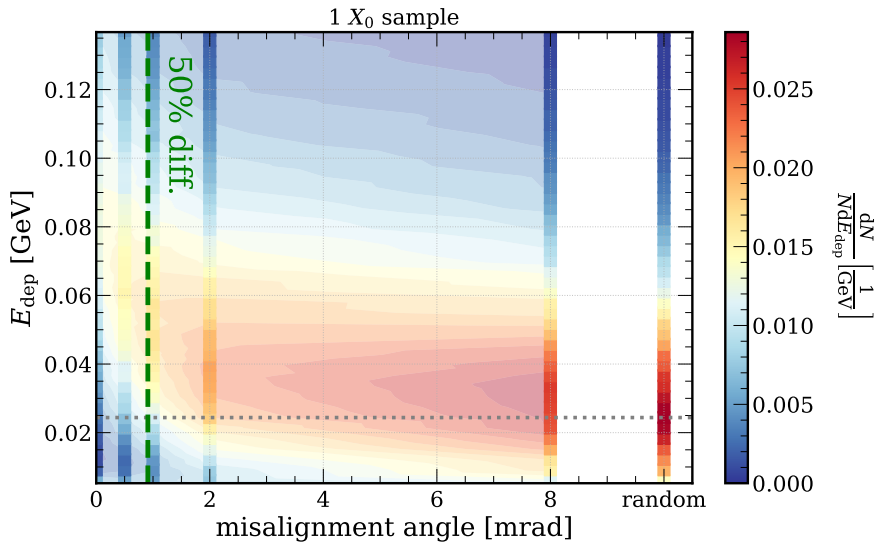


FIGURE 5.31: Scintillation light measured by the SiPMs on the PWO  $1 X_0$  sample as a function of the misalignment angle. The vivid (shaded) parts of the contour plot correspond to the actual data (graphical interpolation). The misalignment angle chosen to plot the random data is not to scale and the MPV of the spectrum measured in the latter is superimposed (dotted grey line).

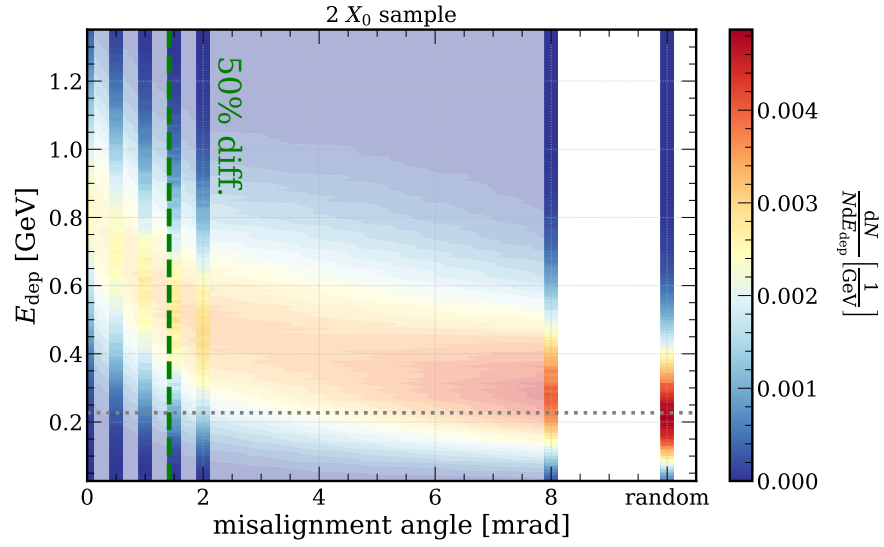


FIGURE 5.32: Scintillation light measured by the SiPMs on the PWO  $2 X_0$  sample as a function of the misalignment angle. The vivid (shaded) parts of the contour plot correspond to the actual data (graphical interpolation). The misalignment angle chosen to plot the random data is not to scale and the MPV of the spectrum measured in the latter is superimposed (dotted grey line).

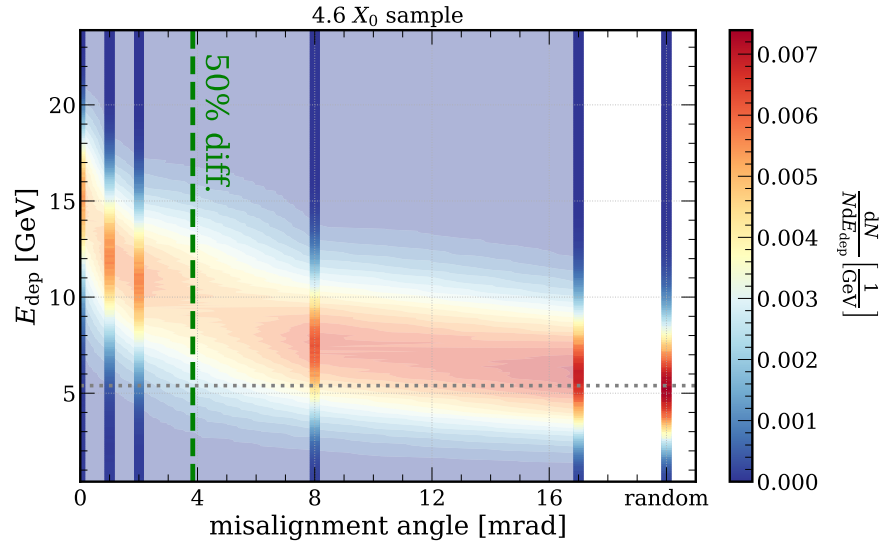


FIGURE 5.33: Scintillation light measured by the SiPMs on the PWO  $4.6 X_0$  sample as a function of the misalignment angle. The vivid (shaded) parts of the contour plot correspond to the actual data (graphical interpolation). The misalignment angle chosen to plot the random data is not to scale and the MPV of the spectrum measured in the latter is superimposed (dotted grey line).



erative estimate of the angular acceptance of the coherent processes, grows with the crystal thickness, which reflects the observations made in section 5.3.7.1. Moreover, the trend observed in figure 5.33 precisely mirrors the result obtained with the calorimeter, shown in figure 5.30.

## 5.4 Future applications

The extensive characterisation of the SF effects in increasingly thick PWO samples performed since 2016 offers a wide view on the potentiality that oriented PWO crystals has as an active medium for high-performance electromagnetic calorimeters. As anticipated in the previous sections, some aspects of the physics underneath these coherent effects, such as their effect on the effective Molière radius, are yet to be experimentally studied.

Nevertheless, applications of the concept described in this chapter to fully operational detectors are already under study. Details on the physics motivation of all the R&D projects that are currently ongoing or considered and on the related technical challenges are provided in the following.

### 5.4.1 OREO

Started at the beginning of 2023, the OREO (ORiEnted calOrimeter) project is the continuation of the INFN research line on oriented PWO. Differently from its predecessors (the latest of which being the STORM project – see section 2.1, chapter 2), OREO is mainly focused on the development of a working prototype of scintillating homogeneous calorimeter based on oriented PWO-II or PWO-UF crystals and on a SiPM-based readout system. The latter would be the first oriented crystal calorimeter worldwide.

A sketch of the prototype is shown in figure 5.34. It comprises two layers:

- the first layer consists of a  $3 \times 3$  matrix of crystals of thickness  $\sim 5 X_0$  and transverse section  $2.5 \times 2.5 \text{ cm}^2$ . All the crystals of this layer would be axially oriented.
- The second layer consists of a  $3 \times 3$  matrix of unaligned crystals of thickness  $\gg 5 X_0$  and of the same transverse section as the ones in the first layer.

Beside the advantages obtained exploiting the coherent effects in the first layer, extensively described in this chapter, another interesting feature of this detector would be the transverse segmentation, typically absent in scintillating homogeneous calorimeters.

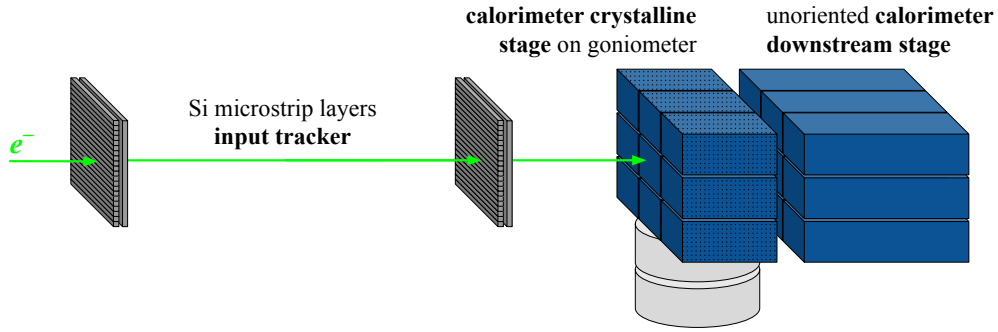


FIGURE 5.34: Sketch of the OREO calorimeter prototype and of the test setup.

In order to successfully develop the OREO prototype, it is necessary to address a few technical issues. For instance:

- it should be possible to control the lattice alignment of each first-layer crystal independently. Alternatively, if all the crystals are cut with the same side-to-axis misalignment, they should be kept in position with, e.g., a strong glue or high-precision mechanical holders.
- A misalignment between the crystal axes and the block sides should be considered, in order to install the detector at an angle with respect to the beam direction, thus avoiding the inefficiencies resulting from the gaps between adjacent blocks.
- The position of the SiPMs that read out the first layer must be optimised. In fact, placing them on the layer rear face would result in their exposure to a large flow of ionising particles and would introduce a relatively large gap in the active volume, which in turn would degrade the calorimeter energy resolution. On the other hand, placing them on the front face would result in less irradiation and in a thinner gap in the active volume, but might result in the loss of the Cherenkov light component and in an overall light collection efficiency reduction.

Dedicated studies are currently being performed on these topics.

#### 5.4.2 The HIKE SAC

As discussed in section 4.1.2.1 (chapter 4), the concept of an oriented crystal calorimeter is considered in the design of the HIKE Small Angle Calorimeter (SAC) [165]. This detector would be placed in the path of the neutral

kaon beam, which comprises large photon and neutron components, with the important purpose of guaranteeing high detection efficiency of the photons from the  $K_L$  decays in the experiment forward region.

In particular, for the background veto performance to be satisfactory, the photon detection inefficiency must be kept  $< 1\%$  for photons of energy between 5 GeV and 30 GeV<sup>3</sup> and  $< 0.01\%$  for higher-energy photons [165]. At the same time, the SAC must be able to handle the massive hadron rate, which requires it to have [165]

- a  $X_0/\lambda_I$  ratio as small as possible;
- excellent single-pulse ( $\lesssim 100$  ps) and double-pulse (a few ns) time resolution values;
- a fine transverse and longitudinal segmentation, in order to provide photon-hadron discrimination through the spatial distribution of the signal inside the detector.

Moreover, given the high beam intensity which it is subject to, this detector must be highly radiation-tolerant [165].

All the requirements listed above would be met by a PWO-based calorimeter consisting of multiple  $\sim 4 X_0$  thick layers of small-section ( $\sim 2 \times 2$  cm<sup>2</sup>) crystals [165]. PWO-UF proves particularly appealing in this design, owing to its small decay time constant, good light yield and high radiation tolerance [165] – see section 5.2.2.

Since the SAC acceptance will extend at most to 2 mrad, i.e., less than the SF angular range measured on  $4.6 X_0$  thick PWO (section 5.3.7), the electromagnetic shower enhancement attained under axial alignment and, in turn, the reduction of the  $X_0/\lambda_I$  ratio can be exploited to build a compact detector with excellent transparency to the neutron component [165, 224]. The details of the design, such as the required total number of layers and number of oriented layers, will be determined with new measurements – performed in synergy with the OREO project – and Geant4 simulations.

### 5.4.3 Satellite-borne calorimeter

The experimental investigation of several fields of astrophysics is based on the observation of multi-GeV  $\gamma$ -ray sources. For instance, in case of the Fermi LAT [98], photons impinge on multiple thin tungsten layers, which force them

---

<sup>3</sup>For an energy of  $< 5$  GeV the SAC can be blind, as the background processes that are not efficiently vetoed by other means do not feature photons within its acceptance [165].

to convert into  $e^+e^-$  pairs [98]. These conversion foils are interleaved with silicon microstrip sensors which track the charged particles and reconstruct the photon incident angle [98]. Then, the produced pair impinges on a scintillating homogeneous calorimeter made of CsI bars with a total thickness of  $10 X_0$ .

Since the cosmic  $\gamma$ -ray sources emit high-energy photons that propagate to Earth with a very narrow angular distribution, the coherent effects discussed in this chapter could be exploited to attain higher-performance observatories. Indeed, next-generation  $\gamma$ -ray telescopes on satellites, based on the same concept as the Fermi LAT and equipped with a pointing system, could be significantly improved using an oriented crystal calorimeter to reduce the detector thickness and, in turn, the payload volume and weight and the launch cost, while attaining the current state-of-the-art performance, or to maintain the same thickness as in current designs with an improvement of the detector energy resolution.

The latter option proves particularly appealing for two reasons. Firstly, in case of a randomly oriented PWO-based detector, the shower peak is located at  $\sim 10 X_0$  for incident 120 GeV particles, and would be at  $> 10 X_0$  for higher-energy particles – see figure 5.11 top. On the other hand, when the detector is axially oriented, the shower peak is well contained in  $10 X_0$  at any energy up to several hundreds of GeV. Secondly, the calorimeter performance would be enhanced when observing a source within the angular acceptance of the coherent effects, and the detector would still operate with the performance typical of the current, not oriented state of the art at larger angles.

Furthermore, a satellite-borne crystal calorimeter would exploit the improved photon-hadron disambiguation and, if finely segmented, would be sensitive to the direction of the incoming charged particles and, in turn, of the parent photon, thus improving the overall angular resolution of the telescope. Similarly, the conversion foils in the tracking system could be made of an oriented heavy metal in crystalline form, in order to exploit the PP enhancement discussed in chapter 4 and, hence, reduce the overall payload weight. Currently, preliminary simulation studies on the development of an oriented crystal calorimeter for a space-borne  $\gamma$ -ray detector are at an early-development stage. An oriented detector of this kind might prove particularly beneficial to a next-generation space mission aimed at, e.g., the observation of  $\gamma$ -ray sources not identified by Fermi, the follow-up of flaring, transient and multi-messenger sources and/or the search of dark matter decays around the galactic centre.



# Conclusions

The strong electromagnetic field experienced by ultrarelativistic particles crossing crystals with a small angle with respect to the lattice axes affects the features of their interactions with the crystalline medium. In particular, both the radiation emission by electrons and positrons and the photon conversion into charged pairs are enhanced with respect to the case of amorphous materials or randomly aligned crystals, which corresponds to a significant acceleration of the development of the electromagnetic shower and, in turn, to a reduction of the effective radiation length experienced by the incident particles.

In recent years, several radiation emission, pair production and shower development measurements have been performed in a wide variety of high- $Z$ , high-density crystalline samples: the aforementioned strong-field effects have been demonstrated and characterised in crystalline tungsten and lead tungstate and in a wide range of energies – from a few hundreds of MeV to more than 100 GeV. Most notably, the spectra of

- the energy of the electromagnetic particles exiting the crystal;
- the crystal output particle multiplicity;
- the energy deposited inside the crystal;
- the light emitted in crystalline inorganic scintillators;

have been measured, for several samples, at different initial energies and beam-to-axis misalignment angles.

Monte Carlo simulation tools are available to reproduce these effects, in the form of a dedicated algorithm that computes the particle dynamics inside the crystalline medium and of an effective modification of the bremsstrahlung and pair production cross sections in the Geant4 toolkit. Full-setup simulations of the measurements presented in this thesis work have been performed: their excellent compatibility with the experimental results validates the performance of the simulation framework. Further improvements

of these tools are envisaged in the future, such as the implementation of the dependence of the interaction features on the misalignment angle.

The enhancement of the electromagnetic processes can be exploited to improve the performance of next-generation particle accelerators and detectors. Crystalline tungsten might be used to develop a high-performance positron source for the next-generation lepton colliders, such as the FCC- $ee$ . In practice, the innovative hybrid positron source scheme comprises an oriented tungsten target to efficiently generate bremsstrahlung photons from the interactions of the high-intensity electron beam, and a thicker amorphous target to convert these photons into  $e^+e^-$  pairs. This solution would allow for a significantly better trade-off between the output positron yield, the output emittance and the deposited energy than the conventional scheme, which is currently used. Several studies have been performed on tungsten samples to prove the feasibility of this concept. In particular, a beamtest was performed at DESY to measure the features of the radiation emitted by 5.6 GeV electrons impinging on crystalline tungsten. At the same time, the performance of the hybrid scheme has been studied, with dedicated simulations, as a function of several setup parameters – the crystal thickness, the amorphous converter thickness, the distance between the two, the presence of collimators and/or magnetic fields in between, etcetera: different configurations have different advantages and disadvantages, and the choice of the best option depends on the features of the downstream accelerating chain, which is yet to be designed in detail.

Moreover, an oriented tungsten target might be placed along the path of a neutral hadron beam with a large photon contamination, in order to efficiently eliminate the latter. Differently from the electromagnetic processes, the hadronic interactions in crystals are not affected by the lattice orientation. As a consequence, the strong-field reduction of the radiation length corresponds to a reduction of the ratio between the radiation length and the nuclear interaction length, so a compact target can be developed with enhanced photon conversion probability and, at the same time, minimum effect on the hadron beam emittance. This concept would be exploited by the HIKE experiment, currently under development at CERN. Dedicated measurements have been performed at the CERN North Area on a thick commercial tungsten sample, which demonstrated that, when the photon beam is aligned to the lattice axes, a significant amount of the incident photons is converted into  $e^+e^-$  pairs, and a macroscopic fraction of the initial energy (which is between  $\sim 20$  GeV and  $\sim 100$  GeV) is absorbed by the sample.

Lead tungstate ( $\text{PbWO}_4$  or PWO) is one of the densest and fastest inorganic scintillators, and is commonly used as the active medium in homoge-

neous electromagnetic calorimeters. Despite its crystalline nature, the lattice orientation has always been ignored in the detector design. Nevertheless, the strong-field shower acceleration might be used to develop homogeneous calorimeters that would rival the current state of the art in terms of energy resolution while being more compact and having improved particle identification performance. This entirely novel possibility has been explored in recent years, and several measurements of the strong-field effects in increasingly thick lead tungstate samples have been performed, at CERN (at 120 GeV – in the strong field regime) and DESY (at 5.6 GeV – in the sub-strong field regime). The on-axis enhancement of the scintillation light emission has been observed for the first time, and shows an excellent agreement with the simulations. The concept of an oriented calorimeter proves particularly appealing for applications with a well-defined and narrow angular spectrum – for instance, accelerator-based experiments with a forward geometry and satellite-borne  $\gamma$ -ray telescopes. In particular, this design is currently considered for the design of the HIKE Small Angle Calorimeter. Meanwhile, the INFN OREO project aims at the development of the operational prototype of a longitudinally (as well as transversely) segmented, oriented crystal calorimeter by 2024.





# APPENDIX **A**

---

## Calorimeter calibrations

One of the most important aspects of the characterisation of the coherent interactions in crystals is the measurement of the energy of the  $e^\pm$  and photons involved. This is done with the calorimeters, which can be arranged in many different configurations depending on the type of measurement to be performed – see section 2.3 (chapter 2).

In order to measure the energy in GeV, the conditioning of the raw data obtained from the calorimeters is required, a summary of which is provided in this appendix. In general, the calibration procedure of a calorimeter – and, in case of multi-channel detector, the equalisation between different channels – is performed with a standard procedure, discussed in section A.1. On the other hand, some of the measurements presented in this work required minor variations with respect to the standard calibration procedure: details on the latter are provided in sections A.2 and A.3.

### A.1 General information

The first step of the data conditioning of a multi-channel calorimeter is the equalisation of the response of the single channels [107]. In general, this is done with a highly collimated muon beam directly impinging on the centre of the active volume of each channel [107].

High-energy muons are MIPs, so the energy they deposit when crossing a target only depends on the material of the latter and on the length of the

section of their trajectory inside it [107]. Therefore, a comparison between the average signals resulting from muons crossing different calorimeter channels with the same impact position at the front and incident angle allows to measure the mutual differences between their responses [107].

This response inhomogeneity is due to differences, e.g., in the quality of the coupling between the channel active volume and the corresponding acquisition chain and in fluctuations of the performance of the latter and can account for macroscopic relative variations [107]. For instance, figure A.1 left shows the Genni single-channel MIP spectra measured in a beamtest on the CERN T9 beamline in 2018 – details can be found in [107].

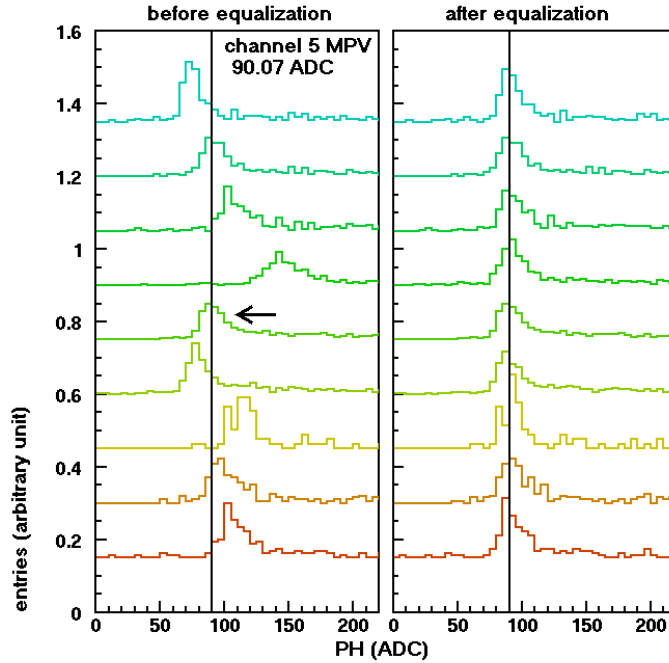


FIGURE A.1: Direct MIP spectra of the Genni calorimeter single channels, before (*left*) and after (*right*) the equalisation procedure. The reference channel is indicated with a black arrow. From [107].

The MPV of each spectrum is obtained by fitting it with a Landau function and one of the channels is chosen as reference [107]. Then, the transformation

$$PH_j \rightarrow PH_j^{\text{eq}} = \frac{MPV_{\text{ref}}}{MPV_j} PH_j \quad , \quad (\text{A.1})$$

where  $\text{MPV}_{\text{ref}}$  is the reference channel MPV spectrum, is applied to the  $j$ -th channel [107]. Figure A.1 right shows the spectra of the equalised calorimeter data.

Once the equalisation procedure has been done, it is possible to sum the signals from all the calorimeter channels and perform the ADC-to-GeV calibration [107]. The latter is obtained from runs performed with different-energy electron beams impinging at the calorimeter centre [107]. Figure A.2 top shows the corresponding spectra. A linear correlation is found between the peak positions of these spectra and the nominal energies of the corresponding beams,  $E$  (figure A.2 bottom left). Moreover, the energy resolution can be estimated as  $\sigma_E/E$ , where  $\sigma_E$  is the width of the monoenergetic spectra [107] (figure A.2 bottom right), which leads to equation 2.2 (chapter 2).

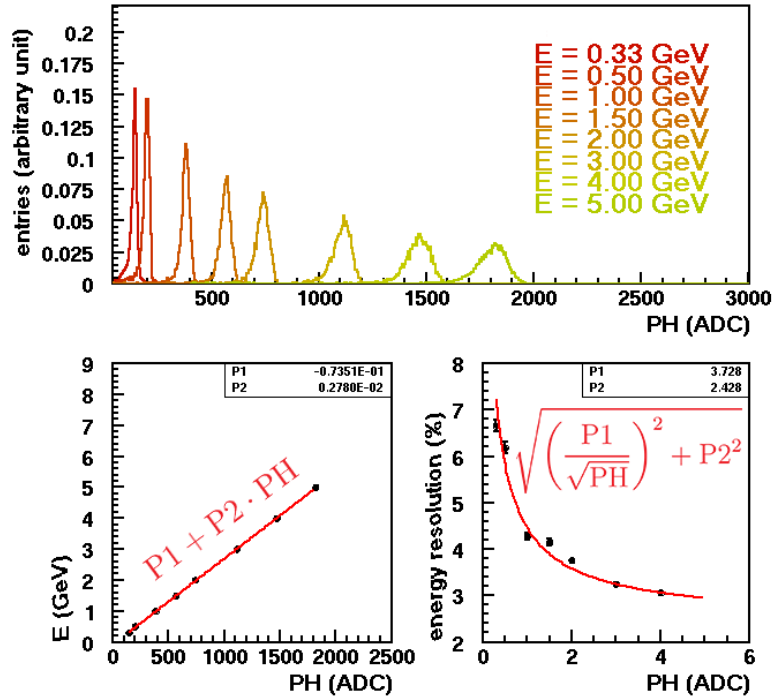


FIGURE A.2: Direct monoenergetic electron beam spectra (*top*), linearity (*bottom left*) and energy resolution (*bottom right*) of the Genni calorimeter. Edited from [107].

## A.2 Genni at the 2019 beamtest on DESY T21

As muon beams are not available on the DESY beamlines, the equalisation procedure has to be performed with electrons. This has a caveat: the single channels of the Genni calorimeter are thin and thus suffer significant lateral leakage, which results in a strong non-linearity of the signal as a function of the incident electron energy. The latter is shown in figure A.3: the MPVs of the monoenergetic peaks are obtained by mirrored Landau fits and are shown in the plot at the bottom in correlation with the nominal electron energy; a saturation is clearly visible already at a few GeV.

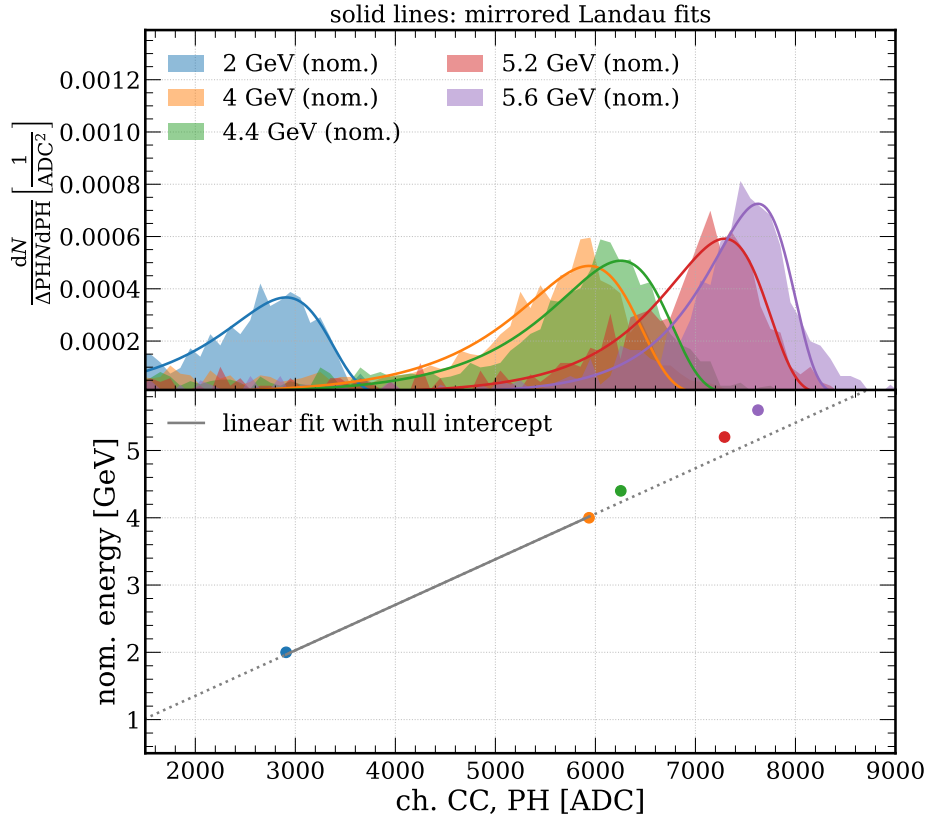


FIGURE A.3: Genni central channel equalisation data: (*top*) PH spectra of the particles impinging on the BGO block at the front centre, measured at different energies, and (*bottom*) correlation between the Landau MPVs obtained from fitting the latter and the corresponding reference energies obtained from simulations.

Each of the nine channels of Genni shows a trend like the one shown in figure A.3 bottom. In order to equalise their response while correcting for the single-channel lateral leakage, these curves are fitted with the function

$$f(k; a^{\text{NL}}, b^{\text{NL}}) = \frac{k}{a^{\text{NL}} - b^{\text{NL}}k} \quad , \quad f^{-1}(k; a^{\text{NL}}, b^{\text{NL}}) = \frac{a^{\text{NL}}k}{1 + b^{\text{NL}}k} \quad , \quad (\text{A.2})$$

and then the transformation

$$\text{PH}_j \rightarrow f^{-1} [f(\text{PH}_j; a_j^{\text{NL}}, b_j^{\text{NL}}); a_{\text{ref}}^{\text{NL}}, b_{\text{ref}}^{\text{NL}}] = \frac{a_{\text{ref}}^{\text{NL}} \text{PH}_j}{(b_{\text{ref}}^{\text{NL}} - b_j^{\text{NL}}) \text{PH}_j + a_j^{\text{NL}}}$$

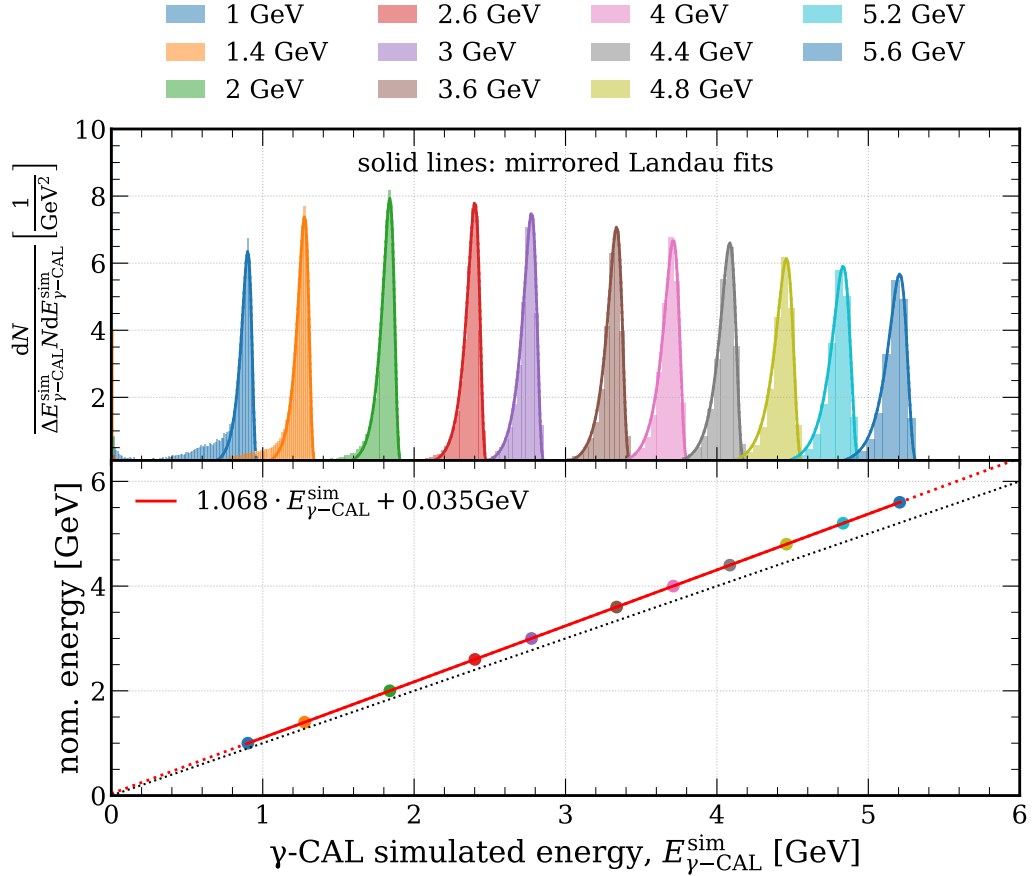


FIGURE A.4: Simulated Genni calibration: (*top*) spectra of the energy deposit in the calorimeter at different input beam energies (different colours), and (*bottom*) correlation between the Landau MPVs obtained from fitting the latter and the corresponding input beam energies.

is applied, where  $a_j^{\text{NL}}$  and  $b_j^{\text{NL}}$  ( $a_{\text{ref}}^{\text{NL}}$  and  $b_{\text{ref}}^{\text{NL}}$ ) are the coefficients obtained for the  $j$ -th channel (for one of the channels chosen as reference). The total energy deposit in ADC is then obtained summing all the  $\text{PH}_j$  values.

As discussed in section 2.3.1.2 (chapter 2), the Genni transverse half section is only  $\sim 1.39 R_{\text{M}}$ . Together with the fact that the beam divergence is rather high (see section 2.2.1, chapter 2) and, hence, the hit points at the detector front are spread throughout its whole face, this results in a non-negligible lateral leakage.

Firstly, the correlation between the nominal beam energy and the energy that is actually deposited in Genni,  $E_{\gamma\text{-CAL}}^{\text{sim}}$ , has been studied with the beamtest Geant4 full simulation – see section 3.2.2.1 (chapter 3). As shown in figure A.4, there is an approximately linear relation between nominal beam energies and the MPVs of the corresponding simulated energy deposit distributions. The latter are  $\sim 1/1.07 \sim 93\%$  of the former.

The ADC-to-GeV calibration of the experimental data (figure A.5) is performed using the values of  $E_{\gamma\text{-CAL}}^{\text{sim}}$  rather than the nominal beam energies. The correlation curve between  $E_{\gamma\text{-CAL}}^{\text{sim}}$  and the MPVs of the experimental distributions obtained at different electron energies in ADC (figure A.5 bottom) clearly shows a non-linear trend due to the lateral leakage, which is corrected choosing a calibration curve of the form of  $f^{-1}$  defined in equation A.2.

## A.3 Lead glass blocks on CERN H2

As discussed in section 2.3.1.2 (chapter 2), the lead glass blocks exploited in several beamtests on the CERN H2 beamline have a transverse section of side  $> 2 R_{\text{M}}$ . As a consequence, a single block can essentially contain an entire shower generated by a primary particle impinging on the centre of its front face. Therefore, the signal of each block can be calibrated individually or equalised with electron beams impinging on the centre of the front face with a negligible lateral leakage. Multi-channel configurations are used to cover large areas like, for instance, that of a magnetic spectrometer (see, e.g., the photon tagging system described in section 2.3.4, chapter 2) or of the particles at the exit of a very thick crystal (see, e.g., the setup described in section 2.3.5, chapter 2, and in section A.3.2 below).

### A.3.1 Single-block performance

Figure A.6 top shows the spectra obtained with different-energy electron beams impinging on one of the lead glass blocks on the H2 beamline in

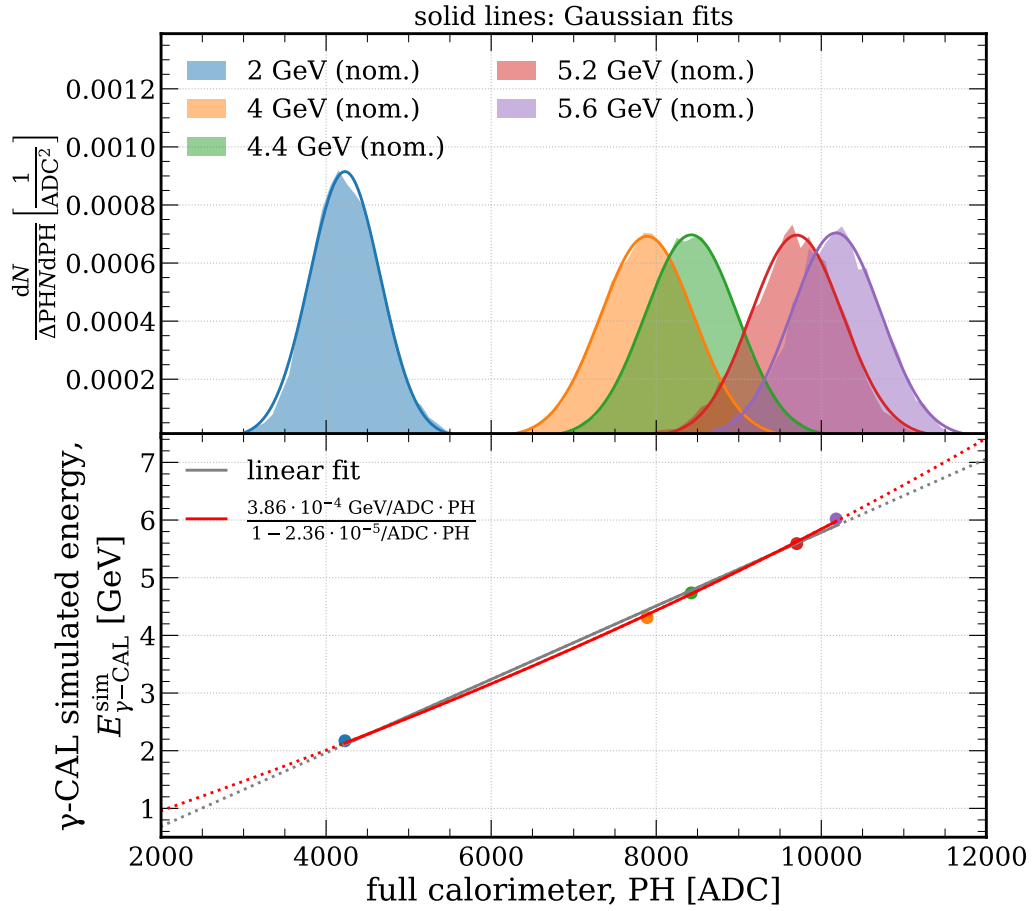


FIGURE A.5: Experimental Genni calibration: (*top*) spectra of the calorimeter PH at different nominal beam energies (different colours), and (*bottom*) correlation between the Gaussian means obtained from fitting the latter and the corresponding simulated energy deposit values.

2022. In each beam, there is a significant number of particles whose energy is below the nominal value – see section 5.3.2.2 (chapter 5). However, the peaks corresponding to the beam core are narrow and can be clearly selected; the corresponding MPVs are found by means of Gaussian fits and show a linear behaviour as a function of the nominal beam energies – see figure A.6 bottom.

The energy resolution of the block (equation 2.3, chapter 2) has been measured, and is shown in figure A.7. The stochastic term is rather large for a homogeneous calorimeter – compared, for instance, to that of Genni in figure A.2 –, whereas the noise term is  $\ll 100$  MeV and the constant term is negli-



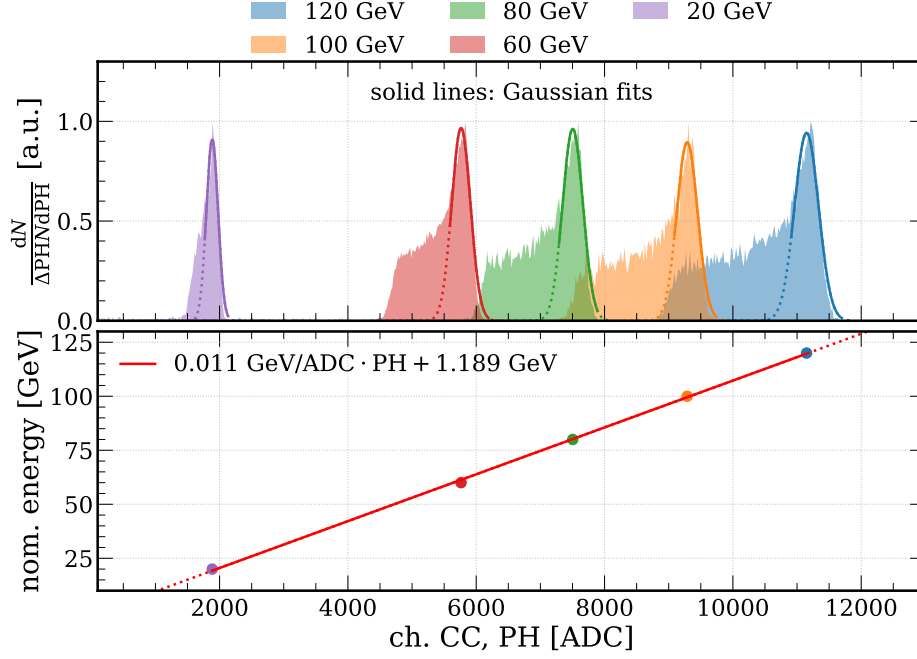


FIGURE A.6: Calibration of the central lead glass block of the calorimeter installed at the 2022 beamtest on CERN H2: (*top*) spectra of the channel PH at different nominal beam energies (different colours), and (*bottom*) correlation between the Gaussian means obtained from fitting the latter and the corresponding nominal beam energies.

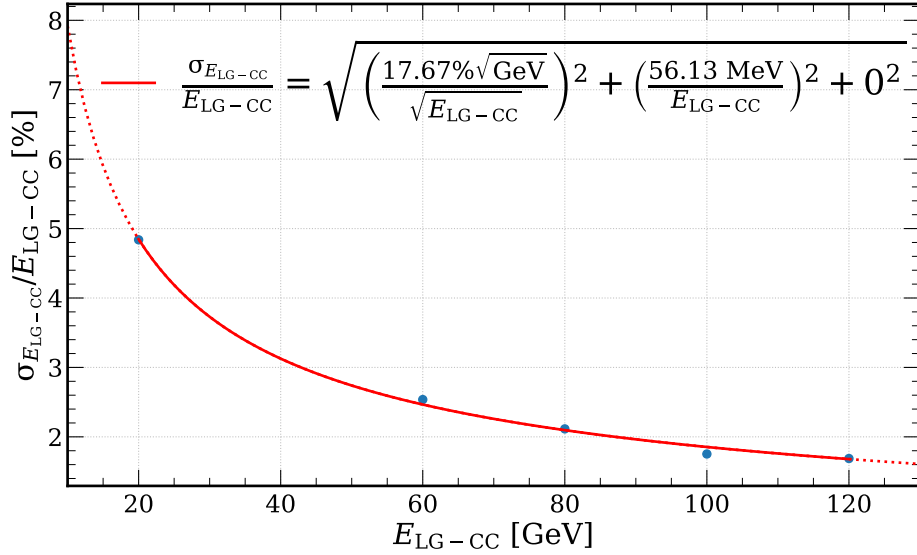


FIGURE A.7: Energy resolution of the central lead glass block of the calorimeter installed at the 2022 beamtest on CERN H2.

ble. All the lead glass blocks installed on the H2 beamline between 2018 and 2022 feature approximately the same performance in terms of energy resolution. However, major biases induced by time instability and non-uniformity of the response were observed in some of the blocks exploited in 2018 – details are provided in appendix C.

### A.3.2 The 2022 hibiscus-like configuration

In the 2022 beamtest on the CERN H2 beamline, the hibiscus-like array of lead glass blocks described in section 2.3.5 (chapter 2) was exploited to measure the energy of all the secondary particles generated in thick crystalline samples. The geometry of the array can be observed in figure A.8, which shows the hit positions of electron beams impinging on the centre of each lead glass block.

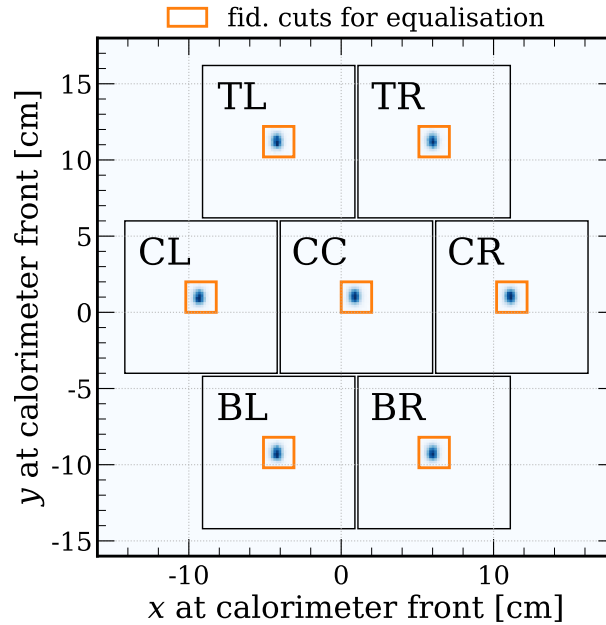


FIGURE A.8: Spatial distribution of the hibiscus-like calorimeter calibration data in the transverse plane.

Data were collected with several different nominal energies up to 120 GeV/ $c$  on the central channel (CC) and 60 GeV/ $c$  on all the lateral channels. The equalisation was performed by means of equation A.1 with the data collected at 60 GeV/ $c$ , and is shown in figure A.9. The calorimeter total signal at different energies and its correlation with the nominal beam energy values

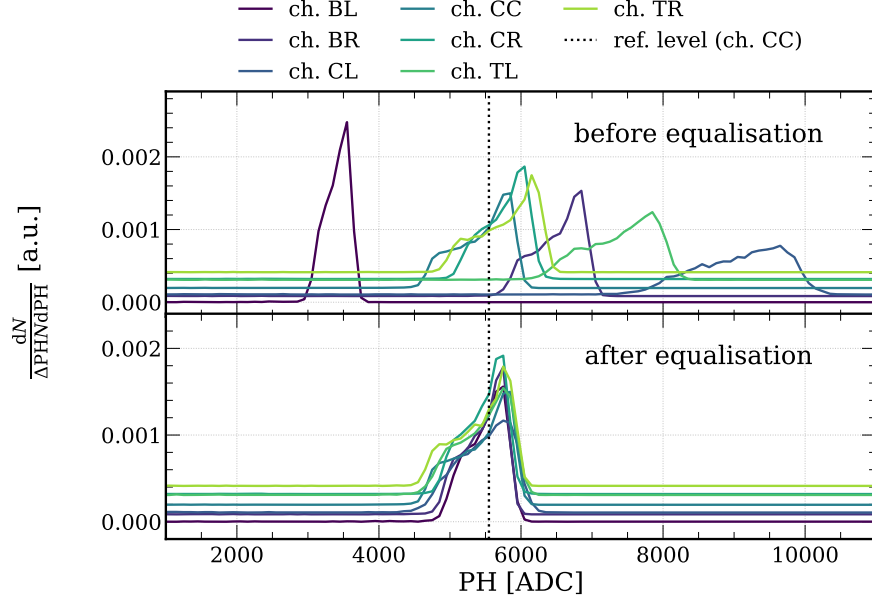


FIGURE A.9: PH spectra of the hibiscus-like calorimeter channels directly hit by 60 GeV/c electrons, before (*top*) and after (*bottom*) equalising the response of all the channels.

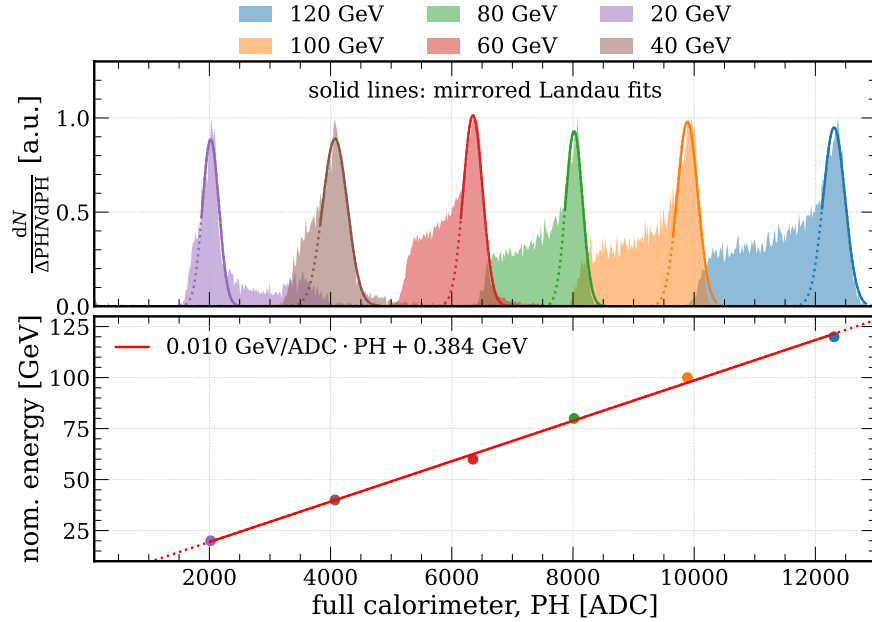


FIGURE A.10: Calibration of the whole hibiscus-like calorimeter installed at the 2022 beamtest on CERN H2: (*top*) spectra of the calorimeter PH at different nominal beam energies (different colours), and (*bottom*) correlation between the Gaussian means obtained from fitting the latter and the corresponding nominal beam energies.

are shown in figure A.10. As expected, the response of the detector is linear in the whole explored energy range.

The energy resolution of the hibiscus-like array is shown in figure A.11. It can be compared to the result obtained for the single lead glass block (figure A.7), which highlights that

- the stochastic term is smaller in this configuration than in case of a single block;
- the noise term is bigger than that of a single block, but the noise term divided by the number of channels is smaller.

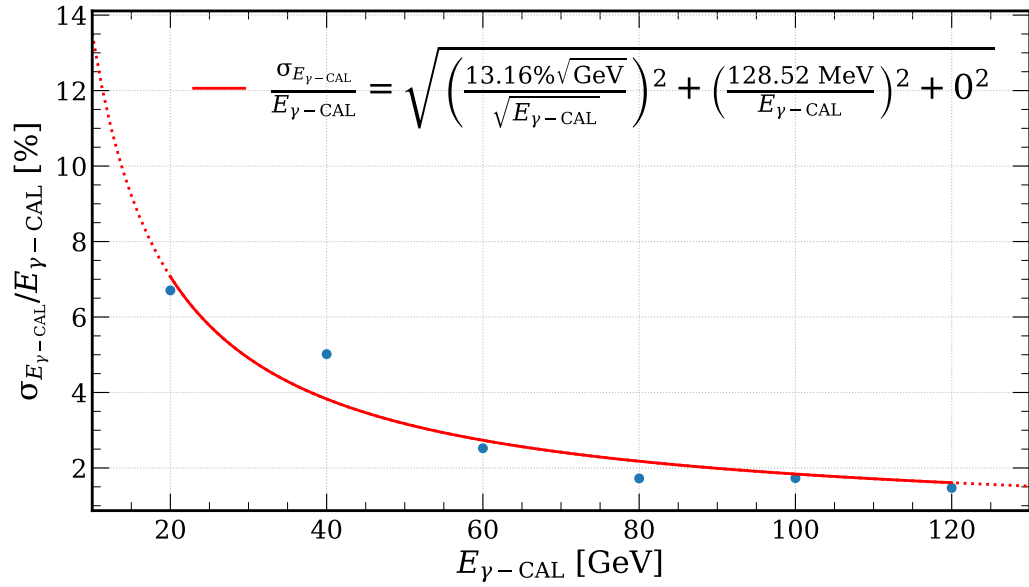


FIGURE A.11: Energy resolution of the whole hibiscus-like calorimeter installed at the 2022 beamtest on CERN H2.



# APPENDIX B

---

## Radiation and heating in tungsten towards the FCC-*ee* intensity

For the investigation on the most suitable positron source scheme for the FCC-*ee* and for the choice of the parameters in both the conventional and the crystal-base hybrid cases to be optimal, radiation hardness and heating resistance tests have to be performed on both crystalline and amorphous targets. This appendix completes the studies presented in chapter 3 with the results of an irradiation session performed at the MAMI (MAInzer MIkrotron) B beamtest facility with a high-intensity, low-emittance, 855 MeV electron beam on [111] tungsten. Furthermore, the results of simulations of energy deposit in amorphous tungsten by 855 MeV electrons, which have been performed with an eye on the preparation of future beamtests at MAMI B, is presented.

### B.1 The MAMI B beamtest facility

The MAMI B facility provides ultra-thin ( $\sim 100\text{ }\mu\text{m}$ ), low-divergence ( $\sim 10\text{ }\mu\text{rad}$ ), high-intensity (from the pA scale to several  $\mu\text{A}$ ) CW electron beams in the sub-GeV energy regime [120] – a 855 GeV beam is typically used. These experimental conditions prove suitable for the measurement of CR

emission. Depending on the material under study, there are limitations on the sample thickness, both for radioprotection-related issues and to guarantee that the number of emitted photons per incident electron is as low as possible – ideally equal to 1, as the single-photon regime can easily be compared to the theoretical predictions.

The crystalline sample is mounted on a remotely controllable goniometer, which allows lateral translations and a high-precision alignment of the lattice axes at specific angular position with respect to the beam direction [120, 226]. In order to keep the beam emittance as low as possible along the whole path, the entire apparatus is kept under vacuum [226]. For the same reason, no tracking system is installed along the incident beam path, nor would be necessary, as the Lindhard angle at 855 GeV is 232  $\mu\text{rad}$  for silicon aligned to the (111) plane and much larger for higher- $Z$ , higher-density materials in axial alignment, i.e., significantly larger than the beam divergence [226].

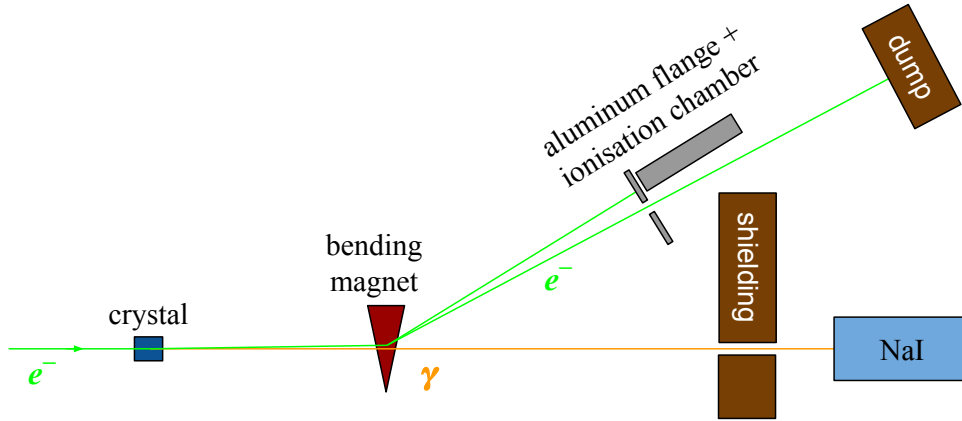


FIGURE B.1: Sketch of the MAMI B beamtest hall.

A bending magnet separates the electron beam and the photons resulting from the interactions in the sample. The former is directed towards a beam dump; ionisation chambers are positioned along the output electron beam path, slightly off with respect to the beam axis: they detect fluctuations in the multiplicity of the electrons with large transverse momentum, which hit an aluminum flange and start an electromagnetic shower; the presence of lattice planes/axes during a scan on one of the goniometer DOFs determines an increase in the MCS by beam electrons and, hence, an increase in the signal of the chambers [104]. The photon component propagates down to a cylindrical NaI calorimeter with a thickness of 25.4 cm and a transverse diameter of 25.4 cm [104] read out by a PMT and surrounded by a 10 cm thick lead shield with a variable-size aperture (typically 40 mm  $\varnothing$ ) at the front [104, 120, 226].

Recently, the possibility of exploiting the beam dump region (top right corner of figure B.1) has been explored: the area is equipped with a remotely controllable goniometer which only allows for lateral movements and proves suitable for heavy-irradiation sessions with very high beam intensity: preliminary tests have been performed at the end of 2021 [227] and preparations are ongoing for future runs – see section B.3.

## B.2 Crystalline tungsten irradiation at the MAMI B hall

Radiation measurements have been performed between 2020 and 2021 on two nearly identical tungsten samples: both were 1 mm thick along the [111] axis, with a transverse size of 8 mm [227]. One was purchased by the INFN Ferrara team, the other one by IJCLab. Radiation spectra emitted by 855 GeV electrons in axial alignment and at a large angle from the axis (random orientation) were measured on both the samples before any long exposure to the high-intensity beam. Then, the crystal by IJCLab was irradiated for  $\sim 22.5$  hours with a CW beam current of 8–10 nA [227], in order to investigate how the heavy irradiation load affects the crystalline potential features.

The photon energy is measured with the NaI calorimeter. In each beamtest, the response of the calorimeter is calibrated exploiting the environmental

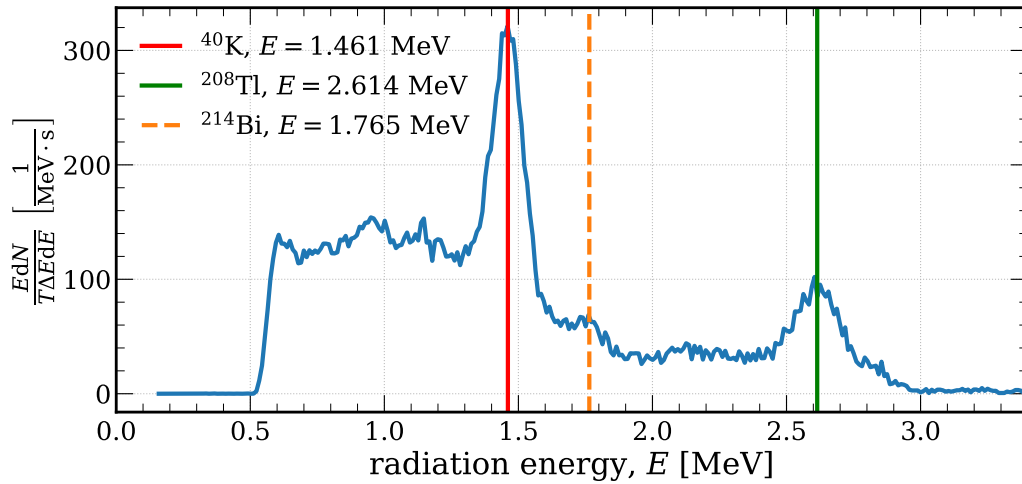


FIGURE B.2: Background spectral intensity after calibrating the NaI calorimeter with the  $^{40}\text{K}$  and  $^{208}\text{Tl}$  peaks (solid lines).



radioactivity in the experimental hall. In particular, as shown in figure B.2, two  $\gamma$ -ray peaks are chosen – the  $^{40}\text{K}$  peak at 1.461 MeV and the  $^{208}\text{Tl}$  peak at 2.614 MeV – and a calibration line is drawn between them. The latter is then validated by correctly attributing the peak at 1.765 MeV to  $^{214}\text{Bi}$  (dashed line).

The physics analysis has been performed using the software available in [228]. Figure B.3 left shows the spectral intensities obtained, in the (0,165) MeV range, on both samples before irradiation and on the IJCLab sample after irradiation, for the random and axial configurations. All the distributions are normalised to the acquisition time – typically  $\sim 300$  s. It is clear that the three datasets differ from one another in the measured frequencies, probably due to variations of the beam intensity between different runs, which were performed with a significant time interval between one another –  $\sim 1$  year in case of the sample by INFN Ferrara.

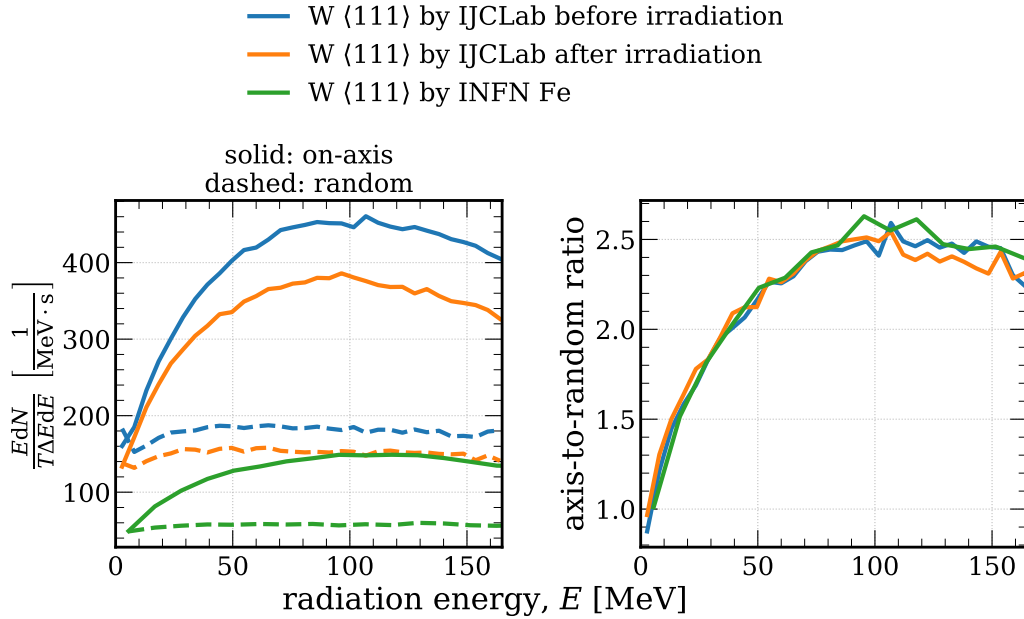


FIGURE B.3: Radiation spectral intensities (*left*) in axial (solid curves) and random (dashed curves) orientation and ratio between the two (*right*) for two different W [111] identical samples: one belongs to INFN Ferrara (green), the other one to IJCLab; the latter was tested before (blue) and after (orange) an irradiation session.

The results for different samples and irradiation stages can be compared to one another independently on the beam relative intensities considering the ratios between axial and amorphous-like spectra rather than the spectra, or

spectral intensities, of the single runs. These ratios are shown in figure B.3 right: a strong axial-to-random enhancement – of up to 250%, at  $\sim 100$  MeV – is observed. This enhancement of the soft component of the radiation spectrum results from the emission of CR which dominates in this energy regime. Furthermore, no variation in the spectrum shape is observed between the runs performed before and after the irradiation session.

### **B.3 Amorphous tungsten irradiation at the MAMI B dump**

In 2021, a preliminary irradiation session has been performed at the beam dump. Two tungsten targets were tested: a 2 mm thick, 8 mm  $\varnothing$  crystal (without any specific lattice orientation) was irradiated for  $\sim 21$  hours and a 2 mm thick, 50 mm  $\varnothing$  amorphous sample was irradiated for  $\sim 23$  hours with a pulsed beam of average current between 1 and 3  $\mu\text{m}$ ; both were instrumented with thermocouples, which allowed for a measurement of the irradiation-induced heating inside the target bulk as a function of the irradiation time. Several difficulties affected the quality of the results collected in this measurement session, which is described in detail in [227]:

- the temperature reached at the surface of the samples was too high (100–150°C in case of the amorphous target and 600–700°C in case of the crystal) for the weld of the thermocouples to resist without melting, therefore some of the thermocouples did not stay in contact with the targets for the whole session.
- In order for the temperature measurements to be compared with proper estimates of the actual energy deposit inside the samples, the size of the beam spot must be known. Since there are no means of directly measuring the beam profile at the beam dump, lateral scans were performed on the holder with the samples and data were collected with one of the thermocouples (with 75  $\mu\text{m}$   $\varnothing$ ) directly hit by the beam: the variation of the thermocouple during the scan provides an estimate of the beam size, which has been found to be of the order of 330  $\mu\text{m}$  (230  $\mu\text{m}$ ) in the horizontal (vertical) direction. For the attainable overall energy deposit value to be close to the benchmark of the FCC-*ee* environment in only  $\sim 24$  hours of irradiation, a smaller beam spot might be necessary, depending on the target size. Moreover, a more precise system for the measurement of the beam profile should be implemented in the experimental setup.

As hardware-related solutions are sought to improve the experimental conditions, i.e., better sample-to-thermocouple coupling and better beam profile measurement system, simulations are performed in order to investigate the correlation between target geometry and beam features and, hence, optimise the future irradiation sessions.

### B.3.1 The simulation software

The simulations have been performed with Geant4, with a customised version of the code exploited for the optimisation of the amorphous stage of the FCC-*ee* PS – see section 3.3.1 (chapter 3). Here, a perfectly parallel (i.e., with null divergence) 855 MeV  $e^-$  beam with box-shaped spot of variable size impinges on a tungsten<sup>1</sup> target of transverse size  $d \sim 20$  mm, i.e., at the scale of the samples typically tested at MAMI B.

Several different geometric configurations of the target have been studied. In particular, both the parallelepiped and the cylindrical shapes have been studied for the target – and the relative mesh. Moreover, runs have been simulated at different target thicknesses in order

- to investigate how the energy deposit and, consequently, the heating pattern are affected by the latter;
- to compute the transition curve.

The results are shown in figure B.4, which completes the study summarised in figure 3.2 (chapter 3) with data generated at 855 MeV. The former item in the list is directly interesting for the preparation of future irradiation sessions, as it is closely related to the integral PEDD attainable and to the sample surface temperature, which in turn has to be taken into account when developing the thermocouple system. On the other hand, the transition curve is not of immediate interest for the beamtests at the MAMI B beam dump, as no measurements of the output positrons will be performed; it merely serves as a preliminary indicator of the performance of the chosen sample as a PS target candidate.

Moreover, figure B.4 highlights that the transition curve has a maximum at 11.5 mm, very close to the value of 11.6 mm found in section 3.3.3.2 (chapter 3) despite the major differences between the two simulation environments in terms of the beam energy and type and of the target geometry.

---

<sup>1</sup>Indeed, four different materials have been studied: tungsten, tantalum ( $Z = 73$ ,  $\rho = 16.7 \text{ g/cm}^3$  [13]) and two metallic alloys, W75Re25 and Ta975W025. All of them might prove suitable options for the FCC-*ee* PS.

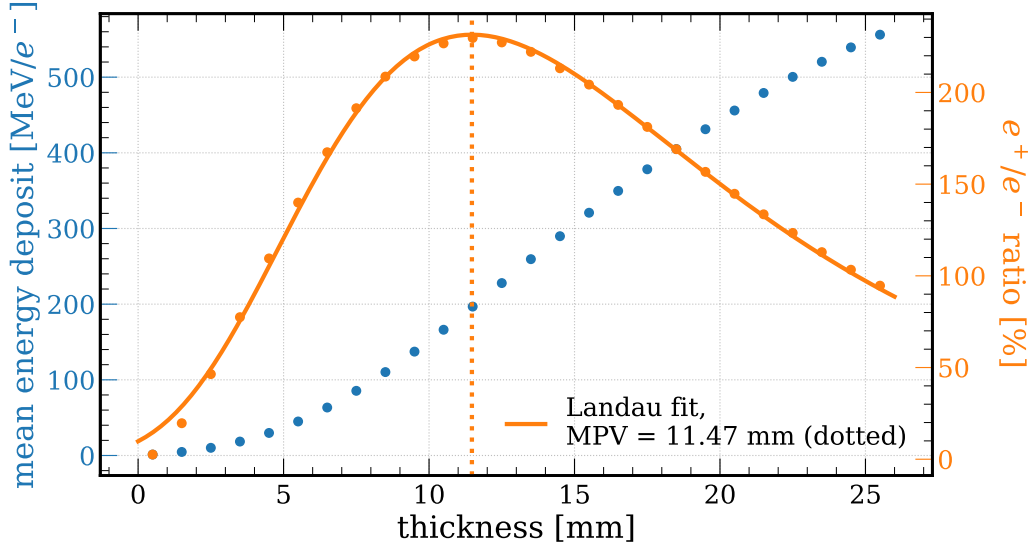


FIGURE B.4: Data from the simulation of 855 GeV electrons on amorphous tungsten: energy deposit (blue) and output positron production rate (orange). The incident beam has a spot size of 300  $\mu\text{m}$ .

### B.3.2 Defining the mesh

It is interesting to investigate how the geometry of the target and hence of the mesh (i.e., shape and voxel size) affects the characterisation of the energy deposit pattern, which is correlated to the heating properties of the bulk. Particular care should be taken in studying how the longitudinal and transverse size of the voxels at the centre of the target affects the computation of the PEDD, especially if the latter is evaluated by merely taking the maximum value of energy density per voxel.

Indeed, bigger voxels imply that a larger fraction of the volume around the energy deposit peak is included in the average; since the energy deposit becomes smaller as the distance from the peak grows, this results in a lower value of energy density associated to the voxel around the peak and, thus, in an underestimation of the PEDD. On the other hand, smaller voxels result in large statistical fluctuations of the corresponding energy density values due to the limited statistics of the simulation. A comparison between different mesh settings, which differ from one another in shape (cylindrical and box-shaped) and voxel size (between 10  $\mu\text{m}$  and 150  $\mu\text{m}$ ), is shown in figure B.5.

In general, there are three possible solutions, each one with specific limitations:

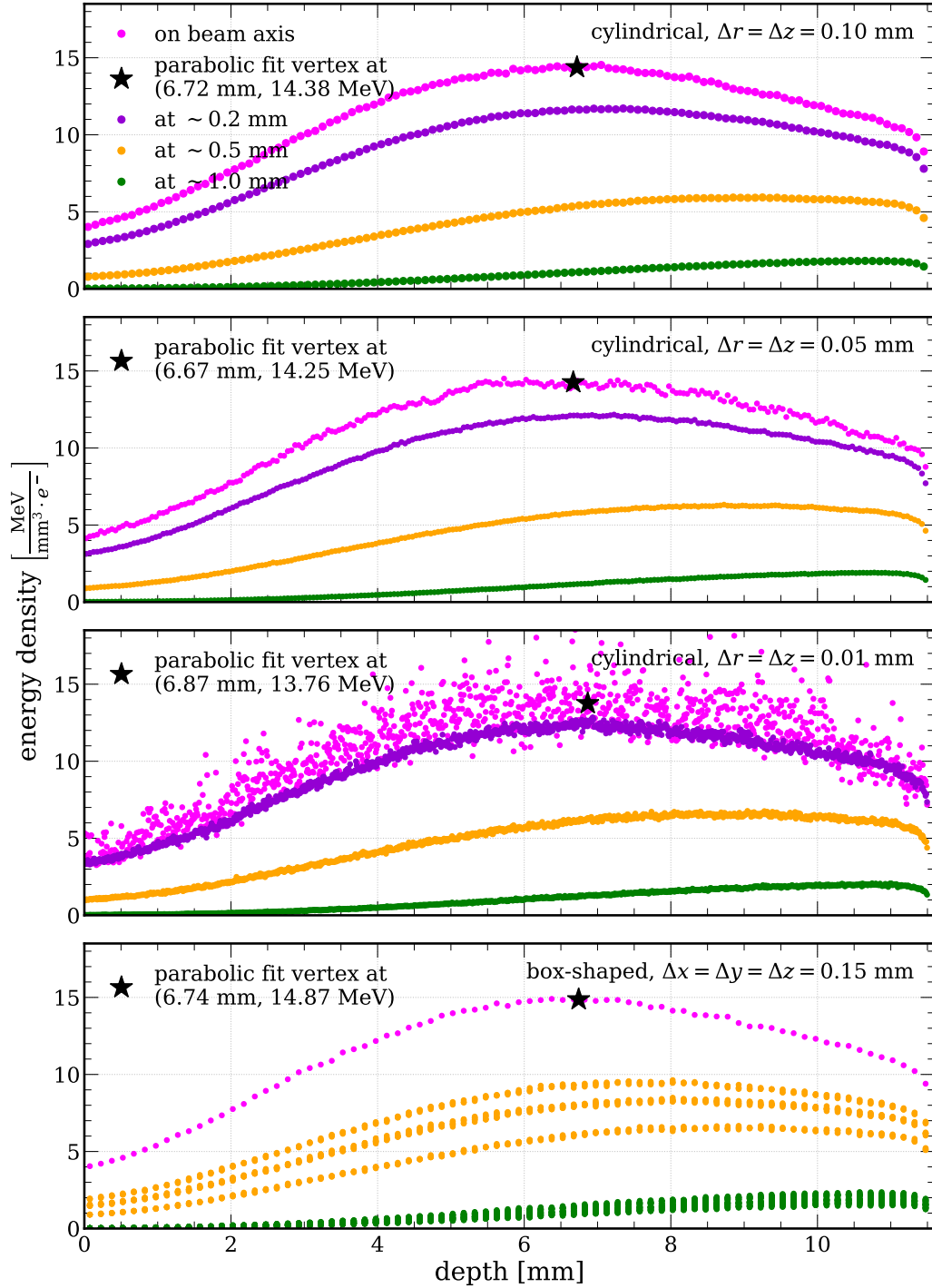


FIGURE B.5: Comparison between the energy density distributions computed from different target and mesh geometries. From top to bottom: cylindrical with  $\Delta r = \Delta z = 100 \mu\text{m}$ , cylindrical with  $\Delta r = \Delta z = 50 \mu\text{m}$ , cylindrical with  $\Delta r = \Delta z = 10 \mu\text{m}$  and box-shaped with  $\Delta x = \Delta y = \Delta z = 150 \mu\text{m}$ . The incident beam has a spot size of  $300 \mu\text{m}$ .

- define a conventional voxel size to be chosen in all the simulations run in the context of the same project, in order to make the results obtained in all the simulated cases comparable to one another. For instance, it is quite typical to choose a voxel transverse size of  $1/3$  or  $1/2$  of the incident beam size. This option is rather inflexible as it makes the mesh features dependent on the beam size, which might vary between different runs, and is ill-defined in case of an input pencil beam, i.e., a beam with point-like spot.
- Choose a small voxel size and increase the simulated statistics. The biggest drawback of this method is the significantly higher cost in terms of computational resources, as both increasing the number of primary events and increasing the voxel density in the mesh result in an increase of the latter.
- Fit the energy density curves as a function of the voxel position inside the target and take the maximum. Albeit the choice of the function to fit these curves with is non-trivial, this method proves very efficient from the standpoint of the computational resources and only loosely dependent on the mesh features.

Indeed, as shown in figure B.5, the third method applied to the transverse energy deposit trend inside the target seems to provide satisfactory results: a parabolic fit is performed on all the on-axis curves, and the resulting peak positions (heights) are distributed within  $\sim 3\%$  ( $\sim 4\%$ ) of the mean value. Eventually, in view of the work presented in this section, cylindrical target and mesh were chosen, which significantly reduces the computational cost – as the cylindrical mesh is two-dimensional (only depending on the longitudinal depth,  $r$  and on the transverse distance from the central axis,  $z$ ) rather than three-dimensional. The voxel dimensions were set to  $\Delta r = 200 \mu\text{m}$  and  $\Delta x = 100 \mu\text{m}$  and a parabolic fit was performed on the on-axis energy density as a function of the longitudinal depth.

### B.3.3 Beam parameters and heating

The energy deposit simulations performed with Geant4 provide results that are averaged over all the primary particles and hence given per incident electron. In order for them to be compared to the values of interest for the FCC- $ee$ , they have to be studied in combination with the information on the beam actually available at MAMI B. Some of the beam parameters have been fixed, i.e.,

- the repetition rate,  $R = 200$  Hz;
- the bunch period,  $\tau = 400$  ps;
- the number of electrons per bunch,  $N_{\text{bunch}} = 1.28 \times 10^5$ .

Indeed, starting from these values and from the average PEDD per primary electron,  $\text{PEDD}_{e^-}$ , it is possible to compute the pulse length

$$T = \frac{\tau \text{PEDD}_{\text{ref}}}{N_{\text{bunch}} \text{PEDD}_{e^-}}$$

required to attain a certain PEDD per pulse,  $\text{PEDD}_{\text{ref}}$ , and the corresponding average current and power deposit in the target,

$$I = \frac{e N_{\text{bunch}} T R}{\tau} \quad \text{and} \quad P = \text{PEDD}_{e^-} I$$

respectively. The latter can then be used to estimate the average temperature at the target surface,  $T_{\text{surf}}$ , by inverting the relation

$$P \sim 2\Sigma \left[ h (T_{\text{surf}} - T_{\text{amb}}) + \epsilon \sigma (T_{\text{surf}}^4 - T_{\text{amb}}^4) \right] \quad (\text{B.1})$$

where

- $\Sigma = \pi d^2/4$  is the area of the target transverse section – it comes with a factor of two because both the front and rear sides are taken into account, whereas the lateral surface is neglected;
- $T_{\text{amb}} = 295$  K is the room temperature in the experimental hall;
- $h = 8$  W/m<sup>2</sup>K is the heat transfer coefficient;
- $\epsilon = 0.7$  is the grey body emissivity;
- $\sigma \sim 5.67 \times 10^{-8}$  W/m<sup>2</sup>K<sup>4</sup> is the Stefan-Boltzmann constant.

The first term in equation B.1 accounts for the heat diffusion by convection [229] whereas the second term accounts for the contribution of grey-body radiation emission [230].

The final results, obtained in a subset of the parameter phase space from the Geant4 simulations and from the beam and thermal analyses performed on the simulation output, are summarised in table B.1.  $\text{PEDD}_{\text{ref}}$  was set to 10.5 J/g, and a beam spot size between 250  $\mu\text{m}$  and 350  $\mu\text{m}$  and a thickness between 2 mm and 8 mm were considered – albeit the irradiation of

samples thicker than a few mm might not be feasible due to radioprotection limitations.

Assuming the bunch features and repetition rate defined above, reaching  $\text{PEDD}_{\text{ref}}$  requires a pulse length between  $\sim 240 \mu\text{s}$  and  $\sim 770 \mu\text{s}$ ; the latter grows as the beam becomes larger and decreases as the target becomes thicker. Average surface temperatures between  $\sim 200^\circ\text{C}$  and  $\sim 1400^\circ\text{C}$  are attained: the large variation of  $T_{\text{surf}}$  is due to the strong dependence on the sample size (both longitudinal and transverse) whereas the dependence on the beam size is only slight. For the sake of more detailed studies on the thermal stress the target might experience, the peak power deposit per single bunch,  $P_{\text{bunch}}$ , is also reported.



Beam size [ $\mu\text{m}$ ]	Thickness [mm]	Energy deposit [MeV/e <sup>-</sup> ]	PEDD [10 <sup>11</sup> J/(g · e <sup>-</sup> )]	$T$ [ $\mu\text{s}$ ]	$P_{\text{bunch}}$ [W]	$I$ [ $\mu\text{A}$ ]	$P$ [W]	$d$ [in]	$T_{\text{surf}}$ [°C]
250	2	7.11	7.48	438.73	364.41	4.50	31.98	1	635.0
250	2	7.11	7.48	438.73	364.41	4.50	31.98	2	341.0
250	2	7.11	7.48	438.73	364.41	4.50	31.98	3	215.5
250	5	37.10	13.07	251.08	1902.24	2.57	95.52	1	944.5
250	5	37.10	13.07	251.08	1902.24	2.57	95.52	2	564.5
250	5	37.10	13.07	251.08	1902.24	2.57	95.52	3	393.0
250	8	97.66	13.90	236.09	5007.09	2.42	236.42	1	1267.5
250	8	97.66	13.90	236.09	5007.09	2.42	236.42	2	799.0
250	8	97.66	13.90	236.09	5007.09	2.42	236.42	3	587.0
250	8	97.66	13.90	236.09	5007.09	2.42	236.42	3	587.0
300	2	7.10	5.56	589.70	364.05	6.05	42.94	1	710.5
300	2	7.10	5.56	589.70	364.05	6.05	42.94	2	395.0
300	2	7.10	5.56	589.70	364.05	6.05	42.94	3	257.0
300	5	37.04	10.24	320.52	1898.94	3.29	121.73	1	1024.0
300	5	37.04	10.24	320.52	1898.94	3.29	121.73	2	622.5
300	5	37.04	10.24	320.52	1898.94	3.29	121.73	3	440.5
300	8	97.66	11.31	290.04	5006.81	2.97	290.44	1	1351.5
300	8	97.66	11.31	290.04	5006.81	2.97	290.44	2	859.5
300	8	97.66	11.31	290.04	5006.81	2.97	290.44	3	637.0
350	2	7.10	4.26	770.09	364.05	7.90	56.07	1	784.0
350	2	7.10	4.26	770.09	364.05	7.90	56.07	2	448.0
350	2	7.10	4.26	770.09	364.05	7.90	56.07	3	298.5
350	5	37.10	8.19	400.63	1902.17	4.11	152.41	1	1102.5
350	5	37.10	8.19	400.63	1902.17	4.11	152.41	2	679.5
350	5	37.10	8.19	400.63	1902.17	4.11	152.41	3	487.5
350	8	97.62	9.41	348.86	5004.85	3.58	349.20	1	1429.5
350	8	97.62	9.41	348.86	5004.85	3.58	349.20	2	916.0
350	8	97.62	9.41	348.86	5004.85	3.58	349.20	3	684.0

TABLE B.1: Summary of the results from the simulations and thermal analyses performed in view of the future tungsten irradiation tests at MAMI B.  $T$  and, hence, all the other beam-related parameters were obtained setting  $\text{PEDD}_{\text{ref}} = 10.5 \text{ J/g}$ .

# APPENDIX C

---

## KLEVER 2018 data conditioning

Significant drifts over time have been observed in the response of some of the detectors installed at the KLEVER 2018 beamtest on the SPS H2 beamline, discussed in chapter 4. In particular, signals from the  $\gamma$ -CAL and from the channel 1 of the  $e$ -CAL (the closest to the photon path) experienced macroscopic drifts, whereas  $e$ -CAL channel 2 showed a less pronounced dependence over time. Moreover, the data collected in photon mode highlight that the response of  $e$ -CAL channel 1 is non-linear in the range of photon energies covered by its acceptance. In this appendix, the data conditioning operations performed to treat these biases and thus reduce the uncertainty on the physics results are discussed.

### C.1 Context

Figure C.1 shows the energy spectra of both the  $\gamma$ -CAL (top) and the  $e$ -CAL (bottom) measured in photon mode with the tungsten sample out of the beam path. These spectra result from the combination of several control runs performed at different times of the beamtest in identical conditions. The  $e$ -CAL channel 1 signal spectrum (orange in figure C.1 bottom) is expected to show a single broad peak in a well-defined range of energies – corresponding to the horizontal spatial acceptance of the lead glass block,

given the coupling between electron momentum and curvature radius introduced by the photon tagging system. On the other hand, several peaks of different widths are observed in a range that spans across  $\sim 70$  GeV, i.e., more than 50% of the primary electron energy.

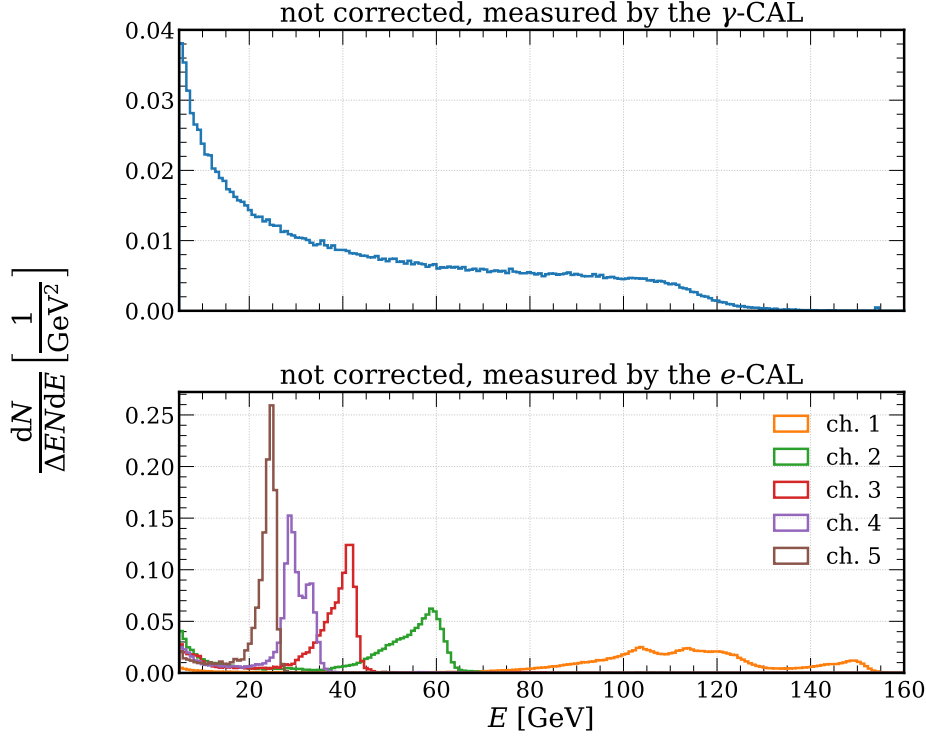


FIGURE C.1: Energy spectra of the calorimeters installed at the KLEVER 2018 beamtest, measured in photon mode without the crystalline sample along the beam path by (*top*) the  $\gamma$ -CAL and (*bottom*) the  $e$ -CAL single channels, before data conditioning. To be compared to figure 4.5.

Albeit difficult to clearly see in figure C.1, deviations from the expected signal distributions have also been observed in  $\gamma$ -CAL (details in section C.2) and in  $e$ -CAL channel 2. All these features hint at a variation of the response of these detector over time in the form of gain drifts and sudden fluctuations. Moreover, figure C.2, which shows the correlation between  $E_{\gamma\text{-tagged}}$  and the  $\gamma$ -CAL energy spectrum from a single run (i.e., photon mode with crystal along the beam path in random alignment), hints at the presence of another problem in the  $e$ -CAL data: indeed, the response of channel 1, whose signal populates this plot between 0 and  $\sim 40$  GeV on the abscissas, shows a strong non-linear dependence on  $E_{\gamma\text{-tagged}}$ . The shape of the latter is time-dependent as well, as it non-trivially changes along the beamtest time.

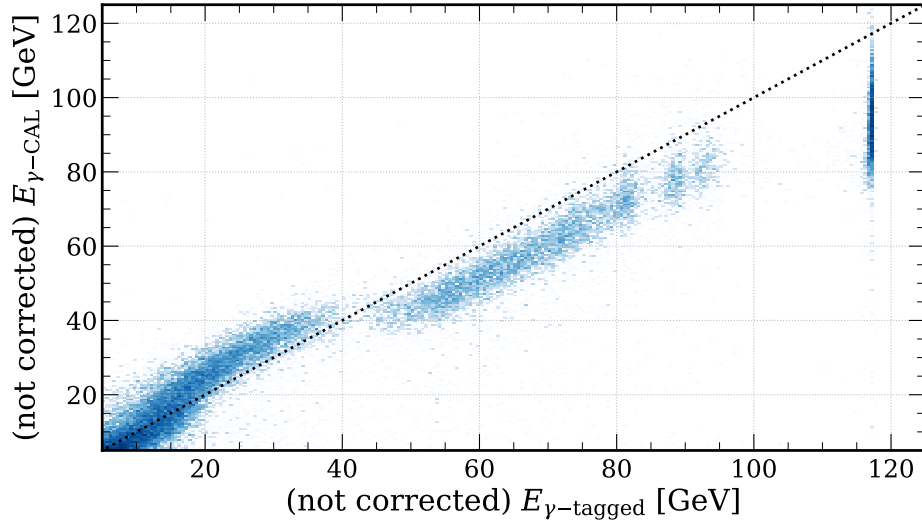


FIGURE C.2:  $E_{\gamma\text{-CAL}}$  as a function of  $E_{\gamma\text{-tagged}}$  with the crystalline sample in random alignment, before data conditioning. To be compared to figure 4.6.

These two problems seem to have different causes and affect the quality of the data independently on one another. In the following, the treatment procedures are discussed, i.e.,

- the time stabilisation algorithms for the  $\gamma$ -CAL (section C.2) and for the  $e$ -CAL (section C.3);
- the linearisation of the latter.

## C.2 $\gamma$ -CAL time drift stabilisation

Figure C.3 shows the PH spectra obtained from all the control runs, i.e., the runs performed along the beamtest time with the bending magnet off and thus with the beam directly impinging on the  $\gamma$ -CAL. It is clear that the response of the latter heavily varies over  $\sim 90$  hours. In particular, the MPV of the spectrum drifts towards lower values as time passes; an overall variation of  $\sim 20\%$  of the initial value is observed.

The drift pattern is clearly visible in figure C.4. The dots represent the MPVs of the distributions shown in figure C.3. All the physics runs have been corrected by weighting the  $\gamma$ -CAL PH with a factor obtained by means of a linear interpolation between pairs of successive control runs ( $s_{\gamma\text{-CAL}}(t)$ ,  $t$  being the epoch – solid lines in figure C.4) normalised to the MPV of the  $\text{PH}_{\gamma\text{-CAL}}$  distribution obtained from the reference control run ( $\text{PH}_{\gamma\text{-CAL}}^{\text{ref}}$  –

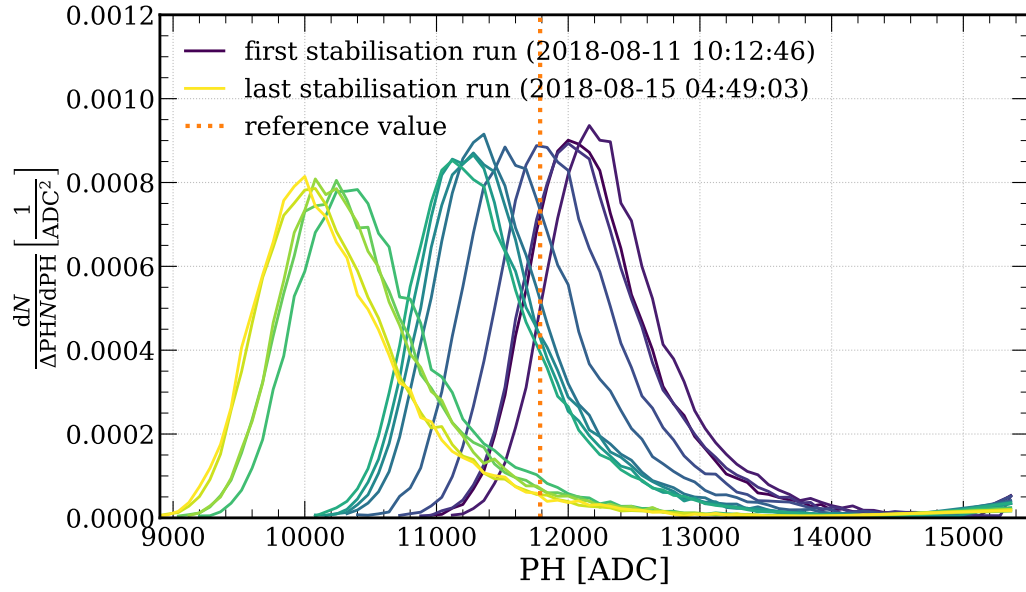


FIGURE C.3: Distributions of the  $\gamma$ -CAL PH from all the no-crystal, direct-beam runs before time stabilisation.

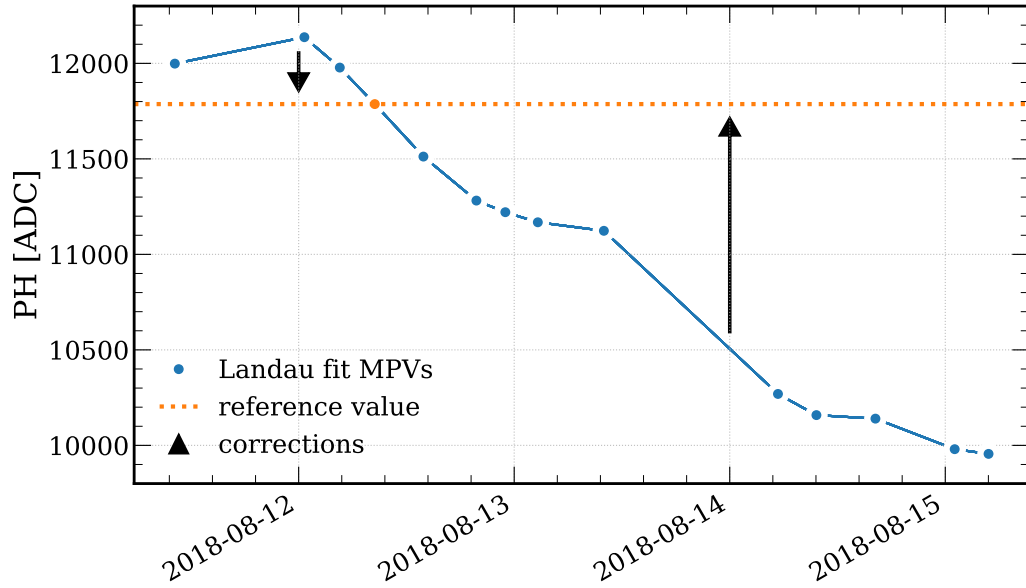


FIGURE C.4:  $\gamma$ -CAL PH MPVs computed for all the no-crystal, direct-beam runs as a function of the run epoch. The black arrows roughly indicate the transformations performed by the stabilisation algorithm.

orange point), chosen because it is the closest in time to the calorimeter calibration runs. In practice, the transformation

$$\text{PH}_{\gamma\text{-CAL}} \rightarrow \frac{\text{PH}_{\gamma\text{-CAL}}^{\text{ref}}}{s_{\gamma\text{-CAL}}(t)} \text{PH}_{\gamma\text{-CAL}} \quad (\text{C.1})$$

has been applied.

The distributions of  $\text{PH}_{\gamma\text{-CAL}}$  obtained from the control run data after applying the transformation in equation C.1 are shown in figure C.5. The response of the  $\gamma$ -CAL after correction does not show any further drift over time.

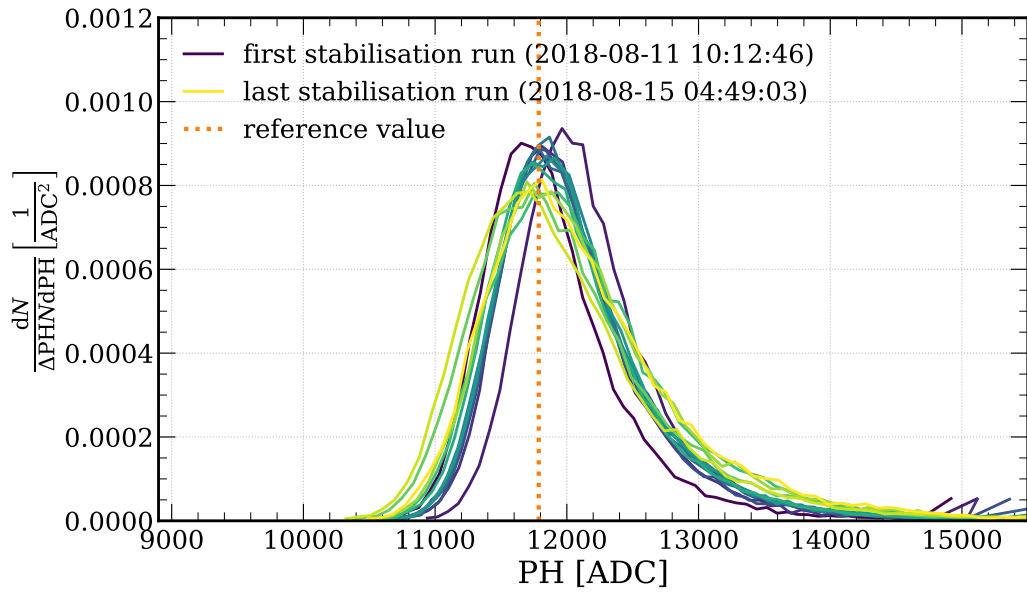


FIGURE C.5: Distributions of the  $\gamma$ -CAL PH from all the no-crystal, direct-beam runs after time stabilisation.

### C.3 $e$ -CAL time drift stabilisation

The blue curve in figure C.6 is a PH spectrum of the  $e$ -CAL channel 1, acquired in a short (a few spills) run in photon mode without the crystal along the beam path. It features a peak around 1300 ADC and a lower-energy edge between  $\sim 5000$  ADC and  $\sim 9000$  ADC; these two structures drift independently on each other over time.

In order to correct for the channel 1 drift in its whole range, it is necessary to separate the contributions of the peak and of the edge and stabilise them

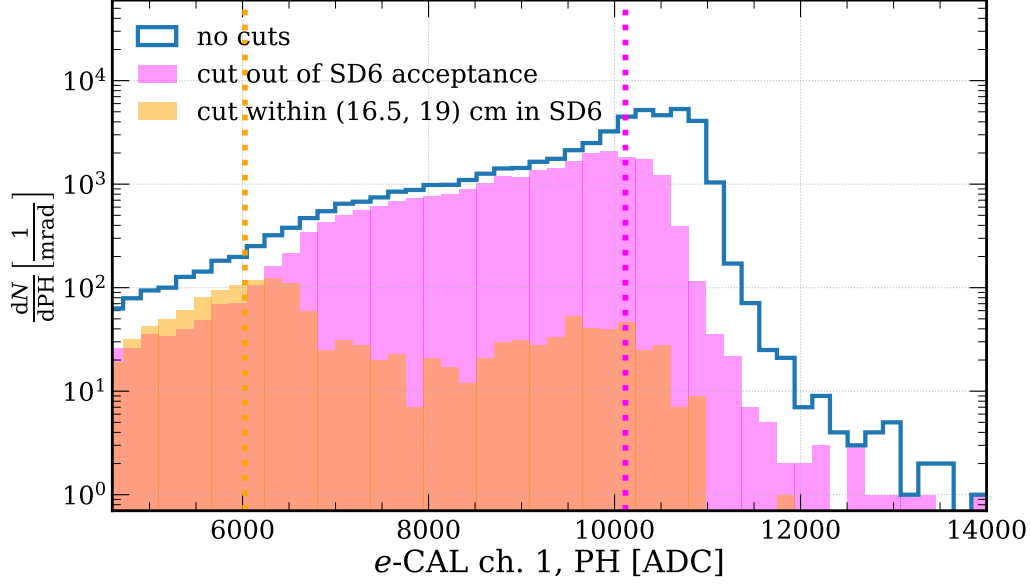


FIGURE C.6: Distributions of the PH in the  $e$ -CAL channel 1 in a short run with different fiducial selections on SD6: no selection (blue), tracks out of the SD6 acceptance (pink) and tracks crossing the  $\sim 3.5$  cm slice of the sensor closest to the photon beam path (orange).

independently on each other. A solution is provided by the correlation between the PH in the  $e$ -CAL channels and the horizontal hit position in the SD6 SiBC (see setup scheme in figure 2.20, chapter 2), highlighted in figure C.7: although the SD6 sensor only covers  $\lesssim 25\%$  of the channel 1 front surface (and SD5 is even farther from the photon beam axis), a  $\sim 2.5$  cm wide selection on the rightmost part of the sensor (grey band) allows to select the events in which the electron impinging on the  $e$ -CAL channel 1 has an energy in the lowest part of the spectrum shown in figure C.6. On the other hand, since all the higher-energy electrons are out of the SD6 acceptance, they can be selected by requiring that no hits are measured on the latter. Indeed, the two aforementioned selections lead to the subsets of events shown in figure C.6 in pink and orange respectively: the respective maxima, around  $\sim 10100$  ADC and  $\sim 6000$  ADC respectively (dashed lines), drift in the same way as the peak and the edge in the full spectrum and, hence, can be exploited to stabilise the signal.

The stabilisation algorithm for the  $e$ -CAL channel 1 works as follows. Each run acquired in photon mode is divided into chunks of 20 spills each, and the maxima of the two components of the channel 1 spectrum (figure C.6) are found – namely,  $\text{PH}_{\text{low}}^{\text{chk}}$  and  $\text{PH}_{\text{high}}^{\text{chk}}$ . Then, the transformation

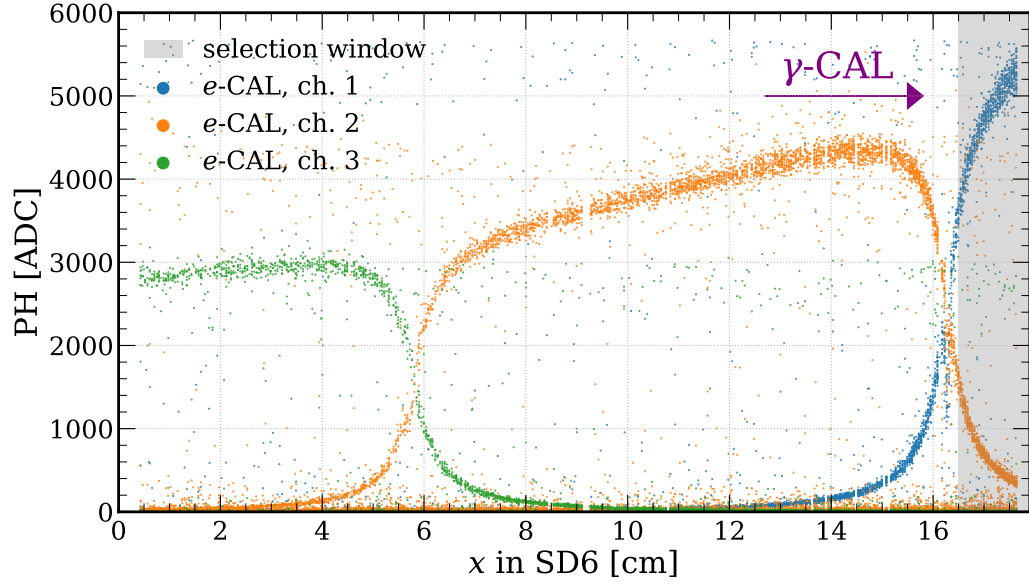


FIGURE C.7: Correlation between the horizontal position on SD6 and the photon tagged PH from the single *e*-CAL channels. The fiducial selection exploited in the time-stabilisation algorithm is highlighted in grey.

$$PH \rightarrow \begin{cases} \frac{PH_{low}^{ref}}{PH_{low}^{chk}} PH & \text{if } PH < PH_{low}^{chk} \\ \left[ (1 - \zeta) \frac{PH_{low}^{ref}}{PH_{low}^{chk}} + \zeta \frac{PH_{high}^{ref}}{PH_{high}^{chk}} \right] PH & \text{if } PH \in (PH_{low}^{chk}, PH_{high}^{chk}) \\ \frac{PH_{high}^{ref}}{PH_{high}^{chk}} PH & \text{if } PH > PH_{high}^{chk} \end{cases} ,$$

is applied, where  $PH_{low}^{ref}$  and  $PH_{high}^{ref}$  are the subset maxima computed in a specific run and spill chunk, taken as reference, and

$$\zeta = \frac{PH - PH_{low}^{chk}}{PH_{high}^{chk} - PH_{low}^{chk}}$$

is an event-by-event indicator of how close the channel 1 PH is to the corresponding  $PH_{low}^{chk}$ .

Examples of application of this algorithm to different physics runs are provided below. In particular,



- figure C.8 shows a dataset in which the signal of channel 1 is stable over the run time but shifted with respect to the higher reference level;
- figure C.9 shows a dataset in which both an overall shift and an approximately constant-slope shift are visible;
- figure C.10 shows a dataset in which the signal shows a sudden jump;
- figure C.11 shows a highly corrupted dataset, with an overall shift, a non-linear drift and several jumps.

Indeed, the algorithm is applied to all the aforementioned cases with excellent results, with the exception of a few spill chunks, e.g., in figures C.10 and C.11, that could not be stabilised and have therefore been manually discarded. The slight drift observed in the *e*-CAL channel 2 response is corrected with a much simpler algorithm. In practice, its PH spectrum only shows a single peak: its position,  $\text{PH}^{\text{chk}}$ , is computed for each spill chunk equalised to a reference value,  $\text{PH}^{\text{ref}}$ , with the transformation

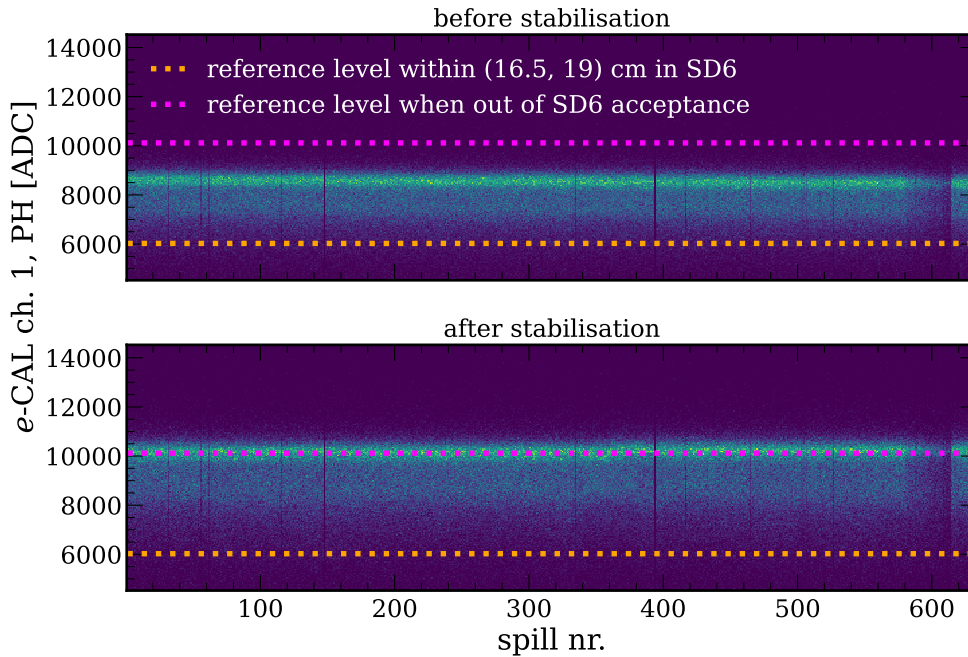


FIGURE C.8: PH of the *e*-CAL channel 1 signal before (*top*) and after (*bottom*) the stabilisation over time; the signal is shifted with respect to the upper reference level but is stable across the run.

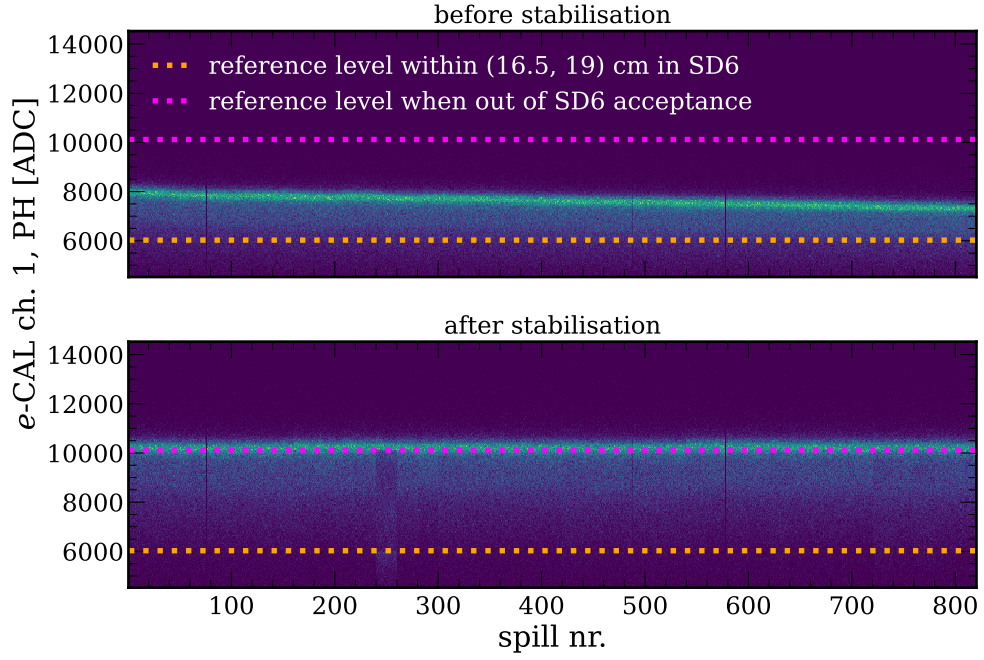


FIGURE C.9: PH of the *e*-CAL channel 1 signal before (*top*) and after (*bottom*) the stabilisation over time; the signal is shifted with respect to the upper reference level and shows a small-scale constant drift across the run.

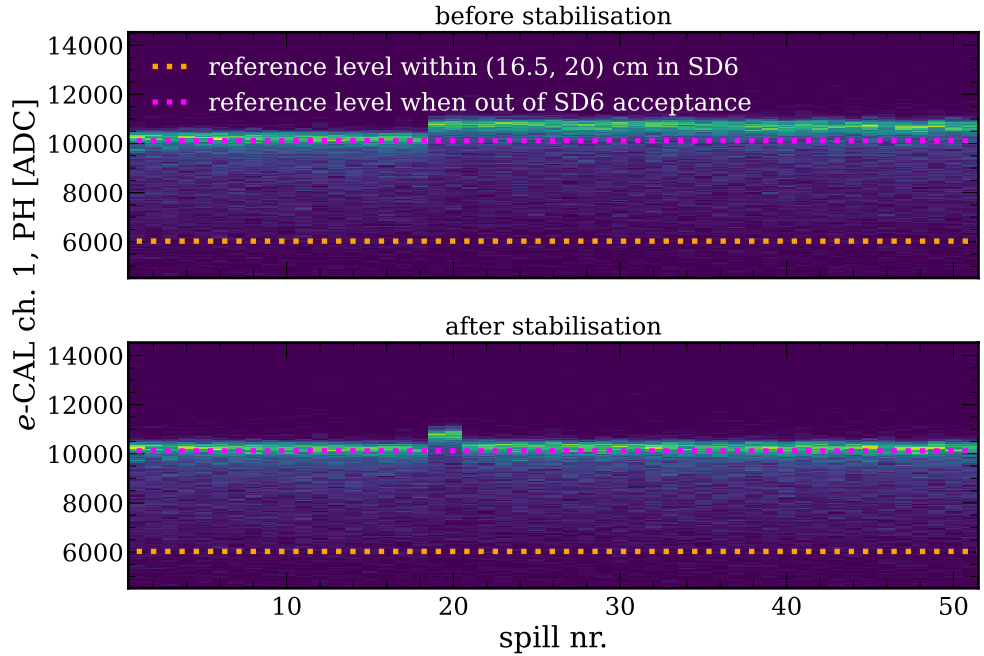


FIGURE C.10: PH of the *e*-CAL channel 1 signal before (*top*) and after (*bottom*) the stabilisation over time; the signal shows a sudden jump around  $\sim 20$  spills after the start of the run.

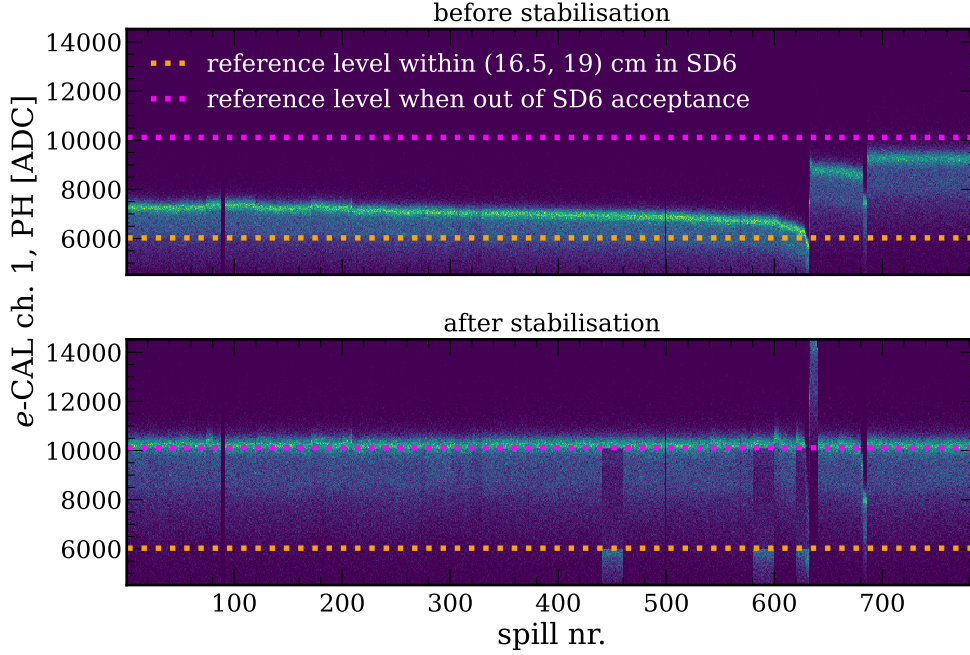


FIGURE C.11: PH of the  $e$ -CAL channel 1 signal before (*top*) and after (*bottom*) the stabilisation over time; the signal significantly discontinuous, with multiple sections of fast drift and several jumps.

$$PH \rightarrow \frac{PH^{\text{ref}}}{PH^{\text{chk}}} PH \quad .$$

## C.4 $e$ -CAL response linearisation and calibration correction

After applying the stabilisation algorithms discussed in section C.3, calibrating the calorimeter channels (details in sections A.1 and A.3, appendix A) and taking data in photon mode, the strong non-linearity observed in figure C.2 is dealt with. In particular, the latter exclusively reflects the non-linear response of the  $e$ -CAL channel 1, as can be seen in figure C.12, which shows the correlation between the tagged photon energy value computed using channel 1 only, i.e.,

$$E_{\gamma\text{-tagged}}^1 = 120 \text{ GeV} - E_{e\text{-CAL}}^1 \quad ,$$

and  $E_{\gamma\text{-CAL}}$  for two different no-crystal runs.

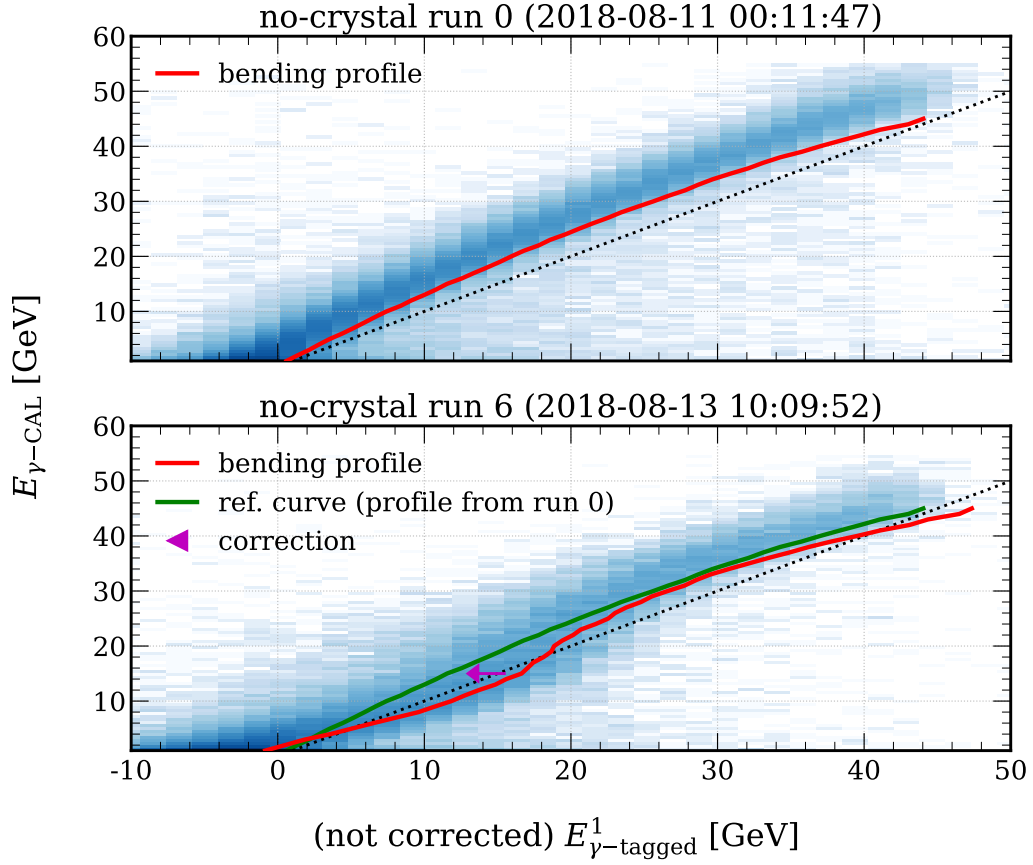


FIGURE C.12: Examples of non-linearity in the  $e$ -CAL channel 1 observed in no-crystal runs in photon mode. The bending correction curves, obtained from the corresponding profile plots and exploited to linearise the channel response in the different runs, are superimposed in red.

In order to correct for this effect, the shape of the correlation is sampled with a profile plot – red curves,  $C^j(E_{e\text{-CAL}}^1)$  – in each no-crystal run. As discussed in section 4.2.2.1 (chapter 4), when the crystal is installed along the beam path, the correlation between  $E_{\gamma\text{-tagged}}$  and  $E_{\gamma\text{-CAL}}$  depends on its lattice orientation. This makes it impossible to define a non-linearity correction algorithm that works on an event-by-event basis, and only the no-crystal data, collected once every few hours during the data taking session, can be exploited. In practice, each one of the datasets collected with the crystal is conditioned using the shape sampled in one of the no-crystal runs, chosen on a time-proximity basis.

In fact, the correction

$$E_{e\text{-CAL}}^1 \rightarrow \frac{C^0(E_{e\text{-CAL}}^1)}{C^j(E_{e\text{-CAL}}^1)} E_{e\text{-CAL}}^1 \quad ,$$

where  $j$  addresses the no-crystal run associated to the dataset currently under study, is applied. As a result, all the correlation curves between the corrected values of  $E_{\gamma\text{-tagged}}^1$  and  $E_{\gamma\text{-CAL}}$  computed with the no-crystal data have the same shape as that of the reference run – green curve in figure C.12 bottom,  $C^0(E_{e\text{-CAL}}^1)$ . This effect might reflect a dependence of the detector response on the particle impact position on its front surface, which is connected to  $E_{\gamma\text{-CAL}}$  by a hyperbolic correlation because of the magnetic field used in photon mode.

For the same reason, the calibration of the  $e\text{-CAL}$  channel 1, which was performed with the electron beam directly impinging at the centre of the channel front surface, might be biased. This can be checked by studying again the correlation between the signal of the  $e\text{-CAL}$  channels, considered individually, and the hit position in the SD6 SiBC.

Indeed, figure C.13 shows that there is a few-GeV offset between the energy measured by the left edge of the  $e\text{-CAL}$  channel 1 (purple dot,  $\tilde{E}_{e\text{-CAL}}^1$ ) and the value extrapolated from a hyperbolic fit performed on channels 2 and 3 (red dot,  $\check{E}_{e\text{-CAL}}^1$ ). Applying the transformation

$$E_{e\text{-CAL}}^1 \rightarrow \frac{\check{E}_{e\text{-CAL}}^1}{\tilde{E}_{e\text{-CAL}}^1} E_{e\text{-CAL}}^1$$

and then computing  $E_{\gamma\text{-tagged}}$  by means of equations 4.1 (chapter 4) and 2.4 (chapter 2) finally leads to the results shown, e.g., in figures 4.5 and 4.6 (chapter 4).

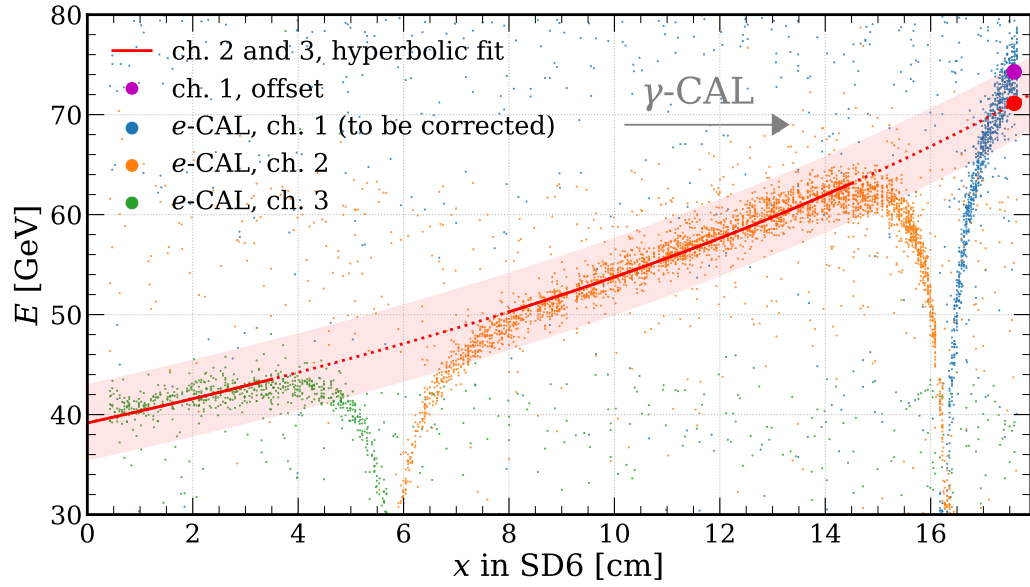


FIGURE C.13: Correlation between the horizontal position on SD6 and the photon tagged energy measured by the single  $e$ -CAL channels after time stabilisation and channel 1 linearisation. The hyperbolic fit performed on channels 2 and 3 to find the final correction factor for channel 1 is superimposed in red.



# List of acronyms

<b>ADC</b>	Analog-to-Digital Converter
<b>AGILE</b>	Astro-rivelatore Gamma a Immagini LEggero
<b>AMBER</b>	Apparatus for Meson and Baryon Experimental Research
<b>ANTI-0</b>	ANTIcoincidence-0
<b>APC</b>	Active Photon Converter
<b>APD</b>	Avalanche PhotoDiode
<b>ASD</b>	AdvanSiD
<b>ASIC</b>	Application-Specific Integrated Circuit
<b>BCC</b>	Body-Centered Cubic
<b>BGA</b>	Ball Grid Array
<b>BSM</b>	Beyond Standard Model
<b>BSU</b>	Belarusian State University
<b>CAEN</b>	Costruzioni Apparecchiature Elettroniche Nucleari
<b>CB</b>	Coherent Bremsstrahlung
<b>CERN</b>	Conseil Européen pour la Recherche Nucléaire
<b>CMS</b>	Compact Muon Solenoid
<b>COMPASS</b>	Common Muon and Proton Apparatus for Structure and Spectroscopy
<b>COG</b>	Centre Of Gravity
<b>CPP</b>	Coherent Pair Production
<b>CPV</b>	Charged-Particle Veto
<b>CR</b>	Channeling Radiation
<b>CSEM</b>	Centre Suisse d'Electronique et Microtechnique
<b>CW</b>	Continuous Wave
<b>DC</b>	Downstream Counter
<b>DAQ</b>	Data Acquisition
<b>DESY</b>	Deutsches Elektronen-Synchrotron
<b>DIBK</b>	Direct Integration of the Baier-Katkov formula
<b>DOF</b>	Degree Of Freedom



---

<b>ECAL</b>	Electromagnetic CALorimeter
<b>ECN</b>	Experimental Cavern North
<b>EHN</b>	Experimental Hall North
<b>ELIOT</b>	ELectromagnetic processes In Oriented crysTals
<b>EMC</b>	ElectroMagnetic Calorimeter
<b>ERNI</b>	Enhanced Routing Network Interconnect
<b>ESRF</b>	European Synchrotron Radiation Facility
<b>FAIR</b>	Facility for Antiproton and Ion Research
<b>FBK-irst</b>	Fondazione Bruno Kessler, Istituto di Ricerca Scientifica e Tecnologica
<b>FCC-<i>ee</i></b>	Future Circular Collider, electron-electron
<b>FCNC</b>	Flavour-Changing Neutral Current
<b>FIP</b>	Feebly Interacting Particle
<b>FLUKA</b>	FLUktuierende KAskade
<b>FTFP_BERT</b>	FriToF Physics list, BERTini
<b>FWHM</b>	Full-Width Half Maximum
<b>G-APD</b>	Geiger-mode APD
<b>GIF</b>	Gamma Irradiation Facility
<b>GSI</b>	Gesellschaft für Schwerionenforschung
<b>HEP</b>	High-Energy Physics
<b>HIKE</b>	High Intensity Kaon Experiments
<b>HRXRD</b>	High-Resolution X-Ray Diffraction
<b>ID</b>	IDentification
<b>IJCLab</b>	Irène Joliot-Curie Laboratory
<b>ILC</b>	International Linear Collider
<b>INFN</b>	Istituto Nazionale di Fisica Nucleare
<b>INP</b>	Institute for Nuclear Problems
<b>IRC</b>	Intermediate-Ring Calorimeter
<b>ISSP</b>	Institute of Solid State Physics
<b>KEK</b>	Kō Enerugī Kasokuki Kenkyū Kikō
<b>J-PARC</b>	Japan Proton Accelerator Research Complex
<b>KLEVER</b>	$K_L$ Experiment for VErY Rare events
<b>KOTO</b>	$K_0$ at TOkai
<b>LAT</b>	Large Area Telescope
<b>LAV</b>	Large Angle Veto
<b>LEP</b>	Large Electron-Positron Collider
<b>LHC</b>	Large Hadron Collider
<b>LKr</b>	Liquid Krypton
<b>LMS</b>	Laboratory of Materials Science
<b>LPM</b>	Landau-Pomeranchuk-Migdal
<b>LY</b>	Light Yield

---

<b>MAMI</b>	MAInzer MIkrotron
<b>MC</b>	Monte Carlo <i>or</i> Multiplicity Counter
<b>MCS</b>	Multiple Coulomb Scattering
<b>MEC</b>	Main Electromagnetic Calorimeter
<b>MIP</b>	Minimum Ionising Particle
<b>MolTech</b>	Molecular Technologies
<b>MPV</b>	Most Probable Value
<b>MUV</b>	MUon Veto detector
<b>NA</b>	North Area
<b>NP</b>	New Physics
<b>NUV</b>	Near-UltraViolet
<b>onsemi</b>	ON Semiconductor
<b>OPAL</b>	Omni-Purpose Apparatus at LEP
<b>PADME</b>	Positron Annihilation into Dark Matter Experiment
<b>PANDA</b>	antiProton ANnihilation at DArmstadt
<b>PCB</b>	Printed Circuit Board
<b>PEDD</b>	Peak Energy Deposition Density
<b>PH</b>	Pulse Height
<b>PMT</b>	PhotoMultiplier Tube
<b>PP</b>	Pair Production
<b>PS</b>	Positron Source
<b>PSD</b>	PreShower Detector
<b>QED</b>	Quantum ElectroDynamics
<b>QGSP_BERT</b>	Quark-Gluon String Physics list, BERTini
<b>R&amp;D</b>	Research and Development
<b>RAM</b>	Random Access Memory
<b>RAS</b>	Russian Academy of Science
<b>SAC</b>	Small Angle Calorimeter
<b>SD</b>	Silicon Detector
<b>SFPP</b>	Strong-Field Pair Production
<b>SI</b>	Système International
<b>SiBC</b>	Silicon Beam Chamber
<b>SiPM</b>	Silicon PhotoMultiplier
<b>SF</b>	Strong Field
<b>SM</b>	Standard Model
<b>SLC</b>	Stanford Linear Collider
<b>SPS</b>	Super Proton Synchrotron
<b>STORM</b>	STrOng cRystalline electroMagnetic field
<b>TAX</b>	Target Attenuator for eXperimental areas
<b>TBD</b>	To Be Defined

<b>VC</b>	Veto Counter
<b>UV</b>	Upstream Veto
<b>VLE</b>	Very Low Energy
<b>VME</b>	Versa Module Europa
<b>VRB</b>	VME Readout Module

# List of figures

1.1	Types of Bravais lattices . . . . .	7
1.2	Commonly studied axes and planes . . . . .	8
1.3	Lattice orientations . . . . .	9
1.4	Crystallographic stereogram . . . . .	11
1.5	W [111] axial potential, single-string . . . . .	15
1.6	W [111] axial potential in the transverse plane . . . . .	18
1.7	Trajectory of a positive particle in axial channelling . . . . .	19
1.8	Axial potentials for positive and negative particles in the transverse plane . . . . .	21
1.9	Standard bremsstrahlung radiation spectral intensity . . . . .	25
1.10	Comparison between standard bremsstrahlung and collisions . . . . .	26
1.11	CR emission . . . . .	29
1.12	Magnetic undulator and wiggler . . . . .	30
1.13	Universal synchrotron radiation function . . . . .	31
1.14	CB radiation emission . . . . .	32
1.15	CB by 10 GeV/c positrons in silicon (110) . . . . .	34
1.16	SF radiation emission . . . . .	37
1.17	Feynman-like diagrams of pair production and bremsstrahlung . . . . .	38
1.18	Standard pair production cross section . . . . .	40
1.19	Coherent electromagnetic shower acceleration . . . . .	44
2.1	Crystalline W unit cell and main axial potentials . . . . .	50
2.2	PWO lattice structure and main axial potentials . . . . .	52
2.3	DESY II Test Beam Facility . . . . .	54
2.4	DESY T21 experimental hall . . . . .	55
2.5	DESY T21 electron beam angles . . . . .	56
2.6	CERN NA beamlines . . . . .	56
2.7	CERN H2 PPE172 experimental area . . . . .	58
2.8	CERN H2 electron beam angles . . . . .	59
2.9	CERN H4 PPE134 experimental area . . . . .	59
2.10	INSULAb Telescope module . . . . .	61

2.11	Silicon Beam Chamber . . . . .	62
2.12	Stefi calorimeter . . . . .	64
2.13	Genni calorimeter . . . . .	65
2.14	Lead glass blocks . . . . .	66
2.15	Active Photon Converter . . . . .	67
2.16	Tracking system readout chain . . . . .	69
2.17	Goniometer and crystal holder . . . . .	71
2.18	Pre-alignment procedure . . . . .	72
2.19	Setup for radiation measurements . . . . .	73
2.20	Setup for PP measurements . . . . .	75
2.21	Downstream stage of the KLEVER 2018 setup . . . . .	76
2.22	PH versus peak time of the veto counter in the KLEVER 2018 setup . . . . .	77
2.23	Setup for total energy measurements . . . . .	78
2.24	Hibiscus-like calorimeter at the STORM 2022 setup . . . . .	79
2.25	Axial correction curves to the Geant4 electromagnetic processes	82
3.1	Simplest PS schemes . . . . .	85
3.2	Results of a conventional PS simulation . . . . .	85
3.3	Optimised PS hybrid schemes . . . . .	89
3.4	W sample probed at DESY 2019 . . . . .	93
3.5	$E_{\gamma-\text{CAL}}$ by 5.6 GeV $e^-$ in W (DESY 2019) . . . . .	95
3.6	APC-DC calibration with simulation data (DESY 2019) . . . . .	96
3.7	APC-DC spectra by 5.6 GeV $e^-$ on W (DESY 2019), compar- ison with simulations . . . . .	97
3.8	APC-DC spectra by 5.6 GeV $e^-$ on W (DESY 2019), axis-to- random transition . . . . .	98
3.9	PS full simulation: setup rendering . . . . .	100
3.10	PS full simulation: beam spots at the crystal stage . . . . .	101
3.11	PS full simulation: beam angles at the crystal stage . . . . .	102
3.12	PS full simulation: momenta at the crystal stage . . . . .	103
3.13	PS full simulation: target mesh . . . . .	105
3.14	Box-shaped mesh reparametrisation into cylindrical coordinates	105
3.15	PS full simulation: energy deposit and PEDD in the target . . . . .	107
3.16	PS full simulation: $e^+$ production rate at the target stage . . . . .	108
3.17	PS full simulation: $e^+$ beam angle and spot size at the target stage . . . . .	110
3.18	PS full simulation: output positron energy mean and standard deviation . . . . .	110
3.19	PS full simulation, optimised: setup rendering . . . . .	111

3.20	PS full simulation, optimised: energy deposit and PEDD in the target . . . . .	113
3.21	PS full simulation, optimised: $e^+$ production rate at the target stage . . . . .	114
4.1	HIKE logo . . . . .	118
4.2	ECN3 cavern and NA62 experiment . . . . .	123
4.3	HIKE layout for neutral kaons . . . . .	123
4.4	W sample probed at KLEVER 2018 . . . . .	131
4.5	KLEVER 2018 calorimeter spectra . . . . .	133
4.6	$E_{\gamma\text{-CAL}}$ versus $E_{\gamma\text{-tagged}}$ in random alignment (KLEVER 2018) . . . . .	134
4.7	Energy absorption by bremsstrahlung photons on W (KLEVER 2018) . . . . .	134
4.8	Real crystal output energy versus input energy by bremsstrahlung photons on W (KLEVER 2018) . . . . .	136
4.9	Output MC PH versus $E_{\gamma\text{-tagged}}$ (KLEVER 2018) . . . . .	137
4.10	Output charged multiplicity by bremsstrahlung photons on W (KLEVER 2018) . . . . .	138
4.11	Real charged multiplicity at crystal output versus initial energy by bremsstrahlung photons on W (KLEVER 2018) . . . . .	138
4.12	Shower development in crystalline W . . . . .	140
5.1	Calorimeter energy resolution . . . . .	146
5.2	CMS ECAL . . . . .	150
5.3	Scintillation pulse in PWO-II and PWO-UF . . . . .	152
5.4	PWO 0.45 $X_0$ probed at CERN between 2016 and 2018 . . . . .	155
5.5	PWO 2 $X_0$ probed at CERN in 2021 . . . . .	155
5.6	Polishing of the PWO samples . . . . .	157
5.7	Photodetection system of the AXIAL 2018 setup . . . . .	159
5.8	INSULAb custom SiPM boards . . . . .	159
5.9	Photodetection system of the STORM 2021 setup . . . . .	160
5.10	Photodetection system of the STORM 2022 setup . . . . .	160
5.11	Shower development in PWO . . . . .	162
5.12	Shower development in PWO, integral . . . . .	163
5.13	CERN H2 electron beam energies . . . . .	164
5.14	CERN H2 beam components at the STORM 2022 beamtest . . . . .	165
5.15	PWO 1 $X_0$ : angular scan (CERN H2) . . . . .	166
5.16	PWO 4.6 $X_0$ : measured stereogram (CERN H2) . . . . .	167
5.17	PWO 4.6 $X_0$ : angular scan (CERN H2) . . . . .	168
5.18	$E_{\gamma\text{-CAL}}$ by 120 GeV $e^-$ in PWO (CERN H2) . . . . .	170
5.19	PWO 0.45 $X_0$ : $E_{\gamma\text{-CAL}}$ by $e^-$ at different energies . . . . .	172

5.20	PWO 1 $X_0$ : $E_{\gamma\text{-CAL}}$ by $e^-$ at different energies . . . . .	172
5.21	PWO 2 $X_0$ : $E_{\gamma\text{-CAL}}$ by $e^-$ at different energies . . . . .	173
5.22	Comparison between $E_{\gamma\text{-CAL}}$ by 120 GeV $e^-$ and $e^+$ in PWO (CERN H4) . . . . .	174
5.23	PWO 0.45 $X_0$ : scintillation light by 120 GeV $e^-$ (CERN H2) .	175
5.24	PWO 1 $X_0$ : scintillation light by 120 GeV $e^-$ (CERN H2) . .	175
5.25	PWO 2 $X_0$ : scintillation light by 120 GeV $e^-$ (CERN H2) . .	176
5.26	PWO 4.6 $X_0$ : scintillation light by 120 GeV $e^-$ (CERN H2) .	176
5.27	Energy deposit by 120 GeV $e^-$ as a function of the sample thickness in PWO (CERN H2) . . . . .	178
5.28	PWO 4.6 $X_0$ : $E_{\text{CAL}}$ by 120 GeV $e^-$ (CERN H2, 2022) . . . .	180
5.29	PWO 1 $X_0$ and 2 $X_0$ : axis-to-random transition in $E_{\gamma\text{-CAL}}$ (CERN H2) . . . . .	183
5.30	PWO 4.6 $X_0$ : axis-to-random transition in $E_{\text{CAL}}$ (CERN H2) .	183
5.31	PWO 1 $X_0$ : axis-to-random transition in scintillation light (CERN H2) . . . . .	184
5.32	PWO 2 $X_0$ : axis-to-random transition in scintillation light (CERN H2) . . . . .	185
5.33	PWO 4.6 $X_0$ : axis-to-random transition in scintillation light (CERN H2) . . . . .	185
5.34	Setup of the OREO beamtests . . . . .	187
A.1	Genni channel equalisation with MIPs . . . . .	196
A.2	Genni linearity and energy resolution . . . . .	197
A.3	Genni channel CC response at different reference energies in the DESY 2019 setup . . . . .	198
A.4	Genni calibration correction with simulations of the DESY 2019 setup . . . . .	199
A.5	Genni calibration at the DESY 2019 beamtest . . . . .	201
A.6	Single lead glass block calibration at the STORM 2022 beamtest	202
A.7	Single lead glass block energy resolution at the STORM 2022 beamtest . . . . .	202
A.8	Spatial distribution of the hibiscus-like calorimeter calibration data at the STORM 2022 beamtest . . . . .	203
A.9	Hibiscus-like calorimeter equalisation at the at the STORM 2022 beamtest . . . . .	204
A.10	Hibiscus-like calorimeter calibration at the at the STORM 2022 beamtest . . . . .	204
A.11	Hibiscus-like calorimeter energy resolution at the at the STORM 2022 beamtest . . . . .	205

B.1	MAMI B beamtest hall . . . . .	208
B.2	Calibration of the MAMI B calorimeter . . . . .	209
B.3	Radiation spectral intensity by 855 MeV $e^-$ in W, before and after irradiation (MAMI B) . . . . .	210
B.4	Simulated energy deposit and $e^+$ production rate by 855 GeV $e^-$ in amorphous W . . . . .	213
B.5	Comparison between different target and mesh geometries in W simulations . . . . .	214
C.1	KLEVER 2018 calorimeter spectra, before correction . . . . .	220
C.2	$E_{\gamma\text{-CAL}}$ versus $E_{\gamma\text{-tagged}}$ in random alignment (KLEVER 2018), before correction . . . . .	221
C.3	$\text{PH}_{\gamma\text{-CAL}}$ in KLEVER 2018 direct-beam runs, before stabilisation	222
C.4	Trend of the $\text{PH}_{\gamma\text{-CAL}}$ over time at the KLEVER 2018 beamtest	222
C.5	$\text{PH}_{\gamma\text{-CAL}}$ in KLEVER 2018 direct-beam runs, stabilised . . . . .	223
C.6	$\text{PH}_{e\text{-CAL}}^{\text{ch.1}}$ with different fiducial cuts at the KLEVER 2018 beamtest . . . . .	224
C.7	$\text{PH}_{\gamma\text{-tagged}}$ versus the position on SD6 in the KLEVER 2018 setup, fiducial cut . . . . .	225
C.8	$\text{PH}_{e\text{-CAL}}^{\text{ch.1}}$ time stabilisation at the KLEVER 2018 beamtest, example 1 . . . . .	226
C.9	$\text{PH}_{e\text{-CAL}}^{\text{ch.1}}$ time stabilisation at the KLEVER 2018 beamtest, example 2 . . . . .	227
C.10	$\text{PH}_{e\text{-CAL}}^{\text{ch.1}}$ time stabilisation at the KLEVER 2018 beamtest, example 3 . . . . .	227
C.11	$\text{PH}_{e\text{-CAL}}^{\text{ch.1}}$ time stabilisation at the KLEVER 2018 beamtest, example 4 . . . . .	228
C.12	$e\text{-CAL}$ channel 1 non-linearity at the KLEVER 2018 beamtest	229
C.13	$E_{\gamma\text{-tagged}}$ versus the position on SD6 in the KLEVER 2018 setup, channel 1 final correction . . . . .	231





# List of tables

2.1	General properties of W and PWO . . . . .	50
2.2	Properties of the main axes of crystalline W and PWO . . . .	51
3.1	Features of the PS of present and future colliders . . . . .	90
3.2	Results of the PS full simulation in different configurations . .	115
4.1	$E_{\gamma-\text{missing}}$ measured at KLEVER 2018 . . . . .	135
5.1	Scintillation properties of PWO . . . . .	151
5.2	Features of the tested PWO samples . . . . .	154
5.3	Measured thickness enhancement and $X_0$ reduction in PWO .	179
B.1	Simulation studies on future irradiation tests on W at MAMI .	218



# Bibliography

1. Biryukov, V. M., Chesnokov, Y. A. & Kotov, V. I. *Crystal channeling and its application at high-energy accelerators* 1st ed. ISBN: 9783662034071 (Springer Berlin, Heidelberg, 1997).
2. Hasan, S. *Bent silicon crystals for the LHC collimation : Studies with an ultrarelativistic proton beam* PhD thesis (Università degli Studi dell'Insubria, 2007).
3. Robinson, M. T. & Oen, O. S. Computer Studies of the Slowing Down of Energetic Atoms in Crystals. *Phys. Rev.* **132**, 2385–2398 (1963).
4. Piercy, G. R., Brown, F., Davies, J. A. & McCargo, M. Experimental Evidence for the Increase of Heavy Ion Ranges by Channeling in Crystalline Structure. *Phys. Rev. Lett.* **10**, 399–400 (1963).
5. Lindhard, J. Influence of crystal lattice on motion of energetic charged particles. *Kongel. Dan. Vidensk. Selsk. Mat. Fys. Medd.* **34**, 1–64 (1965).
6. Dyson, F. J. & Überall, H. Anisotropy of Bremsstrahlung and Pair Production in Single Crystals. *Phys. Rev.* **99**, 604–605 (2 1955).
7. Frisch, O. R. & Olson, D. N. Detection of Coherent Bremsstrahlung from Crystals. *Phys. Rev. Lett.* **3**, 141–142 (1959).
8. Diambrini-Palazzi, G. Interazioni di fotoni ed elettroni di alta energia in cristalli. *Nuovo Cim.* **25**, 88–99 (1962).
9. Kittel, C. *Introduction to solid state physics* 8th ed. ISBN: 9780471415268 (Wiley, 2005).
10. Baier, V. N., Katkov, V. M. & Strakhovenko, V. M. *Electromagnetic Processes at High Energies in Oriented Single Crystals* 1st ed. ISBN: 9789814502542 (World Scientific, 1998).
11. A Star Maths and Physics. <https://astarmathsandphysics.com>.
12. ExtrudeDesign.com. <https://extrudesign.com>.

13. Particle Data Group. <https://pdg.lbl.gov>.
14. Bandiera, L. *Study of coherent interactions between charged particle beams and crystals for beam steering and intense electromagnetic radiation generation*. PhD thesis (Università degli Studi di Ferrara, 2015).
15. Moliere, G. Theorie der Streuung schneller geladener Teilchen I. Einzelstreuung am abgeschirmten Coulomb-Feld. *Z. Naturforsch. A* **2**, 133–145 (1947).
16. Gemmell, D. S. Channeling and related effects in the motion of charged particles through crystals. *Rev. Mod. Phys.* **46**, 129–227 (1974).
17. Doyle, P. A. & Turner, P. S. Relativistic Hartree–Fock X-ray and electron scattering factors. *Acta Cryst. A* **24**, 390–397 (1968).
18. Bagli, E., Guidi, V. & Maisheev, V. A. Calculation of the potential for interaction of particles with complex atomic structures. *Phys. Rev. E* **81**, 026708 (2010).
19. Sørensen, A. H. & Uggerhøj, E. Channelling and channelling radiation. *Nature* **325**, 311–318 (1987).
20. Uggerhøj, U. I. The interaction of relativistic particles with strong crystalline fields. *Rev. Mod. Phys.* **77**, 1131–1171 (2005).
21. Kreiner, H. J. *et al.* Rosette motion in negative particle channelling. *Phys. Lett. A* **33**, 135–136 (1970).
22. Guidi, V., Mazzolari, A., De Salvador, D. & Carnera, A. Silicon crystal for channelling of negatively charged particles. *J. Phys. D* **42**, 182005 (2009).
23. Guidi, V., Bandiera, L. & Tikhomirov, V. Radiation generated by single and multiple volume reflection of ultrarelativistic electrons and positrons in bent crystals. *Phys. Rev. A* **86**, 042903 (2012).
24. Brandt, W. Channeling in Crystals. *Scientific American* **218**, 90–101 (1968).
25. Kumakhov, M. A. On the theory of electromagnetic radiation of charged particles in a crystal. *Phys. Lett. A* **57**, 17–18 (1976).
26. Andersen, S. K. *et al.* Influence of channeling on scattering of 2–15 GeV/c protons,  $\pi^+$ , and  $\pi^-$  incident on Si and Ge crystals. *Nuclear Physics B* **167**, 1–40 (1980).
27. Feldman, L. C. & Appleton, B. R. Multiple Scattering and Planar Dechanneling in Silicon and Germanium. *Phys. Rev. B* **8**, 935–951 (1973).

28. Carrigan, R. A. Negative particle planar and axial channeling and channeling collimation. *Int. J. Mod. Phys. A* **25**, 55–69 (2010).
29. Beloshitsky, V. V., Kumakhov, M. A. & Muralev, V. A. Multiple scattering of channeled ions in crystals. *Radiation Effects* **13**, 9–22 (1972).
30. Tanabashi, M. *et al.* Review of Particle Physics. *Phys. Rev. D* **98**, 030001 (2018).
31. Mazzolari, A. *et al.* Broad angular anisotropy of multiple scattering in a Si crystal. *Eur. Phys. J. C* **80**, 63 (2020).
32. Bonderup, E., Esbensen, H., Andersen, J. U. & Schiøtt, H. E. Calculations on axial dechanneling. *Radiation Effects* **12**, 261–266 (1972).
33. Wiedemann, H. *Particle Accelerator Physics* 4th ed. ISBN: 9783319183176 (Springer Cham, 2015).
34. Bethe, H., Heitler, W. & Dirac, P. A. M. On the stopping of fast particles and on the creation of positive electrons. *Proc. R. Soc. Lond. A* **146**, 83–112 (1934).
35. Fabjan, C. W. & Gianotti, F. Calorimetry for particle physics. *Rev. Mod. Phys.* **75**, 1243–1286 (2003).
36. Hansen, H. D. *et al.* Is the Electron Radiation Length Constant at High Energies? *Phys. Rev. Lett.* **91**, 014801 (2003).
37. Thomsen, H. D. *et al.* On the macroscopic formation length for GeV photons. *Phys. Lett. B* **672**, 323–327 (2009).
38. Shul’ga, N. F., Syshchenko, V. V. & Shul’ga, S. N. On spreading of high energy wave packets and development of radiation process by relativistic electron in space and time. *J. Phys. Conf. Ser.* **236**, 012001 (2010).
39. Andersen, J. U., Bonderup, E. & Pantell, R. H. Channeling Radiation. *Annu. Rev. Nucl. Part. Sci.* **33**, 453–504 (1983).
40. Klein, S. R. *et al.* A Measurement of the LPM Effect. *AIP Conf. Proc.* **302**, 172 (1994).
41. Baryshevsky, V. G. *et al.* On the influence of crystal structure on the electromagnetic shower development in the lead tungstate crystals. *Nucl. Instr. Meth. B* **402**, 35–39 (2017).
42. Wiedemann, H. *Electron-Photon Interaction in Dense Media* 1st ed. ISBN: 9789401003674 (Springer Dordrecht, 2002).

43. Walker, R. L. *et al.* Channeling and Coherent Bremsstrahlung Effects for Relativistic Positrons and Electrons. *Phys. Rev. Lett.* **25**, 5–8 (1970).
44. Kostyuk, A. Recent progress in the theory of the crystalline undulator. *Nucl. Instr. Meth. B* **309**, 45–49 (2013).
45. Motz, H. Applications of the Radiation from Fast Electron Beams. *J. Appl. Phys.* **22**, 527–535 (1951).
46. Bassani, F., Liedl, G. L. & Wyder, P. *Encyclopedia of Condensed Matter Physics* 1st ed. ISBN: 9780123694010 (Elsevier, 2005).
47. Brahme, A. *Comprehensive Biomedical Physics* 1st ed. ISBN: 9780444536334 (Elsevier, 2014).
48. Beloshitsky, V. V. & Kumakhov, M. A. Induced radiation of a beam of channeled relativistic particles. *Phys. Lett. A* **69**, 247–248 (1978).
49. Schwinger, J. On the Classical Radiation of Accelerated Electrons. *Phys. Rev.* **75**, 1912–1925 (1949).
50. Bandiera, L. *et al.* Strong Reduction of the Effective Radiation Length in an Axially Oriented Scintillator Crystal. *Phys. Rev. Lett.* **121**, 021603 (2018).
51. Diambrini-Palazzi, G. High-Energy Bremsstrahlung and Electron Pair Production in Thin Crystals. *Rev. Mod. Phys.* **40**, 611–631 (1968).
52. Apyan, A. *et al.* Coherent bremsstrahlung, coherent pair production, birefringence, and polarimetry in the 20–170 GeV energy range using aligned crystals. *Phys. Rev. Accel. Beams* **11**, 041001 (2008).
53. Chehab, R. *Positron sources for future colliders* <https://agenda.infn.it/event/11770>. (2016).
54. Born, M. Quantenmechanik der Stoßvorgänge. *Z. Phys.* **38**, 803–827 (1926).
55. Li, J., Wang, X. & Wang, T. On the Validity of Born Approximation. *Progress In Electromagnetics Research* **107**, 219–237 (2010).
56. Überall, H. Polarization of Bremsstrahlung from Monocrystalline Targets. *Phys. Rev.* **107**, 223–227 (1957).
57. Akhiezer, A. I. & Shul’ga, N. F. *High Energy Electrodynamics in Matter* 1st ed. ISBN: 9782884490146 (CRC Press, 1996).
58. Andersen, J. Channeling radiation and coherent bremsstrahlung. *Nucl. Instr. Meth.* **170**, 1–5 (1980).

59. Bak, J. *et al.* Channeling radiation from 2–55 GeV/c electrons and positrons: (I). Planar case. *Nucl. Phys. B* **254**, 491–527 (1985).
60. Soldani, M. *et al.* Next-generation ultra-compact calorimeters based on oriented crystals. *Proceedings of Science ICHEP2020*, 872 (2021).
61. Buchanan, M. Past the Schwinger limit. *Nat. Phys.* **2**, 721–721 (2006).
62. Ong, Y. C. Schwinger pair production and the extended uncertainty principle: can heuristic derivations be trusted? *Eur. Phys. J. C* **80**, 777 (2020).
63. Bulanov, S. S. *et al.* Schwinger Limit Attainability with Extreme Power Lasers. *Phys. Rev. Lett.* **105**, 220407 (2010).
64. Ruffini, R., Vereshchagin, G. & Xue, S.-S. Electron–positron pairs in physics and astrophysics: From heavy nuclei to black holes. *Phys. Rep.* **487**, 1–140 (2010).
65. Osmanov, Z., Machabeli, G. & Chkheidze, N. A Novel Mechanism of Pair Creation in Pulsar Magnetospheres. *Universe* **7**, 331 (2021).
66. Kirsebom, K. *et al.* Pair production by 5–150 GeV photons in the strong crystalline fields of germanium, tungsten and iridium. *Nucl. Instr. Meth. B* **135**, 143–148 (1998).
67. Baier, V. N., Katkov, V. M. & Strakhovenko, V. M. Production of Electron Positron Pairs by High-energy Photons in Oriented Crystals. *Sov. Phys. JETP* **63**, 467–475 (1986).
68. Baier, V. N., Katkov, V. M. & Strakhovenko, V. M. Theory of pair creation in aligned single crystals. *Nucl. Instr. Meth. B* **16**, 5–21 (1986).
69. Baier, V. N., Katkov, V. M. & Strakhovenko, V. M. Electromagnetic cascades developing along crystal axes. *Nucl. Instr. Meth. B* **119**, 131–136 (1996).
70. Bjorken, J. D. & Drell, S. D. *Relativistic Quantum Mechanics* 1st ed. ISBN: 9780070054936 (McGraw-Hill, 1965).
71. Jacob, M. & Wu, T. T. Coherent pair production in linear colliders. *Nucl. Phys. B* **327**, 285–306 (1989).
72. Moore, R. *et al.* Measurement of pair-production by high energy photons in an aligned tungsten crystal. *Nucl. Instr. Meth. B* **119**, 149–155 (1996).
73. Angst, M., Brückel, T., Richter, D. & Zorn, R. *Scattering methods for condensed matter research: towards novel applications at future sources* 1st ed. ISBN: 9783893367597 (Forschungszentrum Jülich GmbH Zentralbibliothek, 2012).



74. Belkacem, A. *et al.* Study of  $e^+e^-$  pair creation by 20–150-GeV photons incident on a germanium crystal in alignment conditions. *Phys. Rev. Lett.* **58**, 1196–1199 (12 1987).
75. Baryshevskii, V. G. *Channeling, radiation, and reactions in crystals at high energies* <https://ui.adsabs.harvard.edu/abs/1982IzMin...Q....B.> (1982).
76. Baryshevskii, V. G. & Tikhomirov, V. V. Synchrotron-type radiation processes in crystals and polarization phenomena accompanying them. *Sov. Phys. Usp.* **32**, 1013 (1989).
77. Baïer, V. N., Katkov, V. M. & Strakhovenko, V. M. Interaction of high-energy electrons and photons with crystals. *Sov. Phys. Usp.* **32**, 972 (1989).
78. Chehab, R. *Positron sources* tech. rep. LAL-RT-89-02 (1989).
79. Longo, E. & Sestili, I. Monte Carlo calculation of photon-initiated electromagnetic showers in lead glass. *Nucl. Instr. Meth.* **128**, 283–307 (1975).
80. Kölbig, K. S. *Gamma Function for Real Argument* tech. rep. CERNLIB-C303 (1992).
81. Bandiera, L., Haurylavets, V. & Tikhomirov, V. Compact electromagnetic calorimeters based on oriented scintillator crystals. *Nucl. Instr. Meth. A* **936**, 124–126 (2019).
82. Soldani, M. *et al.* Strong enhancement of electromagnetic shower development induced by high-energy photons in a thick oriented tungsten crystal. *Eur. Phys. J. C* **83**, 101 (2023).
83. Bologna, G., Diambrini, G. & Murtas, G. P. High-Energy Bremsstrahlung from a Silicon Single Crystal. *Phys. Rev. Lett.* **4**, 572–575 (1960).
84. Bologna, G., Diambrini, G. & Murtas, G. P. Electron Pair Production at High Energy in a Silicon Single Crystal. *Phys. Rev. Lett.* **4**, 134–135 (1960).
85. Belkacem, A. *et al.* Observation of Enhanced Pair Creation for 50–110-GeV Photons in an Aligned Ge Crystal. *Phys. Rev. Lett.* **53**, 2371–2373 (1984).
86. Belkacem, A. *et al.* Observation of Enhanced Pair Creation for 50–110-GeV Photons in an Aligned Ge Crystal. *Phys. Rev. Lett.* **54**, 852–852 (1985).
87. Cue, N. *et al.* Observation of Electric Synchrotron Radiation in a Crystal. *Phys. Rev. Lett.* **53**, 972–974 (1984).

88. Chehab, R *et al.* Experimental study of a crystal positron source. *Phys. Lett. B* **525**, 41–48 (2002).
89. Artru, X. *et al.* Summary of experimental studies, at CERN, on a positron source using crystal effects. *Nucl. Instr. Meth. B* **240**, 762–776 (2005).
90. Germogli, G., Mazzolari, A., Guidi, V. & Romagnoni, M. Bent silicon strip crystals for high-energy charged particle beam collimation. *Nucl. Instr. Meth. B* **402**, 308–312 (2017).
91. Bandiera, L. *et al.* Investigation on radiation generated by sub-GeV electrons in ultrashort silicon and germanium bent crystals. *Eur. Phys. J. C* **81**, 284 (2021).
92. Romagnoni, M. *et al.* Bent Crystal Design and Characterization for High-Energy Physics Experiments. *Crystals* **12**, 1263 (2022).
93. Bandiera, L. *et al.* Crystal-based pair production for a lepton collider positron source. *Eur. Phys. J. C* **82**, 699 (2022).
94. Ambrosino, F. *et al.* KLEVER: An experiment to measure  $\text{BR}(K_L \rightarrow \pi^0 \nu \bar{\nu})$  at the CERN SPS. arXiv: 1901.03099 [hep-ex] (2019).
95. Fedel, G. *Il tracciatore al silicio-tungsteno di AGILE: uno strumento innovativo per l'astronomia gamma* Thesis (Università degli Studi di Trieste, 2000).
96. Barbiellini, G. *et al.* The AGILE silicon tracker: testbeam results of the prototype silicon detector. *Nucl. Instr. Meth. A* **490**, 146–158 (2002).
97. Prest, M. *et al.* The AGILE silicon tracker: an innovative  $\gamma$ -ray instrument for space. *Nucl. Instr. Meth. A* **501**, 280–287 (2003).
98. Atwood, W. B. *et al.* The large area telescope on the Fermi Gamma-ray Space Telescope mission. *Astrophys. J.* **697**, 1071 (2009).
99. Annenkov, A. A., Korzhik, M. V. & Lecoq, P. Lead tungstate scintillation material. *Nucl. Instr. Meth. A* **490**, 30–50 (2002).
100. Soldani, M. *et al.* A high-performance custom photodetection system to probe the light yield enhancement in oriented crystals. *J. Phys. Conf. Ser.* **2374**, 012112 (2022).
101. Diener, R. *et al.* The DESY II test beam facility. *Nucl. Instr. Meth. A* **922**, 265–286 (2019).
102. Gatignon, L. *Design and Tuning of Secondary Beamlines in the CERN North and East Areas* tech. rep. CERN-ACC-NOTE-2020-0043 (2020).

103. Banerjee, D. *et al.* *The North Experimental Area at the CERN Super Proton Synchrotron* tech. rep. CERN-ACC-NOTE-2021-0015 (2021).
104. Backe, H., Kunz, P., Lauth, W. & Rueda, A. Planar channeling experiments with electrons at the 855MeV Mainz Microtron MAMI. *Nucl. Instr. Meth. B* **266**, 3835–3851 (2008).
105. Haensel, R. European Synchrotron Radiation Facility (ESRF). *Rev. Sci. Instrum.* **63**, 1571–1572 (1992).
106. Ziegler, E. *et al.* The ESRF BM05 Metrology Beamline: Instrumentation And Performance Upgrade. *AIP Conf. Proc.* **705**, 436–439 (2004).
107. Soldani, M. *MUonE: a high-energy scattering experiment to study the muon  $g-2$*  Thesis (Università degli Studi dell’Insubria, 2019).
108. Abbon, P. *et al.* The COMPASS experiment at CERN. *Nucl. Instr. Meth. A* **577**, 455–518 (2007).
109. Ceccucci, A. *et al.* *Proposal to measure the rare decay  $K^+ \rightarrow \pi^+ \nu \nu$  at the CERN SPS* tech. rep. CERN-SPSC-2005-013 (2005).
110. Cortina Gil, E. *et al.* The beam and detector of the NA62 experiment at CERN. *J. Instrum.* **12**, P05025 (2017).
111. Charitonidis, N. *et al.* The beam lines design for the CERN neutrino platform in the CERN north area and an outlook on their expected performance. *J. Phys. Conf. Ser.* **874**, 012056 (2017).
112. Efthymiopoulos, I. *Particle Beams for Fixed Target Experiments* <https://indico.cern.ch/event/115334/contributions/67588>. Intermediate Accelerator Physics Course (2011).
113. M1 Magnet in H2 Test Beam Area. <https://magnet-m1.web.cern.ch>.
114. Soldani, M. *The INSULAb telescope: a modular and versatile tracking system for beam tests* <https://indico.cern.ch/event/731649/contributions/3237202>. 7th Beam Telescopes and Test Beams Workshop (2019).
115. Aubert, B. *et al.* The BABAR detector. *Nucl. Instr. Meth. A* **479**, 1–116 (2002).
116. Lietti, D. *VISION: a Versatile and Innovative SiIicOn tracking system* PhD thesis (Università degli Studi dell’Insubria, 2015).
117. Ballerini, G., Pugliese, A. & Soldani, M. *INSULAb Telescope Characterization* internal rep. 2018.

118. Bonfanti, S. *The high resolution silicon telescope of the INSULAB group* Thesis (Università degli Studi dell'Insubria, 2012).
119. Ronchetti, F. *The new readout system of the ASACUSA scintillating tracker* Thesis (Università degli Studi dell'Insubria, 2022).
120. Soldani, M. *et al.* Enhanced electromagnetic radiation in oriented scintillating crystals at the 100-MeV and sub-GeV scales. *Proceedings of Science* **EPS-HEP2021**, 853 (2022).
121. Berra, A. *et al.* A SiPM based readout system for lead tungstate crystals. *Nucl. Instr. Meth. A* **732**, 380–383 (2013).
122. Biino, C. The CMS Electromagnetic Calorimeter: overview, lessons learned during Run 1 and future projections. *J. Phys. Conf. Ser.* **587**, 012001 (2015).
123. Raggi, M. *et al.* Performance of the PADME Calorimeter prototype at the DAΦNE BTF. *Nucl. Instr. Meth. A* **862**, 31–35 (2017).
124. Gianotti, P. The PADME Detector. *EPJ Web Conf.* **170**, 01007 (2018).
125. Photonis Photomultiplier Tubes Catalogue. <https://hallcweb.jlab.org/DocDB/0008/000809/001/PhotonisCatalog.pdf>.
126. L. Bomben. *Sistemi di tracking per fasci estratti di particelle* Thesis (Università degli Studi dell'Insubria, 2018).
127. Hamamatsu R9880U-110. [https://www.hamamatsu.com/eu/en/product/optical-sensors/pmt/pmt\\_tube-alone/metal-package-type/R9880U-110.html](https://www.hamamatsu.com/eu/en/product/optical-sensors/pmt/pmt_tube-alone/metal-package-type/R9880U-110.html).
128. SBS Model 618-3/620-3. <https://ecrin.com/datasheets/GEFIP/618-3.pdf>.
129. CAEN V1720. <https://www.caen.it/products/v1720>.
130. Bandiera, L. *et al.* On the radiation accompanying volume reflection. *Nucl. Instr. Meth. B* **309**, 135–140 (2013).
131. Lietti, D., Berra, A., Prest, M. & Vallazza, E. A microstrip silicon telescope for high performance particle tracking. *Nucl. Instr. Meth. A* **729**, 527–536 (2013).
132. Jeckel, M. *Test beam check list* [https://indico.cern.ch/event/700663/contributions/2874577/attachments/1617340/2571297/Test\\_beam\\_check\\_list.pdf](https://indico.cern.ch/event/700663/contributions/2874577/attachments/1617340/2571297/Test_beam_check_list.pdf). H8 Beam Line Users Meeting (2018).
133. Selmi, A. *Electromagnetic Shower Development in Oriented Crystals* Thesis (Università degli Studi dell'Insubria, 2022).

134. Baryshevsky, V. G. & Tikhomirov, V. V. Crystal undulators: from the prediction to the mature simulations. *Nucl. Instr. Meth. B* **309**, 30–36 (2013).
135. INP BSU. <http://www.inp.bsu.by>.
136. Sytov, A. I., Tikhomirov, V. V. & Bandiera, L. Simulation code for modeling of coherent effects of radiation generation in oriented crystals. *Phys. Rev. Accel. Beams* **22**, 064601 (2019).
137. Bandiera, L., Bagli, E., Guidi, V. & Tikhomirov, V. V. RADCHARM++: A C++ routine to compute the electromagnetic radiation generated by relativistic charged particles in crystals and complex structures. *Nucl. Instr. Meth. B* **355**, 44–48 (2015).
138. Baier, V. N. & Katkov, V. M. Concept of formation length in radiation theory. *Phys. Rep.* **409**, 261–359 (2005).
139. Bandiera, L. *et al.* Broad and Intense Radiation Accompanying Multiple Volume Reflection of Ultrarelativistic Electrons in a Bent Crystal. *Phys. Rev. Lett.* **111**, 255502 (2013).
140. Tikhomirov, V. V. A Benchmark Construction of Positron Crystal Undulator. arXiv: 1502.06588 [physics.acc-ph] (2015).
141. *Guide for Physics Lists* <https://geant4-userdoc.web.cern.ch/UsersGuides/PhysicsListGuide/html/index.html>.
142. Chaikovska, I. *et al.* Positron sources: from conventional to advanced accelerator concepts-based colliders. *J. Instrum.* **17**, P05015 (2022).
143. Artru, X. *et al.* Polarized and unpolarized positron sources for electron–positron colliders. *Nucl. Instr. Meth. B* **266**, 3868–3875 (2008).
144. Blue, B. E. *et al.* Plasma-Wakefield Acceleration of an Intense Positron Beam. *Phys. Rev. Lett.* **90**, 214801 (2003).
145. Sievers, P. A stationary target for the CERN-neutrino-factory. *Nucl. Instr. Meth. A* **503**, 344–347 (2003).
146. Artru, X. *et al.* Investigations on a hybrid positron source with a granular converter. *Nucl. Instr. Meth. B* **355**, 60–64 (2015).
147. Craievich, P., Schaer, M., Vallis, N. & Zennaro, R. *FCC-ee Injector Study and the P3 Project at PSI* CHART Scientific Report (2021).
148. Sievers, P. *et al.* Positron source using channeling with a granular converter. *Polarized Positron 2011*, 117–129 (2012).

149. Chaikovska, I. *Crystal-based positron source for the lepton colliders* <https://agenda.infn.it/event/28874/contributions/169176>. 41th International Conference on High Energy Physics (2022).
150. Blondel, A. & Janot, P. FCC-ee overview: new opportunities create new challenges. *Eur. Phys. J. Plus* **137**, 92 (2022).
151. Seeman, J. T. The Stanford linear collider. *AIP Conf. Proc.* **249**, 2035–2081 (1992).
152. Phinney, N. *SLC Final Performance and Lessons* tech. rep. SLAC-PUB-8556 (2000).
153. Akai, K., Furukawa, K. & Koiso, H. SuperKEKB collider. *Nucl. Instr. Meth. A* **907**, 188–199 (2018).
154. Yamamoto, H. The International Linear Collider Project—Its Physics and Status. *Symmetry* **13**, 674 (2021).
155. Ohmi, K. CEPC and FCCee parameters from the viewpoint of the beam–beam and electron cloud effects. *Int. J. Mod. Phys. A* **34**, 1940001 (2019).
156. Guiducci, S. *Positron source options* <https://indico.cern.ch/event/719240/contributions/2966548>. Muon Collider Workshop (2018).
157. *SuperKEKB Collider Achieves the World’s Highest Luminosity* <https://www.bnl.gov/newsroom/news.php?a=117285>.
158. Nagoshi, H. *et al.* A design of an electron driven positron source for the international linear collider. *Nucl. Instr. Meth. A* **953**, 163134 (2020).
159. Metalary. <https://www.metalary.com>.
160. ISSP RAS. <https://issp.ac.ru>.
161. succolib. <https://github.com/mattiasoldani/succolib>. 2020.
162. anaKrys. <https://github.com/mattiasoldani/anaKrys>. 2021.
163. scipy.interpolate.make\_interp\_spline. [https://docs.scipy.org/doc/scipy/reference/generated/scipy.interpolate.make\\_interp\\_spline.html](https://docs.scipy.org/doc/scipy/reference/generated/scipy.interpolate.make_interp_spline.html).
164. *Book For Application Developers* <https://geant4-userdoc.web.cern.ch/UsersGuides/ForApplicationDeveloper/html/index.html>.
165. Hike Collaboration. *HIKE, High Intensity Kaon Experiments at the CERN SPS: Letter of Intent* tech. rep. CERN-SPSC-2022-031 (2022).

166. Cundy, D. C. The CERN neutral KAON CP violation experiment NA31. *Nucl. Phys. B Proc. Suppl.* **1**, 165–176 (1988).
167. Batley, J. R. *et al.* A precision measurement of  $\epsilon'/\epsilon$  in CP violating  $K^0 \rightarrow 2\pi$  decays tech. rep. CERN-SPSC-90-22 (2002).
168. Agrawal, P. *et al.* Feebly-interacting particles: FIPs 2020 workshop report. *Eur. Phys. J. C* **81**, 1015 (2021).
169. Buras, A. J., Uhlig, S. & Schwab, F. Waiting for precise measurements of  $K^+ \rightarrow \pi^+ \nu \bar{\nu}$  and  $K_L \rightarrow \pi^0 \nu \bar{\nu}$ . *Rev. Mod. Phys.* **80**, 965–1007 (2008).
170. Buras, A. J., Buttazzo, D. & Kneijens, R.  $K \rightarrow \pi \nu \bar{\nu}$  and  $\epsilon'/\epsilon$  in simplified new physics models. *Journal of High Energy Physics* **2015**, 166 (2015).
171. Buchalla, G. Kaon and charm physics: theory. *Flavor Physics for the Millennium*, 143–205 (2001).
172. Battaglia, M. *et al.* The CKM matrix and the unitarity triangle. arXiv: hep-ph/0304132 [hep-ex] (2003).
173. Dijk, M. W. U. v. *et al.* The K12 beamline for the KLEVER experiment. *J. Phys. Conf. Ser.* **1350**, 012092 (2019).
174. Lai, A. *et al.* A precise measurement of the direct CP violation parameter  $\text{Re}(\epsilon'/\epsilon)$ . *Eur. Phys. J. C* **22**, 231–254 (2001).
175. Bifani, S., Descotes-Genon, S., Vidal, A. R. & Schune, M.-H. Review of lepton universality tests in B decays. *J. Phys. G* **46**, 023001 (2018).
176. Altarelli, M. P. & Teubert, F. B physics at LHCb. *Int. J. Mod. Phys. A* **23**, 5117–5136 (2008).
177. Kou, E *et al.* The Belle II Physics Book. *Prog. Theor. Exp. Phys.* **2019**, 123C01 (2019).
178. Gatignon, L. *et al.* Report from the Conventional Beams Working Group to the Physics Beyond Collider Study and to the European Strategy for Particle Physics tech. rep. CERN-PBC-REPORT-2022-002 (2022).
179. Ahdida, C. *et al.* Findings of the Physics Beyond Colliders ECN3 Beam Delivery Task Force tech. rep. CERN-PBC-REPORT-2023-001 (2023).
180. Ahn, J. K. *et al.* Search for  $K_L \rightarrow \pi^0 \nu \bar{\nu}$  and  $K_L \rightarrow \pi^0 X^0$  Decays at the J-PARC KOTO Experiment. *Phys. Rev. Lett.* **122**, 021802 (2019).
181. Ahn, J. K. *et al.* Study of the  $K_L \rightarrow \pi^0 \nu \bar{\nu}$  Decay at the J-PARC KOTO Experiment. *Phys. Rev. Lett.* **126**, 121801 (2021).

182. *NA62 in cerca di nuova fisica con i kaoni* <https://w3.lnf.infn.it/na62-in-cerca-di-nuova-fisica-con-i-kaoni>.
183. Jeitler, M. The NA48 liquid-krypton calorimeter. *Nucl. Instr. Meth. A* **494**, 373–377 (2002).
184. Ceccucci, A. *et al.* The New Readout System of the NA62 LKr Calorimeter. *IEEE Trans. Nucl. Sci.* **62**, 2134–2140 (2015).
185. *AIDAInnova's Blue Sky R&D projects will look beyond the limits of existing detector technologies* <https://aidainnova.web.cern.ch/aidainnovas-blue-sky-rd-projects-will-look-beyond-limits-existing-detector-technologies>.
186. *Paving the way for a new generation of fine-sampling calorimeters using nanocomposite scintillating materials* <https://aidainnova.web.cern.ch/paving-way-new-generation-fine-sampling-calorimeters-using-nanocomposite-scintillating-materials>.
187. Van Dijk, M. & Rosenthal, M. *Target studies for the proposed KLEVER experiment* tech. rep. CERN-PBC-Notes-2018-002 (2018).
188. Battistoni, G. *et al.* Overview of the FLUKA code. *Ann. Nucl. Energy* **82**, 10–18 (2015).
189. Fanti, V. *et al.* The beam and detector for the NA48 neutral kaon CP violation experiment at CERN. *Nucl. Instr. Meth. A* **574**, 433–471 (2007).
190. Doble, N., Gatignon, L. & Grafström, P. A novel application of bent crystal channeling to the production of simultaneous particle beams. *Nucl. Instr. Meth. B* **119**, 181–191 (1996).
191. Princeton Scientific. <https://princetonscientific.com>.
192. Livan, M. & Wigmans, R. Misconceptions about Calorimetry. *Instruments* **1**, 3 (2017).
193. Fano, U. Ionization Yield of Radiations. II. The Fluctuations of the Number of Ions. *Phys. Rev.* **72**, 26–29 (1947).
194. Fabjan, C. W. & Schopper, H. *Particle Physics Reference Library: Volume 2: Detectors for Particles and Radiation* 1st ed. ISBN: 9783030353186 (Springer Cham, 2020).
195. Longo, S. *et al.* CsI(Tl) pulse shape discrimination with the Belle II electromagnetic calorimeter as a novel method to improve particle identification at electron–positron colliders. *Nucl. Instr. Meth. A* **982**, 164562 (2020).



196. Lee, S., Livan, M. & Wigmans, R. Dual-readout calorimetry. *Rev. Mod. Phys.* **90**, 025002 (2018).
197. Hulbert, M. *et al.* Effect of a preshower detector on calorimetry performance. *Nucl. Instr. Meth. A* **335**, 427–438 (1993).
198. Erni, W. *et al.* Technical Design Report for PANDA Electromagnetic Calorimeter (EMC). arXiv: 0810.1216 [physics.ins-det] (2008).
199. Torii, H. The ALICE PHOS calorimeter. *J. Phys. Conf. Ser.* **160**, 012045 (2009).
200. Brennan, T. *et al.* The BTeV electromagnetic calorimeter. *Nucl. Instr. Meth. A* **494**, 313–317 (2002).
201. Korzhik, M. *et al.* Ultrafast PWO scintillator for future high energy physics instrumentation. *Nucl. Instr. Meth. A* **1034**, 166781 (2022).
202. *Energy of Electrons and Photons (ECAL)* <https://cms.cern/detector/measuring-energy/energy-electrons-and-photons-ecal>.
203. Lustermann, W. The electromagnetic calorimeter of cms, summary and status. *J. Phys. Conf. Ser.* **160**, 012044 (2009).
204. Lecoq, P. *et al.* Lead tungstate (PbWO<sub>4</sub>) scintillators for LHC EM calorimetry. *Nucl. Instr. Meth. A* **365**, 291–298 (1995).
205. Borisevich, A. *et al.* PWO-II scintillation crystals for the PANDA electromagnetic calorimeter. *2008 IEEE Nucl. Sci. Conf. R.*, 2698–2700 (2008).
206. Novotny, R. W. *et al.* The PANDA Electromagnetic Calorimeter—A High-Resolution Detector Based on PWO-II. *IEEE Trans. Nucl. Sci.* **57**, 1441–1446 (2010).
207. Improvement of several properties of lead tungstate crystals with different doping ions. *Nucl. Instr. Meth. A* **402**, 75–84 (1998).
208. Fegan, S. *et al.* Assessing the performance under ionising radiation of lead tungstate scintillators for EM calorimetry in the CLAS12 Forward Tagger. *Nucl. Instr. Meth. A* **789**, 101–108 (2015).
209. MolTech. <http://www.mt-berlin.com>.
210. ESRF ID11. <https://www.esrf.fr/UsersAndScience/Experiments/StructMaterials/ID11>.
211. Soldani, M. *Strong light yield enhancement in oriented crystalline media for homogeneous calorimetry* <https://indico.cern.ch/event/981823/contributions/4295520>. 5th Technology and Instrumentation in Particle Physics conference (2021).

212. Piemonte, C. & Gola, A. Overview on the main parameters and technology of modern Silicon Photomultipliers. *Nucl. Instr. Meth. A* **926**, 2–15 (2019).
213. Renker, D. Geiger-mode avalanche photodiodes, history, properties and problems. *Nucl. Instr. Meth. A* **567**, 48–56 (2006).
214. Zappa, F., Tisa, S., Tosi, A. & Cova, S. Principles and features of single-photon avalanche diode arrays. *Sens. Actuator A Phys.* **140**, 103–112 (2007).
215. Soldani, M. *Risoluzione spaziale ed efficienza di sistemi di tracciamento veloci* Thesis (Università degli Studi dell’Insubria, 2016).
216. AdvanSiD ASD-RGB4S-P & ASD-NUV4S-P. <https://advansid.com/products/product-detail/asd-rgb-nuv-4s-p>.
217. AdvanSiD Sockets for CSP-SiPMs. <https://advansid.com/products/product-detail/sockets-for-csp-sipms>.
218. AdvanSiD ASD-EP-EB-N. <https://advansid.com/products/product-detail/asd-ep-eb-n>.
219. onsemi ArrayC Series. [https://www.mouser.it/datasheet/2/308/ARRAYC\\_SERIES\\_D-2309928.pdf](https://www.mouser.it/datasheet/2/308/ARRAYC_SERIES_D-2309928.pdf).
220. Selmi, A. *et al.* Experimental layout for the direct measurement of electromagnetic shower acceleration in an oriented crystal scintillator. *Nucl. Instr. Meth. A* **1048**, 167948 (2023).
221. onsemi C-Series SiPM Sensors. <https://www.onsemi.com/pdf/datasheet/microc-series-d.pdf>.
222. succosim. <https://github.com/mattiasoldani/succosim>. 2021.
223. Cifarelli, L. *Scientific Papers of Ettore Majorana: A New Expanded Edition* 1st ed. ISBN: 9783030235093 (Springer Cham, 2020).
224. Monti-Guarnieri, P. *Beamtest characterization of oriented crystals for the KLEVER Small Angle Calorimeter* Thesis (Università degli Studi dell’Insubria, 2023).
225. matplotlib.pyplot.tricontourf. [https://matplotlib.org/stable/api/\\_as\\_gen/matplotlib.pyplot.tricontourf.html](https://matplotlib.org/stable/api/_as_gen/matplotlib.pyplot.tricontourf.html).
226. Bandiera, L. *et al.* Investigation on steering of ultrarelativistic  $e^\pm$  beam through an axially oriented bent crystal. *Eur. Phys. J. C* **81**, 238 (2021).
227. Alharthi, F. *et al.* Target Studies for the FCC- $ee$  Positron Source. *Proc. 13th International Particle Accelerator Conference*, 1979–1982 (2022).

- 228. anaMamiTools. <https://github.com/mattiasoldani/anaMamiTools>. 2022.
- 229. Lienhard IV, J. H. & Lienhard V, J. H. *A Heat Transfer Textbook* 5th ed (Phlogiston Press, 2020).
- 230. Stefan, J. Über die Beziehung zwischen der Wärmestrahlung und der Temperatur. *Sitzungsber. Kaiserl. Akad. Wiss. Math. Naturwiss. Cl. II. Abth.* **79**, 391–428 (1879).

# Hall of Fame

Congratulations! Either venturing alongside me in my PhD years or following in my footsteps as a reader, you have made it to the very end of this academic odyssey.

This formidable quest demanded that I face every side of myself, daring to embrace my own potential to the fullest and at the same time confronting the demons inside me – as well as a fairly good deal of demons outside. Altogether, I was given the (inevitable and yet invaluable) chance to explore the whole spectrum of my own selves. I am most grateful to the Nature for my best self, which I learned to always aspire to. At the same time, this journey taught me how to acknowledge and tame my worst self, despite steadfastly adhering to our differences, as it might prove a proficient teacher and a powerful companion.

Whether you have been a mentor, a colleague, family, a friend, a lover, my significant other, I thank you, fellow adventurer, for standing by my side, both accompanying me in my journey towards my best self – as a researcher and as a human being – and joining forces with me to counter my worst self. And I thank you, reader, for turning to this work in the course of your own quest, whatever it may be.

Perhaps our intrinsic complexity merely reflects the fact that reality itself is multifaceted and puzzling. Indeed, I thank the Nature for existing in such an eclectic shape: it is owing to this shape that we have particles, people, and all the other wonders.

